

IMPERIAL COLLEGE LONDON

DEPARTMENT OF MATHEMATICS

---

# Linear stability and numerical analysis of dipolar vortices and topographic flows

---

*Author:*

Jack Davies

*Supervisor:*

Prof. Pavel Berloff

This thesis is submitted for the degree of *Doctor of Philosophy*

---

## Declaration

The contents of this thesis are a combination of my own original work and the collaboration of works with other people. The material discussed is motivated by both an incomplete understanding surrounding the stability of steady state dipoles in a quasi-geostrophic model, as well as wanting to expand on the research dealing with topographic flows. Many of the topics and ideas presented in this thesis consist of material that is planned for future publications, while currently, the following publications partially contribute to the research presented in this document:

- *Linear stability analysis for flows over sinusoidal bottom topography*, by J. Davies, H. Khatri and P. Berloff (Journal of Fluid Mechanics, 2021),
- *On the spontaneous symmetry breaking of eastward propagating dipoles*, by J. Davies, G. Sutyrin and P. Berloff (Physics of Fluids Letter, 2023),

Again, the work presented in this thesis is my own original work and has not been submitted for the award of degree or diploma or any other qualification at Imperial College London or any other institution.

---

## Copyright

The copyright of this thesis rests with the author. Unless otherwise indicated, its contents are licensed under a Creative Commons Attribution-NonCommercial 4.0 International Licence (CC BY-NC).

Under this licence, you may copy and redistribute the material in any medium or format. You may also create and distribute modified versions of the work. This is on the condition that: you credit the author and do not use it, or any derivative works, for a commercial purpose.

When reusing or sharing this work, ensure you make the licence terms clear to others by naming the licence and linking to the licence text. Where a work has been adapted, you should indicate that the work has been changed and describe those changes.

Please seek permission from the copyright holder for uses of this work that are not included in this licence or permitted under UK Copyright Law.

---

## Abstract

The linear stability and numerical analysis of geophysical flow patterns is carried out on the  $\beta$ -plane in a quasigeostrophic approximation. We consider initial steady state dipoles in a one-and-a-half-layer model that are capable of zonal drift in either direction. Despite previous numerical works suggesting that eastward propagating dipoles are stable, our high resolution simulations identify the spontaneous symmetry breaking of weak dipoles over time. The evolution is associated with a growing critical mode with even symmetry about the zonal axis. On carrying out a linear stability analysis, the critical modes obtained share consistency with the numerical fields. In addition, both methods of analysis show that the linear growth rate is inversely proportional to the dipole intensity. Furthermore, the partner separation becomes more pronounced after the linear growth stage, suggesting that nonlinear effects play a pivotal role in the underlying dynamics. Beyond this, the dynamics of initially tilted dipoles and dipole-rider solutions are considered, while stronger dipoles are further analysed using the method of distillation.

Flows over sinusoidal bottom relief are considered in a two-layer model on the quasigeostrophic beta-plane. Fourier mode solutions are assumed for the layer-wise perturbation field in order to carry out a linear stability analysis, from which a coupled eigenproblem is derived between fluid columns for both zonal and meridional bottom irregularities. The presence of zonally oriented multiple ridges stabilises an otherwise unstable homogeneous zonal current with respect to increases in the number of ridges and ridge amplitude. Moreover, a bifurcation occurs in the unstable mode spectra and is dependent on the number of ridges. The critical eigenmodes in this case are found to be eddy chains of alternating sign, and these share remarkable resemblance with those obtained numerically. Meridionally oriented multiple ridges are also considered, but are found not to affect the maximum growth rate directly.



---

## Acknowledgements

I would like to express my deepest gratitude to my PhD supervisor, Prof. Pavel Berloff, for his guidance, support, and encouragement throughout my doctoral studies. His expertise, wisdom, and patience were instrumental in shaping my research ideas and helping me overcome many challenges along the way. His intellectual generosity has been a great asset during this journey and has helped me develop as a researcher. I am extremely grateful to Dr. Georgi Sutyrin, for spending countless hours discussing the fascinating problems that have made up my research. Your ability to challenge my mind and spark ideas in my head has been invaluable to me, and it has honestly made me enjoy the final stages of putting this thesis together.

I am indebted to Dr. Igor Schevchenko, for his support and feedback during my PhD, and his help in performing computationally expensive linear stability calculations. I am thankful to Matthew Crowe for discussing the dipole problem in depth with me on a few occasions and carrying out computations for me to compare with. I owe a lot to Hermant Khatri, who interacted with me during the early stages of my PhD and was always happy to discuss geophysical fluid dynamics with me.

I would like to thank my parents, Natalie and Paul, for their unwavering love and support throughout my life. Their sacrifices and belief in my abilities have been a constant source of inspiration and motivation for me. I owe them everything I have achieved in my academic and personal life, and without them I would not be half the man I am proud to be. I would like to thank my brother, Ryan, for his constant encouragement and support, and for being someone I can relax and watch anime with. His inspiring work ethic is something that has motivated me throughout my studies.

Finally, I would like to express my gratitude to my beautiful girlfriend, Jenny, for her love, patience, and understanding during this challenging time. Her unwavering support and belief in me have been invaluable in keeping me motivated and focused. My love for you is endless and I am excited to devote more time to our relationship with the conclusion of this thesis. You are the light that has helped me through this journey, and I am the luckiest man in the world to have you in my life.

# List of Figures

2.1	(a) : Bessel function of the first kind; (b) : modified Bessel function of the first kind. . . . .	14
2.2	LRD fields with $\beta = 0.4$ and $c = 0.1$ : (a) shows $\Psi(x, y)$ and (b) shows $Q(x, y)$ . . . . .	15
2.3	LRD-rider fields with $\beta = 0.4$ and different values of $\kappa$ : the left hand side shows streamfunctions, while the right-hand side shows PVA profiles. Panels (a) and (c) correspond to $\kappa = 0.01$ ; (b) and (d) correspond to $\kappa = 0.05$ and (c) and (e) correspond to $\kappa = 0.1$ . . . . .	18
3.1	Nondimensional dipole PV snapshots at: $t = t_s - T$ (panels (a) and (d), where $T$ is the period of oscillation of a growing anomaly on the dipole, as described later), $t = t_s$ (panels (b) and (e)) and $t = t_s + T$ (panels (c) and (f)): top panels correspond to the base problem; bottom panels correspond to solutions in the presence of a no-through-flow zonal wall. Solutions are obtained using parameters in table 3.1 with $\beta = 0.4$ , and the numerical solutions are shown in a fixed frame of reference. . . . .	29
3.2	Invariant plots for a dipole with $\beta = 0.4$ up to $t = t_s$ : (a) energy, (b) enstrophy, (c) maximum PV, (d) $y$ -momentum, (e) $x$ -momentum, (f) PV integral in the upper-half plane (if the corresponding quantity in the lower half is denoted by $M_2$ , then $M = M_1 + M_2$ ). Red curves correspond to solutions with $N = 1024$ and blue curves correspond to solutions with $N = 2048$ . . . . .	30
3.3	Invariant plots for a $\beta = 0.4$ dipole in the presence of a no-flow-through zonal wall between the eddy cores, up until the value of $t_s \sim 215$ (the characteristic time of partner separation for the same dipole without a wall), with $N = 2048$ : (a) energy; (b) enstrophy; (c) $y$ -momentum; (d) $x$ -momentum. . . . .	31

3.4	Time series for dipoles with $\beta = 0.4$ (red) and $\beta = 0.3$ (blue), where $t_s$ is the characteristic time of dipole separation ( $t_s \sim 215$ for $\beta = 0.4$ and $t_s \sim 327$ for $\beta = 0.3$ ): panel (a) shows the zonal propagation velocity, panel (b) shows the meridional center coordinate, panel (c) shows the zonal extrema difference and panel (d) shows the meridional extrema difference (adjusted to start at unity) . . . . .	33
3.5	CABARET PV solutions for the $f$ -plane dipole in the presence of $\beta = 0.4$ : the top rows correspond to the problem described, while panels in the bottom row include a zonal wall between the vortex pair. Snapshots (a) and (e) are taken at $t = 12.5$ , snapshots (b) and (f) are taken at $t = 25$ , snapshots (c) and (g) are taken at $t = 37.5$ and snapshots (d) and (h) are taken at $t = 50$ . . . . .	35
3.6	Fig. 11 in <a href="#">Sutyrin et al. (1994)</a> : (a) panels show the PVA fields, (b) panels show the corresponding streamfunction fields. PVA panels are consistent with our CABARET solutions for the same problem. . . . .	36
3.7	PV solutions for an eastward propagating dipole with $\beta = 0.4$ , at $t \sim 175$ (the value of $t_s$ for $\beta = 0.4$ using $N = 1024$ ): (a) shows the result in a (60, 15)-domain with $4096 \times 1024$ grid points; (b) shows the result in a (120, 30)-domain with $8192 \times 2048$ grid points. . . . .	37
3.8	PV snapshots in a fixed reference frame for a dipole with an intensity of $c/\beta = 1/2$ : (a) $t \sim 200$ ; (b) $t \sim 300$ ; (c) $t \sim 400$ ; (d) $t \sim 500$ . . . . .	38
3.9	PV snapshots of a strong dipole, $c/\beta = 1$ : (a) $t \sim 200$ ; (b) $t \sim 400$ ; (c) $t \sim 600$ . There does not appear to be any significant deviation in the dipole state, and any small deceleration and partner separation could be due to numerical viscosity. . . . .	39
3.10	Time-series for a dipole with an intensity of $c/\beta = 1$ using $N = 2048$ : (a) shows the zonal propagation speed; (b) shows the meridional center coordinate; (c) shows the zonal extrema difference; (d) shows the meridional extrema difference (adjusted to start at unity). Blue curves are for a (120, 30) domain and red curves are for a (60, 15) domain. The $t$ -domain considered is used so that the dipole in the larger domain does not transition through the periodic boundary, and we plot the small domain results for this same value of $t$ for a consistent comparison. . . . .	40
3.11	Dipole-rider snapshots with $\beta = 0.4$ and $\kappa = 0.01$ , in a (60, 15) domain with $N = 2048$ : (a) $t \sim 45$ ; (b) $t \sim 90$ ; (c) $t \sim 135$ ; (d) $t \sim 180$ . . . . .	42

3.12	Dipoles-rider snapshots with $\beta = 0.4$ and $\kappa = 0.1$ , in a $(60, 15)$ domain with $N = 2048$ : (a) $t \sim 60$ ; (b) $t \sim 105$ ; (c) $t \sim 150$ ; (d) $t \sim 195$ ; (e) $t \sim 240$ ; (f) $t \sim 285$ ; (g) $t \sim 320$ ; (h) $t \sim 365$ . . . . .	43
3.13	Time-series for a dipole-rider vortex with $\beta = 0.4$ and $\kappa = 0.1$ , computed in a $(60, 30)$ domain using $N = 2048$ : (a) shows the zonal propagation speed; (b) shows the meridional center coordinate; (c) shows the zonal extrema difference; (d) shows the meridional extrema difference (adjusted to start at unity). . . . .	44
4.1	Snapshots of the growing PVA perturbation field over a full cycle in the co-moving reference frame, with $\beta = 0.4$ : (a) – (i) correspond to $t \sim 143 - 159$ , respectively (panels are with equal time interval $\sim 2$ ). . . . .	47
4.2	Perturbation pattern corresponding to the dipole propagation in the presence of a no-flow-through wall along the zonal axis. This pattern accumulates as a consequence of implicit numerical viscosity. The value of $t$ for which this pattern is taken is within $t \sim 143 - 159$ . . . . .	48
4.3	Snapshots of the growing S-component of PVA for $\beta = 0.4$ , shown over the oscillation period and in the co-moving reference frame: (a) – (i) correspond to $t \sim 143 - 159$ , respectively, and panels are separated by the same time interval $\sim 2$ . Since these patterns share the same symmetry as the numerical viscous accumulation in Fig. 4.2, we expect the numerical viscous contributions to be collected in these S-components. . . . .	50
4.4	Time series for dipoles with $\beta = 0.4$ (red), $\beta = 0.3$ (blue) and $\beta = 0.2$ (black): panel (a) shows the logarithm of enstrophy for the A-component and panel (b) shows the corresponding length scale $L_A = \sqrt{E_A/Z_A}$ . Time intervals differ since weaker dipoles see earlier disintegration. . . . .	51
4.5	Snapshots of the growing A-component of the PVA field for $\beta = 0.4$ , shown over the oscillation period and in the co-moving reference frame: (a) – (i) correspond to $t \sim 143 - 159$ , respectively, and panels are separated by the same time interval $\sim 2$ . . . . .	52
4.6	Period-averaged profiles for the A-component snapshots: (a) is obtained by evaluating the mean over a period of oscillation; (b) is obtained using (4.12) and is consistent with (4.14). . . . .	54
4.7	Reconstruction of the complex-valued critical mode: (a) real part $A(x, y)$ , and (b) imaginary part $B(x, y)$ . . . . .	55

4.8	Linear modes extracted from numerical snapshots using the normal mode decomposition (4.4): (a) – (i) correspond to $t \sim 143 - 159$ , respectively, and panels are separated by the same time interval $\sim 2$ . These panels share remarkable consistency with those presented in Fig. 4.5. . . . .	56
4.9	Curves comparing $\beta = 0.4$ solutions with either numerical viscosity (yellow and purple curves) or Newtonian viscosity (red and blue curves), using $N = 1024$ (purple curve) and $N = 2048$ (red, blue and yellow curves): (a) shows time-series for $\log(Z_S)$ and (b) shows the time-series for $Z_A$ . . . . .	57
4.10	PVA representation of A-components corresponding to $\beta = 0.1$ , in a (60, 15) domain with $N = 2048$ : (a) $t \sim 100$ ; (b) $t \sim 200$ ; (c) $t \sim 400$ ; (d) $t \sim 600$ (fields are centred in the co-moving reference frame). . .	59
4.11	Solutions for $\beta = 0.1$ in a (120, 30) domain with $8192 \times 2048$ grid points: (a) $t \sim 100$ ; (b) $t \sim 200$ ; (c) $t \sim 400$ ; (d) $t \sim 600$ (fields are centred in the co-moving reference frame). . . . .	60
4.12	Time series for $\beta = 0.1$ dipoles in a (60, 15) domain (blue) and a (120, 30) domain (red), using $N = 2048$ : panel (a) shows the logarithm of enstrophy for the A-component and panel (b) shows the corresponding length scale $L_A = \sqrt{E_A/Z_A}$ . . . . .	61
4.13	Curves describing the results for various distillation experiments, where strong dipoles are perturbed by a Davies mode extracted at $\beta = 0.1$ (scaled by a multiple of 3): (a) shows the logarithm of enstrophy for the A-components; (b) shows the time-series for $L_A$ . . . . .	62
5.1	Eigenfunctions for the dipole problem in a (15, 15) domain with $\beta = 0.4$ and $N = 512$ : panels (a) and (c) show the real part of the amplitude function for the streamfunction and PVA perturbations, respectively, while panels (b) and (d) show the imaginary part of the amplitude function for the streamfunction and PVA perturbations, respectively. The growth rate for the critical Davies mode is $\sigma \sim 0.025$ and the period is $T \sim 17$ . . . . .	70

5.2	Eigenfunctions for the dipole problem in a $(7.5, 7.5)$ domain with $\beta = 0.4$ and $N = 512$ : panels (a) and (c) show the real part of the amplitude function for the streamfunction and PVA perturbations, respectively, while panels (b) and (d) show the imaginary part of the amplitude function for the streamfunction and PVA perturbations, respectively. The growth rate for the Davies mode is $\sigma \sim 0.027$ and the period is $T \sim 17$ . . . . .	71
5.3	Eigenspectra associated with linear stability solutions: (a) corresponds to a domain of $(15, 15)$ ; (b) corresponds to a domain of $(7.5, 7.5)$ . As a consequence of symmetry, we only present unstable modes in the positive half-plane. . . . .	72
5.4	PVA snapshots of the linear Davies mode corresponding to Fig. 5.2: (a) – (i) correspond to $t \sim 143 - 159$ , respectively, and panels are separated by the same time interval $\sim 2$ . These are consistent with the numerical results of Davies et al. (2023). . . . .	73
5.5	Eigenfunctions for the dipole problem in a $(7.5, 7.5)$ domain with $\beta = 0.3$ and $N = 512$ : panels (a) and (c) show the real part of the amplitude function for the streamfunction and PVA perturbations, respectively, while panels (b) and (d) show the imaginary part of the amplitude function for the streamfunction and PVA perturbations, respectively. The growth rate for the critical mode is $\sigma \sim 0.015$ and the period is $T \sim 18$ . . . . .	74
5.6	Signals associated with the linear stability analysis of weak dipoles: (a) shows the logarithm of enstrophy for the critical eigenfunction; (b) shows the values of $L_A$ for the critical eigenfunction. . . . .	75
5.7	Eigenfunctions for the dipole problem in a $(7.5, 7.5)$ domain with $\beta = 0.2$ and $N = 512$ : panels (a) and (c) show the real part of the amplitude function for the streamfunction and PVA perturbations, respectively, while panels (b) and (d) show the imaginary part of the amplitude function for the streamfunction and PVA perturbations, respectively. The growth rate for the critical mode is $\sigma \sim 0.009$ and the period is $T \sim 19$ . . . . .	76

5.8	Eigenfunctions for the dipole problem in a $(7.5, 7.5)$ domain with $\beta = 0.15$ and $N = 512$ : panels (a) and (c) show the real part of the amplitude function for the streamfunction and PVA perturbations, respectively, while panels (b) and (d) show the imaginary part of the amplitude function for the streamfunction and PVA perturbations, respectively. The growth rate for the critical mode is $\sigma \sim 0.007$ and the period is $T \sim 20$ . . . . .	77
5.9	Eigenfunctions for the dipole problem in a $(7.5, 7.5)$ domain with $\beta = 0.1$ and $N = 512$ : panels (a) and (c) show the real part of the amplitude function for the streamfunction and PVA perturbations, respectively, while panels (b) and (d) show the imaginary part of the amplitude function for the streamfunction and PVA perturbations, respectively. The growth rate for the critical mode is $\sigma \sim 0.006$ and the period is $T \sim 90$ . . . . .	78
5.10	Eigenfunctions for the dipole problem in a $(7.5, 7.5)$ domain with $\beta = 0.1$ and $N = 512$ : panels (a) and (c) show the real part of the amplitude function for the streamfunction and PVA perturbations, respectively, while panels (b) and (d) show the imaginary part of the amplitude function for the streamfunction and PVA perturbations, respectively. The growth rate for the critical mode is $\sigma \sim 0.004$ and the period is $T \sim 21$ . . . . .	80
6.1	Period-averaged profiles associated with a weak dipole defined by $\beta = 0.4$ in a $(60, 15)$ domain ( $N = 2048$ ): (a) shows $\overline{F}_x$ , the zonal PV flux; (b) shows $\overline{F}_y$ , the meridional PV flux; (c) shows $\overline{I}$ , the nonlinear-self interaction. . . . .	83
6.2	Integral value diagram associated with $\overline{I}$ , describing how the overall PV content is rearranged due to a growing critical Davies mode. The size of arrows is not to scale, but describes the magnitude of net PV flux in the horizontal and meridional directions across the zonal and meridional segments. The circular boundary has unit radius. . . . .	85
6.3	Energy exchange values averaged over a period of oscillation for the critical Davies mode. Negative regions correspond to energy extracted by the perturbation field, while positive regions correspond to energy extracted by the dipole. . . . .	86

6.4	Components of the energy exchange in Fig.6.3, in terms of M- and N-components: (a) shows $(MN)_x$ ; (b) shows $(MN)_y$ ; (c) shows $(NM)_x$ ; (d) shows $(NM)_y$ . . . . .	89
7.1	Panels illustrating physical fields associated with a $(\beta, \xi) = (0.2, 5^\circ)$ tilted dipole: (a) shows the A-component of the PVA; (b) shows the S-component of the PVA; (c) shows the full PVA field (the sum of (a) and (b)); (d) shows the full PV field. . . . .	92
7.2	Snapshots of the dipole propagation for various values of $\beta$ and $\xi$ , using the Dedalus Python package with $N = 2048$ (results are consistent with CABARET simulations): rows correspond to values of $\xi$ , increasing from top to bottom ( $\xi = 5^\circ, 30^\circ, 45^\circ, 60^\circ, 90^\circ$ , respectively); columns correspond to values of $\beta$ , increasing from left to right ( $\beta = 0.1, 0.2, 0.35$ , respectively). . . . .	93
7.3	Comparison between CABARET (thick lines) and Dedalus (dotted lines) solutions (i.e., $y_c$ ) for tilted dipoles with $\beta = 0.2$ : black curves correspond to $\xi = 5^\circ$ ; blue curves correspond to $\xi = 30^\circ$ , red curves correspond to $\xi = 60^\circ$ ; yellow curves correspond to $\xi = 90^\circ$ . The consistency in these curves is a strong case for numerical convergence. . . . .	95
7.4	Panels illustrating physical fields associated with $\beta = 0.35$ and $\xi = 5^\circ$ (thick lines) and $\xi = 30^\circ$ (dotted lines): (a) shows the logarithms of $Z$ (blue) and $Z_A$ (red); (b) shows the length scales of $L_A$ (blue) and $L_S$ (red); (c) shows the zonal center difference, $\Delta x$ (blue) and the meridional center trajectory, $y_c$ (red); (d) shows the meridional center difference, $\Delta y$ (blue) and the rescaled zonal propagation velocity (red). . . . .	96
7.5	Time-series for invariants and derived quantities describing the $\beta = 0.2$ dipole dynamics (thick line) and the analogous dynamics with $\xi = 5^\circ$ (dotted line): (a) shows the logarithms of $Z$ (blue) and $Z_A$ (red); (b) shows the length scales of $L_A$ (blue) and $L_S$ (red); (c) shows the zonal center difference, $\Delta x$ (blue) and the meridional center trajectory, $y_c$ (red); (d) shows the meridional center difference, $\Delta y$ (blue) and the re-scaled zonal propagation velocity (red). The curves corresponding to no tilt continue up until $t \sim 500$ to illustrate the partner separation of the dipole. . . . .	97



7.6	Snapshots of $q_A$ for a dipole with $(\beta, \xi) = (0.2, 5^\circ)$ : (a) occurs at $t \sim 60$ , (b) occurs at $t \sim 120$ , (c) occurs at $t \sim 150$ , (d) occurs at $t \sim 180$ . The circular boundary is a unit circular to highlight deformations in the separatrix. . . . .	98
7.7	Upper panels show the PVA Davies mode development during $150 \leq t \leq 200$ , with $\beta = 0.2$ and $\xi = 5^\circ$ , for different phases over a period of oscillation. Bottom panels show the corresponding deformations of the dipole PVA: (a) elongates the cyclone and compresses the anticyclone, as seen in (e); (b) leads to less elongation in the cyclone more elongation in the anticyclone, looking as a tilted and deformed dipole in (f); (c) behaves as (a), but with the opposite effect on partners in (g); (d) behaves as (b), but with the opposite effect on partners in (h). . . . .	99
7.8	Time-series for invariants and derived quantities describing the $\beta = 0.2$ dipole dynamics with $\xi = 30^\circ$ (thick line) and $\xi = 45^\circ$ (dotted line): (a) shows the logarithms of $Z$ (blue) and $Z_A$ (red); (b) shows the length scales of $L_A$ (blue) and $L_S$ (red); (c) shows the zonal center difference, $\Delta x$ (blue) and the meridional center trajectory, $y_c$ (red); (d) shows the meridional center difference, $\Delta y$ (blue) and the re-scaled zonal propagation velocity (red). . . . .	101
7.9	Transitions in the A-component corresponding to $\beta = 0.2$ and $\xi = 30^\circ$ : (a) $t \sim 60$ , $q_m \sim 0.73$ ; (b) $t \sim 130$ , $q_m \sim 0.62$ ; (c) $t \sim 190$ , $q_m \sim 0.74$ ; (d) $t \sim 270$ , $q_m \sim 0.51$ . The circular boundary is a unit circular to highlight deformations in the separatrix. . . . .	102
7.10	Time-series for invariants and derived quantities describing the $\beta = 0.2$ dipole dynamics with $\xi = 60^\circ$ : (a) shows the logarithms of $Z$ (blue) and $Z_A$ (red); (b) shows the length scales of $L_A$ (blue) and $L_S$ (red); (c) shows the zonal center difference, $\Delta X$ (blue) and the meridional center trajectory, $y_c$ (red); (d) shows the meridional center difference, $\Delta y$ (blue) and the re-scaled zonal propagation velocity (red). . . . .	103
7.11	Transitions in the A-component corresponding to $\beta = 0.2$ and $\xi = 60^\circ$ : (a) $t \sim 60$ ; (b) $t \sim 130$ ; (c) $t \sim 190$ ; (d) $t \sim 270$ . . . . .	104
7.12	Strong dipole curves for $\beta = 0.1$ : (a) shows the logarithms of $Z_A$ with $\xi = 5^\circ$ (blue) and $\xi = 30^\circ$ (red); (b) shows the length scales of $L_A$ for the same values of $\xi$ . . . . .	105

- 8.1 Diagonal structure for the Jacobian matrix in a 1.5-layer system (areas of grey refer to null entries, and the colour shading indicates the magnitude of values, with red being positive and blue being negative). Doubly-periodic boundary conditions are assumed. . . . . 112
- 8.2 Jacobian structure for a 1.5-layer setup, in the presence of doubly-periodic boundary conditions and assuming the integral constraints (8.35). Areas of grey refer to null entries, and the colour shading indicates the magnitude of values, with red being positive and blue being negative. 113
- 9.1 The model domain for the two-layer problem. An eastward background velocity is imposed in the surface layer, with the bottom layer assumed to be at rest. Bottom topography, mean layer depths and density anomalies are denoted by  $\hat{\eta}_b$ ,  $\hat{H}_j$  and  $\hat{\rho}_j$ , respectively ( $j = 1, 2$  is the layer index). The positive  $\hat{x}$ -axis is directed to the right and the positive  $\hat{y}$ -axis points into the figure. . . . . 122
- 9.2 Sinusoidal topographies considered in our analysis. (a): zonally oriented multiple ridges (ZR), (b): meridionally oriented multiple ridges (MR). . . . . 124
- 9.3 ZR results for  $\mathcal{A} = 0.1$  and  $\alpha = 20$  (left panels) and  $\alpha = 30$  (right panels): the top row shows results obtained using  $N = 256$ , while the bottom row shows results obtained using  $N = 512$ . Consistency in the distribution of unstable modes between grids acts as strong evidence for convergence of our linear stability results. . . . . 129
- 9.4 Nondimensional growth rates  $\omega_i > 0$  over flat topography (corresponding parameter values can be found in table 9.1). (a):  $(\omega_i, \ell)$ -plot, with meridional phase speeds  $c_y = \omega_r/\ell$  shown in the colorbar (the speed decreases with increasing  $\ell$ ). (b):  $(\omega_i, k)$ -plot, with zonal phase speeds  $c_x = \omega_r/k$  shown in the colorbar (the speed increases with increasing  $k$ ). Modes are symmetric about  $k, \ell = 0$ ; and so growth rates for only positive wavenumbers are presented. . . . . 130
- 9.5  $(\omega_i, k)$ -plot in the presence of ZR, with  $\mathcal{A} = 0.1$  (corresponding parameters are given in table 9.1). Subplots a-h assume  $\alpha = 1, 3, 5, 10, 15, 20, 25, 30$ , respectively (maximum growth decreases and modes shift towards larger wavenumbers with increasing  $\alpha$ ). Zonal phase speeds are shown in the colorbar (the speed increase with increasing  $k$  and  $\alpha$  and approach the velocity  $U$  in the upper layer, but never exceed it). . . . . 131

- 9.6 Unstable mode distributions for a constant topography slope in  $y$  of value equal to 0.1 (meant to correspond to the ZR case with value of  $\mathcal{A} = 0.1$  used in the study). This shows that maximum growth rate increases compared to the flat bottom case, suggesting that for small  $\alpha$ , the maximum growth rate increases at first. The colorbar corresponds to (a): meridional phase speeds, (b): zonal phase speeds. 132
- 9.7 Equivalent to Fig. 9.5, but for  $\mathcal{A} = 0.2$  (maximum growth decreases, modes shift towards larger wavenumbers and zonal phase speeds increase with increasing values of  $\mathcal{A}$ ). . . . . 133
- 9.8  $(\alpha, \mathcal{A})$ -plot for the maximum growth rate in the presence of ZR. Nondimensional growth rates are shown in the colorbar. For  $\mathcal{A} = 0$  (flat bottom), the maximum growth rate is  $4.6 \times 10^{-3}$  (from Fig. 9.4). . . . . 135
- 9.9 Maximum growth rate contours in nondimensional  $(\alpha, k)$ -parameter space. Subplots **a-d** assume  $\mathcal{A} = 0.05, 0.1, 0.15, 0.2$ , respectively. Growth rates are shown in the colorbar, with white regions referring to zero growth). Two branches form near  $\alpha \approx 10$  for different zonal wavenumbers depending on the value of  $\mathcal{A}$  (these branches evaporate as  $\mathcal{A}$  gets larger). . . . . 136
- 9.10 Contour plots for the perturbation streamfunctions attached to the maximum growth rate in the presence of ZR, with  $\alpha = 1$ . (a): top and bottom layers with  $\mathcal{A} = 0.1$ , (b): top and bottom layers with  $\mathcal{A} = 0.2$ . Dashed black lines denote topographic slopes and symbols **P** and **T** represent peak and trough regions of topography, respectively. The colorbar range is [min, max] from blue to yellow. The zonal extent of eddies reduces in size with increasing  $\mathcal{A}$ . . . . . 137
- 9.11 Same as Fig. 9.10, but with  $\alpha = 3$ . Dashed black lines denote topographic slopes and symbols **P** and **T** represent peak and trough regions of topography, respectively. The eigenmodes are eddy-chains sitting on the northern slopes of topography. . . . . 138

- 9.12 Comparison with numerical simulations in the presence of ZR for  $\mathcal{A} = 0.05$  and  $\alpha = 3$  (a): Structure of eigenmodes (left and right panels for the top and bottom layers, respectively) corresponding to the maximum growth rate, (b): Snapshot of streamfunction field obtained on a  $1024^2$  simulation at roughly 1000 days with parameter values as in table 9.1 (left and right panels for the top and bottom layers, respectively). Dashed black lines denote topographic slopes and symbols **P** and **T** represent peak and trough regions of topography, respectively. The colorbar range is [min, max] from blue to yellow. There are remarkable similarities between the linear solution and numerical simulations, where the differences in spatial structure are attributed to nonlinearities. . . . . 139
- 9.13  $(\omega_i, \ell)$ -plot in the presence of MR, with  $\mathcal{A} = 0.1$  (see table 9.1 for parameter values). Subplots **a-h** assume  $\alpha = 1, 3, 5, 10, 15, 20, 25, 30$ , respectively (maximum growth remains constant and the distribution of unstable modes shifts towards larger wavenumbers with increasing  $\alpha$ ). Meridional phase speeds are shown in the colorbar (magnitude of speeds increase with increasing  $\ell$  and  $\alpha$ ). When  $\alpha = 15$ , a second maximum occurs and weakens with increases in  $\alpha$ . . . . . 140
- 9.14 Same as Fig. 9.13, but with  $\mathcal{A} = 0.2$  (magnitude of phase speeds increase with increasing  $\mathcal{A}$ ). A second maximum appears for different values of  $\alpha$ . . . . . 141
- 9.15 Nondimensional  $(\alpha, \ell)$ -contour plot for the maximum growth rate in the presence of MR. Plots **a-d** assume  $\mathcal{A} = 0.05, 0.1, 0.15, 0.2$ , respectively. Growth rates are shown in the colorbar (with white regions referring to zero growth rate) and these appear to decrease for larger  $\ell$  with increasing  $\mathcal{A}$ . . . . . 141
- 9.16 Eigenmodes corresponding to maximum growth with MR, with  $\alpha = 1$  (ridges are represented by dashed black lines and (**P** denotes the topographic peak). Plots **a, b** refer to  $\mathcal{A} = 0.1, 0.2$ , respectively. The left (right) snapshot denotes the upper (lower) layer. We restrict attention to half an oscillation of topography only as the pattern repeats. Since the maximum growth rate does not change in the presence of MR, the streamfunctions are independent of  $\alpha$  and  $\mathcal{A}$ . Black dashed lines represent topographic slopes. . . . . 142

- 9.17 Numerical simulations with MR for  $\mathcal{A} = 0.05$ , run on a  $1024^2$  grid using parameter values as in table 9.1. **(a)**: Snapshot of streamfunction field for  $\alpha = 1$ , **(b)**: Snapshot of streamfunction field for  $\alpha = 3$ , **(c)**: Snapshot of streamfunction field for  $\alpha = 15$ . The left (right) snapshot denotes the upper (lower) layer and the colorbar range is  $[\min, \max]$  from blue to yellow. Topographic slopes are not illustrated so differences in spatial structure can be easily identified. . . . . 143
- 9.18 The number of unstable modes (top plots) and the sum of positive growth rates (bottom plots) as functions of  $\alpha$ . **(a)**: in the presence of ZR, **(b)**: in the presence of MR. . . . . 144
- 9.19 Thin-upper-layer configuration for ZR with  $\mathcal{A} = 0.1$ . Subplots **a-h** assume  $\alpha = 1, 3, 5, 10, 15, 20, 25, 30$ , respectively. The maximum growth rate increases for small values of  $\alpha = 1, 3$  and then decreases in the proceeding panels ( $\alpha \geq 5$ ). The distribution splits into two clusters, each having a distinct maximum. The maximum of the first cluster is greatly suppressed with increases in  $\alpha$  relative to the weakly suppressed second cluster maxima. The zonal phase speeds are shown in the colorbar. . . . . 146
- 9.20 Thin-upper-layer configuration for ZR with  $\mathcal{A} = 0.2$ . Subplots **a-h** assume  $\alpha = 1, 3, 5, 10, 15, 20, 25, 30$ , respectively. The maximum growth rate increases for  $\alpha = 1$  and then decreases in the proceeding panels ( $\alpha \geq 3$ ). The distribution splits into two clusters, each with distinct maximum. Both cluster maxima weaken with increases in  $\alpha$ ; the decrease in the first cluster being greater than in the second. Comparing with Fig. 9.19, the first cluster maximum is enhanced with increased  $\mathcal{A}$ , while the second cluster maximum is depressed. The zonal phase speeds are shown in the colorbar. . . . . 147

# List of Tables

3.1	Parameter model for numerical simulations of eastward propagating dipoles, where symbols notated with a hat are dimensional, and otherwise nondimensional. Results are computed in a $4L_y \times L_y$ domain and on a $4N \times N$ uniform square grid. If different values are used for an experiment, this will be emphasised in the text. . . . .	28
3.2	Invariant values for various values of $t$ , obtained using $N = 2048$ and $\beta = 0.4$ (we assume the absence of a no-flow through zonal wall). . .	31
9.1	Main parameter values chosen for the linear stability analysis presented in this chapter, assuming equal layer depths. Alternative parameter values used are mentioned in the main text. . . . .	127
9.2	Comparison of the maximum growth rate and corresponding magnitudes of the zonal wavenumbers and zonal phase speeds for the same values of $\mathcal{A}\alpha$ . Initially, small increases in $\alpha$ contribute most to baroclinic stabilisation process. However, for larger increases in $\alpha$ , increases in $\mathcal{A}$ are more efficient at stabilising the system. . . . .	134

# Contents

<b>1</b>	<b>Introduction</b>	<b>1</b>
1.1	Coherent vortices . . . . .	1
1.2	Topographic flows . . . . .	5
1.3	Structure . . . . .	7
<b>2</b>	<b>Dipole vortices</b>	<b>9</b>
2.1	The equivalent-barotropic model . . . . .	9
2.2	Dipole steady states . . . . .	12
2.2.1	Governing equations . . . . .	12
2.2.2	Analytical solution . . . . .	13
2.3	Mathematical extensions . . . . .	16
2.3.1	Axisymmetric riders . . . . .	16
2.3.2	The presence of background flow . . . . .	18
2.3.3	The presence of bottom topography . . . . .	21
2.4	Summary . . . . .	23
<b>3</b>	<b>Spontaneous symmetry breaking</b>	<b>24</b>
3.1	Numerical QG results . . . . .	24
3.1.1	Model description . . . . .	24
3.1.2	Symmetry breaking and weak dipole destruction . . . . .	27
3.1.3	Wall simulations . . . . .	28
3.1.4	Analysis of derived quantities . . . . .	31
3.2	Validating solutions . . . . .	34
3.2.1	$f$ -plane dipoles in the presence of beta . . . . .	34
3.2.2	Domain changes . . . . .	35
3.3	Strong dipoles . . . . .	38
3.4	Dipole-rider dynamics . . . . .	41
3.5	Summary . . . . .	44

<b>4</b>	<b>Critical mode analysis</b>	<b>46</b>
4.1	Flow decomposition . . . . .	46
4.2	Normal mode representation . . . . .	52
4.2.1	Resolution and Newtonian viscosity considerations . . . . .	56
4.3	Further experiments . . . . .	58
4.3.1	Strong dipole analysis . . . . .	58
4.3.2	Distillation . . . . .	59
4.4	Summary . . . . .	63
<b>5</b>	<b>Linear stability of dipoles</b>	<b>64</b>
5.1	Perturbation analysis . . . . .	64
5.2	Weak dipoles . . . . .	69
5.3	Strong dipoles . . . . .	76
5.4	Summary . . . . .	79
<b>6</b>	<b>Nonlinear destruction</b>	<b>82</b>
6.1	Nonlinear interaction . . . . .	82
6.2	Energetics . . . . .	84
6.3	Asymmetry analysis . . . . .	88
6.4	Summary . . . . .	90
<b>7</b>	<b>Tilted dipole dynamics</b>	<b>91</b>
7.1	Small tilt . . . . .	94
7.1.1	Case 1: $\beta = 0.35$ . . . . .	94
7.1.2	Case 2: $\beta = 0.2$ . . . . .	97
7.2	Large tilt . . . . .	101
7.3	Summary . . . . .	104
<b>8</b>	<b>Steady state solver</b>	<b>107</b>
8.1	Newton's method . . . . .	107
8.1.1	Formulating the model . . . . .	107
8.1.2	Finite-difference discretisation . . . . .	110
8.2	LRD initialisation . . . . .	111
8.2.1	Integral constraint . . . . .	112
8.3	Summary . . . . .	118
<b>9</b>	<b>Sinusoidal topographic flows</b>	<b>120</b>
9.1	Two-layer QG approximation . . . . .	120



9.1.1	Nondimensionalisation . . . . .	121
9.1.2	Linearised model with sinusoidal topography . . . . .	123
9.1.3	Formulating the eigenvalue problem . . . . .	124
9.2	Results . . . . .	127
9.2.1	Parameter justifications . . . . .	127
9.2.2	Linear Stability Analysis . . . . .	129
9.2.3	Linear Stability for a Thin-Upper-Layer . . . . .	144
9.3	Summary . . . . .	147
<b>10</b>	<b>Conclusion</b>	<b>149</b>
10.1	Dipole results . . . . .	149
10.2	Topography results . . . . .	152
10.3	Future research . . . . .	153
<b>A</b>	<b>Paraboloid interpolation</b>	<b>166</b>
<b>B</b>	<b>Evolution of tilt</b>	<b>168</b>
<b>C</b>	<b>Critical Velocity Shear</b>	<b>170</b>
<b>D</b>	<b>Topography matrix system</b>	<b>173</b>

# Chapter 1

## Introduction

### 1.1 Coherent vortices

#### Brief review

The dynamics of coherent vortices in rotating and stratified fluids is an active and classical area of research, and is motivated by the desire to understand behaviours and characteristics associated with ubiquitous vortical structures in the ocean and atmosphere. Mesoscale eddies are long-lived oceanic vortices with horizontal length scales ranging from 10-100 km (McWilliams, 2008). These nonlinear structures residing in ocean depths are capable of travelling considerable distances of up to thousands of kilometres (Chelton et al., 2011), while trapping large water masses and passive tracers within their cores (Provenzale, 1999). The presence of these bodies of fluid in the ocean can play a pivotal role in the advection of chemical tracers, energy, heat, momentum, plankton, plastic and salt, as well as contribute to the mixing process at the vortex periphery (Dong et al., 2014). Therefore, developing a thorough understanding of these closed fluid motions is of importance to the geophysical fluid dynamics community.

The formation of these rotating features typically results from flow instability; baroclinic instability being the most efficient mechanism to encourage the birth of eddies through the supply of kinetic energy (Gill et al., 1974). There are many examples of ocean eddies, including meddies (Mediterranean water eddies) and sweddies (slope water eddies) that appear in abundance near the Iberian Peninsula and the Bay of Biscay, respectively. The former of which are intense, anticyclonic, intrathermocline lenses (vortices at 300-1600 m depths) with horizontal scales of 30-60 km, vertical scales of 600-1200 m and lifespans of 3-5 years. The latter

are subsurface, intensified, anticyclonic lenses, with horizontal length scales in the range of 35-50 km and lifetimes exceeding a year. Occasionally, cyclonic satellites arise from the formation of swoddies, consequently resulting in tripolar interaction. However, the Earth's curvature acts to break this structure apart by forcing the swoddies to drift southwestward with significant velocity.

Such ocean characteristics have contrasting thermohaline composition (differing spatial distributions of salinity and temperature) in the form of layer intensification and distinctions in shape (e.g., circular or elliptical). These differences determine the eddy velocity and are related to the associated stability properties. Potential vorticity (PV) is a physical quantity which embodies this information through a combination of isopycnal displacement (i.e., the movement of fluid particles along surfaces of constant density), planetary vorticity and the relative vorticity (RV) of particular interest. This quantity is conserved in the unforced quasigeostrophic (QG) framework, making it an ideal playground to build a mathematical description for oceanic vortex dynamics.

A typical characteristic of vortex motion that has been captured in satellite altimetry and theoretical arguments is the inclination to translate west. This self-propagation results from a dipolar component modifying the axisymmetric eddy shape at initialisation by inducing non-zonal motion. These patterns can form from interactions with other coherent structures and topographic features, and when present has influence over the dynamical properties for significant time periods (Radko and Stern, 1999). Despite these interactions being able to manipulate the eddy trajectory, the main source of this westward drift is attributed to the Earth's rotation. In particular, the beta-effect; defined by the planetary vorticity variability with latitude, induces a dipolar component called the beta-gyre by acting on the vortex (Sutyrin and Flierl, 1994).

Under various assumptions, it has been shown that the magnitude of the beta-drift coincides with that of Rossby waves, with wavelengths far exceeding the baroclinic Rossby radius. However, both numerical experiments and analysis of data conflict with this and give evidence for trajectories exhibiting strong meridional and random variability. At present, candidates affiliated with altering trajectories beyond that expected of the dipolar component are background flows, eddy interactions and Rossby wave radiation (due to the vortex translation). Moreover, these factors excite vortical deformations and filamentation, which engage in the inverse energy cascade (i.e, the exchange of energy from large to small length scales).

## Steady state solutions

A class of approximately circular two-dimensional vortices have been shown to follow a steady translation in Radko (2020b). The solutions sought after were arranged as an overlapping vortex pair, such that one vortex patch contains the other. Under the condition of zero net vorticity, these structures become capable of considerable self-propagation - induced by the presence of a weak dipolar component. An interesting feature of these solutions is that all V-states (solutions which exhibit rectilinear translation) obtained are shown to be unstable. However, many of these solutions appear to have extremely small growth rates, and are demonstrated through numerical simulations to have persistent propagation without spatial deformation or loss of eddy intensity. In particular, this is true for quasi-monopolar vortices which carry a small inner patch of vorticity, while larger inner patches see the initial state disintegrate.

Coherent vortices in a barotropic fluid were shown to retain information of initially weak perturbations for up to many months in Radko (2021). In the presence of these initial asymmetries, trajectories differed by as much as hundreds of kilometers relative to the axisymmetric states. This analysis considered both zero and non-zero net angular momentum vortices, and concluded that the persistent propagation tendencies in response to these small disturbances were a consequence of nonlinear processes concerning the beta-induced evolution of the asymmetric component. However, eddies on the  $f$ -plane were shown to behave differently than those on the  $\beta$ -plane in a barotropic model, as they were unable to efficiently expel angular momentum, which meant they were not suitable for self-propagation over large distances.

In the two-layer study Sutyurin and Radko (2021), comparisons between inviscid analytic solutions and numerical simulations were made to suggest that the cause for extremely long eddy lifetimes was a result of reduced potential vorticity gradient in the surface layer of westward background flows. This scenario imposes weak disturbances on the eddy over a lengthy duration - providing a favourable setting for eddy persistence. Moreover, this is contrasted with enhanced abyssal-layer potential vorticity gradient, which causes the vortex to generate a Rossby wake as it translates. Consequently, this generates an oppositely signed lower-layer vortex, which interacts with the structure in the upper-layer (a so-called heton pair, see Hogg and Stommel (1985)) and plays into the corresponding surface vortex evolution.

In the sequel to this research paper (Sutyurin et al., 2021), a class of steadily propagating vortices were identified, and were found not to decay while radiating Rossby waves. This is achieved in both stable and unstable westward background

flows through the extraction of available potential energy. Since baroclinic instability cannot be the cause of energy cascade in stable flows, this tells us that an exchange of energy from large-scales to mesoscales can also be attributed to a moving and radiating vortical body.

A more classical solution than those discussed so far concerns the dipole steady state, which has been a subject of research for many decades. Such solutions originate from the Lamb-Chaplygin profile that solves the two-dimensional (2D) Euler equations (Dryden et al., 1932; Meleshko and Van Heijst, 1994). This solution is stable in the presence of 2D perturbations (Luzzatto-Fegiz and Williamson, 2012), however, 2D unstable modes have been found in the presence of viscosity (Brion et al., 2014).

As an analogue to the Lamb-Chaplygin dipole, a stationary dipole solution was obtained on the barotropic  $\beta$ -plane by Stern (Stern, 1975), and even more generally, a zonally drifting equivalent-barotropic solution was derived in Larichev and Reznik (1976). In the barotropic limit when the Rossby radius is infinite, the Larichev-Reznik dipole (hereafter, LRD) is only capable of eastward drift; otherwise, it can drift in either zonal direction (see Reznik (2010) for a review of LRDs). Numerical experiments suggest that the eastward propagating LRDs remain stable during limited times of integration: for example, when exposed to short-wave perturbations (McWilliams et al., 1981), weak friction (Swaters and Flierl, 1989), and topographic perturbations (Carnevale et al., 1988). However, many attempts at proofs for the stability of eastward propagating dipoles were found to possess flaws (Nycander, 1992; Muzylev and Reznik, 1992; Swaters, 2004), and it is still an open question whether these objects are stable or unstable.

On the  $\beta$ -plane, it was shown that the fate of unsteady  $f$ -plane dipoles depends on their initial direction of propagation and intensity (Sutyrin et al., 1994). In particular, initially strong eastward propagating dipoles decelerate and adjust into a steadily propagating state, whereas, initially weak eastward propagating dipoles break-up into two well-separated monopolar vortices drifting in the opposite, westward direction. Another study with a focus on LRDs tilted away from the zonal direction found that their ability to adjust to steady eastward propagating states depends on the initial tilt and intensity (Hesthaven et al., 1993).

The dipoles we have discussed up until this point have been of a special kind, namely, they are contained within a circular boundary called a separatrix. In the case of circular dipole steady states, the streamfunction can be related to the potential vorticity anomaly (PVA) through a linear balance, i.e.,  $q \sim \psi$ , where  $q$  is the PVA and

$\psi$  is the corresponding streamfunction. However, analogous steady state solutions have also been extracted numerically, where the separatrix boundary is either assumed elliptical and a nonlinear functional relationship between the streamfunction and PVA is obtained (Boyd and Ma, 1990; Kizner et al., 2003a; Khvoles et al., 2005), or a nonlinear functional relationship is first postulated and the deviated separatrix solution is found (Verkley, 1993). Such elliptical dipole models are favourable to study given that an approximation for the characteristic eddy shape; based on satellite altimetry, is a mathematical ellipsoid (Chen et al., 2019). Despite this, we do not consider such models in this thesis, and restrict attention to dipoles with a circular boundary.

Steady state dipoles have also been considered in multi-layer models (so-called baroclinic modons). In this case, Kizner et al. (2002) carried out numerical simulations and showed that two-layer baroclinic modons seemingly displayed stable behaviour over many periods of oscillation. In addition, topographic modons that are exact steady state solutions in the presence of a meridional slope exist and have been studied extensively in Reznik and Sutyrin (2001); Kizner et al. (2003b). The stability of nonstationary dipoles has also been considered in the presence of variable bottom relief such as ridges and random topography (Carnevale et al., 1988).

## 1.2 Topographic flows

Bottom irregularities play an important role in the overall oceanic circulation (Marshall, 1995; Gille et al., 2004). It has been shown that mesoscale ocean eddies and ubiquitous multiple alternating jets form and exhibit significant variability localised over topographic features (Thompson and Richards, 2011; Boland et al., 2012; Stern et al., 2015; Chen et al., 2015; Lazar et al., 2018; Khatri and Berloff, 2018, 2019). This variation in oceanic flows and flow-topographic interactions can contribute to many processes such as the eddy-induced transport, eddy energetics and ocean ventilation (Thompson, 2010; Abernathey and Cessi, 2014; Youngs et al., 2017; Tamsitt et al., 2017; Barthel et al., 2017; Klocker, 2018).

The presence of variable bottom relief can result in the modification of baroclinic growth rates in regions upstream and downstream of topography (Thompson and Sallée, 2012; Abernathey and Cessi, 2014; Thompson and Naveira Garabato, 2014; Chapman et al., 2015; Youngs et al., 2017). Consequently, eddies tend to be very energetic downstream of topography, resulting in regions with large eddy-induced meridional transport (Tamsitt et al., 2017). Given the complexity presented when

dealing with flow-topographic interactions, many simplifications are made when addressing oceanic flow stability in the literature. The simplest approach that can be employed to investigate flow instability is to assume that the ocean bottom is flat, and this has been the focus of various works (Orlanski and Cox, 1972; Tang, 1975; Killworth, 1980; Niino and Misawa, 1984). On the other hand, barotropic dynamics has also been assumed in many papers to explore stability over topographic features (Benilov, 2000a,b; Vanneste, 2003; Benilov et al., 2004). Despite these simplistic frameworks being beneficial to work with mathematically, it is important to consider the topographic effects on baroclinic instability as it is a crucial process impacting the large-scale ocean circulation. Various works have carried out linear stability analysis and showed that topographic slopes greatly affect the baroclinic-instability growth rates (Hart, 1975a,b; Sutyrin, 2007; Chen and Kamenkovich, 2013; LaCasce et al., 2019). Notably, Chen and Kamenkovich (2013) concluded that zonal flows are strongly destabilised by zonal slopes (i.e., flow perpendicular to isobaths) due to the PV gradient obtaining an additional zonal component. In this case, even small-scale topography can result in destabilisation, with the magnitude of the most unstable growth rates increasing with elevated bottom relief. In contrast to this, meridional slopes (i.e., surface shear parallel to isobaths) are shown to either stabilise or destabilise zonal flows through altering the PV gradient in the abyssal fluid layer. Such suppression of baroclinic instability is consistent with the findings of LaCasce et al. (2019), which considered the stability of a zonal jet. In particular, suppression over large topographic slopes looks to be stronger (weaker) when the flow is perpendicular (parallel) to the topography propagation.

The effect of sinusoidal bottom topography on baroclinic instability in a two-layer QG model has been studied using the method of asymptotic expansion (Benilov, 2001). These results, which are only applicable to small scale topography, e.g., topographic height and horizontal spatial scale taken to be 200 m and 5 km, respectively, suggest that such bottom features suppress baroclinic instability when the isobaths (i.e., lines that connect points of equal elevation) are parallel to the vertical velocity shear, and have no influence when the isobaths are perpendicular. In addition to this, it is shown that varying the layer depths results in topography having a weak (strong) effect on flows localised in thin (thick) upper layers (Benilov, 2001).

Following this, Radko (2020a), considered the influence of submesoscale sinusoidal ridges on baroclinic instability in both multi-layer QG and shallow-water models. In this case, the method of multiple scales expansion was used to exploit the short topographic wavelengths of 1-10 km. The results are verified with doubly periodic

numerical solutions (Radko, 2020a), and are found to be similar to Benilov (2001). These indicate a suppression in baroclinic instability by submesoscale topography. Furthermore, linear stability solutions in LaCasce et al. (2019) support submesoscale stabilisation by demonstrating that a sinusoidal ridge with an amplitude of 10 m and a wavelength of 1 km is sufficient at suppressing baroclinic instability.

## 1.3 Structure

The material discussed in this thesis can be split into two parts: the majority will focus on the stability of oceanic dipoles, while the later portion will consider the stability of topographic flows. These are both classical problems in the field of geophysical fluid dynamics and hydrodynamic stability theory, thus making them natural topics to discuss in this dissertation. In the case of the dipole discussion, we break this up into several chapters:

- Chapter 2 - we introduce the reader to some important background material for steady state dipoles under the QG approximation;
- Chapter 3 - the spontaneous symmetry breaking of eastward propagating dipoles that are initialised by steady state solutions is found for the first time and is analysed numerically;
- Chapter 4 - we relate the dipole destruction to linear instability by extracting a critical mode that develops over time;
- Chapter 5 - a linear stability analysis is carried out and results are compared with those obtained numerically;
- Chapter 6 - the mathematics of PV flux and energy exchange is used to demonstrate that the mixing process acts as the mechanism for dipole destruction;
- Chapter 7 - tilted dipoles are analysed numerically and found to transition through different stages of behaviour depending on the parameter space.

In the second part of this thesis:

- Chapter 8 - we derive a nonlinear solution method using Newton's method to extract steady state solutions in a two-layer model QG model;



- Chapter 9 - we consider a two-layer QG framework for the discussion of topographic flows, where we carry out a spectral linear stability analysis for various scales of sinusoidal topography;

Finally, we draw conclusions from our analysis throughout this thesis and discuss routes of progression in Chapter 10.

# Chapter 2

## Dipole vortices

In this chapter we introduce the class of LRD steady states, which are solutions to the equivalent-barotropic QG equations on a  $\beta$ -plane. The topic of dipole-rider solutions is also briefly discussed. Furthermore, through deriving the LRD we obtain an existence criteria, which we demonstrate can change depending on the value of beta and the presence of background flow and bottom topography.

### 2.1 The equivalent-barotropic model

To investigate vortex dynamics in geophysical flows, we consider an equivalent-barotropic QG framework in the presence of the beta-effect and the absence of bottom topography. More specifically, this system can be written in the following form (see Vallis (2017); Pedlosky et al. (1987) for a complete derivation):

$$\frac{D\hat{\Pi}}{Dt} = \hat{\nu} \nabla^4 \hat{\psi}, \quad \hat{\Pi} = \hat{\nabla}^2 \hat{\psi} - \frac{1}{\hat{R}_d^2} (\hat{\psi} - \hat{v}_R \hat{y}), \quad (2.1)$$

where  $\hat{\psi} = \hat{\psi}(\hat{x}, \hat{y}, \hat{t})$  denotes the streamfunction,  $\hat{\Pi} = \hat{\Pi}(\hat{x}, \hat{y}, \hat{t})$  is the full PV field and a Lagrangian invariant conserved for the individual fluid elements,  $\hat{R}_d$  refers to the Rossby radius of deformation,  $\hat{v}_R = \hat{\beta} \hat{R}_d^2$  represents the maximum Rossby wave speed in the zonal direction (we specify this since Rossby waves can also be radiated in the meridional direction),  $\hat{\beta}$  notates the meridional gradient of the Coriolis parameter and  $\hat{\nu}$  denotes eddy viscosity. For compactness, we contain the

information pertaining to the material transport in the Lagrangian derivative<sup>1</sup>,

$$\frac{D}{Dt} = \frac{\partial}{\partial t} - \frac{\partial \hat{\psi}}{\partial \hat{y}} \frac{\partial}{\partial \hat{x}} + \frac{\partial \hat{\psi}}{\partial \hat{x}} \frac{\partial}{\partial \hat{y}}, \quad (2.2)$$

and we use hat notation to emphasise that these variables are dimensional. The validity of this framework is determined by the Rossby number being sufficiently small, that is  $\varepsilon = \hat{U}/\hat{f}_0\hat{L} \ll 1$ , where  $\hat{L}$  and  $\hat{U}$  are natural length and velocity scales, respectively, and  $\hat{f}_0$  is the leading-order Coriolis parameter.

To identify scales of importance, we can rewrite our system in non-dimensional form by introducing the coordinate transformation

$$(\hat{x}, \hat{y}) = \hat{L}(x, y), \quad \hat{t} = \frac{\hat{L}}{\hat{U}}t, \quad \hat{\psi} = \hat{L}\hat{U}\psi, \quad (2.3)$$

where variables notated without hats are dimensionless. With this change of variables in mind, (2.1) can be recast as

$$\frac{\partial q}{\partial t} + \mathbb{J}(\psi, q) + \beta \frac{\partial \psi}{\partial x} = \nu \nabla^4 \psi, \quad (2.4)$$

where  $q = \nabla^2 \psi - S\psi$  is the nondimensional PVA,  $S = (\hat{L}/\hat{R}_d)^2$  is the nondimensional inverse Rossby scale or stratification parameter, the nondimensional beta-term is  $\beta = \hat{\beta}\hat{L}^2/\hat{U}$ ,  $\nu = \hat{\nu}/\hat{L}\hat{U}$  is the inverse Reynolds number and

$$\mathbb{J}(A, B) = \frac{\partial A}{\partial x} \frac{\partial B}{\partial y} - \frac{\partial A}{\partial y} \frac{\partial B}{\partial x} \quad (2.5)$$

is the Jacobian derivative for functions  $A = A(x, y)$  and  $B = B(x, y)$ . It is easy to show that for inviscid flows (i.e.,  $\nu = 0$ ), integral invariants such as energy and enstrophy are conserved:

$$\frac{dE}{dt} = \frac{dZ}{dt} = 0, \quad (2.6)$$

where energy and enstrophy are defined by

$$E = \frac{1}{2} \int \left[ (\nabla \psi)^2 + S\psi^2 \right] dx dy, \quad Z = \frac{1}{2} \int q^2 dx dy, \quad (2.7)$$

---

<sup>1</sup>The negative sign in the Lagrangian derivative does not appear in classical fluid dynamics, and is a consequence of geostrophic balance being used in the derivation of the QG equations, i.e., the Coriolis force is assumed to balance with the pressure gradient.

respectively, and integrals are taking over an infinite domain (though this also holds true in a doubly-periodic spatial domain). In addition, linear invariants such as kinetic moment and  $x$ -momentum,

$$M = \int \psi \, dx \, dy, \quad M_x = \int qy \, dx \, dy, \quad (2.8)$$

respectively, are also conserved for an infinite domain with Newtonian viscosity, i.e., the case where  $\nu \neq 0$  in (2.4). However,  $y$ -momentum defined by

$$M_y = \int qx \, dx \, dy, \quad (2.9)$$

is not conserved in the same way and instead satisfies the equality

$$\frac{dM_y}{dt} = \beta M. \quad (2.10)$$

Since we are interested in the dynamics of vortical structures, it is convenient to center our problem with the vortex center of interest, i.e.,  $(x_c(t), y_c(t))$  (in the case of a dipole, we can use symmetry to extract this directly). We can do this by introducing the coordinate transformation  $(x, y) \rightarrow (x - x_c, y - y_c)$ , which in turn allows us to rewrite (2.4) in the form

$$\frac{\partial q}{\partial t} - \frac{dx_c}{dt} \frac{\partial q}{\partial x} - \frac{dy_c}{dt} \frac{\partial q}{\partial y} + \mathbb{J}(\psi, q) + \beta \frac{\partial \psi}{\partial x} = \nu \nabla^4 \psi \quad (2.11)$$

With this equation in mind, we can evaluate the stability characteristics of our vortex solutions by rewriting the streamfunction as

$$\psi(x, y, t) = \Psi(x, y) + \delta \psi'(x, y, t), \quad (2.12)$$

where  $\Psi$  is a steady state solution and  $\psi'$  is some small disturbance, which is highlighted by the presence of the small parameter  $0 < \delta \ll 1$ . On substitution of (2.12) into (2.11), the leading-order balance yields the steady state governance

$$-\frac{dx_c}{dt} \frac{\partial Q}{\partial x} - \frac{dy_c}{dt} \frac{\partial Q}{\partial y} + \mathbb{J}(\Psi, Q) + \beta \frac{\partial \Psi}{\partial x} = \nu \nabla^4 \Psi, \quad (2.13)$$

where  $Q = \nabla^2 \Psi - S\Psi$  and the perturbation equation is derived by considering terms

at  $\mathcal{O}(\delta)$ :

$$\frac{\partial q'}{\partial t} - \frac{dx_c}{dt} \frac{\partial q'}{\partial x} - \frac{dy_c}{dt} \frac{\partial q'}{\partial y} + \mathbb{J}(\psi', Q) + \mathbb{J}(\Psi, q') + \beta \frac{\partial \psi'}{\partial x} = \nu \nabla^4 \psi', \quad (2.14)$$

with  $q' = \nabla^2 \psi' - S\psi'$ . We can derive an eigenproblem for the linear stability equation, though we leave the details of this for Chapter 5, where we perform various linear stability analyses for a steady state dipole in the QG framework.

## 2.2 Dipole steady states

### 2.2.1 Governing equations

The class of LRD steady states are inviscid dipole solutions to (2.13) when Newtonian viscosity is assumed negligible, i.e., when  $\nu = 0$ . Since these dipole solutions are steady states, the corresponding zonal and meridional propagation speeds can be assumed uniform. Therefore, they can be rewritten as

$$\frac{dx_c}{dt} = c_x, \quad \frac{dy_c}{dt} = c_y, \quad (2.15)$$

for constants  $c_x$  and  $c_y$ . In addition, the class of LRD solutions are only capable of zonal drift, meaning  $c_y = 0$ . With this in mind, (2.13) can be expressed in the form

$$\mathbb{J}(\Psi + cy, \nabla^2 \Psi + \beta' y) = 0, \quad (2.16)$$

where  $\beta' = \beta + Sc$  and  $c = c_x$ ; from which it follows that

$$\nabla^2 \Psi + \beta' y = F(\Psi + cy). \quad (2.17)$$

This tells us that the quantity on the LHS of (2.17) is fixed along streamlines in the co-moving coordinate system  $\Psi + cy = K$ , where  $K$  is some arbitrary constant. Moreover, if we consider spatially localised solutions, those being ones where

$$\Psi \rightarrow e^{-pr}/\sqrt{r} \text{ as } r \rightarrow \infty, \text{ with } r^2 = x^2 + y^2, \quad (2.18)$$

then it is clear that in the far field when  $y \rightarrow \infty$ ,  $\Psi \rightarrow 0$ . Thus, in the exterior domain, it follows that

$$F(cy) = \beta' y \implies \nabla^2 \Psi = p^2 \Psi, \quad (2.19)$$

with  $p^2 = \beta'/c > 0$ . Furthermore, if we assume solutions have a circular boundary, then this means that the PVA and streamfunction fields are associated with one another through a linear relationship<sup>2</sup>, i.e.,  $q \sim \psi$ . Therefore, with (2.17) in mind, we seek the following linear relationship in the interior region,

$$\nabla^2 \Psi + \beta' y = -k^2(\Psi + cy), \quad (2.20)$$

where  $k$  is some positive constant to be determined. From (2.20), we can deduce that

$$\nabla^2 \Psi = -k^2 \Psi - c(k^2 + p^2)y. \quad (2.21)$$

Hence, assuming the discriminating streamline (or separatrix),  $\Gamma$ , is a circle of unit radius, then this corresponds to the streamline

$$\Psi + c \sin \vartheta = K, \quad (2.22)$$

for  $r = 1$ , and we can set  $K = 0$  without loss of generality. Note that we can generalise this for a separatrix arbitrary positive radius, however, if we choose this to be our length scale, then we can always recast our problem with having unit radius after nondimensionalisation.

### 2.2.2 Analytical solution

To derive the analytical solution to (2.19) and (2.21), we reformulate the problem in polar coordinates so that

$$\left( \frac{\partial^2}{\partial r^2} + \frac{1}{r} \frac{\partial}{\partial r} - \frac{1}{r^2} \right) f(r) = \begin{cases} -k^2 f(r) - (k^2 + p^2)r, & r \leq 1, \\ p^2 f(r), & r > 1, \end{cases} \quad (2.23)$$

under the ansatz

$$\Psi(r, \vartheta) = cf(r) \sin \vartheta, \quad \text{with } \vartheta \in [-\pi/2, \pi/2]. \quad (2.24)$$

On solving (2.23) subject to the boundary conditions

$$|f(0)| < \infty, \quad \lim_{r \rightarrow \infty} f(r) = 0, \quad (2.25)$$

---

<sup>2</sup>If this relationship were nonlinear, then the separatrix would be non-circular, e.g., approximately elliptical.

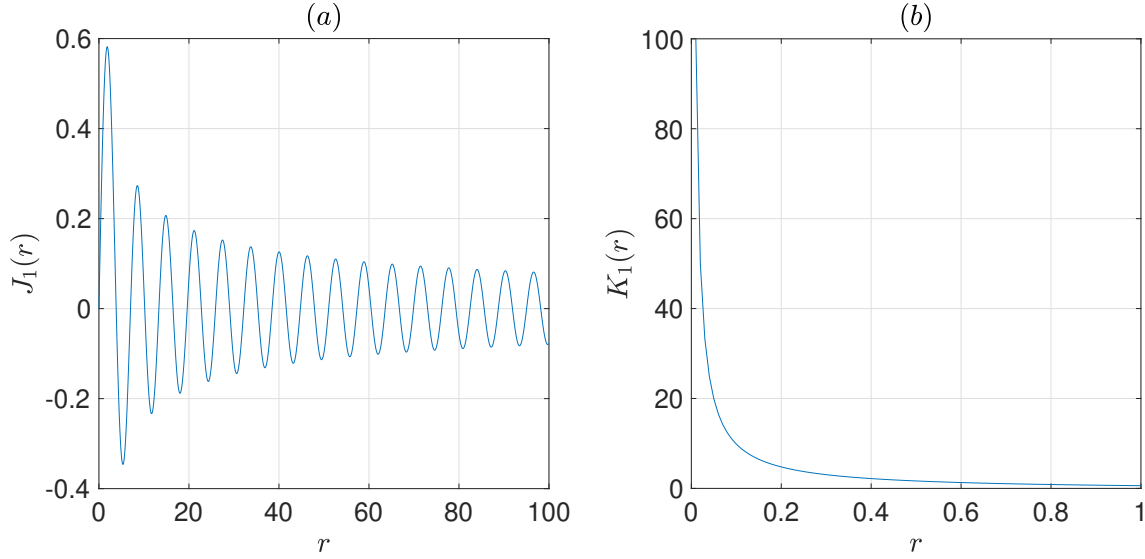


**Figure 2.1:** (a) : Bessel function of the first kind; (b) : modified Bessel function of the first kind.

it follows that

$$f(r) = \begin{cases} (p/k)^2 (J_1(kr)/J_1(k) - r) - r, & r \leq 1, \\ -K_1(pr)/K_1(p), & r > 1, \end{cases} \quad (2.26)$$

where  $J_\mu$  and  $K_\mu$  denote order  $\mu$  Bessel and modified Bessel functions of the first kind, respectively, and constant coefficients are derived from the condition of continuity across  $\Gamma$ , or rather, derived from the equations

$$\Psi + cr \sin \vartheta \Big|_{r=1^-} = \Psi + cr \sin \vartheta \Big|_{r=1^+} = 0. \quad (2.27)$$

Furthermore,  $k$  is a root of the nonlinear equality

$$\frac{k J_1(k)}{J_2(k)} = -\frac{p K_1(p)}{K_2(p)}, \quad (2.28)$$

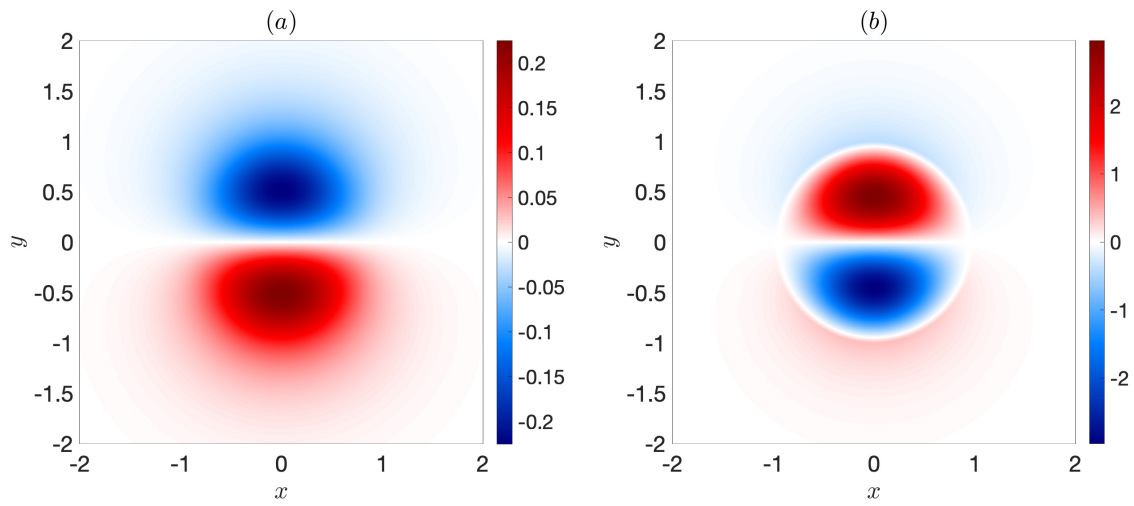


**Figure 2.2:** LRD fields with  $\beta = 0.4$  and  $c = 0.1$ : (a) shows  $\Psi(x, y)$  and (b) shows  $Q(x, y)$ .



which is obtained using continuous differentiability:

$$\left. \frac{\partial \Psi}{\partial r} \right|_{r=1-} = \left. \frac{\partial \Psi}{\partial r} \right|_{r=1+}. \quad (2.29)$$

Equation (2.28) has an infinite number of solutions, each of which corresponds to a different radial mode. In our case, we are interested in dipole solutions associated with the smallest possible value of  $k$ , and we extract this by solving the Bessel equality in MATLAB for relevant parameters. In the case of  $\beta = 0.4$  and  $c = 0.1$  (i.e., Fig. 2.2), the smallest nondimensional value is  $k = 4.11$ , to 3 s.f., whereas, for  $\beta = 0.1$  and the same value of  $c$ , the value becomes  $k = 3.98$ .

As briefly mentioned already, the translation tendency of the LRD is purely zonal drift as a consequence of  $c_y = 0$ . In particular, there is no bound on the eastward translation, however, the westward drift is defined by

$$p^2 = \frac{S|c| - \beta}{|c|} > 0 \implies |c| > \frac{\beta}{S} = v_R, \quad (2.30)$$

telling us that steady states moving towards the west must exceed the maximum Rossby wave phase speed in the zonal direction. Whereas, in the absence of  $\beta$ , we obtain the corresponding steady state dipole on an  $f$ -plane with  $p^2 = S$ . Because of this change in the drift condition, these steady states without beta drift are capable of unbounded zonal translation.

## 2.3 Mathematical extensions

### 2.3.1 Axisymmetric riders

Despite dipolar motions being present in the atmosphere and ocean, more common oceanic features such as rings and surface eddies are approximately axisymmetric, thus, this motivates investigating structures with an axisymmetric component (hereafter, we refer to these components as a 'rider'). A solution of this kind is the dipole-rider steady state,

$$\Psi(r, \vartheta) = \Psi_1(r, \vartheta) + \kappa \Psi_2(r), \quad (2.31)$$

where  $\Psi_1$  is the original LRD solution defined by (2.24) and  $\Psi_2$  is the axisymmetric addition multiplied by a nonzero constant,  $\kappa$ . To derive this solution, the relative vorticity condition is adjusted by the addition of some constant  $C$  in the interior

region, i.e.,

$$\nabla^2 \Psi = \begin{cases} -k^2 \Psi - c(k^2 + p^2)y + C, & r \leq 1, \\ p^2 \Psi, & r > 1, \end{cases} \quad (2.32)$$

and we note that the boundary continuity conditions become

$$\Psi + cr \sin \vartheta|_{r=1^-} = \Psi + cr \sin \vartheta|_{r=1^+} = \kappa, \quad (2.33)$$

or equivalently,  $\Psi_2 = 1$  when  $r = 1$ . Hence, on substituting (2.31) into the (2.32), we find that

$$\frac{d^2 \Psi_2}{dr^2} + \frac{1}{r} \frac{d\Psi_2}{dr} = \begin{cases} -k^2 \Psi_2 + C/\kappa, & r \leq 1, \\ p^2 \Psi_2, & r > 1. \end{cases} \quad (2.34)$$

On solving (2.34) subject to the boundary conditions

$$|\Psi_2(0)| < \infty, \quad \lim_{r \rightarrow \infty} \Psi_2(r) = 0, \quad (2.35)$$

we obtain

$$\Psi_2(r) = \begin{cases} AJ_0(kr) + C/\kappa k^2, & r \leq 1, \\ BK_0(pr), & r > 1, \end{cases} \quad (2.36)$$

where continuity at the separatrix and continuous differentiability of first derivatives yields the constants

$$A = \frac{BpK_1(p)}{kJ_1(k)}, \quad B = \frac{1}{K_0(p)}, \quad \kappa = \frac{CK_0(p)J_1(k)}{k(kK_0(p)J_1(k) - pJ_0(k)K_1(p))}. \quad (2.37)$$

Given solutions at the origin are assumed to be finite, this tells us that the value of  $\kappa$  is arbitrary and there exists a family of LRD-rider solutions (see Fig. 2.3). This is an interesting feature of the dipole-rider solution, since it means we can consider dipole dominant solutions (i.e., where the rider contribution is small), rider dominant solutions (i.e., where the rider contribution is large) and solutions where both components scale with one another.

Previous numerical simulations suggest that these LRD-rider fields are unstable. In particular, the study Swenson (1987) showed numerically that moderate and strong rider amplitudes yielded unstable dynamics, which is likely a consequence of

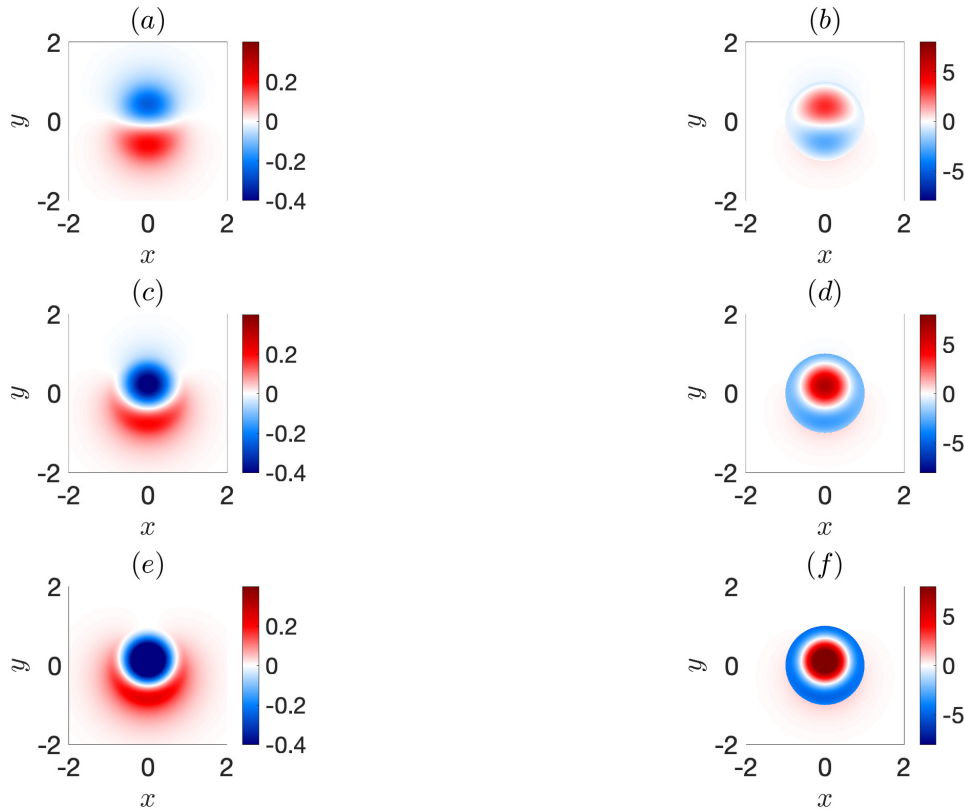


**Figure 2.3:** LRD-rider fields with  $\beta = 0.4$  and different values of  $\kappa$ : the left hand side shows streamfunctions, while the right-hand side shows PVA profiles. Panels (a) and (c) correspond to  $\kappa = 0.01$ ; (b) and (d) correspond to  $\kappa = 0.05$  and (e) and (f) correspond to  $\kappa = 0.1$ .

clear discontinuity at the separatrix in the PVA profiles (see Fig. 2.3b, d, f). However, the study of weaker rider amplitudes was not considered. This was because of the method employed and the argument that solutions with weak rider amplitudes are not as physically relevant. Nevertheless, an investigation of the entire parameter space is desirable.

### 2.3.2 The presence of background flow

So far, we have neglected background flow when discussing LRDs. However, since introducing background flow will adjust the beta contribution and change the denominator in (2.30), the existence criteria for solutions becomes more complicated. Thus, we take some time to explore how a homogeneous zonal current can influence the solution space.

In the presence of a homogeneous zonal current,  $U_b$ , the steady state system (2.16) sees adjustment through the transformation  $c \rightarrow c - U_b$ . Therefore, consideration of the far field (i.e., in the limit as  $r \rightarrow \infty$ ) reveals that we must have

$$p^2 = \frac{\beta + Su}{u}, \quad (2.38)$$

where  $u = c - U_b$ . It is clear from (2.38) that  $c \neq U_b$ . This existence criteria demonstrates the influence background shear has on the underlying dynamics of the dipole, and we can describe the various outcomes as follows:

1. If  $U_b = 0$ , then we obtain the criteria derived by Larichev and Reznik, that is

$$p^2 = \frac{\beta + Sc}{c} > 0.$$

This tells us that either

$$c > 0 \text{ or } c < -\beta S^{-1},$$

i.e., the vortex can either translate to the east with boundless speed, or translate to the west with a speed exceeding the Rossby wave zonal phase speed. This is a consequence of westward translating solutions radiating Rossby waves, meaning they have to drift faster than the radiated waves to maintain their structure. Clearly, westward rectilinear motion on the beta-plane is not possible in the limit as  $S \rightarrow 0$ , since in this case we require  $c > 0$ .

2. If  $c, U_b > 0$ , then

$$p^2 = \frac{\beta + Su}{u} = \frac{\beta + S(|c| - |U_b|)}{|c| - |U_b|} > 0.$$

Clearly, if the denominator is positive, then the numerator is always positive, and so it follows that

$$|c| - |U_b| > 0 \implies |c| > |U_b| \implies c > U_b > 0.$$

Alternatively, if the denominator is negative, then we require the numerator to be negative, which constrains us to

$$|U_b| - \beta S^{-1} < |c| < |U_b|.$$

3. If  $c > 0$  and  $U_b < 0$ , then

$$p^2 = \frac{\beta + S(|c| + |U_b|)}{|c| + |U_b|} > 0,$$

which is always satisfied for any eastward propagation and westward shear, and clearly holds when  $S \rightarrow 0$ .

4. If  $c < 0$  and  $U_b > 0$ , then

$$p^2 = \frac{S(|c| + |U_b|) - \beta}{|c| + |U_b|} > 0.$$

Since the denominator is always positive, the numerator must satisfy

$$|c| > \beta S^{-1} - |U_b|.$$

If  $|U_b| < \beta S^{-1}$ , then it follows that

$$c < -(\beta S^{-1} - U_b) = U_b - \beta S^{-1},$$

whereas, if  $|U_b| > \beta S^{-1}$ , then the numerator is always positive and solutions exist for all values of  $c < 0$ .

5. If  $c, U_b < 0$ , then

$$p^2 = \frac{\beta + S(|U_b| - |c|)}{|U_b| - |c|} > 0.$$

In the case when both the numerator and denominator are positive, we can show that

$$|c| < |U_b| \implies c < U_b,$$

whereas, the inequality can also be satisfied provided that

$$|c| > |U_b| + \beta S^{-1} \implies c < -(|U_b| + \beta S^{-1}) = U_b - \beta S^{-1}.$$

6. If  $c = 0$ , then

$$p^2 = \frac{SU_b - \beta}{U_b} > 0,$$

which is satisfied provided either of the following inequalities hold true:

$$U_b < 0 \text{ or } U_b > \beta S^{-1}.$$

From our discussion of background flow, it is clear that the presence of a homogeneous zonal current can significantly influence the existence criteria for LRD solutions. In particular, the condition for westward propagating dipoles will can change significantly. Given these are all steady states in the QG approximation, it would be fascinating to explore the stability characteristics of the time evolution while varying the values of  $(\beta, c, U_b)$ . Such analysis has yet to be extensively carried out in the literature for the dipole problem and should be the subject of future research. An investigation along these lines would be similar to [Kravtsov and Reznik \(2021\)](#); [Reznik and Kravtsov \(2021\)](#); [Kravtsov and Reznik \(2023\)](#), where the focus was on monopoles.

### 2.3.3 The presence of bottom topography

In addition to background flow, we can extend the LRD steady state solutions we consider to those in the presence of a topographic slope. If we introduce a meridional slope into the problem, say  $\eta = my$ , with  $m$  being the gradient of topographic features, then the barotropic QG system becomes

$$\mathbb{J}(\Psi + cy, \nabla^2 \Psi + \beta_T y) = 0, \quad (2.39)$$

where  $\beta_T = \beta + \alpha m$  is the topographic beta term and  $\alpha$  is a positive constant defined through nondimensionalisation (thus, the value of  $\alpha$  depends on the topographic length scale assume). If we replace  $\beta'$  with  $\beta_T$  in (2.24), then we obtain a steady state solution in the presence of a meridional slope. Since it has been shown that a meridional slope can either stabilise or destabilise zonal flows through altering the abyssal PV gradient ([Chen and Kamenkovich, 2013](#)), an analysis of the topographic effects on the dipole stability is a natural avenue of experimentation.

Since a 1.5-layer framework assumes that the bottom layer depth is infinite, we are unable to consider nonzero bottom topographies in this setting. Furthermore, in the one-layer model, despite us now being able to consider variable bottom relief, the effects of stratification are no longer present (i.e., effects due to the presence of the inverse Rossby scale). Therefore, the coupled effects of stratification and topography cannot be analysed for the dipole propagation, and must be considered separately. However, topographic modons in a two-layer model can be used to investigate the

coupling of stratification and topographic effects on the dipole motion (Reznik and Sutyrin, 2001; Kizner et al., 2003b).

In we introduce a constant background flow, then the existence criteria for dipoles over a nonzero bottom slope is given by

$$p^2 = \frac{\beta + \alpha m}{c - U_b} > 0, \quad (2.40)$$

It is clear from this that the sloping bottom directly affects the Rossby wave mechanism, since the topography slope replaces the stratification term in this framework. This is consistent with bottom relief modifying the background PV gradient, so that the Rossby waves generated are a hybrid between beta-plane and topographic Rossby waves. In the case that  $m > 0$ , the existence criteria for barotropic steady state dipoles over a meridional slope yields the following:

- If  $U_b = 0$ , then the numerator is always positive, so we require  $c > 0$ ,
- If  $U_b > 0$  and  $c > 0$ , then we require that  $|c| > |U_b|$ ,
- If  $U_b > 0$  and  $c < 0$ , then the inequality never holds,
- If  $U_b < 0$  and  $c > 0$ , then the inequality is always satisfied,
- If  $U_b < 0$  and  $c < 0$ , then we must have  $|c| < |U_b|$ ,
- If  $c = 0$ , then  $U_b < 0$ .

On the contrary, if  $m < 0$ , we find that

$$\frac{\beta - \alpha|m|}{c - U_b} > 0,$$

and the criteria now tells us that:

- If  $\beta - \alpha|m| > 0$ , then the conditions above apply,
- If  $\beta - \alpha|m| < 0$ , then the conditions above are inverted.

Overall, exploration of the dipole problem in the presence of background flow and variable topography looks to be a fruitful research avenue. Beyond the elementary extensions to the LRD that we have presented, we can numerically investigate these problems in the presence of variable background flows and irregular bottom reliefs, such as ridges and other random features (Carnevale et al., 1988). In addition, we

can apply these changes to the class of dipole-riders. Given these objects appear unstable based on previous numerical experiments (Swenson, 1987), background flow and topography considerations might identify regimes of stability or new dynamical behaviours.

## 2.4 Summary

Throughout this chapter, we introduced the equivalent barotropic QG framework using a beta-plane approximation. As detailed in the text, a class of analytical steady state solutions can be derived (see (2.24) and (2.26)); we refer to these as LRD solutions and they are analogous to the classical Lamb-Chaplygin dipole<sup>3</sup>. An interesting feature due to the  $\beta$ -effect is the restriction on the dipole translation. In particular, the equivalent steady state solution on the  $f$ -plane can propagate steadily in any direction, whereas, the LRD is limited to purely zonal drift.

By extension, we showed that the addition of a radially symmetric field to the LRD is another family of steady state solutions, the so-called dipole-rider fields defined by (2.39) and (2.37). Despite the LRD having continuous PVA, the dipole-rider has discontinuous PVA near the separatrix (see Fig. 2.3*b, d, f*). On the other hand, the magnitude of the rider is arbitrary, meaning that these steady state solutions can either be dipole dominant (i.e., antisymmetric about the zonal axis) or rider dominant (i.e., symmetric about the zonal axis).

When these fields are exposed to a homogeneous zonal current, we showed that the existence criteria for steady state solutions changes significantly depending on the direction of vortex propagation (see (2.38)). This analysis highlighted how the dynamics of the LRD can change with background flow and motivates the study of the dipole evolution with respect to parameter shifts in  $(\beta, c, U_b)$ . In the absence of stratification and the presence of a meridional bottom slope, exact steady state solutions can also be derived.

With this material in mind, we are now in a position to explore the dynamics over time, which will be the focus of Chapter 3.

---

<sup>3</sup>The Lamb-Chaplygin dipole is a well-known steady state solution to the two-dimensional Euler equations.



# Chapter 3

## Spontaneous symmetry breaking

Some of the contents of this chapter are derived from our work published in the Journal of Physics and Fluids: *"On the spontaneous symmetry breaking of eastward propagating dipoles"*, by J. Davies, G. Sutyrin and P. Berloff.

In this chapter, we discuss the time evolution of various eastward propagating dipoles, initialised as LRD steady states. Despite the time evolution of these objects appearing to be stable in previous works, we find that weak dipoles spontaneously break apart and disintegrate into the background. On the other hand, we notice that with parameter shifts in  $\beta$  towards stronger dipole regimes, the vortex pair sees delay in the asymmetric breakdown. When  $\beta = 0.1$ , it becomes unclear from our limited time integration whether or not the stronger dipole is stable or unstable; motivating further study of these objects.

### 3.1 Numerical QG results

#### 3.1.1 Model description

Now that we have introduced classes of steady states to (2.13) in Chapter 2, we proceed in this portion of the thesis to explore the dynamics of various LRD solutions defined by (2.24) and (2.26) as they evolve over time. To do this, we solve (2.13) numerically with an LRD imposed in the fluid at intialisation. In addition, we impose periodic boundary conditions in both zonal and meridional directions, on a uniformly distributed  $4N \times N = 8192 \times 2048$  rectangular grid in a  $(4L_y, L_y) = (60, 15)$  domain (where  $L_y$  denotes the nondimensional meridional domain scale). On doing this, the zonal and meridional spatial coordinates become discrete on the grid, and we denote these by  $(x_m, y_n)$ , where  $m$  and  $n$  are the zonal and meridional grid

indices, i.e.,  $m = 1, 2, \dots, 4N$  and  $n = 1, 2, \dots, N$ . Given the nondimensional domain we consider, it follows that

$$x_m = -2L_y + \frac{(m-1)N}{L_y}, \quad y_n = -\frac{L_y}{2} + \frac{(n-1)N}{L_y}. \quad (3.1)$$

Mathematically, our initial condition can be written as

$$r_{m,n} = \sqrt{x_m^2 + y_n^2}, \quad \forall x_m, y_n, \quad (3.2a)$$

$$\vartheta_{m,n} = \begin{cases} \arctan(y_n/x_m), & x_m > 0, \forall y_n, \\ \pi/2, & x_m = 0, y_n > 0, \\ -\pi/2, & x_m = 0, y_n < 0, \\ \arctan(y_n/x_m) + \pi, & x_m < 0, y_n \neq 0, \\ \pi, & x_m < 0, y_n = 0, \\ 0, & x_m = y_n = 0, \end{cases} \quad (3.2b)$$

$$\Psi_{m,n} = cf_{m,n} \sin \vartheta_{m,n}, \quad (3.2c)$$

$$f_{m,n} = f(r_{m,n}) = \begin{cases} (p/k)^2 (J_1(kr_{m,n})/J_1(k) - r_{m,n}) - r_{m,n}, & r_{m,n} \leq 1, \\ -K_1(pr_{m,n})/K_1(p), & r_{m,n} > 1, \end{cases} \quad (3.2d)$$

$$q_{m,n} = \begin{cases} -(k^2 + S)\Psi_{m,n} - c(k^2 + p^2)r_{m,n} \sin \vartheta_{m,n}, & r_{m,n} \leq 1, \\ (p^2 - S)\Psi_{m,n}, & r_{m,n} > 1. \end{cases} \quad (3.2e)$$

and the doubly-periodic boundary conditions can be expressed as the following equations:

$$\Psi_{0,n} = \Psi_{4N,n}, \quad \Psi_{4N+1,n} = \Psi_{1,n}, \quad \Psi_{m,0} = \Psi_{m,N}, \quad \Psi_{m,N+1} = \Psi_{m,1}. \quad (3.3)$$

Since our initial condition is known, we can calculate derivatives directly. However, when integrating (2.4) in time with respect to our initial-boundary conditions, we need some way to differentiate the output field systematically. We can do this by making use of second-order central finite difference discretisation at each time step, i.e., we approximate derivatives using the following stencils that are second-order accurate in space:

$$\frac{\partial \Psi_{m,n}^i}{\partial x} \approx \frac{N(\Psi_{m+1,n}^i - \Psi_{m-1,n}^i)}{2L_y}, \quad (3.4a)$$

$$\frac{\partial \Psi_{m,n}^i}{\partial y} \approx \frac{N(\Psi_{m,n+1}^i - \Psi_{m,n-1}^i)}{2L_y}, \quad (3.4b)$$

$$\nabla^2 \Psi_{m,n}^i \approx \frac{N^2(\Psi_{m+1,n}^i + \Psi_{m-1,n}^i + \Psi_{m,n+1}^i + \Psi_{m,n-1}^i - 4\Psi_{m,n}^i)}{L_y^2}, \quad (3.4c)$$

$$\begin{aligned} \frac{\partial}{\partial x} \nabla^2 \Psi_{m,n}^i &\approx \left(\frac{N}{L_y}\right)^3 \left[ 2(\Psi_{m-1,n}^i - \Psi_{m+1,n}^i) \right. \\ &\quad \left. + \frac{1}{2}(\Psi_{m+2,n}^i - \Psi_{m-2,n}^i + \Psi_{m+1,n-1}^i - \Psi_{m-1,n-1}^i + \Psi_{m+1,n+1}^i - \Psi_{m-1,n+1}^i) \right], \end{aligned} \quad (3.4d)$$

$$\begin{aligned} \frac{\partial}{\partial y} \nabla^2 \Psi_{m,n}^i &\approx \left(\frac{N}{L_y}\right)^3 \left[ 2(\Psi_{m,n-1}^i - \Psi_{m,n+1}^i) \right. \\ &\quad \left. + \frac{1}{2}(\Psi_{m,n+2}^i - \Psi_{m,n-2}^i + \Psi_{m+1,n+1}^i - \Psi_{m+1,n-1}^i + \Psi_{m-1,n+1}^i - \Psi_{m-1,n-1}^i) \right], \end{aligned} \quad (3.4e)$$

where  $i$  denotes the time index, i.e., the reference index for an instant or snapshot in time. Therefore, when we input our output field back into the system as our initial condition, the derivatives of this new field can be approximated using (3.4a-3.4e).

Our choice of basin size is motivated by the presence of a wake that forms behind the dipole as it propagates. Since we are solving the problem in a doubly-periodic domain, beyond a certain point a nonphysical interaction with the wake might occur through periodicity. This artificial event can potentially lead to unreliability in our numerical findings, and should be avoided if possible. Therefore, we choose our zonal domain scale to be four times the size of  $L_y$ , in an attempt to allow any instability to develop before the periodic wake interaction could become problematic. Moreover, the LRD is a steady state solution in an infinite domain, which is not the same as our doubly-periodic domain. Therefore, a larger domain is important to implement since we expect the doubly-periodic solution to converge to the infinite domain solution as we increase the size of the grid. Clearly, a sensitivity analysis of solutions to changes in the domain size is important to evaluate whether or not the dynamics we investigate in a doubly-periodic domain would arise in an infinite domain. We address the influence of domain changes later on in the chapter.

The parameter space for the dipole motion is extremely vast; consisting of various intensities, length scales and initial asymmetries, which allows for a plethora of research potential. For the purposes of this chapter, since vortex scales of  $L \sim R_d$  are reflective of oceanic features, we adopt such scales in our analysis. In addition, we assume antisymmetric dipoles about the zonal axis, translating in the eastward

direction with a velocity given by  $c = 0.1$ . In [Sutyrin et al. \(1994\)](#), strong and weak dipoles were defined by keeping the beta contribution fixed and varying the propagating speed. More specifically, values were chosen in this study so that the corresponding dipole intensities, defined by  $c/v_R$ , were 1 and 0.25, for strong and weak dipoles, respectively. Instead, here we consider the case where  $\beta$  is allowed to be variable and  $c$  is assumed fixed. With this in mind, we consider weak dipoles with  $\beta = 0.4, 0.3$  and  $0.2$ , as well as a stronger dipole with  $\beta = 0.1$ .

We consider a variety of weak dipoles to analyse how sensitive the dynamical behaviours are to parameter shifts in the beta contribution. The stronger dipole is used to identify whether there could exist a critical threshold for dipole intensity that separates dipoles into stable and unstable solutions. Throughout our analysis in this chapter, we refer the reader to [table 3.1](#) for a summary of parameter values assumed in our simulations.

The methodology we adopt uses the CABARET scheme to solve the initial-boundary value problems described by [\(3.2a-3.2e\)](#) and [\(3.3\)](#), for the parameter space summarised in [table 3.1](#). For details of the numerical model, we direct the reader to [\(Karabasov et al., 2009\)](#) for technical details. In addition, the corresponding numerical convergence properties can be found in [\(Shevchenko and Berloff, 2015, 2017\)](#). Despite previous studies for similar problems relying on pseudo-spectral methodology when carrying out numerical analysis, the highlight of the advanced CABARET advection scheme is that it allows the use of coarser grids for the same numerical accuracy and minimises numerical dissipation implicit in the background. Unfortunately, we cannot eliminate numerical viscosity completely using this method, however, we will demonstrate later that when comparing solutions obtained using different values of explicit Newtonian viscosity, the numerical viscosity achieved is sufficiently small for inviscid flow considerations.

### 3.1.2 Symmetry breaking and weak dipole destruction

During the time evolution of dipoles with weak intensities, our solutions appear to preserve a steady eastward propagation for a significant amount of time. However, after a long enough time elapses, we begin to see oscillatory behaviour develop in the dipole (see [Fig. 3.1a](#)), which results in the deceleration of the structure up until  $t = t_s$ , with  $t_s$  being a time where zero zonal drift and proceeding partner separation of the eddy pair occur. More specifically, at  $t = t_s$ , we see the dipole reach a stationary state before it changes direction and translates in the westward direction (see [Figs. 3.1b, c](#)). Beyond this, the partners break apart and the eddy cores

Symbols	Parameter	Dimensional	Nondimensional
$(\hat{R}_d, R_d)$	Rossby radius	28 km	1
$(\hat{L}_y, L_y)$	Meridional scale	$15\hat{R}_d$	15
$(\hat{\beta}, \beta)$	Coriolis gradient	$(2, 4, 6, 8) \times 10^{-11} \text{ m}^{-1} \text{ s}^{-1}$	(0.1, 0.2, 0.3, 0.4)
$(\hat{v}_R, v_R)$	Rossby wave speed	$\hat{\beta}\hat{R}_d^2$	$\beta$
$(\hat{S}, S)$	Inverse Rossby scale	$\hat{R}_d^{-2}$	1
$(\hat{c}, c)$	Dipole speed	$1.57 \text{ cm s}^{-1}$	0.1

**Table 3.1:** Parameter model for numerical simulations of eastward propagating dipoles, where symbols notated with a hat are dimensional, and otherwise nondimensional. Results are computed in a  $4L_y \times L_y$  domain and on a  $4N \times N$  uniform square grid. If different values are used for an experiment, this will be emphasised in the text.

disintegrate into the background.

We use parabolic interpolation to accurately extract  $t_s$  from discrete snapshots of numerical data. In particular, we consider the time series for  $x_c$  (where the dipole center is accurately obtained using paraboloid interpolation, as described in Appendix A). From this, we find the corresponding grid extrema,  $x_m$ , and choose two values to the immediate left and right of this value,  $x_-$  and  $x_+$ , respectively. With this in mind, we assume that the true extrema between grid points lies on a parabola defined by these points. Therefore, locally to the extrema the zonal center coordinate can be expressed as  $x_c = at^2 + bt + c$ , with  $a, b$  and  $c$  defined by the values  $x_m, x_-, x_+$  and the corresponding values of  $t$ . It then follows from differentiation that the maximum value is defined at  $t_s = -b/2a$ .

We found that the time characterising dipole separation was  $t_s \sim 215$  when  $\beta = 0.4$  (the corresponding snapshot can be seen in Fig. 3.1b) and larger  $t_s \sim 327$  for smaller  $\beta = 0.3$ . For values of  $t$  exceeding this critical value, the zonal drift of the dipole changes direction and acts westward, as is the case for monopolar vortices described in Sutyris et al. (1994).

### 3.1.3 Wall simulations

To identify the physical significance of the symmetry breaking of the dipole, as seen in the upper panels of Fig. 3.1, we draw comparisons between dipoles propagating in the presence of a zonal wall between partners, where no flow can move between the upper and lower half-planes (with the exception of moving through the periodic boundaries). To impose this constraint, we set the values of the PVA field equal to zero at each iteration on the grid points  $(i, N/2)$ , for all  $i$  (recall that  $N$  is the

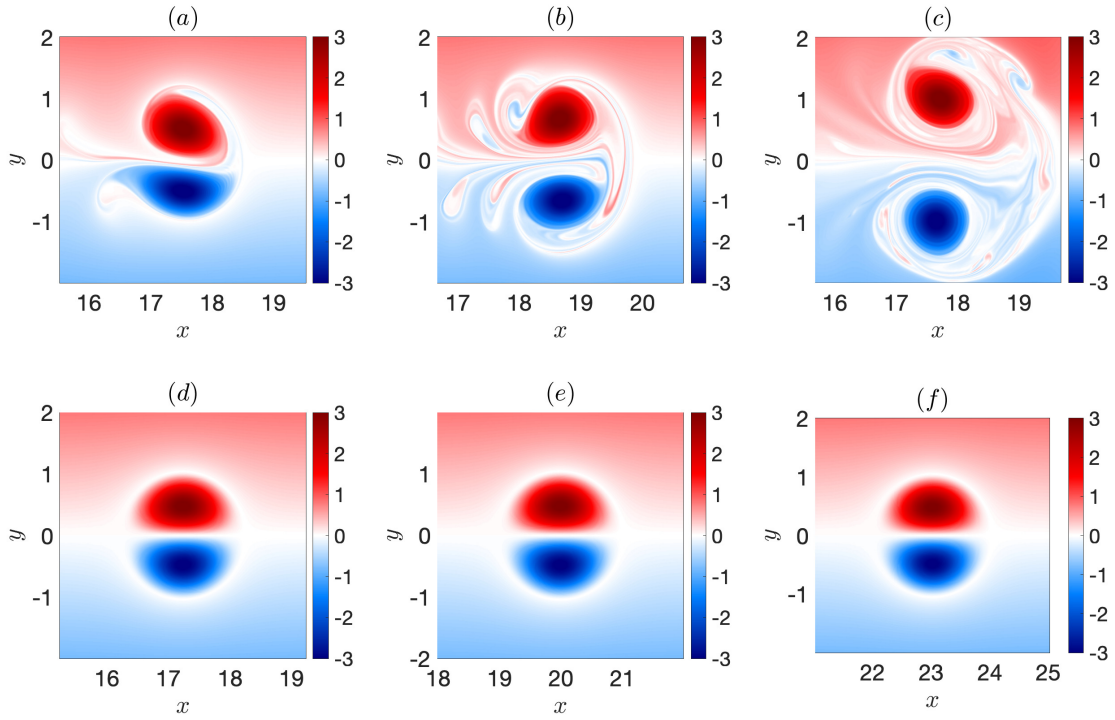


**Figure 3.1:** Nondimensional dipole PV snapshots at:  $t = t_s - T$  (panels (a) and (d), where  $T$  is the period of oscillation of a growing anomaly on the dipole, as described later),  $t = t_s$  (panels (b) and (e)) and  $t = t_s + T$  (panels (c) and (f)): top panels correspond to the base problem; bottom panels correspond to solutions in the presence of a no-through-flow zonal wall. Solutions are obtained using parameters in table 3.1 with  $\beta = 0.4$ , and the numerical solutions are shown in a fixed frame of reference.

number of grid points in the meridional direction). In our original dipole setup, since we consider an even number of grid points in both horizontal directions, we center our initial state on the node  $(N/2 + 1/2, N/2 + 1/2)$ . Therefore, we would ideally want to position a wall along the points  $(i, N/2 + 1/2)$ , however, it is not obvious how to impose a wall between grid points, and so we instead reposition the dipole center at initialisation when considering the presence of a wall. The caveat of this approach is that this technically skews the symmetry of the problem, with the upper-half plane consisting of more grid points than the lower half-plane. Thus, we considered a variety of center positions for the dipole to see how the instability develops in different cases, and found that despite subtle differences in solutions, the overall results obtained remained consistent with each other. With this in mind, we proceed with the wall imposition as previously described.

When the wall is present, we clearly see no significant deviation in the PV field for the LRD (Figs. 3.1d, e, f), which suggests that one potential cause for the

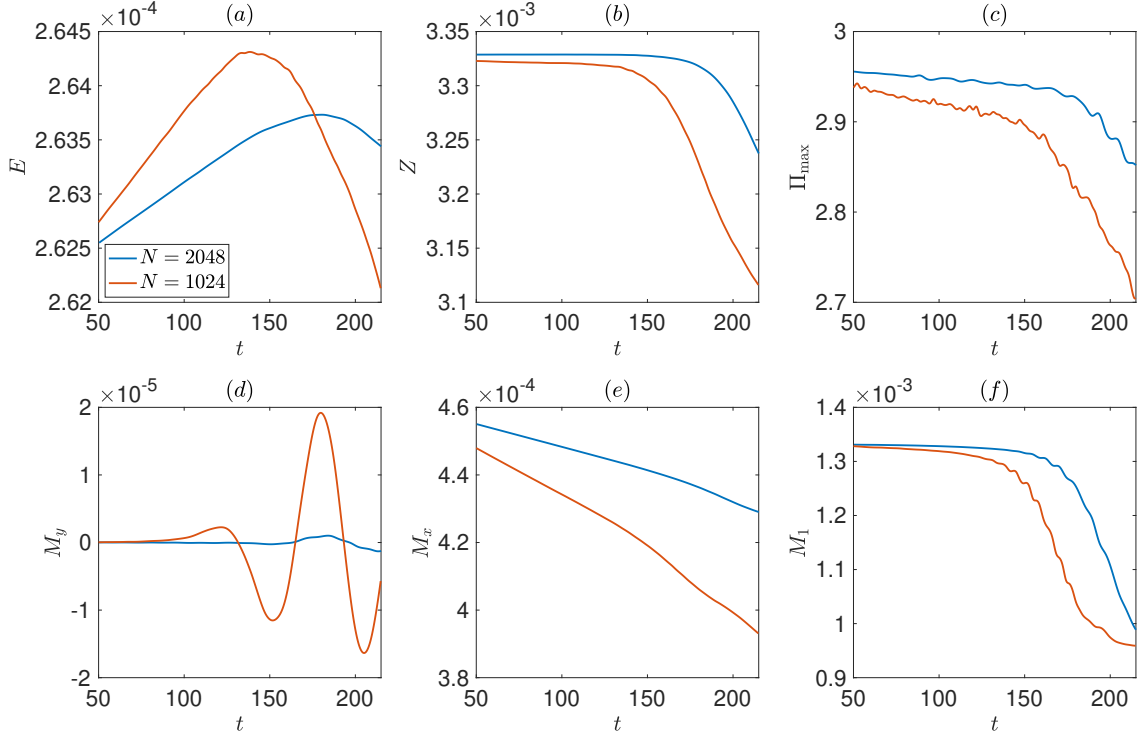


**Figure 3.2:** Invariant plots for a dipole with  $\beta = 0.4$  up to  $t = t_s$ : (a) energy, (b) enstrophy, (c) maximum PV, (d)  $y$ -momentum, (e)  $x$ -momentum, (f) PV integral in the upper-half plane (if the corresponding quantity in the lower half is denoted by  $M_2$ , then  $M = M_1 + M_2$ ). Red curves correspond to solutions with  $N = 1024$  and blue curves correspond to solutions with  $N = 2048$ .

spontaneous symmetry breaking is the exchange of PV between the vortex pair. We can evaluate the hypothesis of PV exchange being the mechanism for spontaneous symmetry breaking by considering the integrals of the PVA field in the upper and lower half plane, separately. Since total PVA is conserved in our numerical solutions, we expect these quantities to evolve in opposite directions if PV exchange occurs. We find that the upper-half plane integral experiences a tiny decrease over time, as in Fig. 3.2f (the lower-half plane integral sees an opposite change in value as a consequence of PV conservation). This could suggest this PV exchange is insignificant, or that even an extremely small PV exchange of the dipole can disturb the solution and force the phenomena to occur. To expand on this further, consideration of PV flux components would reveal how PV is distributed in the domain, and this will be discussed further in Chapter 6.

Invariant	$t = 50$	$t = 150$	$t = t_s$
$E$	$2.626 \times 10^{-4}$	$2.636 \times 10^{-4}$	$2.634 \times 10^{-4}$
$Z$	$3.329 \times 10^{-3}$	$3.328 \times 10^{-3}$	$3.232 \times 10^{-3}$
$M$	$-3.29 \times 10^{-11}$	$3.35 \times 10^{-10}$	$-6.65 \times 10^{-11}$
$\Pi_{\max}$	2.956	2.939	2.845

**Table 3.2:** Invariant values for various values of  $t$ , obtained using  $N = 2048$  and  $\beta = 0.4$  (we assume the absence of a no-flow through zonal wall).

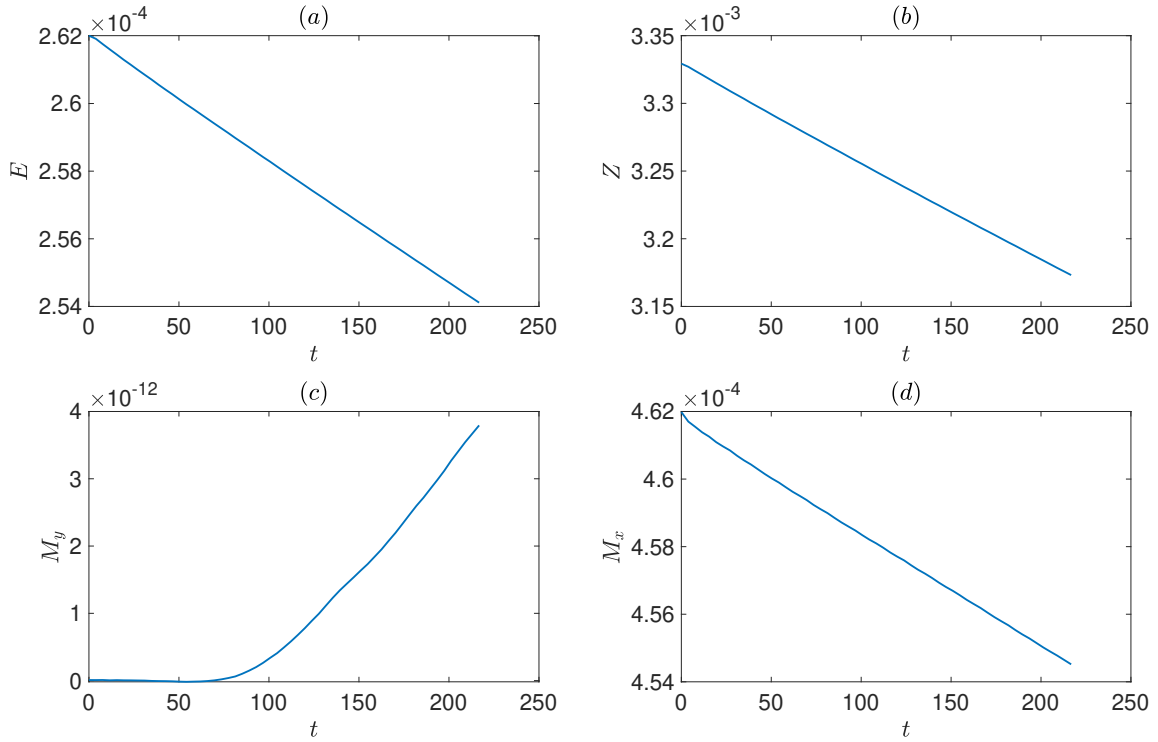


**Figure 3.3:** Invariant plots for a  $\beta = 0.4$  dipole in the presence of a no-flow-through zonal wall between the eddy cores, up until the value of  $t_s \sim 215$  (the characteristic time of partner separation for the same dipole without a wall), with  $N = 2048$ : (a) energy; (b) enstrophy; (c)  $y$ -momentum; (d)  $x$ -momentum.

### 3.1.4 Analysis of derived quantities

To assess the merit of our results, we draw comparisons between the time series for several integral invariants using  $N = 1024$  and  $N = 2048$  (particular values obtained with  $N = 2048$  can be found in table 3.2 and the time evolution can be seen in Fig. 3.2). If we consider energy, enstrophy and maximum PV conservation for the  $N = 1024$  solutions, then the quantities change over the time domain  $50 \leq t \leq 150$  as follows:  $\Delta E = 0.609\%$ ,  $\Delta Z = -0.545\%$  and  $\Delta \Pi_{\max} = -1.40\%$ , respectively.



Whereas, in the case of  $N = 2048$  solutions, we find that  $\Delta E = 0.381\%$ ,  $\Delta Z = -0.0300\%$  and  $\Delta \Pi_{\max} = -0.575\%$ . This can be interpreted as energy conservation being roughly 37% better on a  $8192 \times 2048$  uniform grid, while the conservation of enstrophy and maximum PV is approximately 95% and 59% better, respectively, when solving the problem on the finer grid. When approaching  $t = t_s$ , it is clear from Fig. 3.2 that there is a sudden decrease in energy and enstrophy, though this is more controlled for higher resolution. Such energy and enstrophy losses are consistent with increased dissipation of the advection scheme on steep gradients emerging on violent growing perturbations.

Despite the quantities  $M_y$  and  $M_x$  only being conserved in an infinite domain, it is still useful to analyse these quantities. In particular, given the flow symmetry of the initial LRD, we expect the value of  $y$ -momentum to be zero. What is evident from Fig. 3.2d is clear non-zero deviation in the time-series for  $y$ -momentum. This further confirms the development of dipole asymmetry. In addition, it is clear from most panels that the separation of partners occurs sooner on a coarser grid. This is likely a consequence of implicit numerical viscosity being fixed in the background, and we can only overcome this by increasing the resolution of the grid. To evaluate viscous dissipation in the system, it is important to carry out a sensitivity analysis to different values of explicit Newtonian viscosity. This will allow us to better understand whether or not this dipole phenomena would occur in the absence of viscosity, which is important to address, given the solutions we consider are for the inviscid case. We leave this sensitivity study for Chapter 4.

We can also perform an analysis of invariants for the wall simulations presented in the bottom panels of Fig. 3.1. This informs us that the corresponding energy, enstrophy and  $x$ -momentum see approximately linear decrease in value (see Fig. 3.3), where the loss in each of these invariants over the time domain considered is roughly 3%, 4.5% and 1.5%, respectively. These decreases are a consequence of numerical viscous effects in the system. These effects are also captured in Fig. 3.3c, where the time-series for  $y$ -momentum clearly increases when  $t > 70$ . Such behaviour relates to asymmetry in the dipole propagation, however, in the interval considered, this presence is not obvious from simulations and is essentially negligible.

To better understand the development of oscillatory motion for weak dipoles, we extract the coordinates corresponding to the positive and negative dipole extrema,  $(x_1, y_1)$  and  $(x_2, y_2)$ , respectively, using parabolic interpolation (see Appendix A). This procedure allows us to track the center trajectory,  $(x_c, y_c)$ , where  $x_c = (x_1 + x_2)/2$  and  $y_c = (y_1 + y_2)/2$ . In addition, we can get physical insight from the derived

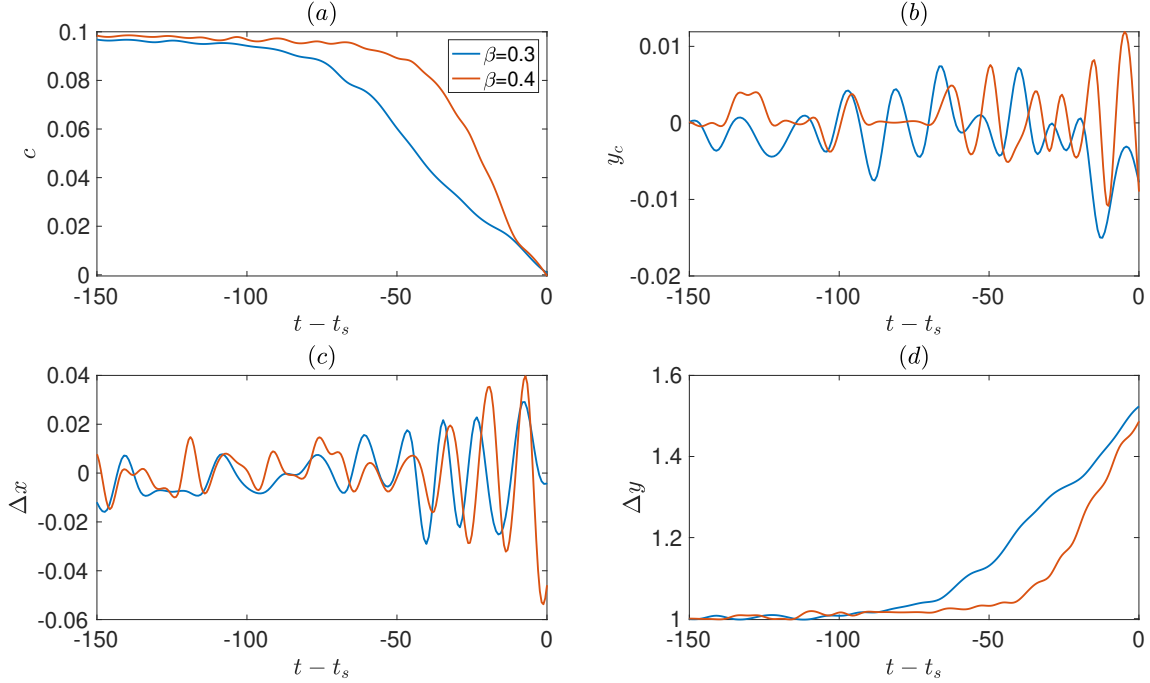


**Figure 3.4:** Time series for dipoles with  $\beta = 0.4$  (red) and  $\beta = 0.3$  (blue), where  $t_s$  is the characteristic time of dipole separation ( $t_s \sim 215$  for  $\beta = 0.4$  and  $t_s \sim 327$  for  $\beta = 0.3$ ): panel (a) shows the zonal propagation velocity, panel (b) shows the meridional center coordinate, panel (c) shows the zonal extrema difference and panel (d) shows the meridional extrema difference (adjusted to start at unity)

quantities:  $c = dx_c/dt$  (zonal drift speed),  $\Delta x = x_1 - x_2$  (the characteristic of the dipole tilt) and  $\Delta y = (y_1 - y_2)/(y_1(1) - y_2(1))$  (the separation of the dipole partners to start at unity), and so we present the time-series associated with these quantities in Fig. 3.4. In panel (a), we see small oscillations of the drift speed for the dipole with an intensity of 0.25 slowly growing up until  $t \sim t_s - 50$ ; beyond which the propagation speed quickly decreases until it reaches zero at  $t = t_s$  ( $t_s \sim 215$  for  $\beta = 0.4$ ). Such behaviour is similar for dipoles with larger intensity of 0.33, however, the dipole deceleration develops later, after  $t \sim t_s - 70$  ( $t_s \sim 327$  for  $\beta = 0.3$ ).

Figs. 3.4b,c imply the wobbling of the dipole over the time evolution through frequent oscillations in curves for  $y_c$  and  $\Delta x$ . From these time-series, we see that the symmetry breaking begins before the partner separation. This is clear from the dipole center oscillations in the meridional center coordinate and the zonal extrema difference. As  $t$  approaches  $t_s$ , we see that the oscillations in  $\Delta x$  become more pronounced, indicating further development of partner asymmetry. When analysing  $\Delta y$  (see Fig. 3.4d), we clearly see the separation of partners as we get closer to the time of separation. For both weak dipole intensities considered, the meridional

distance between the dipole extrema is close at  $t = t_s$ . This could be suggestive of a critical distance existing where if the eddy separation exceeds this, a westward drift of the eddy pair takes over the dipole motion. On the other hand, since the  $\beta = 0.3$  dipole sees a slightly greater separation of partners before spontaneously breaking apart, this could also inform us that stronger dipoles can have their cores drift further apart from one another before the inevitable dipole destruction.

## 3.2 Validating solutions

### 3.2.1 $f$ -plane dipoles in the presence of beta

The instability we have presented so far is completely new and disagrees with many previous studies discussing the stability of dipoles propagating in the eastward direction (McWilliams et al., 1981; Swaters and Flierl, 1989; Carnevale et al., 1988). Because of this, it makes sense for us to show that our methodology can replicate the results of a solution that is better understood. A problem of this kind includes the  $f$ -plane equivalent LRD dipole. These objects were studied in Sutyrin et al. (1994), where the beta-effect was imposed in the background to see how solutions were modified. It was found that weak eastward propagating dipoles see symmetric breakup very quickly as the cores drift to the west. This change in translation is a consequence of a superimposed beta-gyre that propagates in the westward direction, rather than a result of instability as in the case of the initialised LRD. Therefore, unlike in Fig. 3.1, verification of our CABARET solutions would involve reproducing the same results with and without a wall along the dipole axis.

For consistency with snapshots in Sutyrin et al. (1994), we must account for a difference in nondimensionalisation, as described in the previous subsection. If we denote our time scale by  $T$ , then this can be associated with the time scale used in Sutyrin et al. (1994),  $T_s$ , as  $T_s = T/4$ . For example, a snapshot at  $t = 100$  with fixed  $\beta$  corresponds to snapshots in our solution space at  $t = 25$ . With this in mind, we present snapshots of CABARET solutions for the  $f$ -plane exposed to  $\beta = 0.4$  in Fig. 3.5. Drawing comparisons between Fig. 3.5 and Fig. 11 in Sutyrin et al. (1994) (see Fig. 3.6), we clearly see consistency in solutions obtained. In addition, if we consider the presence of a no-flow-through wall oriented along the zonal axis, then we find that the dynamics remains unchanged (see bottom panels in Fig. 3.5). Hence, this shows that the CABARET advection scheme does not associate instability with  $f$ -plane dipoles in the presence of the beta-effect; giving merit to our findings

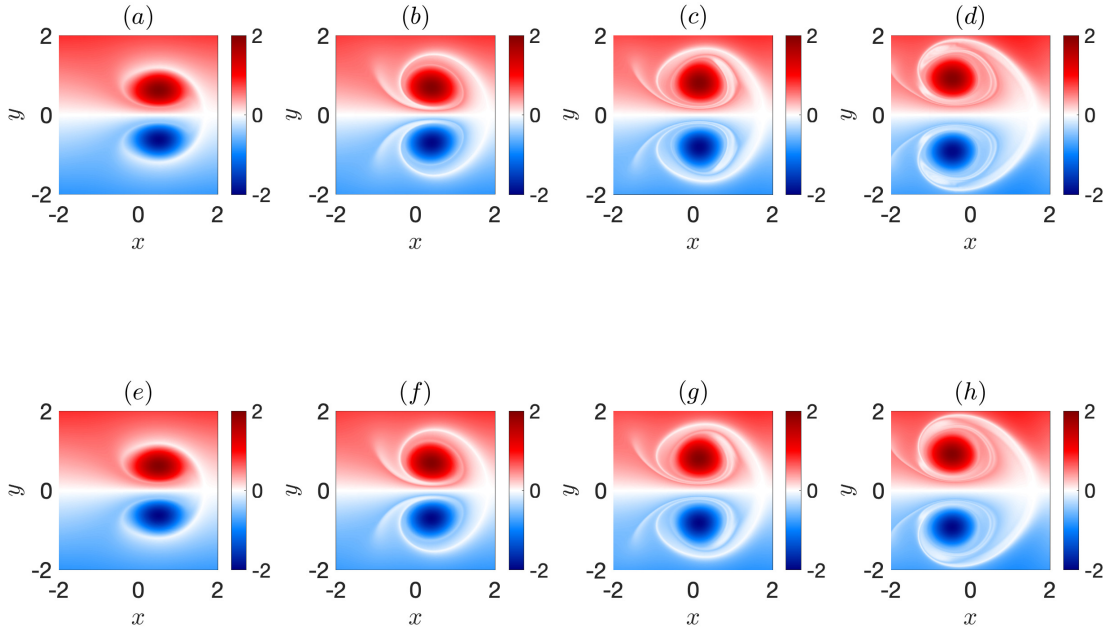


**Figure 3.5:** CABARET PV solutions for the  $f$ -plane dipole in the presence of  $\beta = 0.4$ : the top rows correspond to the problem described, while panels in the bottom row include a zonal wall between the vortex pair. Snapshots (a) and (e) are taken at  $t = 12.5$ , snapshots (b) and (f) are taken at  $t = 25$ , snapshots (c) and (g) are taken at  $t = 37.5$  and snapshots (d) and (h) are taken at  $t = 50$ .

of instability for the time evolution of initial LRD steady states.

### 3.2.2 Domain changes

As we have previously mentioned, the decision for using a four times longer domain in the zonal direction was to allow instability to develop before the dipole reaches the periodic boundary. Since the dipole generates a trailing wake as it propagates, if the vortex pair transitions through the end of the domain, then the dipole becomes exposed to the wake through periodicity and the resulting artificial interaction could potentially lead to unreliable results. However, it could also be the case that this interaction is weak and does not significantly change the overall dynamics, unless the time of exposure is long enough. Another important point is that our results assume a doubly-periodic domain, despite the fact that the LRD solution is derived in an infinite domain. This means that instead of considering a single isolated dipole in infinite space, we are technically considering an infinite family of periodic

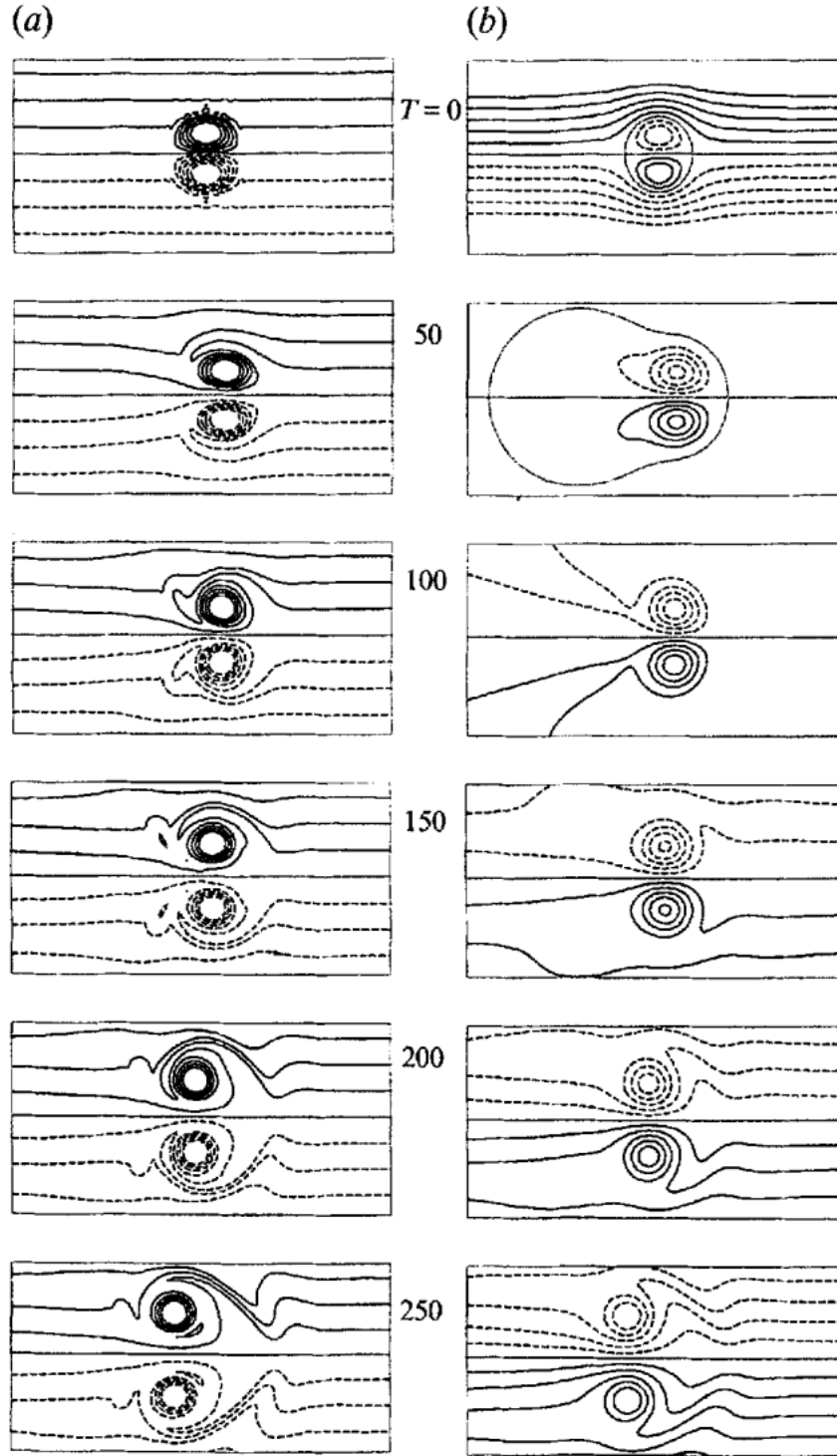


**Figure 3.6:** Fig. 11 in [Sutyryn et al. \(1994\)](#): (a) panels show the PVA fields, (b) panels show the corresponding streamfunction fields. PVA panels are consistent with our CABARET solutions for the same problem.

dipoles, which can result in mirror image interactions that could be the cause of the instability.

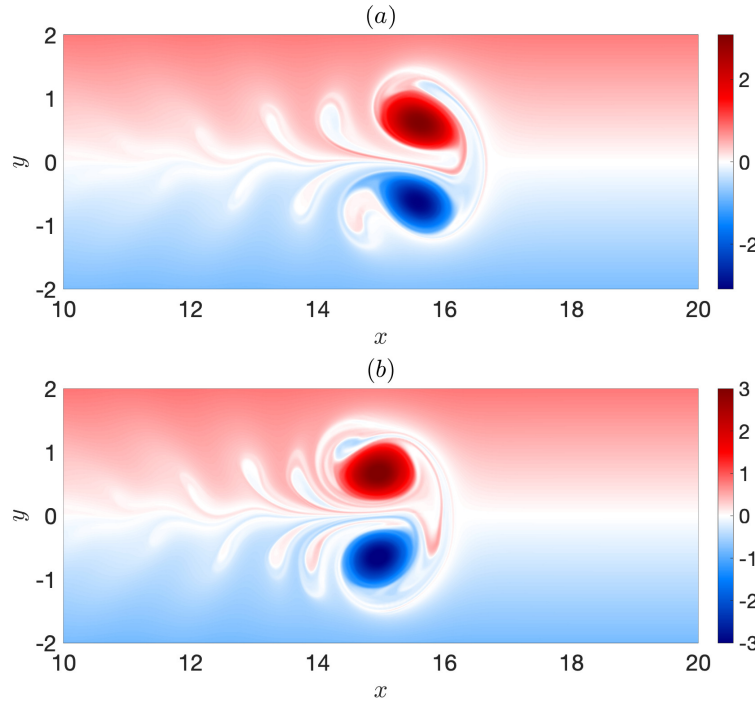


**Figure 3.7:** PV solutions for an eastward propagating dipole with  $\beta = 0.4$ , at  $t \sim 175$  (the value of  $t_s$  for  $\beta = 0.4$  using  $N = 1024$ ): (a) shows the result in a  $(60, 15)$ -domain with  $4096 \times 1024$  grid points; (b) shows the result in a  $(120, 30)$ -domain with  $8192 \times 2048$  grid points.

To investigate this further, we can analyse how changes in domain size influence the dipole dynamics. If the dipole instability is attributed to mirror interaction with periodic dipoles, then this would be evident in simulations with different domains, where larger domains would see longer dipole persistence. Therefore, we consider a  $(60, 15)$ -domain with  $4096 \times 1024$  grid points and a  $(120, 30)$ -domain with  $8192 \times 2048$  grid points (see Fig. 3.7) to identify whether this is the case or not. Snapshots in Fig. 3.7 $a, b$  reveal that the time scale on which partner separation acts is similar for both solutions. Interestingly, the dipole breakup occurs slightly earlier in the doubly-sized domain, which is the complete opposite behaviour to that expected if periodicity is the cause for eventual dipole destruction. Despite these small differences, other studies have observed such changes when simulating over different domains (Hesthaven et al., 1993). Furthermore, since the solutions we consider are spatially localised and the dynamics we observe in Fig. 3.7 $a, b$  appears similar, this suggests that these dynamical behaviours in the dipole motion might also occur in an infinite domain.



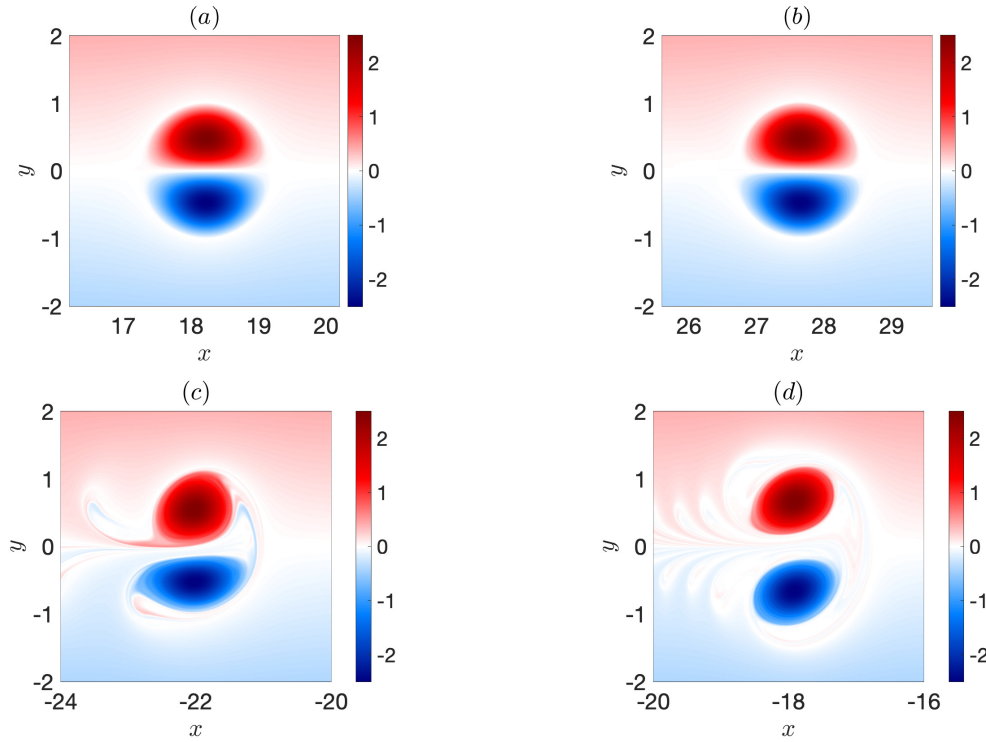


**Figure 3.8:** PV snapshots in a fixed reference frame for a dipole with an intensity of  $c/\beta = 1/2$ : (a)  $t \sim 200$ ; (b)  $t \sim 300$ ; (c)  $t \sim 400$ ; (d)  $t \sim 500$ .

### 3.3 Strong dipoles

So far, we have limited our discussion to weak dipoles in our description of beta-plane dynamics. Given we see a growing instability for these weaker dipoles, it makes sense to see if this instability also develops for stronger dipoles. Comparisons between  $\beta = 0.4$  and  $\beta = 0.3$  demonstrate an increase in the value of  $t_s$  as we decrease the value of  $\beta$ . Moreover, curves in Fig. 3.4 appear to show a more controlled partner separation for a slightly stronger dipole. To support this further, simulating a  $c/\beta = 1/2$  intensity dipole shows us that the partner separation is even more controlled, with deviations in the dipole state subtly occurring at  $t \sim 300$  in Fig. 3.8b, while parabolic interpolation tells us that  $t_s \sim 562$ . This means that the dipole maintains itself for roughly 260 units of  $t$  while in this disturbed state; significantly longer than the weaker dipoles we have previously considered.

Given that the asymmetry introduced to the dipole occurs near the periodic boundary, it could be the case that waves or dipole images disturb the dipole through periodicity, leading to artificial deviations. Because of the solution symmetry, if this is broken even slightly, this could result in the spontaneous symmetry breaking we

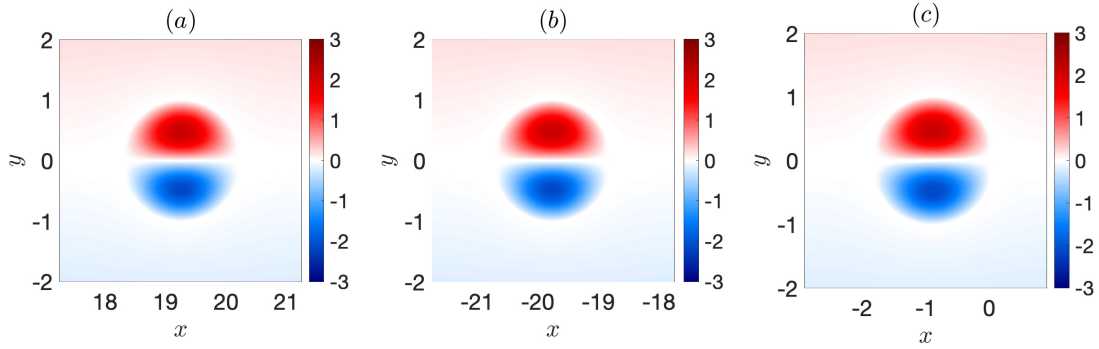


**Figure 3.9:** PV snapshots of a strong dipole,  $c/\beta = 1$ : (a)  $t \sim 200$ ; (b)  $t \sim 400$ ; (c)  $t \sim 600$ . There does not appear to be any significant deviation in the dipole state, and any small deceleration and partner separation could be due to numerical viscosity.

see in Fig. 3.8c, d. If this is the case, despite the outcome not being physical, it tells us that the dipole can be disturbed through wave interaction. However, since we clearly see the value of  $t_s$  increase as we decrease the value of  $\beta$ , it could also be the case that the dipole would naturally begin to wobble in a larger domain, meaning it could also be coincidence that small asymmetry appears as the dipole approaches the edge of the boundary.

Next, we consider a strong initial LRD corresponding to  $c/\beta = 1$ , which from Fig. 3.9, clearly resembles the time evolution for a dipole in the presence of a no-flow-through wall between the vortex pair (see Figs. 3.1d, e, f). With our current methodology, it is difficult to assess whether this solution is actually stable or just has a very small growth rate, because significantly longer time integrations require longer domains (to avoid artificial interaction with the wake in periodic domain) and finer grid resolution (to reduce long-term effects of numerical viscosity). Regardless, with this in mind, and considering the seemingly more controlled symmetry breaking as we increase the dipole intensity, there could exist a critical threshold in the range  $0.5 < c/\beta < 1$ , where dipoles with intensities less than this critical value experience the symmetry breaking phenomena, while those with greater intensities



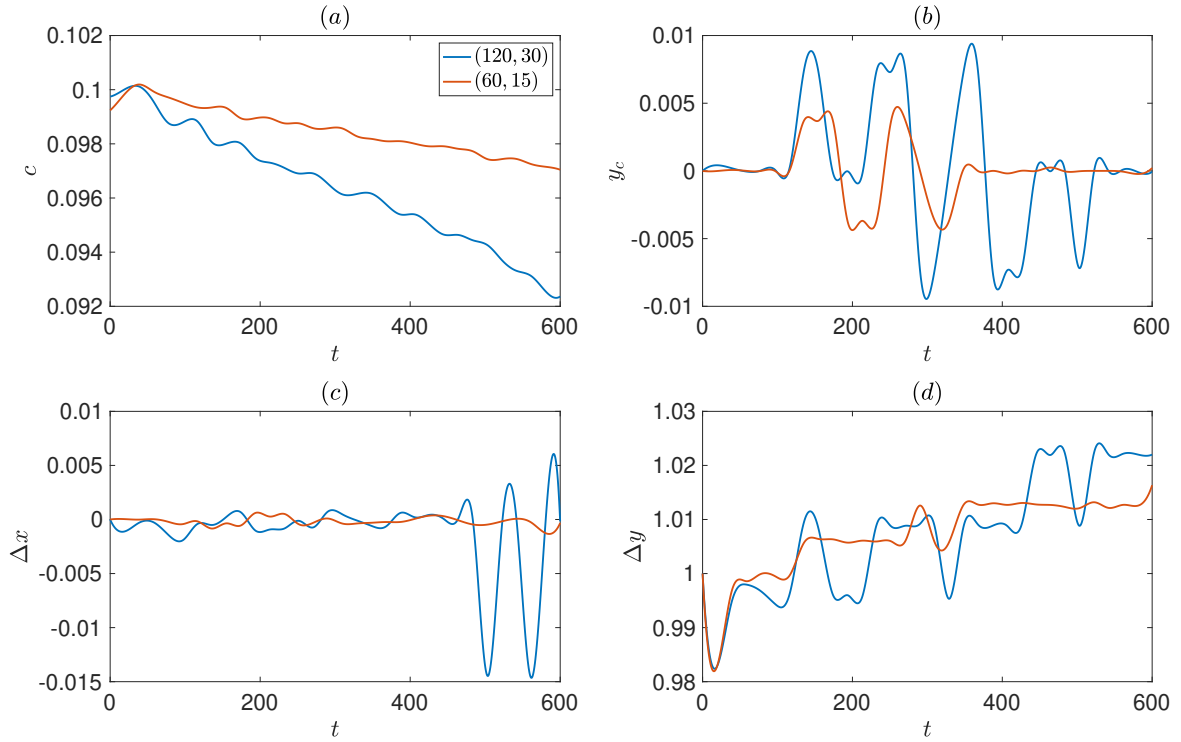


**Figure 3.10:** Time-series for a dipole with an intensity of  $c/\beta = 1$  using  $N = 2048$ : (a) shows the zonal propagation speed; (b) shows the meridional center coordinate; (c) shows the zonal extrema difference; (d) shows the meridional extrema difference (adjusted to start at unity). Blue curves are for a  $(120, 30)$  domain and red curves are for a  $(60, 15)$  domain. The  $t$ -domain considered is used so that the dipole in the larger domain does not transition through the periodic boundary, and we plot the small domain results for this same value of  $t$  for a consistent comparison.

remain steadily propagating.

To explore this problem in more detail, we can consider a doubly-sized domain for the strong dipole evolution. Given the high resolution we consider throughout this thesis, it is not feasible to double the number of grid points in each direction to preserve overall domain resolution. Instead, we keep the same number of grid points, meaning we have weaker resolution for the same amount of space. Regardless, longer domain simulations allow us to explore the dipole evolution for a lengthier time duration. Moreover, from our resolution analysis, we observed earlier disintegration on a coarser grid, so we expect to see dipole deviations sooner in the longer domain run.

Indeed, in the longer domain (see blue curves in Fig. 3.10), we see some significant deviation in the value of  $\Delta x$  at roughly  $t \sim 500$  (see Fig. 3.10c). This wobbling of the dipole could be interpreted as the same mechanism we have seen

for weak dipoles, which is consistent with the value of  $t_s$  increasing as we decrease the value of  $\beta$ . On the other hand, the dipole is exposed to numerical viscosity for significantly longer in this experiment, so it could be viscous dissipation that encourages the disturbance. This is supported by the rate of deceleration in the dipole translations (see Fig. 3.10a), where the smaller domain simulation displays weaker deceleration (a loss of  $\sim 3\%$ ) relative to the larger domain simulation (a loss of  $\sim 8\%$ ). In summary, this analysis alone seems insufficient at identifying whether strong dipoles are stable or unstable. If we assume there is a change in dynamics between strong and weak dipoles, then to analyse strong dipoles further, we can carry out a bifurcation analysis, where we explore the dynamics for different values of  $\beta$  in an attempt to identify a critical value where a transition in dynamics occurs. We leave the details of this for Chapter 4.

### 3.4 Dipole-rider dynamics

In Chapter 2, we briefly introduced the class of dipole-rider steady states, where an axisymmetric component is imposed on the LRD field. Previously, a hypothesis for numerical simulations of these vortices appearing unstable was because of discontinuity at the separatrix in the corresponding PVA field (Reznik, 2010). However, in light of our numerical results, this instability could be a consequence of the LRD destruction we see in Fig. 3.1. Since the presence of a rider acts to perturb the LRD state, if the LRD destruction is a consequence of dipole instability, then we expect the addition of a rider to encourage this instability. On the other, since the rider amplitude is unbounded, there could be cases where the rider dominates the dipole dynamics and becomes unstable for other reasons (perhaps related to the behaviour observed for moderate and strong dipole-rider solutions in Swenson (1987)).

We begin by exploring the dynamics of a weak dipole-rider vortex with intensity  $c/\beta = 1/4$  and  $\kappa = 0.01$  (see Fig. 3.11). In this case, the initial state looks similar to an LRD, however, the symmetry with respect to the zonal axis is broken slightly in favour of the positive region, and continuity at the boundary is lost. In Fig. 3.11a, we see the dipole-rider vortex expel some PV as it propagates. As it does this, the solution looks to adjust to a more familiar dipole state (similar to an LRD). We notice that this process leads to the solution seeing slight meridional displacement (see Fig. 3.11b), which was not present in our numerical results for the pure dipole propagation. After this initial adjustment, the dipole state continues to propagate in the eastward direction. Throughout the translation, the dipole state sees developing

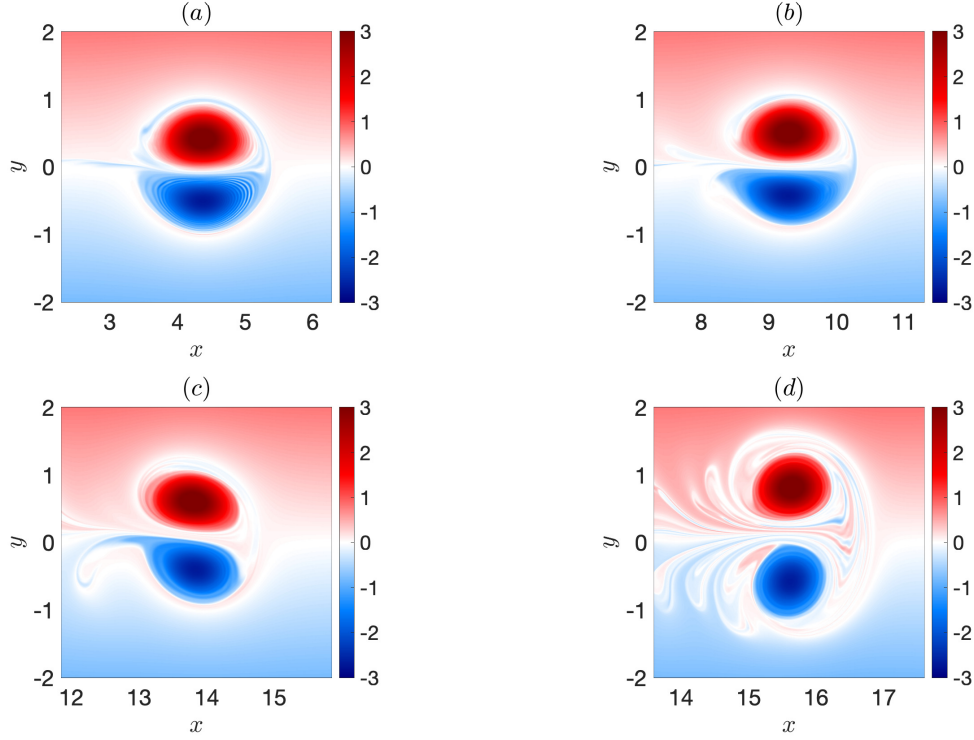


**Figure 3.11:** Dipole-rider snapshots with  $\beta = 0.4$  and  $\kappa = 0.01$ , in a  $(60, 15)$  domain with  $N = 2048$ : (a)  $t \sim 45$ ; (b)  $t \sim 90$ ; (c)  $t \sim 135$ ; (d)  $t \sim 180$ .

oscillatory behaviour that eventually turns into the spontaneous symmetry breaking phenomena (see Figs. 3.11c, d). In this case, the time of partner separation occurs earlier than in the pure dipole propagation ( $t_s \sim 188$ ); consistent with the dipole destruction mechanism being a consequence of instability.

On the other hand, when we increase the amplitude of the rider contribution to  $\kappa = 0.1$ , we see very different behaviour unfold (see Fig. 3.12). More specifically, the initial state (as in Fig. 2.3d) consists of positive PV region inside a vortex of negative PV. This state is similar to the vortex patches considered in Radko (2020b). As the solution begins to propagate, the dipole-rider quickly breaks apart as the inner positive PV escapes from the structure. During this process, the vortex sees significant filamentation; expelling PV into the background and leaving a trail of waves behind. Following this, the positive eddy core begins to oscillate with the negative eddy core, and this allows the structure to translate both zonally and meridionally. Indeed, we noticed subtle meridional drift when  $\kappa = 0.01$  (see Fig. 3.11), however, in this case there is significant meridional displacement of the newly formed dipole structure (see Fig. 3.13b).

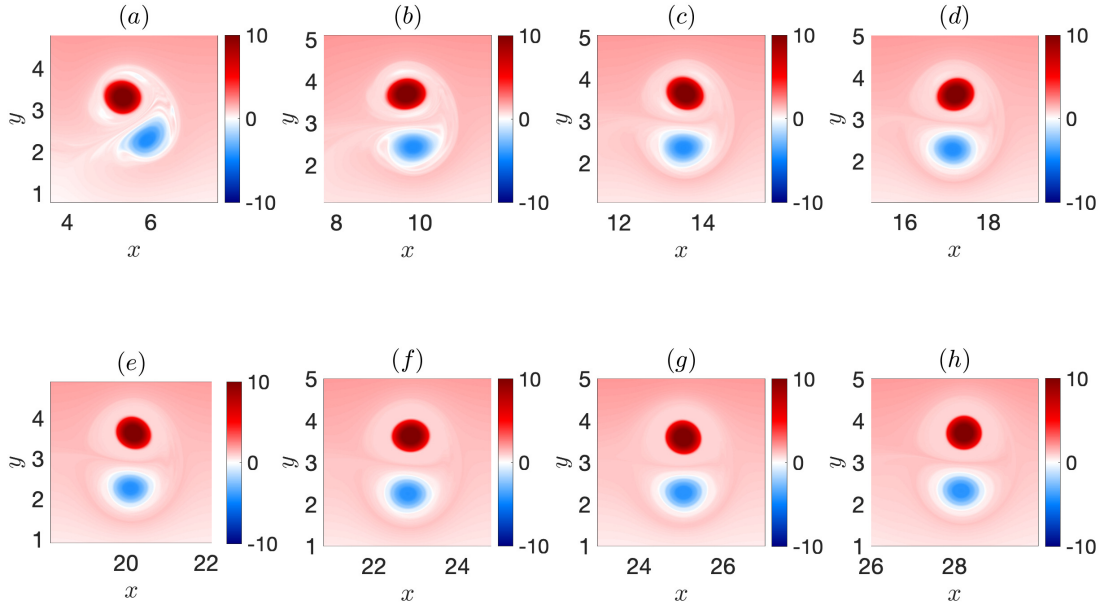


**Figure 3.12:** Dipoles-rider snapshots with  $\beta = 0.4$  and  $\kappa = 0.1$ , in a  $(60, 15)$  domain with  $N = 2048$ : (a)  $t \sim 60$ ; (b)  $t \sim 105$ ; (c)  $t \sim 150$ ; (d)  $t \sim 195$ ; (e)  $t \sim 240$ ; (f)  $t \sim 285$ ; (g)  $t \sim 320$ ; (h)  $t \sim 365$ .

It is clear from Fig. 3.13 $b, c$  that the vortex pair reaches a maximum displacement and begins to see decreasing oscillations in the interval  $75 \leq t \leq 215$ . Outside of this interval, the eddy structure appears to adjust to an elliptical dipole form (see Fig. 3.12), with the core separation being more pronounced than a circular LRD (see Fig. 3.13 $b$ ). From Fig. 3.13 $a$ , the elliptical couple does not look to display any obvious deceleration that would be representative of spontaneous symmetry breaking. From this, it appears that the initial dipole-rider steady state has adjusted to a new elliptical steady state dipole over time. This result contradicts the instability findings of Swenson (1987), which could be due to the weak resolution they used in their analysis compared to our superior numerical results, however, it could be the case that the elliptical structure breaks apart in a longer time domain. On the other hand, since Radko (2020b) showed that similar initial vortex patches were linearly unstable, but were able to see longevity due to weak very linear growth rates being present, the same could be the case for our dipole-rider input. Overall, our simulations motivate an extensive study of dipole-rider dynamics, though given the amount of material we already discuss in this thesis, we do not present further study here and leave this for future research.

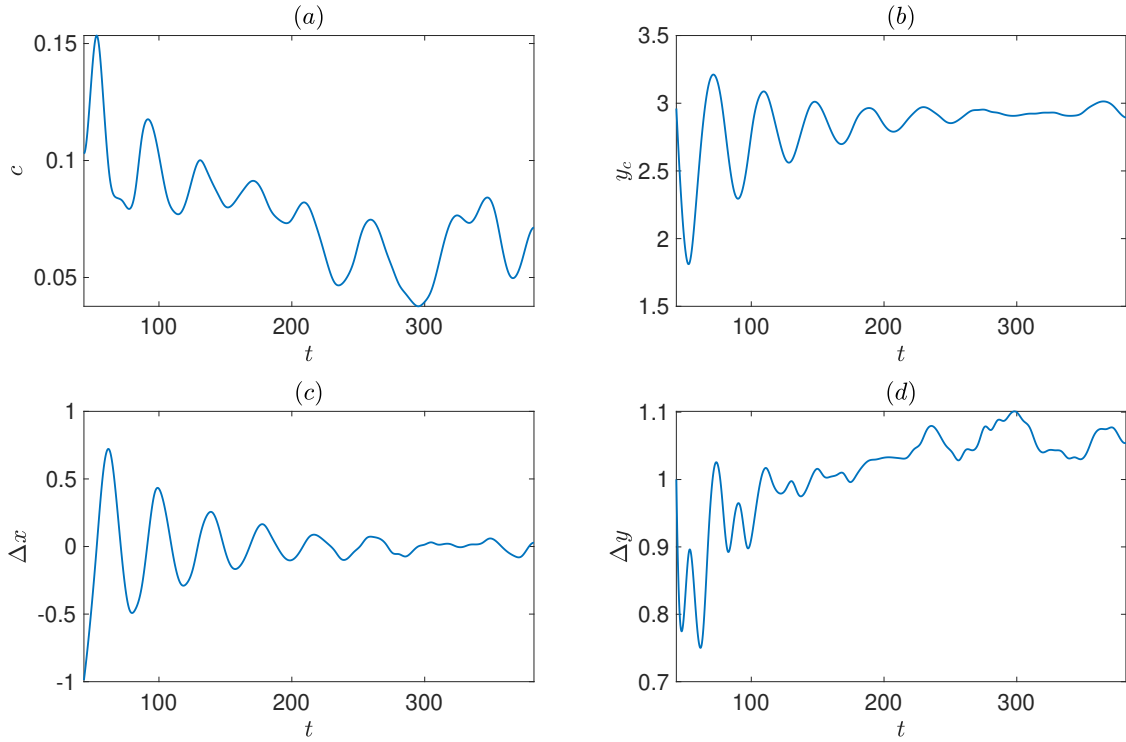


**Figure 3.13:** Time-series for a dipole-rider vortex with  $\beta = 0.4$  and  $\kappa = 0.1$ , computed in a  $(60, 30)$  domain using  $N = 2048$ : (a) shows the zonal propagation speed; (b) shows the meridional center coordinate; (c) shows the zonal extrema difference; (d) shows the meridional extrema difference (adjusted to start at unity).

### 3.5 Summary

In this chapter, we expanded on the material in Chapter 2 by simulating the dipole dynamics over time. To explore the class of LRD solutions, we fixed the value of  $c$  and considered different values for the parameter  $\beta$ . Changes in these values corresponds to dipole considerations with differing intensities, where decreasing the value of  $\beta$  is equivalent to considering the dynamics of a stronger dipole. Moreover, we limited attention to vortex scales commensurate to the Rossby radius of deformation, since these are a better representation of oceanic scales.

To solve for the dynamics numerically, we discretise the QG system on a rectangular grid with doubly-periodic boundary conditions and a discrete LRD imposed as the initial condition. Furthermore, to integrate in time, we make use of the advanced CABARET advection scheme, which we find preserves the conservation of integral invariant such as energy and enstrophy relatively well for the grid resolution we consider, i.e.,  $8192 \times 2048$  grid points. A fascinating result of our numerical simulations is the spontaneous symmetry breaking of initially weak LRDs. We first observed small

oscillatory behaviour develop in the dipole, which became more pronounced as the dipole continued to propagate in the eastward direction. As the dipole continued to translate, clear deceleration and small partner separation occur up until the time  $t = t_s$ , beyond which the dipole changed direction and the partners drift far apart and disintegrate into the background.

This peculiar behaviour captured in our analysis disagrees with the seemingly stable trajectories that eastward propagating dipoles were previously thought to follow, as described in the literature up until this point. Because of this, we solved the same problem for different domain considerations, and found that the results remain consistent. Moreover, we showed that the CABARET scheme can reproduce the results of other dipole problems considered in the literature, which supports our CABARET findings for the LRD initialisation.

As we increased the dipole intensity, we found that the dipole propagation was longer lived, with the partner separation occurring later in time. However, in the case of strong dipoles with  $\beta = 0.1$ , these appeared to follow steady trajectories with no noticeable deviation inside of the domain. Given our limited time integrations, it is possible that such strong dipoles are either steadily propagating or very weakly unstable. To confirm this, we could employ longer and more computationally expensive numerical simulations, however, these are beyond the scope of this thesis. Alternatively, we could apply different methodology such as linear stability theory to the strong dipole problem, and we carry out such analysis in Chapter 5.

Finally, we discussed the time evolution of the dipole-rider initialisation. In the case of a small symmetric addition to the LRD, we observed the spontaneous symmetry breaking phenomena, with this occurring earlier than in the absence of a symmetric rider. This behaviour is expected if the LRD is unstable, since we would anticipate small disturbances to encourage instability growth. On the other hand, when we considered a larger rider addition, the dipole-rider initially separated into two cores of opposite sign. Unlike the LRD, this solution experienced significant meridional translation. Eventually, the vortex appeared to adjust to a new elliptical dipole state, after which, the vortex propagated with approximately steady drift in the zonal direction at the new meridional level.

Now that we have identified the spontaneous symmetry breaking of weak dipoles, we would like to understand how and why this phenomena occurs. This will be our line of questioning in the next chapter.

# Chapter 4

## Critical mode analysis

Some of the contents of this chapter are derived from our work published in the Journal of Physics and Fluids: *"On the spontaneous symmetry breaking of eastward propagating dipoles"*, by J. Davies, G. Sutyrin and P. Berloff.

In Chapter 3, we captured the instability of eastward propagating dipole steady states through high resolution numerical simulations. Throughout this chapter, we make use of the flow symmetry to associate this phenomena with a growing instability mode that can be fitted to a normal mode representation; further supporting this behaviour to be related to linear instability. Following this, we perform a variety of additional experiments to explore the strong dipole problem.

### 4.1 Flow decomposition

Now that we have identified the spontaneous symmetry breaking of dipoles that propagate to the east, we are interested in explaining how this develops over time, and more importantly, we want to develop an understanding of the mechanisms that play into this physical process. Given the dipole sees spontaneous symmetry breaking over the time evolution, it could be the case that the long-time dynamics we capture in our numerical simulations is associated with a slowly growing instability. In this case, analysis of the corresponding perturbation field would reveal any deviations from the initial LRD state. If these deviations were to evolve, then this could be related to dipole instability. On the other hand, if these deviations were to remain negligible, then this would make the instability argument void.

To analyse the perturbation field,  $\psi' = \psi - \Psi$ , we must subtract the initialised LRD from the simulated solution. However, the simulated solution is dependent on some time variable, whereas, the LRD solution is a steady state that is initially placed



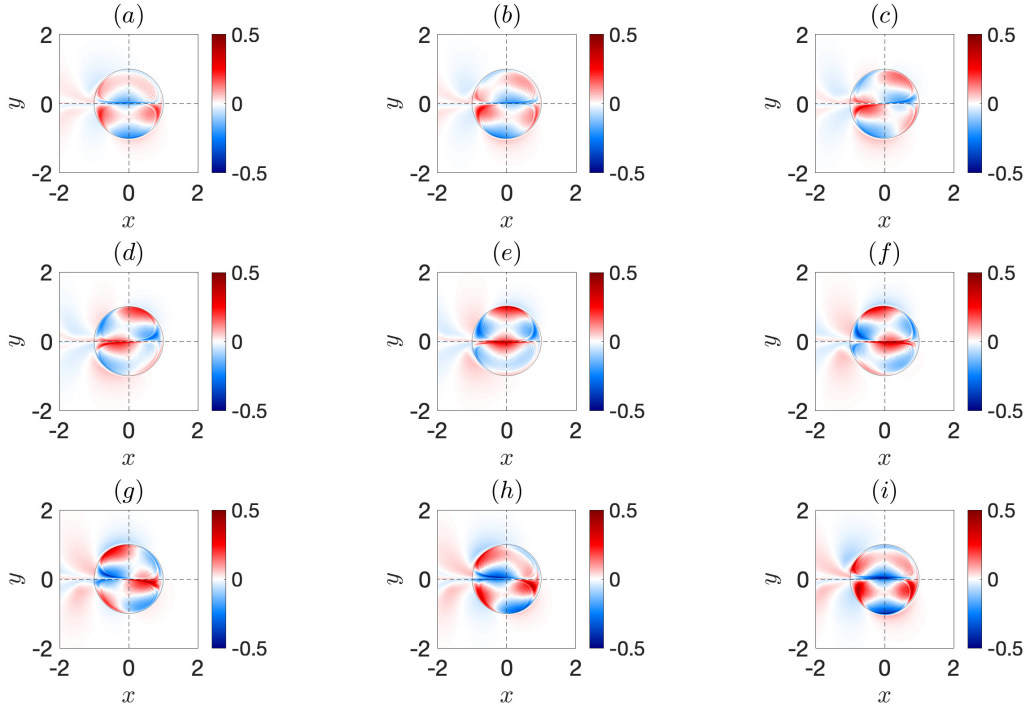


**Figure 4.1:** Snapshots of the growing PVA perturbation field over a full cycle in the co-moving reference frame, with  $\beta = 0.4$ : (a) – (i) correspond to  $t \sim 143 - 159$ , respectively (panels are with equal time interval  $\sim 2$ ).

in the center of the domain. Because of this, we must translate the LRD so that it is centered with the center of the simulated solution, and then we can subtract the fields from one another to obtain the disturbance profile. If we animate the time evolution of the perturbation for a weak dipole, we notice that approximate periodic behaviour appears to develop for  $t \sim 130$ , and these approximately periodic cycles repeat themselves. One such example of these cycles can be seen in Fig. 4.1. We can approximate the growth rate between panels (a) and (i); where these correspond to snapshots of the PVA perturbation over roughly a period of its oscillation. In particular, if we denote the growth rate by  $\sigma$ , then we can estimate this quantity as

$$\sigma = \frac{1}{T} \ln \left[ \frac{q_m(159)}{q_m(143)} \right], \quad (4.1)$$

where  $q_m = \max(q')$  and  $T \sim 16$  denotes the approximate period of oscillation for the perturbation profile. On calculation, we find that  $\sigma \sim 0.035$ , demonstrating growth over a full rotation.

Despite the first and last panels in Fig. 4.1 appearing similar, closer inspection of



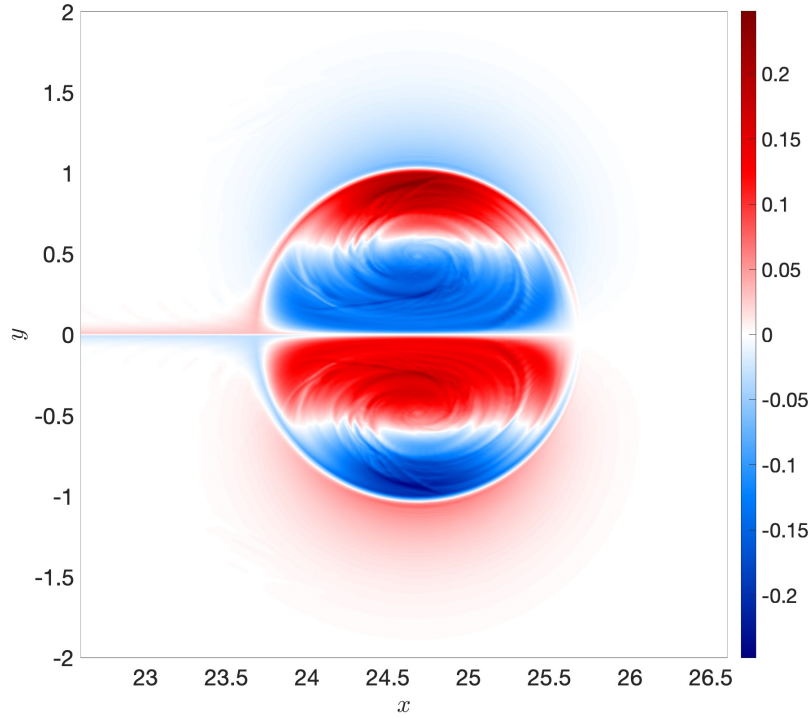


**Figure 4.2:** Perturbation pattern corresponding to the dipole propagation in the presence of a no-flow-through wall along the zonal axis. This pattern accumulates as a consequence of implicit numerical viscosity. The value of  $t$  for which this pattern is taken is within  $t \sim 143 - 159$ .

panel (e) clearly shows that our snapshots disagree with the hypothesis of oscillatory motion, since there are characteristic differences from pure periodic oscillation. More specifically, if we considered this to be a linear instability, then panel (e) would resemble panel (a), but with opposite sign. However, it is clear there is also a rotation of  $180^\circ$  (or a reflection in the zonal axis) in addition to this sign difference. This inconsistency in panels suggests that either the problem cannot be characterised as a linear instability, or that there is some information in our solution that we have not accounted for.

To highlight the case of the latter, we look to the perturbation field associated with the wall simulations. Since these solutions appear to be stable in our numerical simulations, intuition suggests that perturbations will be small and negligible. However, it is evident from Fig. 4.2 that there is an antisymmetric (with respect to the zonal axis) perturbation pattern attached to the solutions in the presence of a no-flow-through zonal wall. Because the wall simulations appear to be stable, this perturbation pattern does not contribute to the dipole destruction that occurs in the absence of a

wall. Instead, we can explain this pattern as an accumulation of numerical viscosity over time. If we compare this anomaly on a grid with half the number of grid points in both horizontal directions, then we see that the pattern is roughly four times more intense. This is exactly how we expect numerical viscous effects to behave with respect to resolution, and so we can deduce that this pattern in the wall case is a consequence of numerical viscosity acting in the background.

Given that an antisymmetric pattern with respect to the zonal axis develops on the dipole due to implicit numerical viscosity, this likely contributes to the apparent asymmetry in Fig. 4.1. Ideally, we would like to discard numerical viscous accumulation from our solution to examine the true behaviour of the growing disturbance. To do this, we can make use of the flow symmetry. Since the initial LRD has odd PVA relative to the zonal axis, if we were to decompose the PVA field into the components

$$q_A = \frac{1}{2} \left[ q(x, y, t) + q(x, -y, t) \right], \quad q_S = \frac{1}{2} \left[ q(x, y, t) - q(x, -y, t) \right], \quad (4.2)$$

where  $q_A$  and  $q_S$  are the A- and S- components of the full field, respectively, then the viscous accumulation would be collected in  $q_S$  only. This is because the A-component has purely even PVA relative to the zonal axis, whereas, the S-component has odd PVA with respect to the zonal axis, so the viscous pattern will appear in the S-component. In addition, since at initialisation the A-component is zero, any non-zero evolution in this contribution would be related to a growing unstable mode on top of the dipole. We can see from Fig. 4.3 that the S-component of the perturbation field appears similar to Fig. 4.2, which tells us that viscous accumulation is collected in the S-component and that the A-component must be the pure critical mode.

The quadratic invariants of energy and enstrophy of each component can be obtained by integrating over the entire doubly-periodic domain:

$$E_{A,S} = \frac{1}{2} \int \left[ (\nabla \psi_{A,S})^2 + S \psi_{A,S}^2 \right] dx dy, \quad Z_{A,S} = \frac{1}{2} \int q_{A,S}^2 dx dy, \quad (4.3)$$

where the summations  $E_A + E_S$  and  $Z_A + Z_S$  are conserved in the inviscid limit.

The energy  $E_A$  and enstrophy  $Z_A$  of the A-component begin to grow from zero due to the spontaneous breaking of symmetry (Fig. 4.4a). After the period of small initial oscillations, during an intermediate period of linear growth in the interval  $t_1 < t < t_2$ , the value of  $Z_A$  grows at a nearly constant rate  $\sigma_Z$ . For the weakest dipole with  $\beta = 0.4$ , we approximated  $\sigma_Z \sim 0.07$ ,  $t_1 \sim 100$ ,  $t_2 \sim 180$ . As the value of  $\beta$  decreases, we found that the value of  $\sigma_Z$  sees decay.

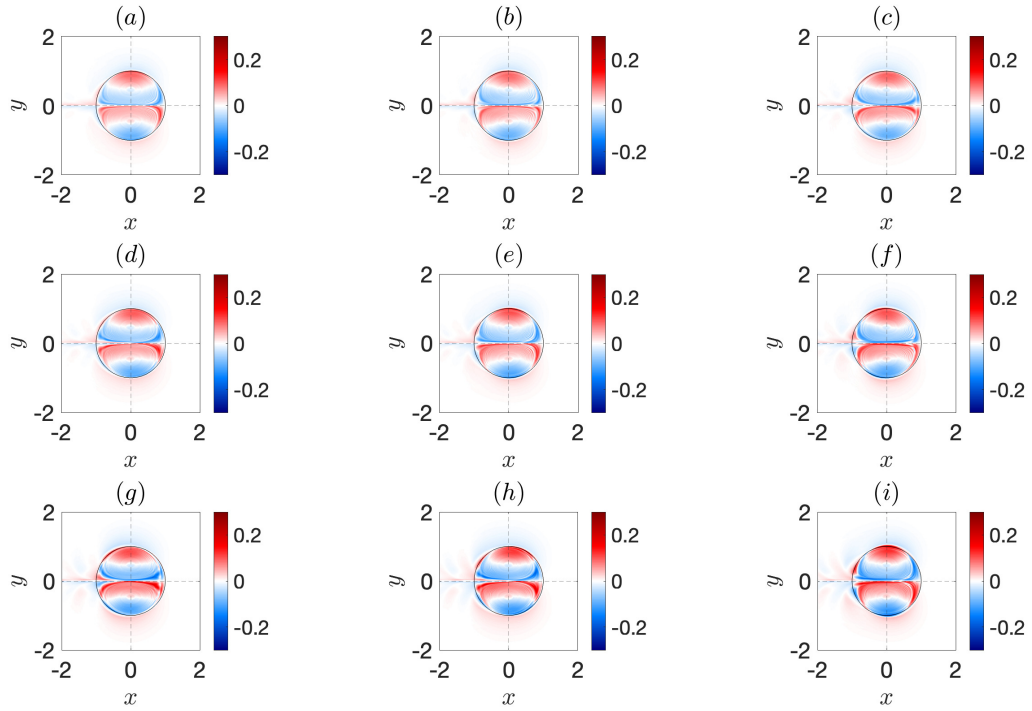


**Figure 4.3:** Snapshots of the growing S-component of PVA for  $\beta = 0.4$ , shown over the oscillation period and in the co-moving reference frame: (a)–(i) correspond to  $t \sim 143$ –159, respectively, and panels are separated by the same time interval  $\sim 2$ . Since these patterns share the same symmetry as the numerical viscous accumulation in Fig. 4.2, we expect the numerical viscous contributions to be collected in these S-components.

In Fig. 4.4b, the characteristic length scale derived from the A-component,  $L_A = \sqrt{E_A/Z_A}$ , indicates that initially antisymmetric perturbations appear at grid scale, grow towards the scale of the most unstable mode until  $t \sim t_1$ , and then remain at around  $L_A \sim 0.2$ . The dipole evolution for other  $\beta$  values look qualitatively similar, however:

- Oscillations before the linear stage are greater,
- Periods of oscillations in the linear stage are lengthier,
- Decreases in  $L_A$  beyond the linear growth stage are slower for more intense dipoles.

These differences are the most notable when  $\beta = 0.2$ , where the dipole maintains itself for significantly longer and experiences slower deceleration, before the partners drift apart from one another at  $t_s \sim 562$ .

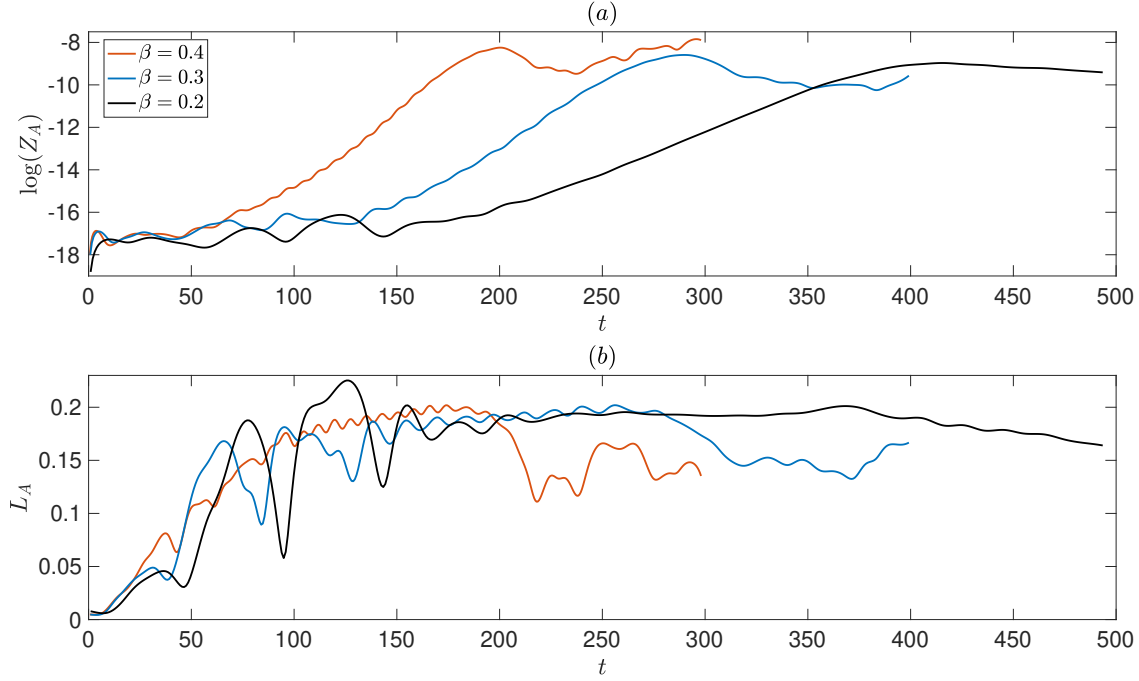


**Figure 4.4:** Time series for dipoles with  $\beta = 0.4$  (red),  $\beta = 0.3$  (blue) and  $\beta = 0.2$  (black): panel (a) shows the logarithm of enstrophy for the  $A$ -component and panel (b) shows the corresponding length scale  $L_A = \sqrt{E_A/Z_A}$ . Time intervals differ since weaker dipoles see earlier disintegration.

Fig. 4.5 presents  $q_A$  snapshots in the linear growth stage for  $\beta = 0.4$ , when small oscillatory motion becomes pronounced in Fig. 4.4. From the panels in Fig. 4.5, we can see a nearly time-periodic spatial structure for the growing  $A$ -perturbations. These fields are analogous to the growing  $A$ -mode shown in Fig. 12 in Brion et al. (2014). The corresponding period is  $T \sim 16$ , which we approximate from the phase evolution, and the growth rate is estimated from the increase in  $A$ -perturbation amplitude over the period:  $\sigma \sim 0.035$ . Therefore,  $\sigma_Z \sim 2\sigma$ , which is consistent with the growth rate of quadratic invariants if we assume that the PVA field grows exponentially<sup>1</sup>. In addition, similar estimates for stronger dipoles result in approximately the same period, but with a slower growth rate:  $\sigma \sim 0.027$  for  $\beta = 0.3$  and  $\sigma \sim 0.02$  for  $\beta = 0.2$ .

<sup>1</sup>If  $q_A \sim e^{\sigma t}$ , then it follows that  $Z_A \sim e^{2\sigma t}$ .

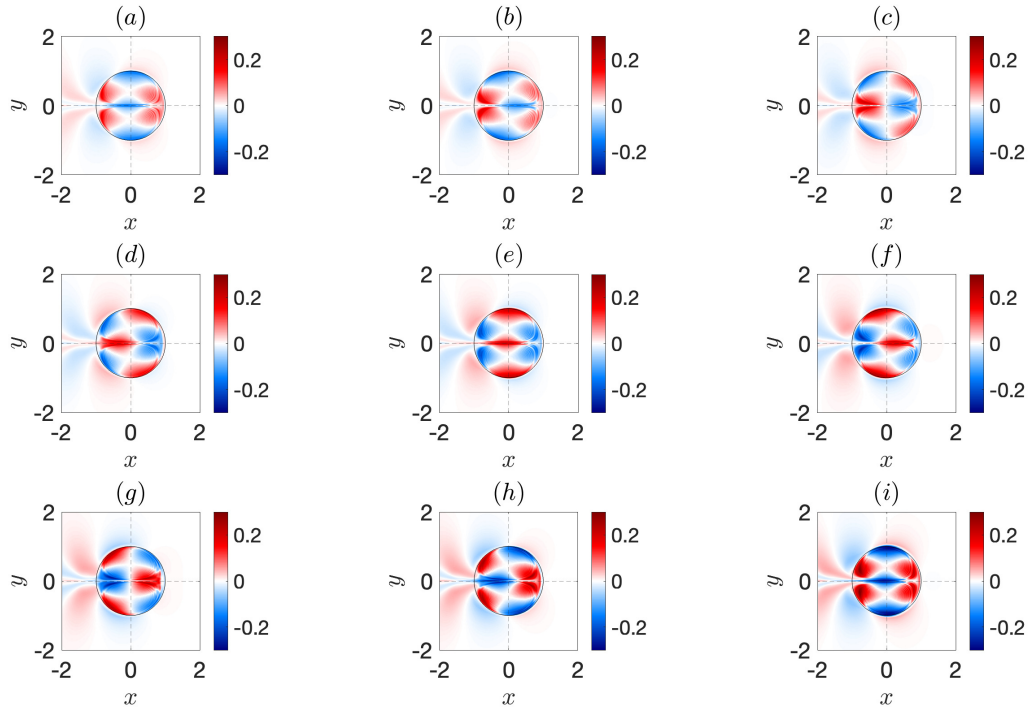


**Figure 4.5:** Snapshots of the growing A-component of the PVA field for  $\beta = 0.4$ , shown over the oscillation period and in the co-moving reference frame: (a) – (i) correspond to  $t \sim 143 - 159$ , respectively, and panels are separated by the same time interval  $\sim 2$ .

## 4.2 Normal mode representation

We can associate the A-perturbation pattern with a linear instability mode of the dipole by seeking  $q_A$  of the following normal mode form:

$$q_A = \left[ A(x, y) \cos(\omega t) - B(x, y) \sin(\omega t) \right] e^{\sigma t}, \quad (4.4)$$

where  $A, B$  are the real and imaginary parts of the mode, respectively;  $\omega = 2\pi/T$  is the oscillation frequency, and  $\sigma$  is the linear growth rate.

### Amplitude components

The functions  $A$  and  $B$  can be derived by considering the following moments or snapshots:

$$q_1 = \left[ A \cos(\omega t_1) - B \sin(\omega t_1) \right] e^{\sigma t_1}, \quad (4.5)$$

$$q_2 = - \left[ A \sin(\omega t_1) + B \cos(\omega t_1) \right] e^{\sigma t_1} e^{\sigma T/4}, \quad (4.6)$$

where  $q_1 = q_A(x, y, t_1)$  and  $q_2 = q_A(x, y, t_1 + T/4)$ . On multiplying (4.5) by  $\cos(\omega t_1)$  and (4.6) by  $\sin(\omega t_1) e^{-\sigma T/4}$ , the resulting difference allows us to derive the function  $A$ , namely

$$A = \left[ q_1 \cos(\omega t_1) - q_2 \sin(\omega t_1) e^{-\sigma T/4} \right] e^{-\sigma t_1}. \quad (4.7)$$

In a similar fashion, on multiplying (4.5) by  $\sin(\omega t_1)$  and (4.6) by  $\cos(\omega t_1) e^{-\sigma T/4}$ , the resulting summation yields

$$B = - \left[ q_1 \sin(\omega t_1) + q_2 \cos(\omega t_1) e^{-\sigma T/4} \right] e^{-\sigma t_1}. \quad (4.8)$$

### Time-mean integral

With this linear decomposition in mind, we can formulate an analytic form for the time-mean over a period of oscillation. If we consider the interval  $[t_1, t_1 + T]$ , then it follows that

$$\overline{q_A} = \frac{1}{T} \int_{t_1}^{t_1+T} q' dt = \frac{1}{T} \left[ A \int_{t_1}^{t_1+T} \cos(\omega t) e^{\sigma t} dt - B \int_{t_1}^{t_1+T} \sin(\omega t) e^{\sigma t} dt \right]. \quad (4.9)$$

By means of integration by parts, we find that

$$\int_{t_1}^{t_1+T} \cos(\omega t) e^{\sigma t} dt = \left( \frac{e^{\sigma T} - 1}{\sigma^2 + \omega^2} \right) \left[ \sigma \cos(\omega t_1) + \omega \sin(\omega t_1) \right] e^{\sigma t_1}, \quad (4.10)$$

$$\int_{t_1}^{t_1+T} \sin(\omega t) e^{\sigma t} dt = \left( \frac{e^{\sigma T} - 1}{\sigma^2 + \omega^2} \right) \left[ \sigma \sin(\omega t_1) - \omega \cos(\omega t_1) \right] e^{\sigma t_1}, \quad (4.11)$$

and thus, it follows that

$$\overline{q_A} = \Lambda \left[ (A\omega - B\sigma) \sin(\omega t_1) + (A\sigma + B\omega) \cos(\omega t_1) \right] e^{\sigma t_1}, \quad (4.12)$$

where

$$\Lambda = \frac{1}{T} \left( \frac{e^{\sigma T} - 1}{\sigma^2 + \omega^2} \right). \quad (4.13)$$

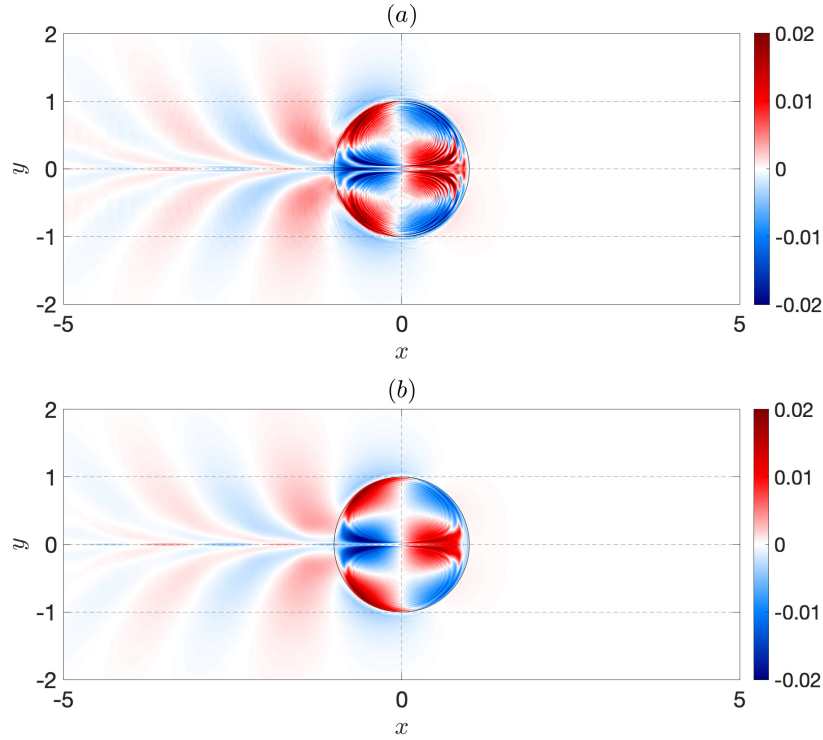


**Figure 4.6:** Period-averaged profiles for the A-component snapshots: (a) is obtained by evaluating the mean over a period of oscillation; (b) is obtained using (4.12) and is consistent with (4.14).

Moreover, if we substitute (4.7) and (4.8) into (4.12), then we find that

$$\overline{q_A} = \Lambda(\sigma q_1 - \omega q_2 e^{-\sigma T/4}). \quad (4.14)$$

Fitting (4.12) with only two snapshots from Fig. 4.5 allows us to obtain  $A$  and  $B$  (see Fig. 4.7), such that (4.5) produces panels consistent with those obtained numerically (see Fig. 4.8). Hence, we conclude that the growing A-component can be interpreted as a critical linear-instability mode with a period of  $T \sim 16$  and a linear growth rate of  $\sigma \sim 0.035$ . Given the importance of these instability modes when discussing the dipole instability, we refer to these from now on as either A-modes (to describe critical modes obtained with even symmetry about the zonal axis) or Davies modes (this use is specific to LRDs and is motivated by these critical mode patterns being undiscovered until recently, see Davies et al. (2023)).

The spatial structure of  $A$  and  $B$  (Fig. 4.7) is complex when compared with the 2D viscous linear instability A-mode associated with the Lamb-Chaplygin dipole (Brion et al. (2014), Fig. 8). The real part of the latter A-mode corresponds to

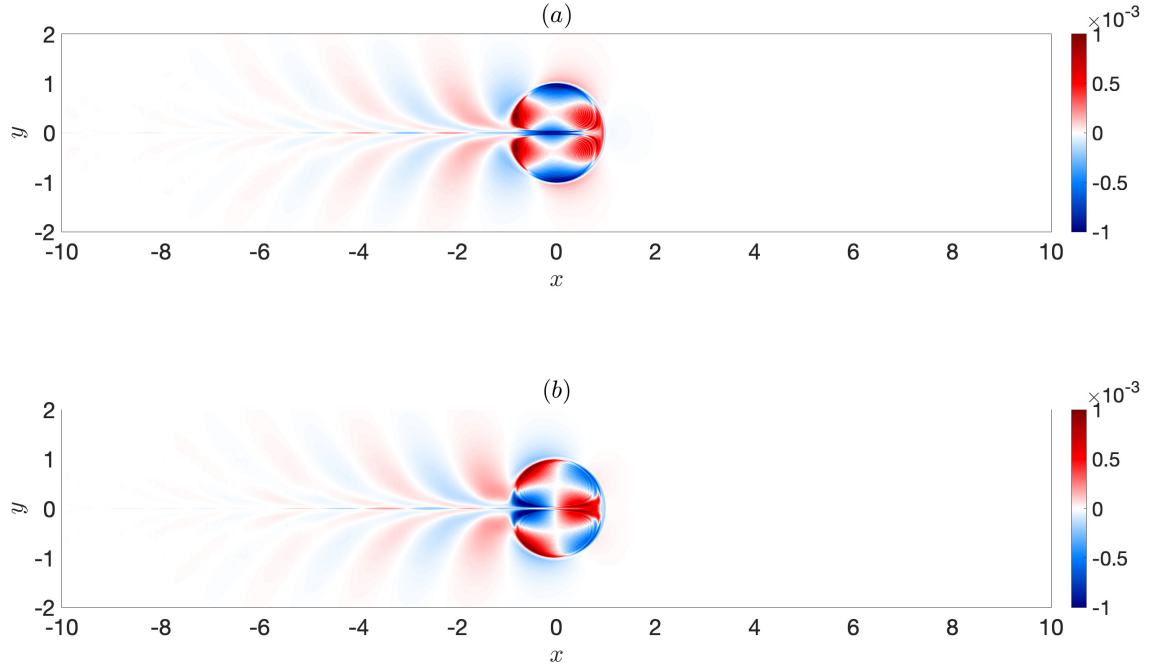


**Figure 4.7:** Reconstruction of the complex-valued critical mode: (a) real part  $A(x, y)$ , and (b) imaginary part  $B(x, y)$ .

meridional displacement of the dipole, and the imaginary part corresponds to tilting of the dipole axis. The wake formed behind the drifting dipole is visible in both the real and imaginary parts and results from viscosity. In contrast, the Davies mode pattern (Fig. 4.7) describes elongation and contraction of counter-rotating PVA cores in the dipole partners. Note that emergence of quadrupolar instability in circular  $f$ -plane equivalent-barotropic vortices has been reported in [Berloff and Meacham \(1998\)](#), but in this case the novel aspect is the A-mode synchronisation of two such instabilities in the vortex pair.

It is clear from the average Davies mode (see Fig. 4.6) that there is an associated symmetric wake about the zonal axis. The formation of which may be a consequence of the mechanism of Rossby wave radiation, in contrast with the viscous mechanism forming the wake in the Lamb-Chaplygin dipole. Furthermore, the Davies mode wake fans out (potentially due to meridional Rossby wave radiation), whereas, the Lamb-Chaplygin viscous wake thins out, which could be due to the absence of Rossby waves. In the Lamb-Chaplygin dipole, the instability is attributed to a dipole-wake interaction ([Brion et al., 2014](#)): wake formation affects the dipole motion, in turn amplifying the wake, and thus this positive feedback mechanism



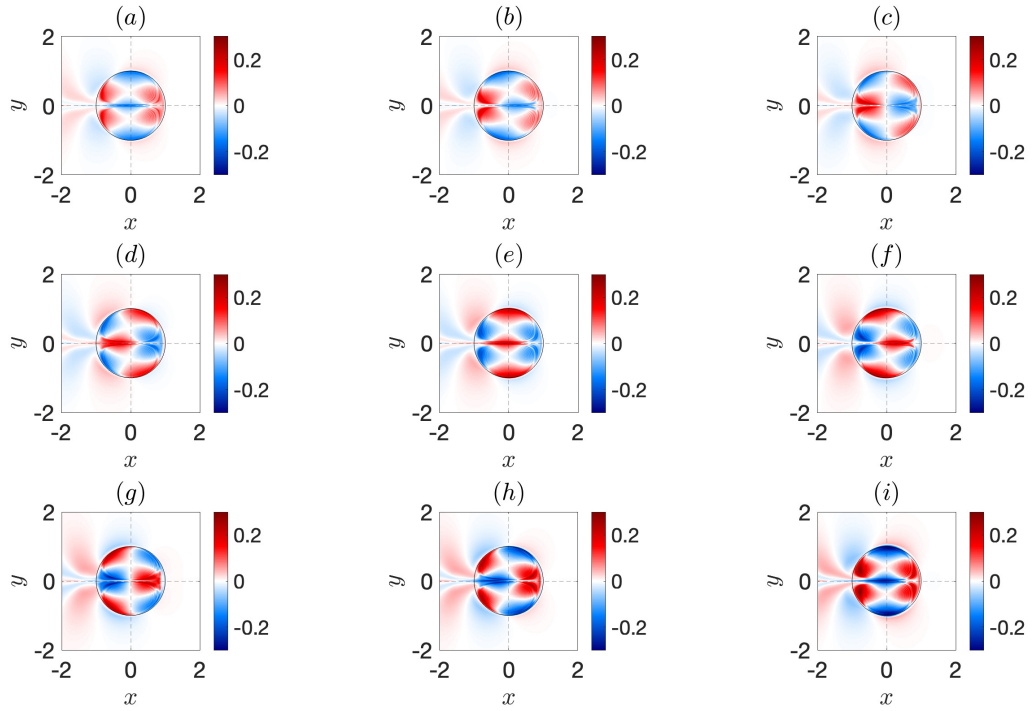


**Figure 4.8:** Linear modes extracted from numerical snapshots using the normal mode decomposition (4.4): (a) – (i) correspond to  $t \sim 143 - 159$ , respectively, and panels are separated by the same time interval  $\sim 2$ . These panels share remarkable consistency with those presented in Fig. 4.5.

supports the instability growth. Despite our weak dipoles producing similar wakes to the Lamb-Chaplygin dipole in the presence of viscosity, we leave the analysis of these wakes and their feedback roles for future analysis. However, we appreciate that a similar feedback mechanism could apply here.

#### 4.2.1 Resolution and Newtonian viscosity considerations

In Chapter 3, we mentioned that it is important to investigate the effects of viscous dissipation due to implicit numerical viscosity. Therefore, we compare our CABARET results obtained using numerical viscosity with those obtained using different explicit Newtonian viscosities. Not only is it important to identify any differences in results between different viscosities used, comparison studies of this kind are useful in identifying the dependence of the instabilities we have identified on viscosity in the system. This is particularly interesting since the class of LRD steady states are inviscid solutions in an infinite domain, whereas, we simulate the problem in a doubly-periodic domain with either numerical or Newtonian viscosity. In Fig.

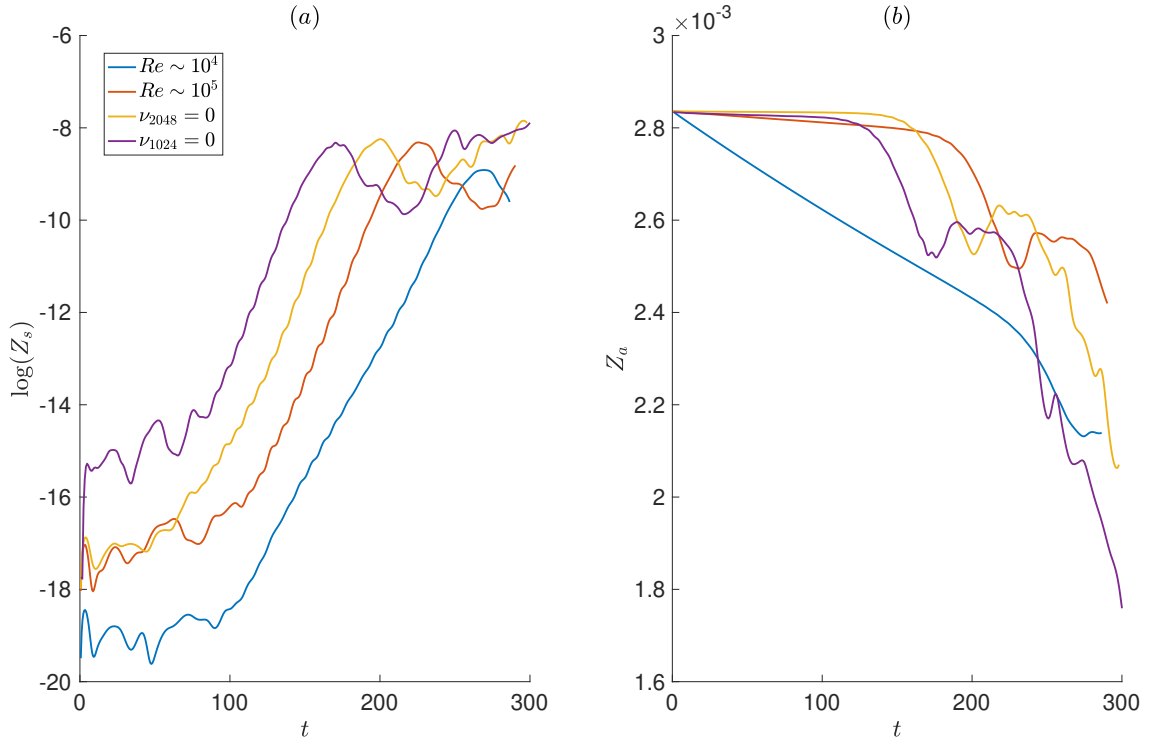


**Figure 4.9:** Curves comparing  $\beta = 0.4$  solutions with either numerical viscosity (yellow and purple curves) or Newtonian viscosity (red and blue curves), using  $N = 1024$  (purple curve) and  $N = 2048$  (red, blue and yellow curves): (a) shows time-series for  $\log(Z_s)$  and (b) shows the time-series for  $Z_A$ .

4.9, we present enstrophy solutions obtained using different Newtonian viscosities, as well as with solutions obtained using implicit numerical viscosity. In addition, we also present results using both  $N = 1024$  and  $N = 2048$ , since we previously observed earlier dipole destruction in the case of weaker resolution (see Fig. 3.2). From these curves, the numerical viscosity solutions appear similar to those obtained with  $Re \sim 10^5$ , where  $Re = \hat{L}\hat{U}/\hat{\nu}$  is the Reynolds number. When  $Re \sim 10^4$ , we see significant loss of enstrophy (resulting from viscous dissipation of the dipole, see Fig. 4.9b), whereas, all other curves appear more consistent. Therefore, we can deduce that numerical viscosity in our system is approximately  $\hat{\nu} \sim 0.04 \text{ m}^2 \text{ s}^{-1}$ , which is consistent with the viscosity sensitivity and convergence analysis for CABARET solutions in Shevchenko and Berloff (2015).

## 4.3 Further experiments

### 4.3.1 Strong dipole analysis

It is evident from our analysis up to this point that the behaviour of strong dipoles is still unclear, i.e., it is not obvious whether these solutions are stable or unstable. It could be the case that these objects are stable and will only see eventual disintegration due to numerical viscosity in the background. On the other hand, these solutions could also be unstable and simply experience very weak growth rates when compared to weaker dipoles. In the former instance, we expect there to be no developing Davies mode on the dipole, while in the later scenario, there should exist a developing critical mode. If we consider the strong dipole propagation with  $\beta = 0.1$ , then we can see how the A-component behaves over time in Fig. 4.10. The anomaly we see develop on the dipole looks different initially when compared with the Davies mode we are familiar with (see Fig. 4.6), though it does look to grow in intensity (see Fig. 4.10a, b) and have a nonzero period of oscillation (see Fig. 4.10b, c). However, we notice that a Davies mode develops with a clear wake outside of the rectangular domain (see Fig. 4.10d). It could be that this would occur naturally, on the other hand, the formation of this pattern could be due to artificial dipole-wake interaction or numerical dissipation.

To investigate this further, we can consider a dipole in a doubly-sized domain. In this case, to retain resolution, we would need to double the number of grid point in each horizontal direction. However, this is a taxing task numerically, so instead we keep the same number of grid points and sacrifice resolution in both directions. From our previous numerical analysis, the main differences with using a weaker resolution of  $N = 1024$  were that the spontaneous symmetry breaking occurred slightly earlier in the time integration. This is likely a consequence of numerical viscosity in the system encouraging viscous dissipation of the dipole, in addition to the already growing dipole instability. In any event, we expect to see the development of a Davies mode sooner in simulations using this weaker resolution. In Fig. 4.11, we see the clear development and growth of a Davies mode before the dipole transitions through the periodic boundary.

To draw comparisons between these simulations, we consider how the time-series for invariants look relative to each other (see Fig. 4.12). Clearly, the enstrophy behaviour associated with the A-component appears similar in both cases (see Fig. 4.12a). Despite the lower resolution solution increasing earlier than the higher resolution outputs, there still seems to be a linear growth stage associated with the

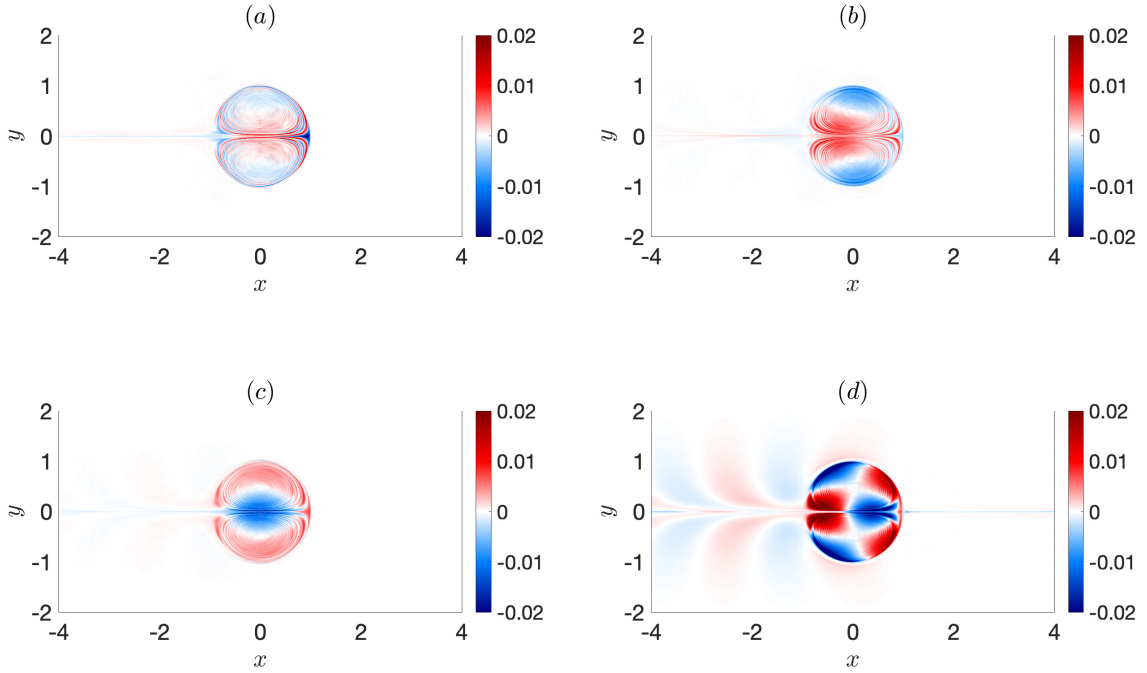


**Figure 4.10:** PVA representation of A-components corresponding to  $\beta = 0.1$ , in a  $(60, 15)$  domain with  $N = 2048$ : (a)  $t \sim 100$ ; (b)  $t \sim 200$ ; (c)  $t \sim 400$ ; (d)  $t \sim 600$  (fields are centred in the co-moving reference frame).

dynamics in a smaller domain. As mentioned previously, the Davies mode begins to develop after transitioning through the periodic domain, and so it could be argued that the presence of this field is artificial and will not play into the destruction of the strong dipole. Regardless, the similarity in curves is worth noting and could suggest that the strong dipole exhibits very weak instability. This is further supported by similarities in the evolving length scale  $L_A$  (see Fig. 4.12b). Observations of long-lived weakly unstable solutions have been captured for different initial states (Radko, 2020b).

### 4.3.2 Distillation

Another method we can apply to the strong dipole problem is the process of distillation. This is a numerical procedure that involves the following steps:

- Simulate the dipole motion as normal,
- Extract a growing perturbation field associated with the dipole motion,

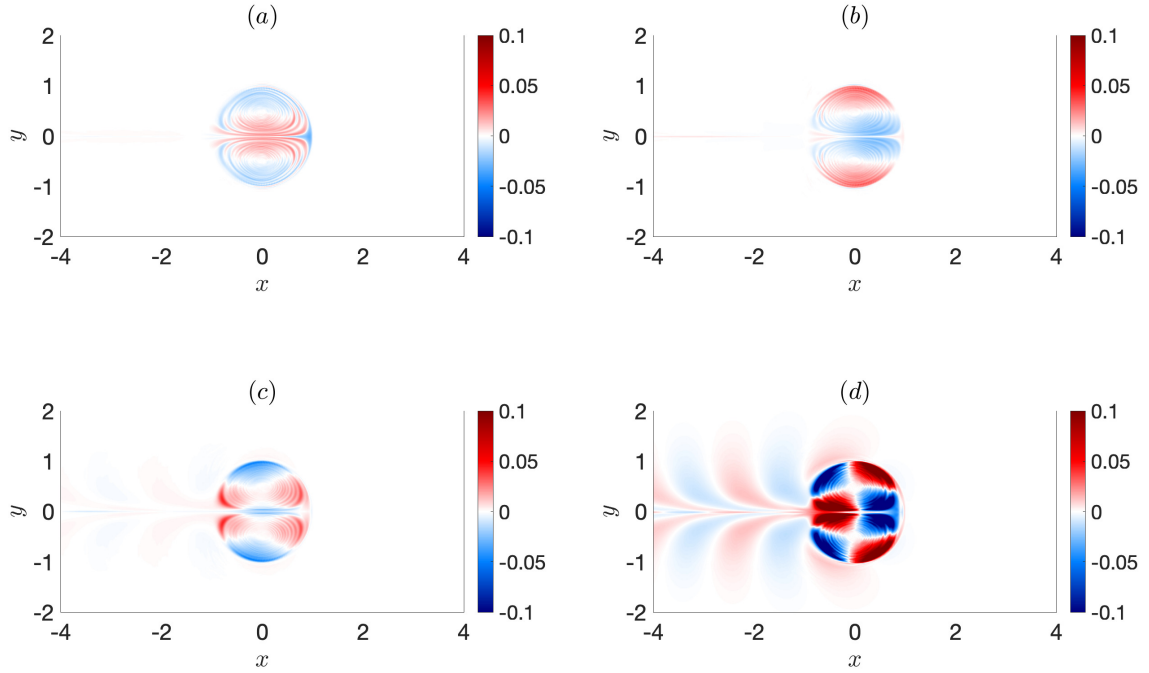


**Figure 4.11:** Solutions for  $\beta = 0.1$  in a  $(120, 30)$  domain with  $8192 \times 2048$  grid points: (a)  $t \sim 100$ ; (b)  $t \sim 200$ ; (c)  $t \sim 400$ ; (d)  $t \sim 600$  (fields are centred in the co-moving reference frame).

- Perturb the LRD initialisation by some multiple of the extracted anomaly,
- Simulate the perturbed LRD in an attempt to induce more pronounced instability at an earlier stage in the time evolution.

If a strong dipole experiences weak instability, then disturbing the vortex in this way should act to encourage the inevitable dipole destruction (similar to what we observed with the dipole-rider dynamics in Fig. 3.11). On the other hand, there might exist a bifurcation point in the  $(\beta, c)$ -parameter plane, where the dipole dynamics transitions from being unstable and prone to destruction, to solutions that remain steadily drifting. We can begin to consider this problem by carrying out distillation experiments for dipoles of different intensity. More specifically, we extract the Davies mode as in Fig. 4.10 and set this to be the disturbance we impose on the dipole (scaled up by a factor of 3 to account for the weak amplitude of the profile). Following this, we simulate the disturbed dipole dynamics for solutions with  $\beta = 0.125, 0.1, 0.075$ , with the intention of identifying whether or not any of these trajectories deviate significantly relative to one another. Naturally, we expect the weakest of these

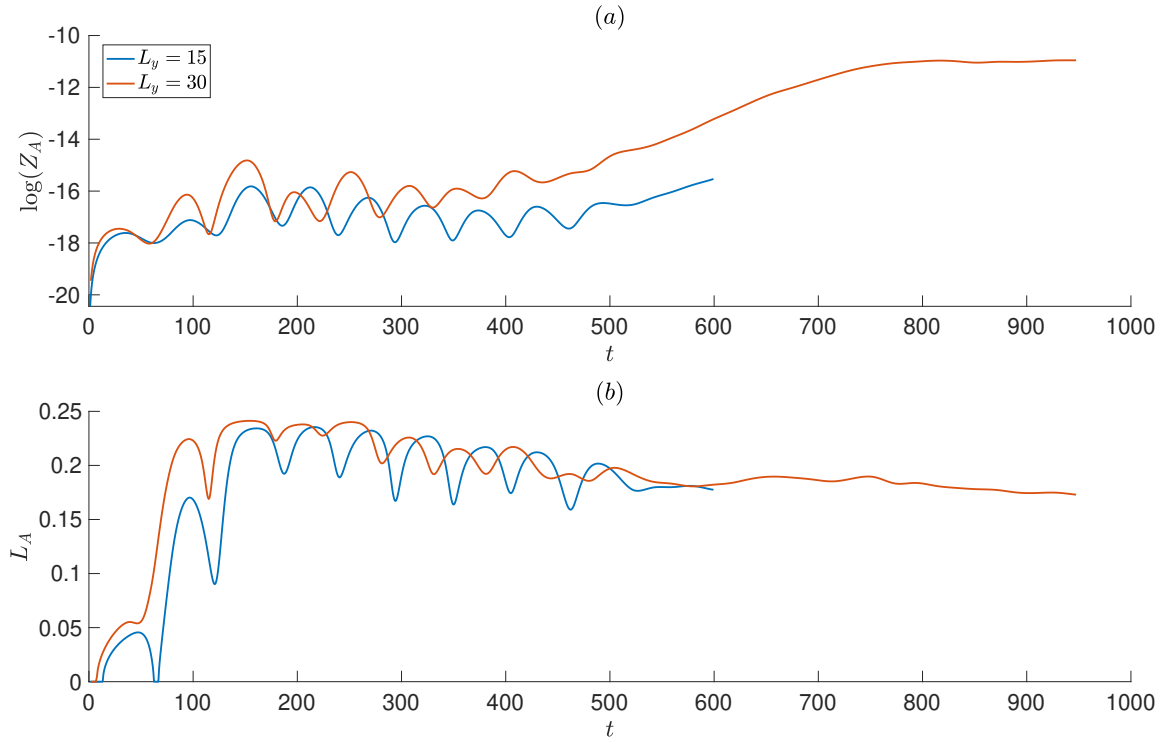


**Figure 4.12:** Time series for  $\beta = 0.1$  dipoles in a  $(60, 15)$  domain (blue) and a  $(120, 30)$  domain (red), using  $N = 2048$ : panel (a) shows the logarithm of enstrophy for the A-component and panel (b) shows the corresponding length scale  $L_A = \sqrt{E_A/Z_A}$ .

dipoles ( $\beta = 0.125$ ) to behave the most disturbed, however, if for example, this vortex were to breakdown or show obvious signs of symmetry breaking; while the others maintained themselves, then this would suggest that a critical transition occurs for some value in the range  $0.1 \leq \beta \leq 0.125$ .

On analysing the distillation results in Fig. 4.13, the enstrophy time-series for the corresponding A-components appears to be consistent across all cases, up until  $t \sim 80$ . However, as we simulate further, we notice that the weakest dipole we consider ( $\beta = 0.125$ ) sees an approximate linear increase in enstrophy (see red curve in Fig. 4.13a). Moreover, the stronger dipoles also see an increasing tendency, although, more pronounced oscillations occur during this phase for dipoles of increasing intensity (see blue and yellow curves in Fig. 4.13a). This could be interpreted as the weakest of these dipoles experiencing small linear growth during this increasing phase (consistent with our analysis showing that linear growth decreases with increasing dipole intensity). It could be argued that even though the stronger dipoles see similar growth tendencies, the presence of oscillatory signals could be indicative of transient behaviour (i.e., these dipoles are showing signs of

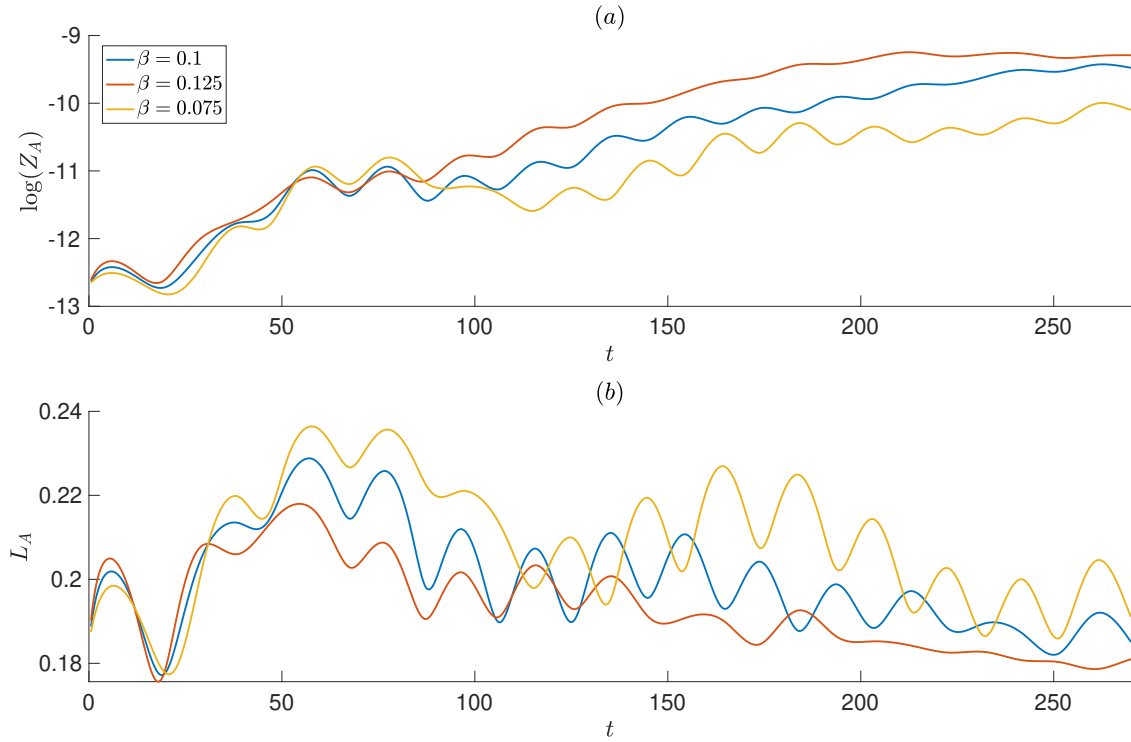


**Figure 4.13:** Curves describing the results for various distillation experiments, where strong dipoles are perturbed by a Davies mode extracted at  $\beta = 0.1$  (scaled by a multiple of 3): (a) shows the logarithm of enstrophy for the A-components; (b) shows the time-series for  $L_A$ .

disturbance, but this might not result in dipole destruction). On the other hand, since this oscillatory behaviour for the stronger dipoles appears to be decaying over time, perhaps the solution is approaching a linear growth phase.

If we analyse how the A-component deforms over time, we notice that the length scale for  $\beta = 0.125$  seems to settle down during the phase of approximate linear growth, with  $L_A \sim 18$  (see Fig. 4.13b). This behaviour is similar to what we observed for weak dipoles in Fig. 4.4. In comparison with the cases of  $\beta = 0.1$  and  $\beta = 0.075$ , these curves appear more disturbed for the same range of  $125 \leq t \leq 250$ . However, in the case of  $\beta = 0.1$ , even though the signal is oscillatory, the value of  $L_A$  appears to be decreasing slowly. Though it could be argued that the case of  $\beta = 0.075$  behaves in a similar way, the deviations in  $L_A$  are still significant and make it difficult to decipher whether or not the A-component is approaching the critical mode scale in our limited time simulations (we limit attention to before periodic transition through the domain boundary). Given all curves have characteristics in common, this acts to support the hypothesis that strong dipoles experience weak instability.

## 4.4 Summary

In this chapter, we related the spontaneous symmetry breaking phenomena discussed in Chapter 3 to linear instability of the LRD solution. We were able to extract a growing periodic field by considering the A-component of the dipole evolution. To associate this with linear growth, we sought a normal mode representation for the growing field. On fitting the normal mode form with snapshots of the numerically simulated data, we achieved snapshot correspondence between our numerical results and our normal mode panels. This consistency supports the linear instability hypothesis for the LRD steady state. Moreover, we call the critical mode pattern a Davies mode to highlight that the eastward propagating LRD was previously thought to be stable.

To evaluate the numerical viscosity present in the background of our CABARET simulations, we carried out various simulations with different explicit Newtonian viscosities, as well as numerical viscosity on grids of different resolution. Our analysis demonstrated that our numerical viscosity results were similar to those obtained with  $Re \sim 10^5$ , suggesting that CABARET is suitable for high Reynolds number flows (i.e., inviscid fluid dynamics).

Despite us showing that weak dipoles were linear unstable, the behaviour of strong dipoles required further investigation. To do this, we consider the A-component evolution for the strong dipole. We found that a Davies mode pattern develops, but not until after the dipole has transitions through the periodic domain. Because of this, it is unclear whether or not this mode develops naturally, or as a consequence of periodic wake interaction.

In addition to our strong dipole simulations, we carried out distillation experiments, where we perturbed various strong dipoles with the Davies mode pattern we extracted for the strong dipole. The purpose of this was to encourage instability to develop if the strong dipole were unstable, as well as to pinpoint a more exact value of  $\beta$  for which there is a clear shift between stable and unstable behaviours. Based on the deviations in time-series and consistencies in curves between different values of  $\beta$ , this supports the idea that stronger dipoles are weakly unstable relative to weak dipoles.

Now that we have strong evidence to suggest that the LRD is unstable due to a growing critical Davies mode, it makes sense to analyse the linear stability of the class of LRD solutions. This material will be the focus of Chapter 5.



# Chapter 5

## Linear stability of dipoles

Motivated by the normal mode representation for the dipole evolution reproducing panels for the Davies mode extracted numerically, we carry out a linear stability analysis for various initial value problems. We find that the results are consistent with our findings for weak dipoles, while the case of strong dipoles appears more complicated, with a Davies-type mode appearing further down the eigenspectrum.

### 5.1 Perturbation analysis

Previously, we showed that fitting normal mode solutions with numerical snapshots of the growing A-component in Fig. 4.5 produced remarkable panel correspondence (see Fig. 4.8); acting as strong evidence that the spontaneous symmetry breaking phenomena we have found for eastward propagating dipoles is a consequence of linear instability. Because of this, we can think of the evolving A-component as a critical instability mode, and we called this an A-mode or Davies mode, where the former of these emphasises the flow symmetry, while the later emphasises that these modes have not been discovered up until the work of this thesis and [Davies et al. \(2023\)](#).

Encouraged by the consistency we see with the normal mode representation, we perform a linear stability analysis for the dipole problem. If the dipole is unstable, then we expect to extract the most unstable mode using linear stability theory. This involves solving the perturbation governance (2.13), which we can achieve by seeking normal mode solutions. Given this approach is different to the previous numerical methodology we used in the previous chapters, we take some time to detail the linear stability methodology. Furthermore, we derive the linear stability system for a two-layer QG model (since the two-layer application can find use outside

of this thesis) and simplify the equations to obtain the equivalent for the 1.5-layer case.

## Linearisation

Consider a two-layer QG model on the beta-plane with variable bottom topography,  $\eta_b(x, y)$ . Then, in nondimensional form,

$$\left[ \frac{\partial}{\partial t} + \left( U_j - \frac{\partial \psi_j}{\partial y} \right) \frac{\partial}{\partial x} + \frac{\partial \psi_j}{\partial x} \frac{\partial}{\partial y} \right] q_j + \beta_j \frac{\partial \psi_j}{\partial x} + \alpha \delta_{2j} U_j \frac{\partial \eta_b}{\partial x} + \alpha \delta_{2j} \mathbb{J}(\psi_j, \eta_b) = \nu \nabla^4 \psi_j - \delta_{2j} \gamma \nabla^2 \psi_j, \quad (5.1)$$

where  $\psi_j$  denotes the layer-wise streamfunction,  $q_j = \nabla^2 \psi_j + S_j(\psi_{3-j} - \psi_j)$  is the layer-wise PVA,  $U_j$  denotes a homogenous zonal current imposed in each fluid column,  $\beta_j = \beta + S_j(U_j - U_{3-j})$ , the constant  $\alpha$  is defined by how we nondimensionalise the topography term,  $\nu$  and  $\gamma$  are eddy viscosity and bottom friction respectively, and  $\delta_{i,j}$  is notation for the Kronecker delta function.

On imposing a surface-layer vortex, say  $\Psi_1(x, y)$ , we can recast our problem in a coordinate system translating with the vortex center,  $(x_c, y_c)$ . Therefore, if we decompose fields according to  $\psi_j = \Psi_j(x, y) + \epsilon \psi'_j(x, y, t)$ , where  $0 < \epsilon \ll 1$ , then we can derive the perturbation governance at  $\mathcal{O}(\epsilon)$ :

$$\left[ \frac{\partial}{\partial t} + u_j \frac{\partial}{\partial x} + v_j \frac{\partial}{\partial y} \right] q'_j + \mathbb{J}(\psi'_j, Q_j) + \beta_j \frac{\partial \psi'_j}{\partial x} + \alpha \delta_{2j} \mathbb{J}(\psi'_j, \eta_b) = \nu \nabla^4 \psi'_j - \delta_{2j} \gamma \nabla^2 \psi'_j, \quad (5.2)$$

where

$$u_j = U_j - c_x - \frac{\partial \Psi_j}{\partial y}, \quad v_j = \frac{\partial \Psi_j}{\partial x} - c_y, \quad (5.3)$$

and we define the perturbation PVA as

$$q'_j = \nabla^2 \psi'_j + S_j(\psi'_{3-j} - \psi'_j). \quad (5.4)$$

## Matrix system

We can seek Fourier solutions of the form

$$\psi_j = \phi_j(x, y)e^{-i\lambda t}, \quad (5.5)$$

where  $\lambda = \omega + i\sigma$ , to rewrite (5.2) in the form

$$\lambda \tilde{q}_j = i \left\{ \nu \nabla^4 \phi_j - \delta_{2j} \gamma \nabla^2 \phi_j - \left( u_j \frac{\partial}{\partial x} + v_j \frac{\partial}{\partial y} \right) \tilde{q}_j + \mathbb{J}(Q_j, \phi_j) + \alpha \delta_{2j} \mathbb{J}(\eta_b, \phi_j) \right\}, \quad (5.6)$$

where  $\tilde{q}_j = \nabla^2 \phi_j + S_j(\phi_{3-j} - \phi_j)$ . We can discretise this system on a uniform grid with  $N \times N$  grid points by introducing the second-order central finite difference approximations,

$$\begin{aligned} \frac{\partial \phi_j}{\partial x} &= \frac{\phi_j^{m+1,n} - \phi_j^{m-1,n}}{2h}, \quad \frac{\partial \phi_j}{\partial y} = \frac{\phi_j^{m,n+1} - \phi_j^{m,n-1}}{2h}, \\ \nabla^2 \phi_j &= \frac{\phi_j^{m+1,n} + \phi_j^{m-1,n} + \phi_j^{m,n+1} + \phi_j^{m,n-1} - 4\phi_j^{m,n}}{h^2}, \\ \frac{\partial}{\partial x} \nabla^2 \phi_j &= \frac{1}{h^3} \left[ 2(\phi_j^{m-1,n} - \phi_j^{m+1,n}) \right. \\ &\quad \left. + \frac{1}{2}(\phi_j^{m+2,n} - \phi_j^{m-2,n} + \phi_j^{m+1,n-1} - \phi_j^{m-1,n-1} + \phi_j^{m+1,n+1} - \phi_j^{m-1,n+1}) \right], \\ \frac{\partial}{\partial y} \nabla^2 \phi_j &= \frac{1}{h^3} \left[ 2(\phi_j^{m,n-1} - \phi_j^{m,n+1}) \right. \\ &\quad \left. + \frac{1}{2}(\phi_j^{m,n+2} - \phi_j^{m,n-2} + \phi_j^{m+1,n+1} - \phi_j^{m+1,n-1} + \phi_j^{m-1,n+1} - \phi_j^{m-1,n-1}) \right], \\ \nabla^4 \phi_j &= \frac{1}{h^4} \left[ 20\phi_j^{m,n} - 8(\phi_j^{m+1,n} + \phi_j^{m-1,n} + \phi_j^{m,n+1} + \phi_j^{m,n-1}) + 2(\phi_j^{m+1,n+1} \right. \\ &\quad \left. + \phi_j^{m-1,n+1} + \phi_j^{m+1,n-1} + \phi_j^{m-1,n-1}) + \phi_j^{m+2,n} + \phi_j^{m-2,n} + \phi_j^{m,n+2} + \phi_j^{m,n-2} \right], \end{aligned}$$

where  $m$  and  $n$  denote the zonal and meridional grid point indices, respectively,  $h = \hat{L}_x / N \hat{L}$  denotes the spacing between grid points,  $\hat{L}_x$  is the scale of the horizontal domain and  $\hat{L}$  is our adopted length scale. For simplicity, we can choose our length scale so that  $h = 1$ , and can rescale variables more suitable for the vortex problem after solutions are obtained. Thus, on substitution of these stencils into (5.6) and in the presence of the doubly-periodic boundary conditions,

$$\psi_j^{N+1,n} = \psi_j^{1,n}, \quad \psi_j^{0,n} = \psi_j^{N,n}, \quad \psi_j^{m,N+1} = \psi_j^{m,1}, \quad \psi_j^{m,0} = \psi_j^{m,N}, \quad (5.7)$$

we obtain the eigenproblem

$$i\mathbf{A}\phi = \lambda\mathbf{B}\phi, \quad (5.8)$$

where  $\phi$  denotes the corresponding eigenfunctions through

$$\phi = (\phi_1^{1,1}, \phi_1^{2,1}, \dots, \phi_j^{N,1}, \phi_1^{1,2}, \dots, \phi_1^{N,N}, \phi_2^{1,1}, \dots, \phi_2^{N,N})^T, \quad (5.9)$$

the nonzero elements of  $\mathbf{B}$  are given by

$$\phi_j^{k,n} : 1, \text{ for } k = m \pm 1, \forall n, \quad (5.10)$$

$$\phi_j^{m,n} : -(4 + S_j), \quad (5.11)$$

$$\phi_{3-j}^{m,n} : S_j, \quad (5.12)$$

and the nonzero elements of  $\mathbf{A}$  are

$$\phi_j^{m+1,n+1} : 2\nu - \frac{(u_j + v_j)}{2}, \quad (5.13)$$

$$\phi_j^{m+1,n-1} : 2\nu - \frac{(u_j - v_j)}{2}, \quad (5.14)$$

$$\phi_j^{m-1,n+1} : 2\nu + \frac{(u_j - v_j)}{2}, \quad (5.15)$$

$$\phi_j^{m-1,n-1} : 2\nu + \frac{(u_j + v_j)}{2}, \quad (5.16)$$

$$\phi_j^{m+2,n} : \nu - u_j, \quad (5.17)$$

$$\phi_j^{m-2,n} : \nu + u_j, \quad (5.18)$$

$$\phi_j^{m,n+2} : \nu - v_j, \quad (5.19)$$

$$\phi_j^{m,n-2} : \nu + u_j, \quad (5.20)$$

$$\phi_j^{m+1,n} : -8\nu - \delta_{2j}\gamma - 5\beta_j + 2u_j + \frac{1}{2} \left[ S_j(U_j - c_x) - \frac{\partial Q_j}{\partial y} - \alpha\delta_{2j} \frac{\partial \eta_b}{\partial y} \right], \quad (5.21)$$

$$\phi_j^{m-1,n} : -8\nu - \delta_{2j}\gamma + 5\beta_j - 2u_j + \frac{1}{2} \left[ S_j(c_x - U_j) + \frac{\partial Q_j}{\partial y} + \alpha\delta_{2j} \frac{\partial \eta_b}{\partial y} \right], \quad (5.22)$$

$$\phi_j^{m,n+1} : -8\nu - \delta_{2j}\gamma + 2v_j + \frac{1}{2} \left[ \frac{\partial Q_j}{\partial x} - S_j c_y + -\alpha\delta_{2j} \frac{\partial \eta_b}{\partial x} \right], \quad (5.23)$$

$$\phi_j^{m,n-1} : -8\nu - \delta_{2j}\gamma - 2v_j - \frac{1}{2} \left[ \frac{\partial Q_j}{\partial x} - S_j c_y - -\alpha\delta_{2j} \frac{\partial \eta_b}{\partial x} \right], \quad (5.24)$$

$$\phi_j^{m,n} : 20\nu + 4\delta_{2j}\gamma, \quad (5.25)$$

$$\phi_{3-j}^{m+1,n} : -\frac{S_j u_j}{2}, \quad (5.26)$$

$$\phi_{3-j}^{m-1,n} : \frac{S_j u_j}{2}, \quad (5.27)$$

$$\phi_{3-j}^{m,n+1} : -\frac{S_j v_j}{2}, \quad (5.28)$$

$$\phi_{3-j}^{m,n-1} : -\frac{S_j v_j}{2}, \quad (5.29)$$

$$(5.30)$$

To apply this to the LRD in the 1.5-layer model, the relevant matrix system can be obtained by neglecting bottom layer contributions and setting  $\hat{\nu} = \hat{\gamma} = \hat{c}_y = \hat{\eta}_b = \hat{U}_1 = 0, \hat{S}_1 = \hat{S} = 1/\hat{R}_d^2$  (where we use hat notation for dimensional quantities). Moreover, we nondimensionalise the 1.5-layer system with the length and velocity scales  $\hat{L} = \hat{L}_x/N$  and  $\hat{U} = 1 \text{ cm s}^{-1}$ , respectively. Once we obtain solutions, we can re-scale variables with  $\hat{L} = \hat{R}_d$  and  $\hat{U} = \hat{c}_x$ , so that our nondimensional results are consistent with our previous scale considerations in Chapters 3 and 4.

## Evaluating the approach

The benefit of finite differences is the simplicity offered when applying the method, however, the drawback is the need for high resolution to resolve the problem. This can be a computationally expensive demand since our method solves for the entire eigenspectra, meaning that we make no assumptions about the matrix decomposition. However, fortunately we know the flow symmetry for the Davies mode, and so we can impose this even symmetry with respect to the zonal axis through additional boundary conditions. Doing this is equivalent to halving the number of grid points in the meridional direction. Without imposing this symmetry condition, our current resources only allow us to solve for solutions on a  $256^2$  grid. However, halving the number of grid points in one of the horizontal directions allows us to perform our analysis on a  $512 \times 256$  rectangular grid, which is equivalent to obtaining solutions on a  $512^2$  grid once we have accounted for the symmetry. Mathematically, this means if our method extracts the amplitude functions  $\Phi^{m,n}$ , where  $m$  and  $n$  are zonal and meridional grid indices, respectively, then we can reconstruct the corresponding amplitude for the critical mode as

$$\phi^{m,n} = \begin{cases} \Phi^{m,n}, & \forall m, 1 \leq n \leq N/2, \\ \Phi^{m,N-n+1}, & \forall m, N/2 + 1 \leq n \leq N, \end{cases} \quad (5.31)$$

where  $N = 512$  in our case.

A clear difference with our numerical simulations is the domain we compute over. More specifically, when solving the problem numerically in Chapters 3 and 4, we considered a four times longer domain in the zonal direction, whereas, for our linear stability analysis, we assume a square domain. For consistency between our numerics, we choose this square domain to have the previous meridional domain scale in each direction, i.e.,  $(L_x, L_y) = (15, 15)$ .

We also impose four times weaker resolution constraints when carrying out our linear stability analysis. Unfortunately, we cannot increase the grid resolution directly since this problem is computationally expensive. However, we can improve our grid resolution indirectly by decreasing the domain size for the same number of grid points. For example, if we halve the domain size, then we in turn double the grid resolution when fixing the number of grid points. Therefore, if we solve the symmetric linear stability problem in a  $(7.5, 7.5)$  domain with  $512 \times 256$  grid points, this is equivalent to solving the problem in a  $(15, 15)$  domain with  $1024 \times 512$  grid points over the space the domains have in common. A caveat of this is we sacrifice information in the far field. In our numerical analysis, a large domain was considered to avoid artificial results due to periodic interactions between the dipole and the wake in the far field. However, since our initial LRD profile does not contain this wake, our linear stability analysis does not have information relevant to the wake. Hence, after proper convergence is achieved, the domain size should not significantly change our solutions.

## 5.2 Weak dipoles

Now that we have described our approach, we proceed by carrying out the linear stability analysis for the class of weak eastward propagating dipoles. In our numerical analysis, weak dipoles were those that developed instability over time, so we expect to extract a critical mode using our linear stability methodology. To verify the convergence of our solutions, we solve the case of  $\beta = 0.4$  with the following inputs:

- $(L_x, L_y) = (15, 15)$  and  $N = 512$  (see Fig. 5.1),
- $(L_x, L_y) = (7.5, 7.5)$  and  $N = 512$  (see Fig. 5.2).

In the first instance, the real and imaginary parts of the amplitude streamfunction are presented in Fig. 5.1a, b. These fields appear to be relatively smooth, with the corresponding PVA amplitudes in Fig. 5.1c, d resembling those obtained in Fig. 4.7. However, the PVA fields do not look as smooth as the streamfunction counterparts,

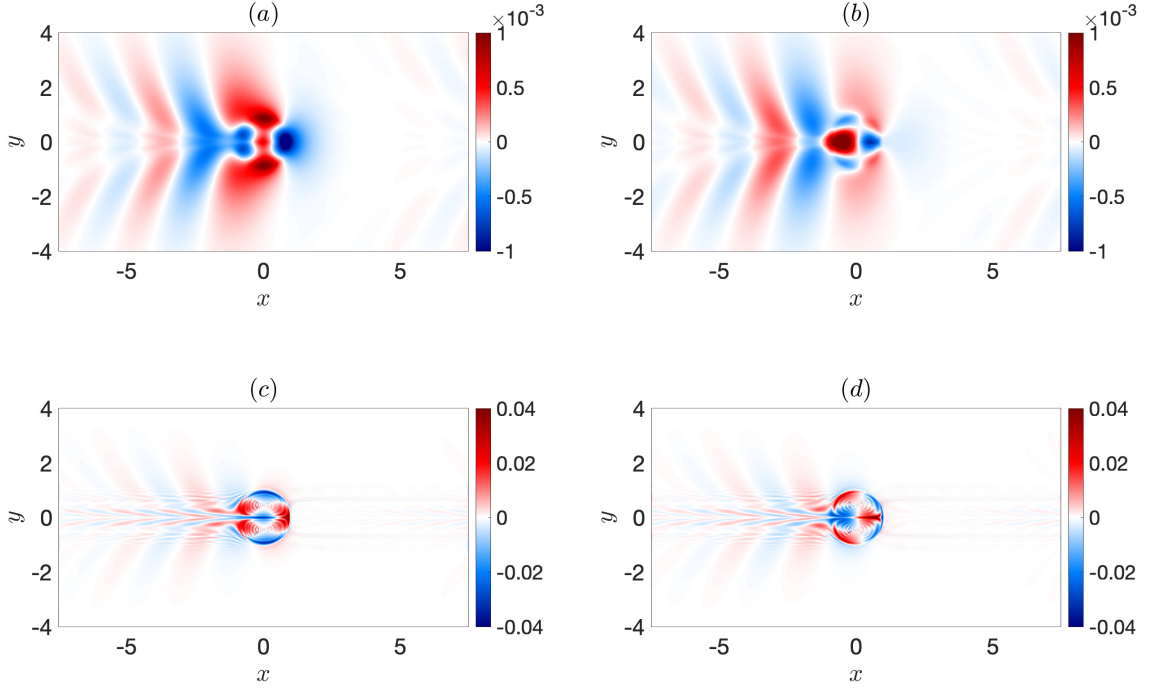


**Figure 5.1:** Eigenfunctions for the dipole problem in a  $(15, 15)$  domain with  $\beta = 0.4$  and  $N = 512$ : panels (a) and (c) show the real part of the amplitude function for the streamfunction and PVA perturbations, respectively, while panels (b) and (d) show the imaginary part of the amplitude function for the streamfunction and PVA perturbations, respectively. The growth rate for the critical Davies mode is  $\sigma \sim 0.025$  and the period is  $T \sim 17$ .

with there appearing to be discontinuities local to the centres in each half-quadrant. When comparing with linear solutions in a half-sized domain, streamfunction panels look very similar (see Fig. 5.2a, b), with some minor changes in the symmetry of the central structures and the flow amplitude (though our linear stability solutions can be re-scaled by constant multiplication). This also applies for the PVA panels (see Fig. 5.2c, d), with the addition of these fields appearing smoother, likely due to the higher resolution used for the same amount of space. Overall, the consistency in solutions obtained is convincing evidence for our linear stability solutions converging.

An interesting feature of both sets of solutions is the presence of a wake to the left of the central structures. These are particularly clear in the streamfunction panels, though they are still visible in the PVA panels. In the larger domain, we do not see these waves to the right of the central modes, but in the smaller domain, these waves appear throughout the domain since they interact with the periodic boundaries. Regardless, periodicity does not seem to dramatically change solutions in a smaller

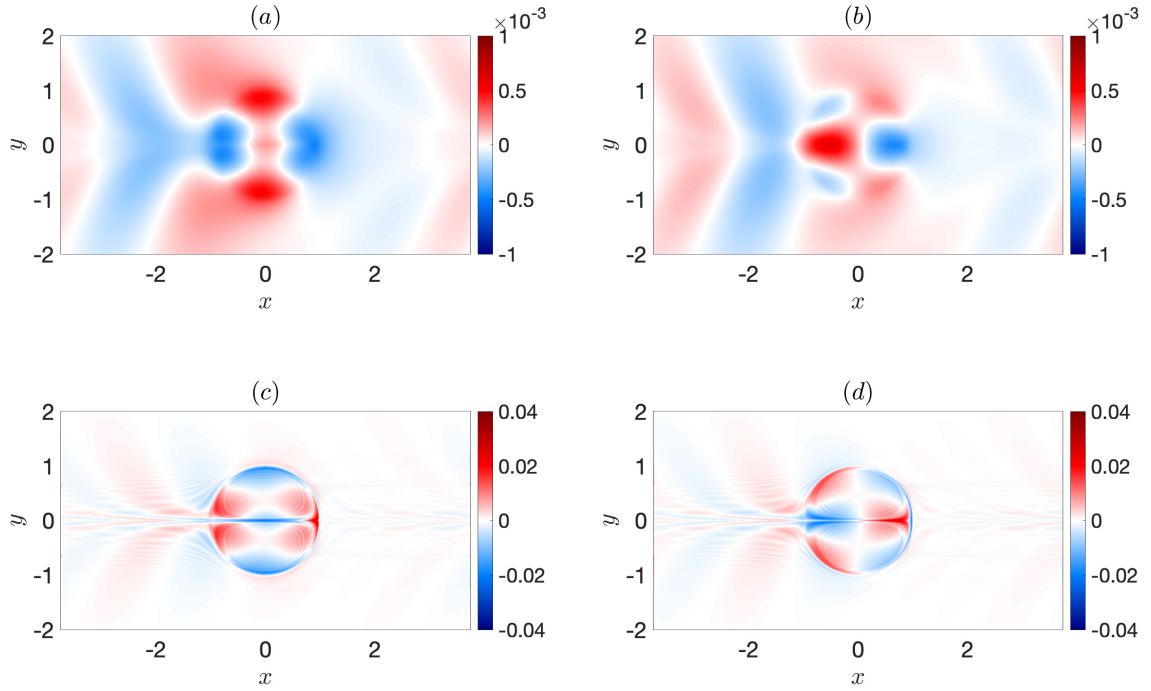


**Figure 5.2:** Eigenfunctions for the dipole problem in a  $(7.5, 7.5)$  domain with  $\beta = 0.4$  and  $N = 512$ : panels (a) and (c) show the real part of the amplitude function for the streamfunction and PVA perturbations, respectively, while panels (b) and (d) show the imaginary part of the amplitude function for the streamfunction and PVA perturbations, respectively. The growth rate for the Davies mode is  $\sigma \sim 0.027$  and the period is  $T \sim 17$ .

domain, as the overall symmetries appear consistent between Fig. 5.1 and Fig. 5.2. The reason the wake is notable in the linear stability solutions is because it suggests that the wake forms as a consequence of linear instability. If we recall the critical mode analysis in Brion et al. (2014) for the viscous Lamb-Chaplygin dipole, it was hypothesised that the wake generated from the dipole motion subsequently interacted with the dipole; acting as a mechanism for instability growth. The presence of a wake in our dipole simulations could be related to this mechanism, however, since the wake appears in the Davies mode pattern when extracted using our linear stability solver, this suggests that the wake is a characteristic of instability, rather than a mechanism for instability.

Some important features of linear stability are  $\sigma$  and  $T = \omega/2\pi$ , namely the linear growth rate and period of oscillation associated with the most unstable mode. In our numerical analysis, we approximated these to be  $\sigma \sim 0.035$  and  $T \sim 16$  for  $\beta = 0.4$ . In comparison with the linear stability theory, we found that  $(\sigma, T) \sim$



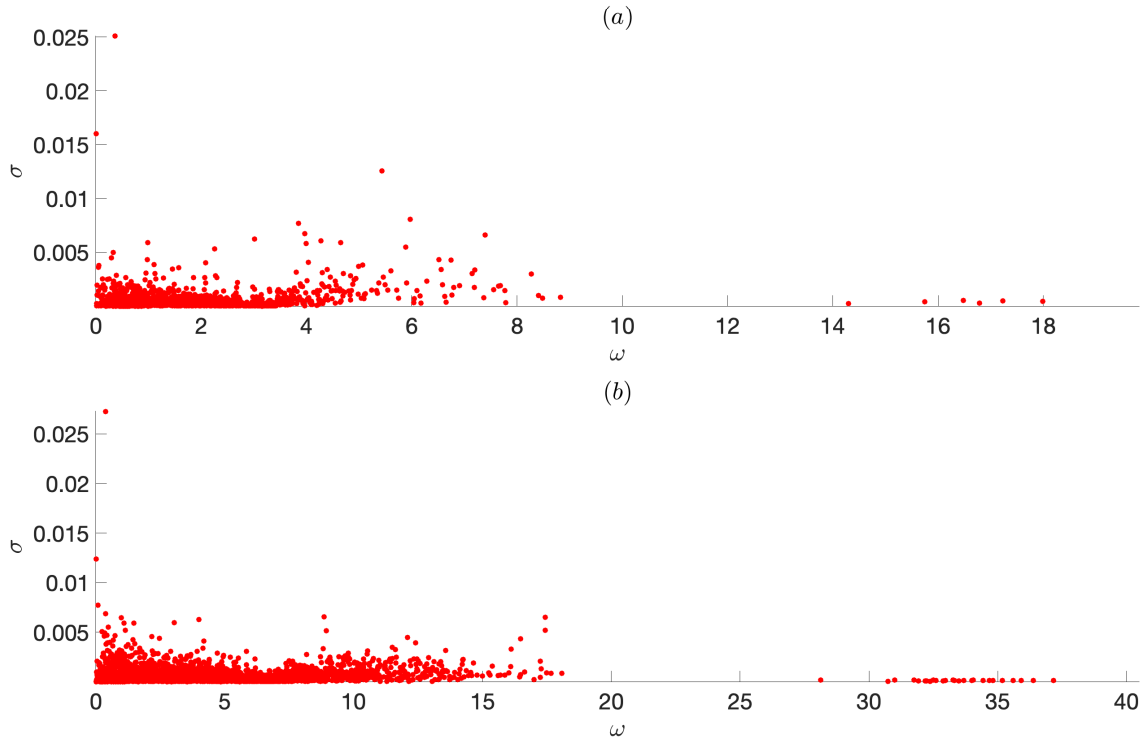


**Figure 5.3:** Eigenspectra associated with linear stability solutions: (a) corresponds to a domain of  $(15, 15)$ ; (b) corresponds to a domain of  $(7.5, 7.5)$ . As a consequence of symmetry, we only present unstable modes in the positive half-plane.

$(0.025, 17)$  in the larger domain, and  $(\sigma, T) \sim (0.027, 17)$  in the smaller domain (see Fig. 5.3 for the corresponding eigenspectra). Not only is the similarity in our linear stability results between domains a good indicator of method convergence, but the consistency with numerical results is also strong evidence of dipole instability (where differences in value are likely a consequence of limited time integration when performing numerical simulations). Furthermore, using our linear stability results, we computed the PVA modes as they evolved over a period of oscillation (see Fig. 5.4). These results are consistent with our numerical analysis and normal mode solutions, further supporting our linear stability analysis.

Performing the same analysis for  $\beta = 0.3$  is also informative. In our numerical experiments, we deduced that the instability was weaker when considering more intense dipoles. In particular, we found that a dipole with  $\beta = 0.3$  had an approximate linear growth rate of  $\sigma \sim 0.027$ , while the period of oscillation remained roughly the same as found for the  $\beta = 0.4$  linear stability solution. Whereas, on implementing our linear stability solver, we found that  $\sigma \sim 0.015$  and  $T \sim 18$ . Therefore, even though our analysis is consistent with the growth rate decreasing, we also see a

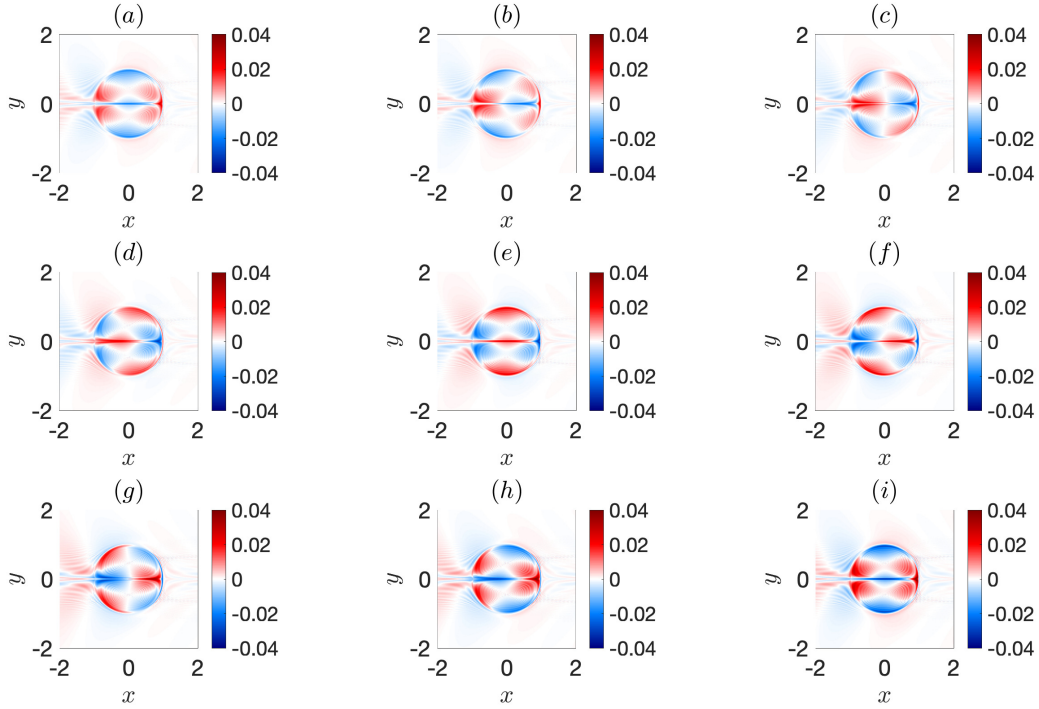


**Figure 5.4:** PVA snapshots of the linear Davies mode corresponding to Fig. 5.2: (a) – (i) correspond to  $t \sim 143 - 159$ , respectively, and panels are separated by the same time interval  $\sim 2$ . These are consistent with the numerical results of Davies et al. (2023).

small increase in the oscillation period in our linear analysis. This could be related to the Davies mode associated with stronger dipoles being less efficient at extracting energy from the background flow and reducing the PV contrast in the dipole (see Chapter 6 for a discussion of energetics and PV flux exchange).

Clearly, from Fig. 5.5, we see similarity between our eigensolutions for  $\beta = 0.3$  and  $\beta = 0.4$  (see Fig. 5.2). However, the contributions look to be reversed (i.e., real and imaginary parts appear interchanged). Regardless, since the solutions we seek are linear, any scalar multiple of these fields is also a solution, including those multiplied by  $\pm i$ . On multiplying panels in Fig. 5.5 by the imaginary unit, we retrieve panel correspondence with Fig. 5.2. Despite this, comparison of the PVA representations reveals discontinuities near the central regions of the upper and lower halves of the critical mode components for  $\beta = 0.3$ . This is similar to what we observed in Fig. 5.1, which suggests that the corresponding Davies modes become more challenging to resolve with increasing dipole intensity in our linear stability analysis.

To smooth out the PVA amplitudes, we would either need to use a greater

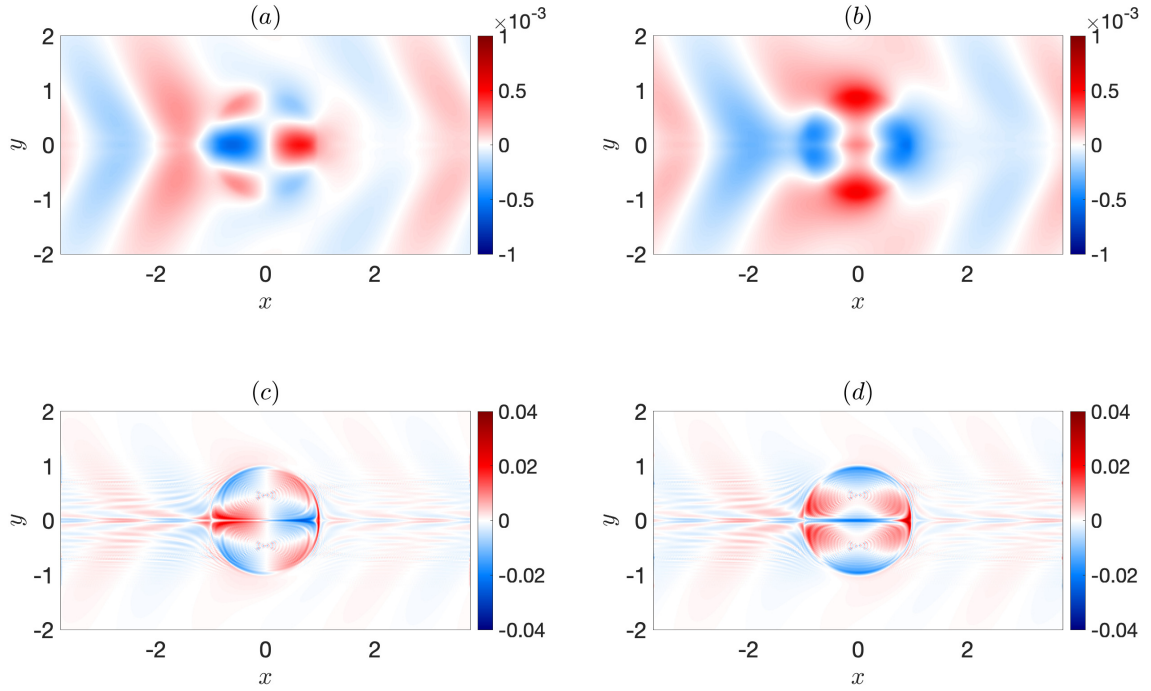


**Figure 5.5:** Eigenfunctions for the dipole problem in a  $(7.5, 7.5)$  domain with  $\beta = 0.3$  and  $N = 512$ : panels (a) and (c) show the real part of the amplitude function for the streamfunction and PVA perturbations, respectively, while panels (b) and (d) show the imaginary part of the amplitude function for the streamfunction and PVA perturbations, respectively. The growth rate for the critical mode is  $\sigma \sim 0.015$  and the period is  $T \sim 18$ .

number of grid points, or halve the domain size again and use the same number of grid points. We have already mentioned why the former of these is not currently feasible, meaning we have to rely on the later approach. Given the scale of the Davies modes, we are only able to halve the domain size once more. Nonetheless, even with the presence of these discontinuities, the overall structure is clearly visible and the existence of these modes still supports the idea of dipole instability.

Similar to the analysis we performed in Chapter 4, we can consider the curves for  $Z_A$  and  $L_A$  associated with our linear stability solutions for weak dipoles (see Fig. 5.5). From these signals, the linear growth displayed in the enstrophy curves is similar to the intermediate growth stage that appears in the corresponding plots for the numerical solutions (see Fig. 4.4a). This is also the case for the oscillations in  $L_A$ , which appear during the growth phase for our numerical results (see Fig. 4.4b). When comparing the curves for different values of  $\beta$ , this further highlights the idea that the linear growth rate decreases as we increase the dipole intensity

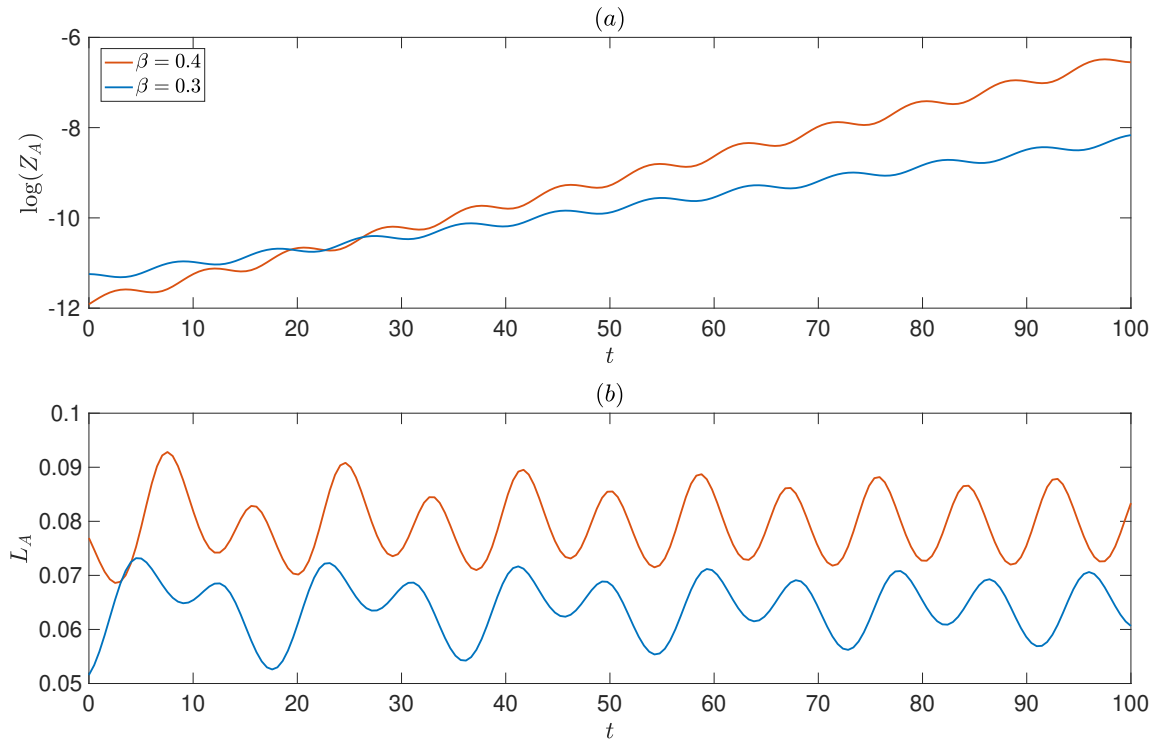


**Figure 5.6:** Signals associated with the linear stability analysis of weak dipoles: (a) shows the logarithm of enstrophy for the critical eigenfunction; (b) shows the values of  $L_A$  for the critical eigenfunction.

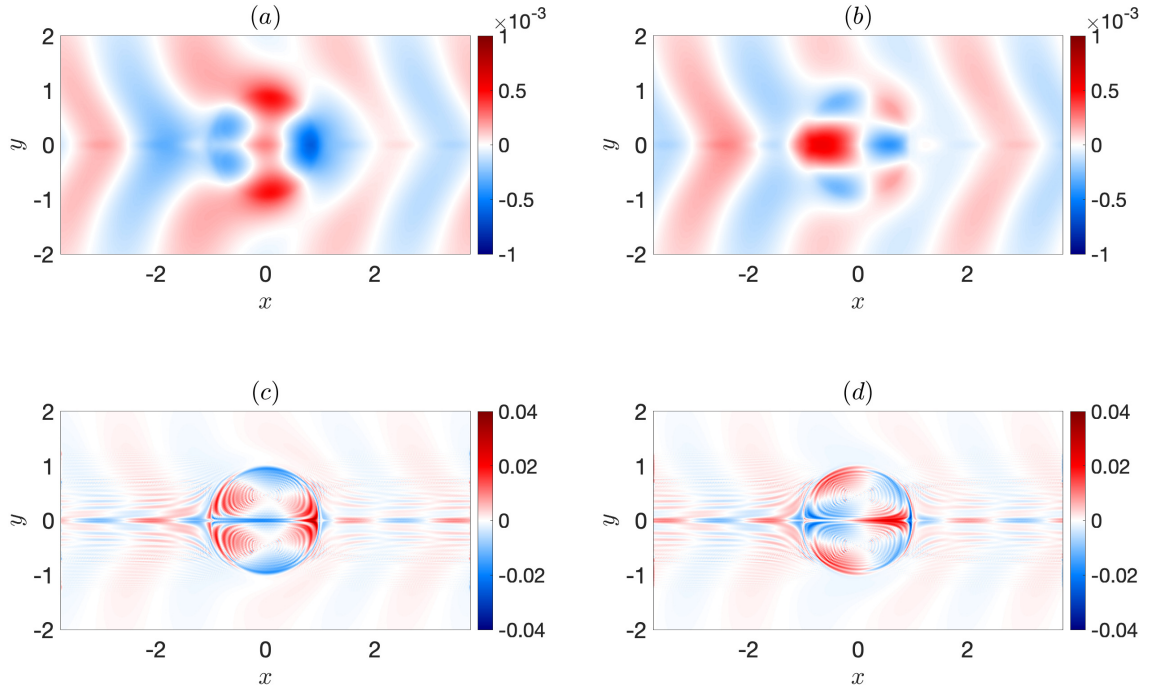


**Figure 5.7:** Eigenfunctions for the dipole problem in a  $(7.5, 7.5)$  domain with  $\beta = 0.2$  and  $N = 512$ : panels (a) and (c) show the real part of the amplitude function for the streamfunction and PVA perturbations, respectively, while panels (b) and (d) show the imaginary part of the amplitude function for the streamfunction and PVA perturbations, respectively. The growth rate for the critical mode is  $\sigma \sim 0.009$  and the period is  $T \sim 19$ .

(see Fig. 5.6a). Moreover, there are subtle differences in phase between curves (see Fig. 5.6b), suggesting that the deformation of the Davies modes differs depending on the value of  $\beta$ .

### 5.3 Strong dipoles

In our numerical results, we identified the dipole destruction of solutions with weak intensities, however, our analysis was not as straight forward for stronger dipoles. More specifically, dipoles with an intensity of  $c/\beta = 1/2$  only saw significant asymmetric deformation after transitioning through the periodic boundary. This could be taken to mean that the dipole sees weaker instability growth, and thus a lengthier dipole destruction process (supported by the formation of a Davies mode in the larger domain simulations, albeit, weaker resolution was assumed in this case). On the other hand, it could also be argued that the potential interference through periodicity,

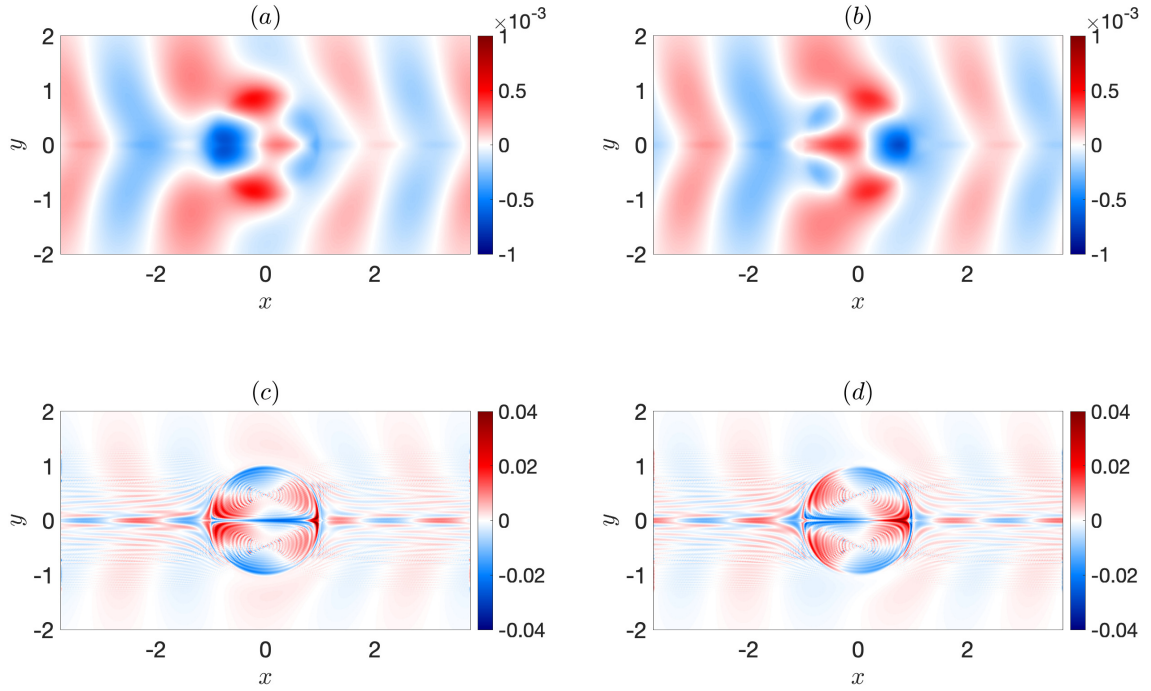


**Figure 5.8:** Eigenfunctions for the dipole problem in a  $(7.5, 7.5)$  domain with  $\beta = 0.15$  and  $N = 512$ : panels (a) and (c) show the real part of the amplitude function for the streamfunction and PVA perturbations, respectively, while panels (b) and (d) show the imaginary part of the amplitude function for the streamfunction and PVA perturbations, respectively. The growth rate for the critical mode is  $\sigma \sim 0.007$  and the period is  $T \sim 20$ .

or the prolonged exposure to numerical viscosity, are what cause the stronger dipole to disintegrate, and without these factors the vortex solution would continue to propagate undisturbed.

Carrying out our linear stability analysis for a stronger dipole with  $\beta = 0.2$ , we extract a critical mode (see in Fig. 5.7) that has similar real and imaginary parts to those seen for weaker dipoles (see Figs. 5.4, 5.5). Again, the PVA amplitude components for a smaller value of  $\beta$  look less resolved than those obtained for a larger value of  $\beta$  using the same resolution and domain size. Despite this, the streamfunction amplitude panels do not seem massively unchanged, with some notable features being subtle phase differences and the presence of a weak disturbance along the zonal axis (likely a consequence of the problem demanding higher resolution to resolve the Davies mode structure). Consistent with our previous linear stability results, the linear growth rate decreases to  $\sigma \sim 0.009$  and the oscillation period is roughly  $T \sim 19$ .

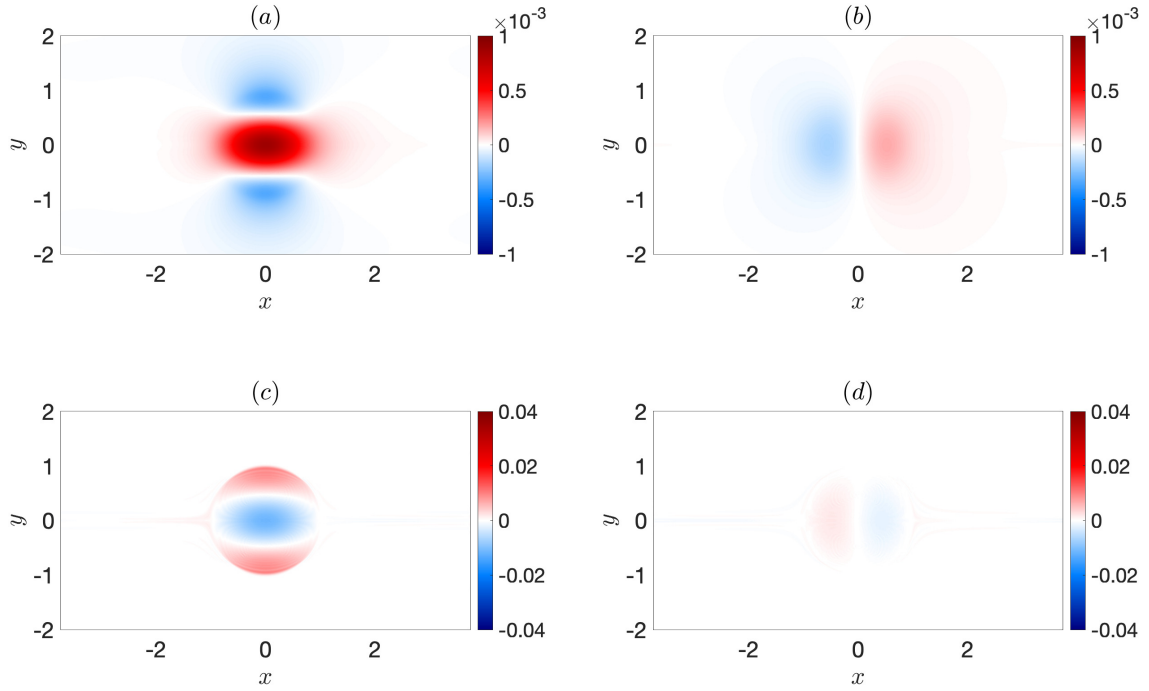


**Figure 5.9:** Eigenfunctions for the dipole problem in a  $(7.5, 7.5)$  domain with  $\beta = 0.1$  and  $N = 512$ : panels (a) and (c) show the real part of the amplitude function for the streamfunction and PVA perturbations, respectively, while panels (b) and (d) show the imaginary part of the amplitude function for the streamfunction and PVA perturbations, respectively. The growth rate for the critical mode is  $\sigma \sim 0.006$  and the period is  $T \sim 90$ .

Similar results also appear when  $\beta = 0.15$ , where  $(\sigma, T) \sim (0.007, 20)$ . However, the real and imaginary contributions see more obvious phase shifts in comparison to weaker dipoles results. When we consider  $\beta = 0.1$ , our linear stability results change somewhat. For example, a critical mode pattern extracted through our linear stability analysis is presented in Fig. 5.9, and this clearly does not resemble the Davies mode pattern we associate with linear instability. Despite this, we do observe a similar pattern to the real part when considering the A-component of a strong dipole in our numerical simulations (see Fig. 4.10, and note that this mode did not appear for other dipoles considered in our numerical experiments). Associated with these linear stability solutions are the values  $\sigma \sim 0.006$  and  $T \sim 90$ , which is consistent with the decreasing growth rate, but the period of oscillation is substantially longer than for the Davies mode. This is consistent with the longevity of the stronger dipole propagation observed in our numerical simulations (see Chapter 3), with the presence of a very small growth rate also suggesting that the strong dipole case experiences slow instability development.



Further investigation of the strong dipole linear stability analysis also identifies a lower order unstable mode presented in Fig. 5.10. Similar to when  $\beta = 0.15$ , the eigensolutions have shifted phases relative to those corresponding to weaker dipoles. However, they share better similarity with the Davies modes we have associated with dipole instability throughout this thesis. The corresponding characteristic values are  $\sigma \sim 0.004$  and  $T \sim 21$ , which are more reminiscent of what we have found for weaker dipoles. It is clear from these eigensolutions that the PVA amplitude is not well resolved, with obvious noise present in the fields. However, the pattern is still visible, and these solutions are likely lower down in the eigenspectra as a consequence of insufficient resolution to resolve the problem accurately.

It could be the case that given higher resolution, the true critical mode would be this Davies-type mode. However, it could also be the case that since these eigensolutions in Figs. 5.9, 5.10 are not orthogonal, they interact with one another through nonlinear processes. If this is the case, then a hypothesis could be that the lower order Davies mode becomes excited when exposed to external factors (as in Fig. 4.10d, where the Davies mode formed outside of the periodic domain).

## 5.4 Summary

Motivated by the panel correspondence between the Davies modes obtained numerically and those obtained using a normal mode representation (as discussed in Chapter 4), in this chapter we performed linear stability analyses for various LRD solutions. The linear stability equations were derived using finite difference discretisation, and the method can also be implemented in a two-layer QG model. The approach requires us to solve a complex eigenproblem, where the eigenfunctions contain information about the normal mode amplitude functions  $A$  and  $B$ , while the eigenvalues contain information about the linear growth rate,  $\sigma$ , and the period of unstable mode oscillation,  $T$ .

In the case of weak dipoles, our linear stability results showed eigenfunctions consistent with the amplitude functions obtained from numerical data. Moreover, as we increased the value of  $\beta$ , we found that the linear growth rates decreased, in accord with our observations of growth seen in our numerical simulations in Chapter 3. This methodology was able to reproduce the Davies mode pattern extracted from our numerics, which supports the findings of linear instability of the class of LRD steady states.

On the other hand, when considering a strong dipole with  $\beta = 0.1$ , the critical



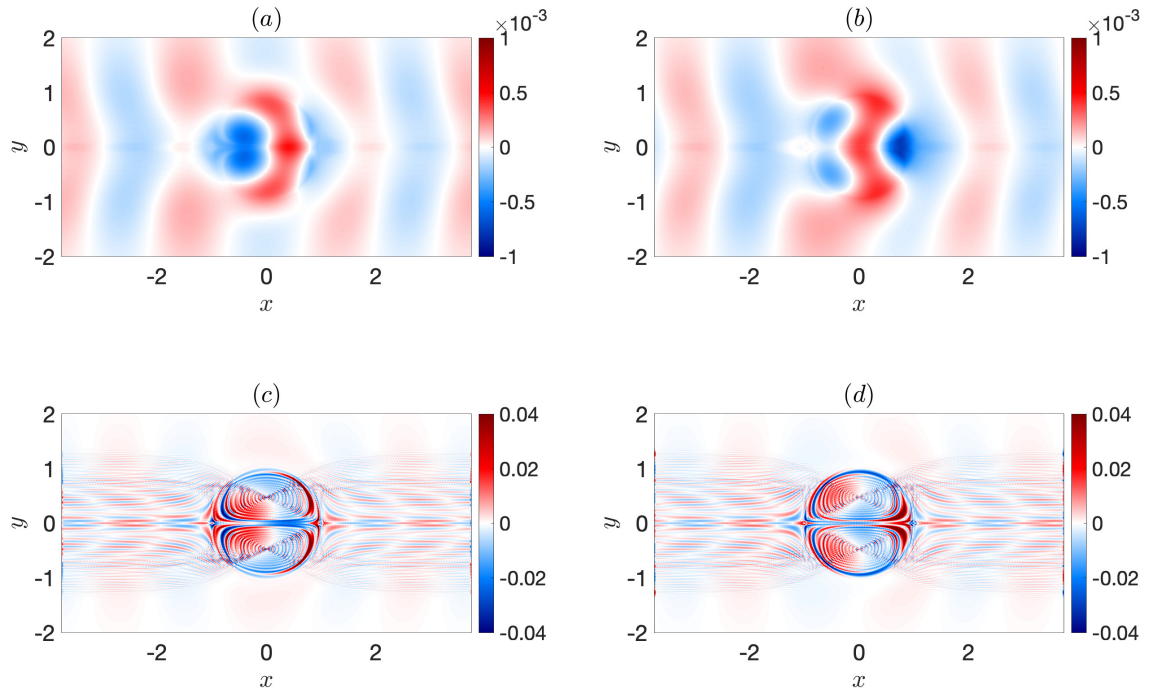


**Figure 5.10:** Eigenfunctions for the dipole problem in a  $(7.5, 7.5)$  domain with  $\beta = 0.1$  and  $N = 512$ : panels (a) and (c) show the real part of the amplitude function for the streamfunction and PVA perturbations, respectively, while panels (b) and (d) show the imaginary part of the amplitude function for the streamfunction and PVA perturbations, respectively. The growth rate for the critical mode is  $\sigma \sim 0.004$  and the period is  $T \sim 21$ .

mode extracted did not resemble the Davies mode pattern. However, when considering lower order unstable modes in the eigenspectra, we found an eigenfunction that appeared more consistent with the Davies mode pattern. A notable feature of these solutions is the presence of noise, which is likely a consequence of the limited resolution we could use to solve the linear stability system. To overcome this and better analyse the linear stability of strong dipoles, performing these calculations on a supercomputer would be ideal.

Given we have now analysed the LRD from the perspective of linear stability theory, it would also be interesting to carry out a nonlinear analysis for the dipole steady state. This will be what we discuss in [Chapter 6](#).

# Chapter 6

## Nonlinear destruction

The instability associated with the critical Davies mode can be related to the growing A-component on the dipole having non-zero meridional velocity. As a consequence of this, the Davies mode is capable of exchanging PV between the vortex cores of opposite sign value, thus, resulting in the 'cool down' of the PV content. Moreover, this causes the background flow to lose energy, with the compensation of this loss being an increase in perturbation energy (due to inviscid energy conservation). Therefore, unstable modes grow through the extraction of background energy in response to the PV mixing mechanism, with the Davies mode being the most efficient at doing this.

### 6.1 Nonlinear interaction

Now that we have identified the destruction of weak dipoles (see Chapter 3) and found a growing critical mode associated with the disturbance of partners (see Chapters 4 and 5), we turn our attention to unravelling the mechanism that encourages instability growth. In Chapter 3, we briefly discussed the exchange of PV between the eddy cores. Integral considerations suggested that the movement in PV between the upper and lower half planes was very small, but it was hard to deduce if this fluid movement was insignificant or not in regard to the outcome of spontaneous symmetry breaking. From simulations of the weak dipole propagation, there appears initial zonal and meridional oscillations in the PV content, suggesting that the overall PV exchange contributes to the resulting dipole destruction. This is further supported by the no-flow through zonal wall simulations appearing stable over the same time domain (see Fig. 3.1).

To better understand the mixing process throughout the dipole translation, we

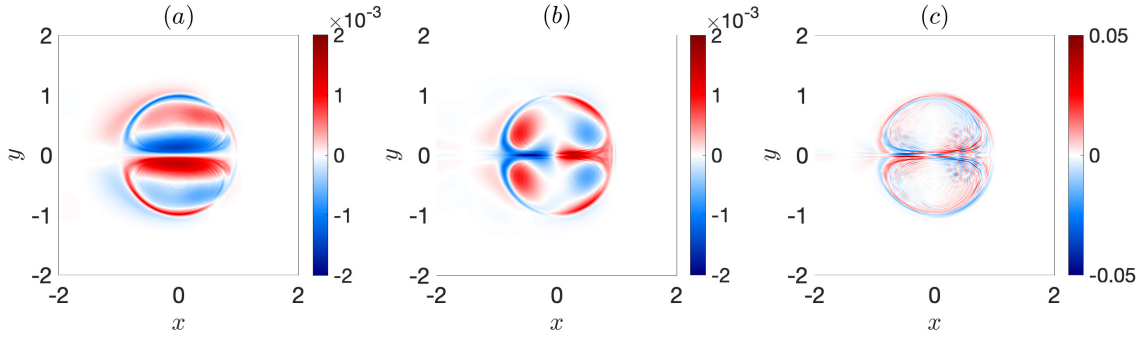


**Figure 6.1:** Period-averaged profiles associated with a weak dipole defined by  $\beta = 0.4$  in a  $(60, 15)$  domain ( $N = 2048$ ): (a) shows  $\overline{F}_x$ , the zonal PV flux; (b) shows  $\overline{F}_y$ , the meridional PV flux; (c) shows  $\overline{I}$ , the nonlinear-self interaction.

consider the flux of PV content. Given the distribution of PV will only change in response to the growing critical mode (i.e., without the growing A-component, the vortex would remain a pure S-component and see no developing asymmetries), we consider the PV flux due to the Davies mode in our analysis. Mathematically, the zonal and meridional flux components can be written as

$$F_x = -\frac{\partial \psi_A}{\partial y}(q_A + \beta y), \quad F_y = \frac{\partial \psi_A}{\partial x}(q_A + \beta y), \quad (6.1)$$

respectively. These can be related to the nonlinear interaction,  $I = -\mathbb{J}(\psi_A, q_A + \beta y)$ , through the equality

$$I = -\nabla \cdot \mathbf{F}, \quad (6.2)$$

where  $\mathbf{F} = (F_x, F_y)^T$ . The field for the nonlinear interaction can be informative since it illustrates how PV is distributed in the presence of a rotating Davies mode, while the flux components inform us of the direction in which PV moves.

So that we can develop an understanding of the net fluid dynamics in the system, we average the nonlinear self-interaction over a period of the Davies mode oscillation and use this as a reference point for our discussion of flux exchange. In this case, it follows that

$$\overline{I}(x, y) = \frac{\overline{\partial \psi_A}}{\partial y} \frac{\overline{\partial q_A}}{\partial x} - \frac{\overline{\partial \psi_A}}{\partial x} \frac{\overline{\partial q_A}}{\partial y}, \quad (6.3)$$

as a consequence of mean velocity being zero<sup>1</sup>. We present this information in Fig. 6.1, along with the average zonal and meridional flux components. From these panels, it is clear that all fields are odd with respect to the zonal axis. Moreover, Fig. 6.1a shows us how the PV content moves from left (negative blue regions) to right (positive red regions), while Fig. 6.1b shows us how PV is transferred up (positive red regions) and down (negative blue regions).

The nonlinear interaction (see Fig. 6.1c) has a complex structure that is difficult to digest on initial inspection. Perhaps, a more informative way to appreciate the nonlinear interaction is through Fig. 6.2, where the integral values of  $\bar{I}$  are presented for eight separate regions in the domain. From the distribution of values, it is clear that the upper (lower) region is negative (positive) dominant. In summary, this can be interpreted as the Davies mode working to reduce the PV contrast in the dipole (hereafter, we refer to this process as 'dipole cooling'). To investigate this, we performed simulations for a weak dipole initial multiplied by factors of 0.95 and 1.05, and found that the time of partner separation decreased and increased, respectively. This is consistent with our hypothesis of dipole cooling and is also consistent with what we have observed for dipoles of different intensities throughout this thesis (see Chapter 3).

The arrows in Fig. 6.2 correspond to the net PV flux along each of the zonal and meridional central lines. In particular, the size of the arrows is not to scale, but does represent the magnitude of flux in a particular direction. Therefore it is clear that the main transfer route that contributes to dipole cooling through meridional PV rearrangement is across the interval  $[-1, 0]$  along the zonal axis. In the outer negative region, meridional flux along the zonal axis is also negative, though not as significant. Regardless, this clearly demonstrates that the majority of meridional PV exchange occurs near the point of intersection between the dipole and the zonal axis. In addition, there appears to be a net cyclonic (counter-clockwise) circulation of PV inside the dipole, telling us that the Davies mode also zonally rearranges PV. This dynamics explains the zonal elongations we observed in our numerical simulations for the weak dipole propagation (see Fig. 3.1).

## 6.2 Energetics

We can also describe how the role of energy contributes to the destruction of weak dipoles. Since we have a growing critical mode attached to the dipole propagation,

<sup>1</sup>The beta-term vanishes due to  $\overline{\partial\psi_A/\partial x} = 0$ , since the critical Davies mode is periodic.

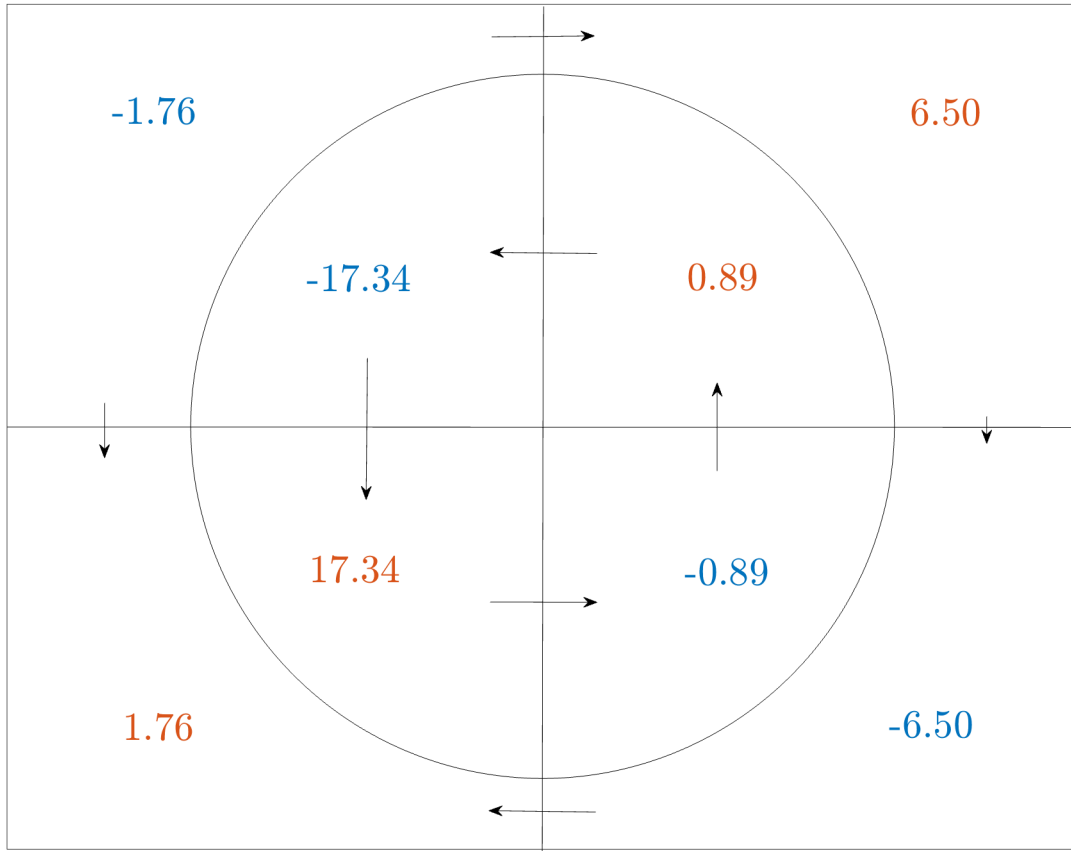


**Figure 6.2:** Integral value diagram associated with  $\bar{I}$ , describing how the overall PV content is rearranged due to a growing critical Davies mode. The size of arrows is not to scale, but describes the magnitude of net PV flux in the horizontal and meridional directions across the zonal and meridional segments. The circular boundary has unit radius.

this would suggest that the Davies mode becomes more energetic by extracting energy from the background flow. We can make this more convincing by deriving equations for the perturbation energy and steady state energy. Since we see a slowly developing instability in our numerical simulations, we can make use of the method of multiple scales in our derivation. If we let  $\tau_f$  denote the fast time scale defining the growing critical mode, and let  $\tau_s$  denote the slow time scale defining the evolution of the LRD steady state, then we can seek the Reynolds decomposition for the streamfunction:

$$\psi(x, y, t) = \Psi(x, y, \tau_s) + \psi'(x, y, \tau_s, \tau_f), \quad (6.4)$$

where  $\Psi = \overline{\psi}$  is the LRD profile (here, the overline notation is used to represent

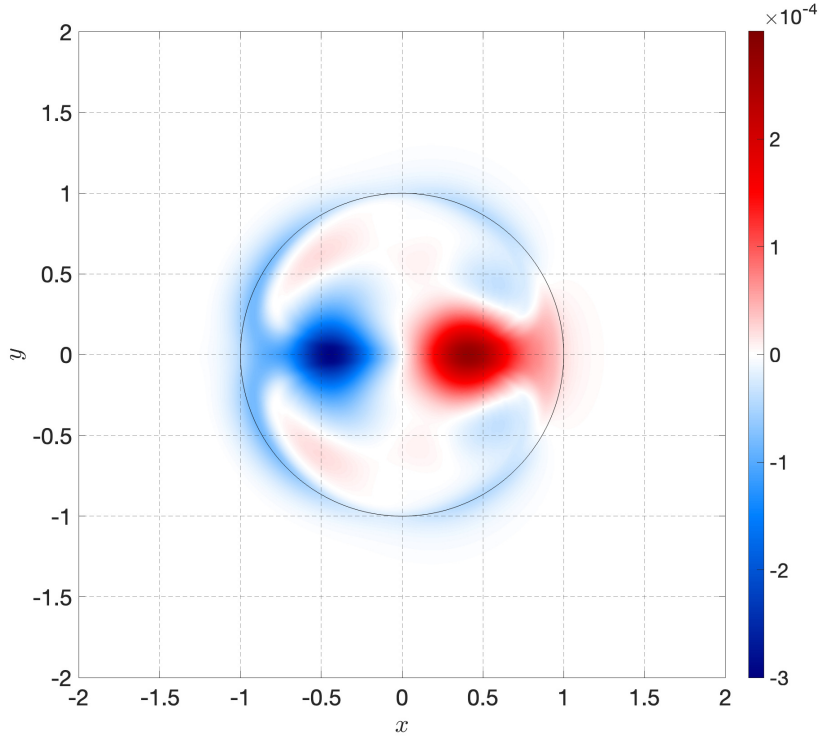


**Figure 6.3:** Energy exchange values averaged over a period of oscillation for the critical Davies mode. Negative regions correspond to energy extracted by the perturbation field, while positive regions correspond to energy extracted by the dipole.

taking an average with respect to the fast time scale) and  $\psi'$  is the corresponding perturbation field. On substitution of (6.4) into the inviscid equivalent of (2.4), it follows that

$$\frac{\partial Q}{\partial \tau_s} + \frac{\partial q'}{\partial \tau_s} + \frac{\partial q'}{\partial \tau_f} + \mathbb{J}(\Psi, \nabla^2 \Psi) + \mathbb{J}(\Psi, \nabla^2 \psi') + \mathbb{J}(\psi', \nabla^2 \Psi) + \mathbb{J}(\psi', \nabla^2 \psi') + \beta \left( \frac{\partial \Psi}{\partial x} + \frac{\partial \psi'}{\partial x} \right) = 0, \quad (6.5)$$

where  $Q = \nabla^2 \Psi - S\Psi$  and  $q' = \nabla^2 \psi' - S\psi'$ . From this, we can multiply both sides by  $\Psi$  and integrate over a period of oscillation for the mode of growing instability:

$$\Psi \frac{\partial Q}{\partial \tau_s} + \Psi \mathbb{J}(\Psi, \nabla^2 \Psi) + \Psi \overline{\mathbb{J}(\Psi, \nabla^2 \psi')} + \Psi \overline{\mathbb{J}(\psi', \nabla^2 \Psi)} + \Psi \overline{\mathbb{J}(\psi', \nabla^2 \psi')} + \beta \Psi \frac{\partial \Psi}{\partial x} = 0, \quad (6.6)$$

where we have assumed that  $\overline{\psi'} = 0$  (this is a typical assumption in turbulence modelling) and that  $\Psi$  does not see significant deviation over integration with respect to the fast time scale. In addition, if we expand the Jacobian terms, contributions that are linear in  $\psi'$  will be eliminated under the assumption of time averaging.

Therefore, we can simplify the governance so that

$$\Psi \frac{\partial Q}{\partial \tau_s} + \Psi \mathbb{J}(\Psi, \nabla^2 \Psi) + \Psi \overline{\mathbb{J}(\psi', \nabla^2 \psi')} + \beta \Psi \frac{\partial \Psi}{\partial x} = 0. \quad (6.7)$$

On manipulating this further, we can recast in terms of the steady state energy,

$$E = \frac{1}{2} \left[ (\nabla \Psi)^2 + S \Psi^2 \right], \quad (6.8)$$

to obtain the energy balance

$$\frac{\partial E}{\partial \tau_s} = \nabla \cdot \mathbf{S} + L, \quad (6.9)$$

where the mean energy flux can be written as

$$\begin{aligned} \mathbf{S} = & \mathbf{i} \left[ \Psi \frac{\partial^2 \Psi}{\partial x \partial \tau_s} + \frac{\Psi^2}{2} \left( \beta + \overline{\nabla^2 \frac{\partial \psi'}{\partial y}} \right) - \Psi \frac{\overline{\partial \psi'}}{\partial y} \nabla^2 \psi' + \frac{\partial \Psi}{\partial x} \frac{\overline{\partial \psi'}}{\partial x} \frac{\partial \psi'}{\partial y} - \frac{1}{2} \frac{\partial \Psi}{\partial y} \left( \frac{\overline{\partial \psi'^2}}{\partial x} - \frac{\partial \psi'^2}{\partial y} \right) \right] \\ & - \mathbf{j} \left[ \frac{\Psi^2}{2} \overline{\nabla^2 \frac{\partial \psi'}{\partial x}} - \Psi \frac{\overline{\partial \psi'}}{\partial x} \nabla^2 \psi' + \frac{\partial \Psi}{\partial y} \frac{\overline{\partial \psi'}}{\partial x} \frac{\partial \psi'}{\partial y} + \frac{1}{2} \left( \frac{\partial \Psi}{\partial x} \frac{\overline{\partial \psi'^2}}{\partial x} - \frac{\partial \psi'^2}{\partial y} \right) - \Psi \frac{\partial^2 \Psi}{\partial y \partial \tau_s} \right], \end{aligned} \quad (6.10)$$

with  $\mathbf{i}$  and  $\mathbf{j}$  denoting unit normal vectors in the zonal and meridional directions, respectively, and

$$L = \overline{\left( \frac{\partial \psi'}{\partial x} \right)^2} \frac{\partial^2 \Psi}{\partial x \partial y} - \frac{\overline{\partial \psi'}}{\partial x} \frac{\overline{\partial \psi'}}{\partial y} \frac{\partial^2 \Psi}{\partial x^2} + \frac{\overline{\partial \psi'}}{\partial y} \frac{\overline{\partial \psi'}}{\partial x} \frac{\partial^2 \Psi}{\partial y^2} - \overline{\left( \frac{\partial \psi'}{\partial y} \right)^2} \frac{\partial^2 \Psi}{\partial x y}, \quad (6.11)$$

is the energy exchange. Similarly, we can multiply (6.5) by  $\psi'$  and average over the period of oscillation to obtain the perturbation energy evolution

$$\frac{\partial \overline{E'}}{\partial \tau_s} = \overline{\nabla \cdot \mathbf{S}'} - L, \quad (6.12)$$

where  $\mathbf{S}'$  is the perturbation energy flux that can be derived similar to (6.10) and the perturbation energy can be expressed as

$$E' = \frac{1}{2} \left[ (\nabla \psi')^2 + S \psi'^2 \right]. \quad (6.13)$$

Since the exchange term,  $L$ , appears in both (6.9) and (6.12) with opposite sign value, this describes an exchange of energy between the background flow and the



perturbation field.

For our purposes, we assume that  $\psi' = \psi_A$ . Note that in our assumption of the energetics derivation, we made use of the result  $\overline{\psi'} = 0$ . This might seem to contradict the nonzero period-averaged profile for the critical Davies mode we found in Chapter 4, i.e.,  $\overline{\psi_A} \neq 0$ . However, on comparing the time averaged obtained (see Fig. 4.6) with the time evolution of the Davies mode (see Fig. 4.5), we can see that the amplitude of the averaged field is roughly an order of magnitude smaller than the panels used for the averaging. Therefore, we assume that  $\overline{\psi_A}$  is very small and that the nonzero correction is likely negligible. With our energy discussion in mind, we plot the energy exchange contribution in Fig. 6.3. From this, we see a nearly antisymmetric pattern with respect to the meridional axis. The positive region near the front of the dipole corresponds to energy from the background flow being extracted by the dipole (acting to stabilise the vortex), whereas, the negative region near the rear of the dipole corresponds to energy from the background flow being extracted by the perturbation field (acting to destabilise the vortex and encourage growth of the Davies mode).

### 6.3 Asymmetry analysis

By construction, the critical Davies mode has even symmetry about the zonal axis, however, no assumption is made about the symmetry across the meridional axis. Since there is small asymmetry in the energy exchange with respect to the meridional axis (see Fig. 6.3), this suggests that it is because of small asymmetry in the Davies mode that the dipole propagation exhibits instability and is eventually destroyed. We can analyse this further by introducing M- and N-components, such that

$$\psi_M = \frac{1}{2} \left[ \psi_A(x, y, t) + \psi_A(-x, y, t) \right], \quad \psi_N = \frac{1}{2} \left[ \psi_A(x, y, t) - \psi_A(-x, y, t) \right], \quad (6.14)$$

where the M-component is a field with even symmetry about the meridional axis and the N-component is a field with odd symmetry about the meridional axis. If we define  $q_{M,N}$  in a similar way, then the term describing energy exchange can be

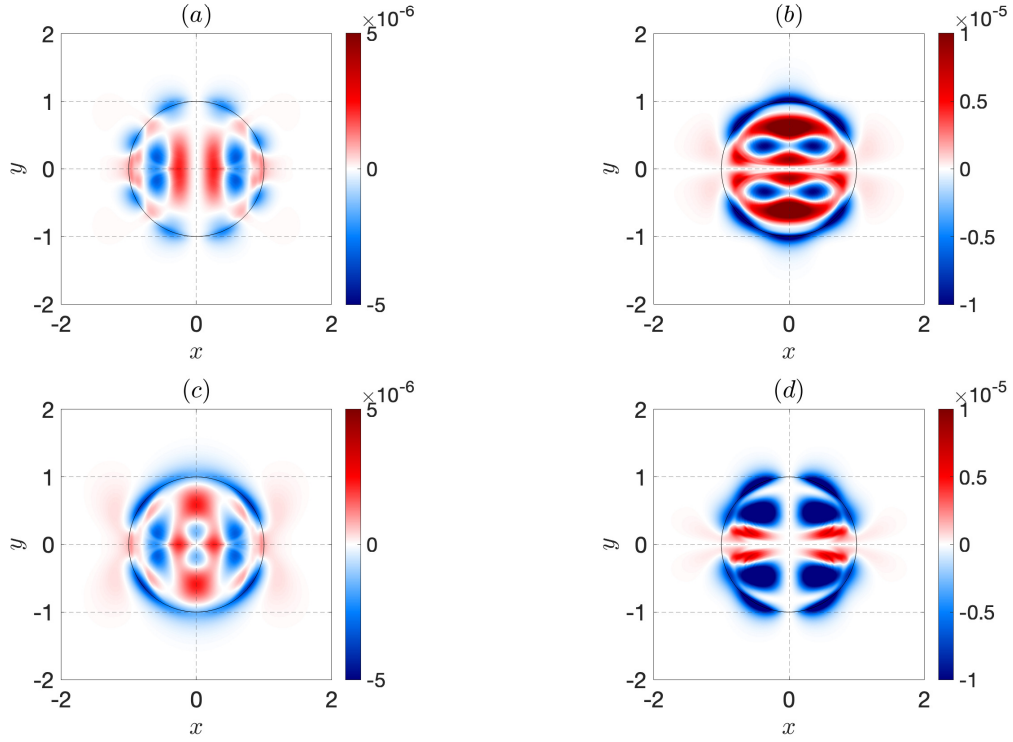


**Figure 6.4:** Components of the energy exchange in Fig.6.3, in terms of M- and N-components: (a) shows  $(MN)_x$ ; (b) shows  $(MN)_y$ ; (c) shows  $(NM)_x$ ; (d) shows  $(NM)_y$ .

expanded as

$$\begin{aligned}
 L = & \overline{\frac{\partial \psi_M}{\partial x} \mathbb{J} \left( \psi_M, \frac{\partial \Psi}{\partial x} \right)} + \overline{\frac{\partial \psi_M}{\partial x} \mathbb{J} \left( \psi_N, \frac{\partial \Psi}{\partial x} \right)} + \overline{\frac{\partial \psi_N}{\partial x} \mathbb{J} \left( \psi_M, \frac{\partial \Psi}{\partial x} \right)} + \overline{\frac{\partial \psi_N}{\partial x} \mathbb{J} \left( \psi_N, \frac{\partial \Psi}{\partial x} \right)} \\
 & + \overline{\frac{\partial \psi_M}{\partial y} \mathbb{J} \left( \psi_M, \frac{\partial \Psi}{\partial y} \right)} + \overline{\frac{\partial \psi_M}{\partial y} \mathbb{J} \left( \psi_N, \frac{\partial \Psi}{\partial y} \right)} + \overline{\frac{\partial \psi_N}{\partial y} \mathbb{J} \left( \psi_M, \frac{\partial \Psi}{\partial y} \right)} + \overline{\frac{\partial \psi_N}{\partial y} \mathbb{J} \left( \psi_N, \frac{\partial \Psi}{\partial y} \right)}.
 \end{aligned} \tag{6.15}$$

Each of the eight contributions in (6.15) is either symmetric in both horizontal directions, or consists of antisymmetry in one of the directions. A consequence of the latter means that net integral considerations yield zero outcomes for these antisymmetric contributions. The terms that are eliminated through integration consist of either pure M- or pure N-component derivatives (outside of the derivatives for the LRD). In summary, the surviving integral contributors to the energy exchange are presented in Fig. 6.4 and given by

$$(MN)_x = \overline{\frac{\partial \psi_M}{\partial x} \mathbb{J} \left( \psi_N, \frac{\partial \Psi}{\partial x} \right)}, \tag{6.16}$$

$$(MN)_y = \frac{\partial \psi_M}{\partial y} \mathbb{J} \left( \psi_N, \frac{\partial \Psi}{\partial y} \right), \quad (6.17)$$

$$(NM)_x = \frac{\partial \psi_N}{\partial x} \mathbb{J} \left( \psi_M, \frac{\partial \Psi}{\partial x} \right), \quad (6.18)$$

$$(NM)_y = \frac{\partial \psi_N}{\partial y} \mathbb{J} \left( \psi_M, \frac{\partial \Psi}{\partial y} \right). \quad (6.19)$$

Since these are combinations of M- and N-components, this tells us that despite being small, it is due to the Davies mode asymmetry that a growing instability develops during the vortex propagation. Moreover, the perturbation energy extraction is mostly due to  $(NM)_y$ , which has the most negative integral value. In contrast,  $(MN)_x$  has positive integral value and thus acts to stabilise the dipole by feeding energy into the vortex.

## 6.4 Summary

We expanded on the analysis of the LRD in this chapter by considering the nonlinear interaction and the corresponding energy exchange between the background flow and the perturbation field. Our discussion of the nonlinear interaction allowed us to describe the net PV flux in the horizontal and meridional directions, due to the presence of a growing Davies mode. From this, it was clear that the main cause of dipole cooling was due to meridional PV rearrangement across the interval  $[-1, 0]$  along the zonal axis. Furthermore, we observed a net cyclonic PV circulation within the dipole, which causes zonal elongations to occur in the dipole over time.

In the case of energetics, we found that the field describing energy exchange between the background and perturbation flows was asymmetric across the meridional axis. This motivated us to consider meridionally symmetric and antisymmetric components of the critical Davies mode to see whether or not this was the cause of the dipole instability. Indeed, we found that most of the perturbation energy extraction was due to a combination of these components, which tells us that a growing instability develops due to the asymmetry in the Davies mode.

Throughout this thesis, we have heavily analysed the LRD from various points of view. However, there are variants of the LRD that are also very interesting to investigate, and so we will consider variations of the LRD in the next chapter.

# Chapter 7

## Tilted dipole dynamics

Throughout this thesis, we have considered the dynamics of eastward propagating dipoles and associated them with the phenomena of spontaneous symmetry breaking over time. As we have already discussed, this behaviour disagrees with many previous studies that have attempted to solve this problem. One related work of interest is [Hesthaven et al. \(1993\)](#), where a plethora of numerical experiments were carried out for tilted dipoles on the beta-plane. In particular, initially symmetric LRDs were considered under various degrees of inclination to the dipole axis. They considered both eastward and westward propagating dipoles and found that for different values of  $\beta$  and  $\xi$ , where  $\xi$  is the notation we use to denote the dipole tilt, initially nonstationary dipoles were able to adjust to steadily translating states in many cases.

These fascinating observations are naturally of interest to us since they directly disagree with our current findings. Given we have identified the separation and destruction of partners in the case of weak symmetric dipoles, we would expect to see the same when we tilt these objects, despite the work by [Hesthaven et al. \(1993\)](#) suggesting otherwise. A potential limitation of the experiments presented in this paper is that they assumed resolution constraints of at most  $512 \times 128$ , which is extremely low when compared to our  $8192 \times 2048$  numerical simulations. It might be the case that these tilted dipole results are not well resolved on these coarse grids, and the true dynamics can only be extracted accurately using finer resolutions. On the other hand, the numerical method adopted in [Hesthaven et al. \(1993\)](#) is a pseudospectral scheme, which differs from our CABARET methodology. Because of this, it is important to compare numerical solutions using higher resolution and both CABARET and pseudospectral solvers, so that we can identify what is the true cause for discrepancies.

In the case of the tilted dipole problem, this is equivalent to initialising our solver

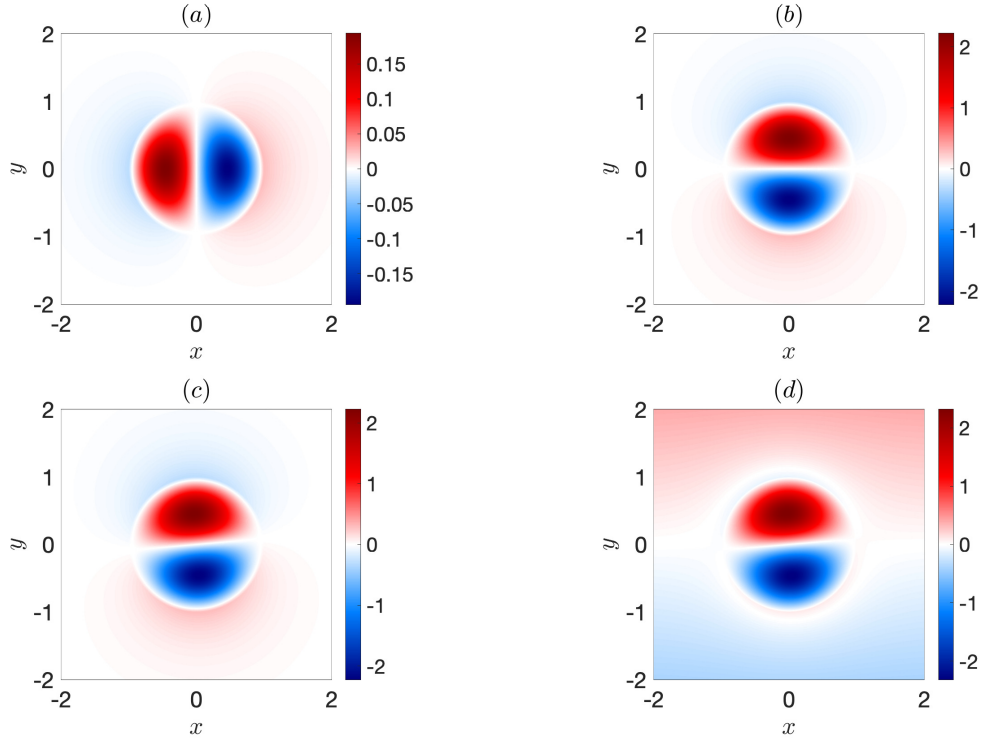


**Figure 7.1:** Panels illustrating physical fields associated with a  $(\beta, \xi) = (0.2, 5^\circ)$  tilted dipole: (a) shows the A-component of the PVA; (b) shows the S-component of the PVA; (c) shows the full PVA field (the sum of (a) and (b)); (d) shows the full PV field.

with the PVA profile

$$Q(r, \vartheta) = Q_A(r, \vartheta) + Q_S(r, \vartheta), \quad (7.1)$$

where  $Q_A = -xG(r) \sin \xi$ ,  $Q_S = yG(r) \cos \xi$ ,

$$G(r) = - \begin{cases} c(F(r) + 1)(S + k^2) + \beta, & r \leq 1, \\ -\beta F(r), & r > 1, \end{cases} \quad (7.2)$$

and  $F(r) = f(r)/r$ , where the function  $f$  is defined in (2.24). Clearly, the presence of tilting means that the initial A-component is nonzero, unlike in the symmetric case. To explore this problem, we nondimensionalise so that  $c = 0.1$  and  $S = 1$  (consistent with Chapter 3), and consider the following parameter space:

$$(\beta, \xi) = [0.1, 0.2, 0.35] \times [0^\circ, 5^\circ, 45^\circ, 30^\circ, 60^\circ, 90^\circ], \quad (7.3)$$

where  $\beta = 0.2, 0.35$  are our weak dipole considerations,  $\beta = 0.1$  is our strong dipole

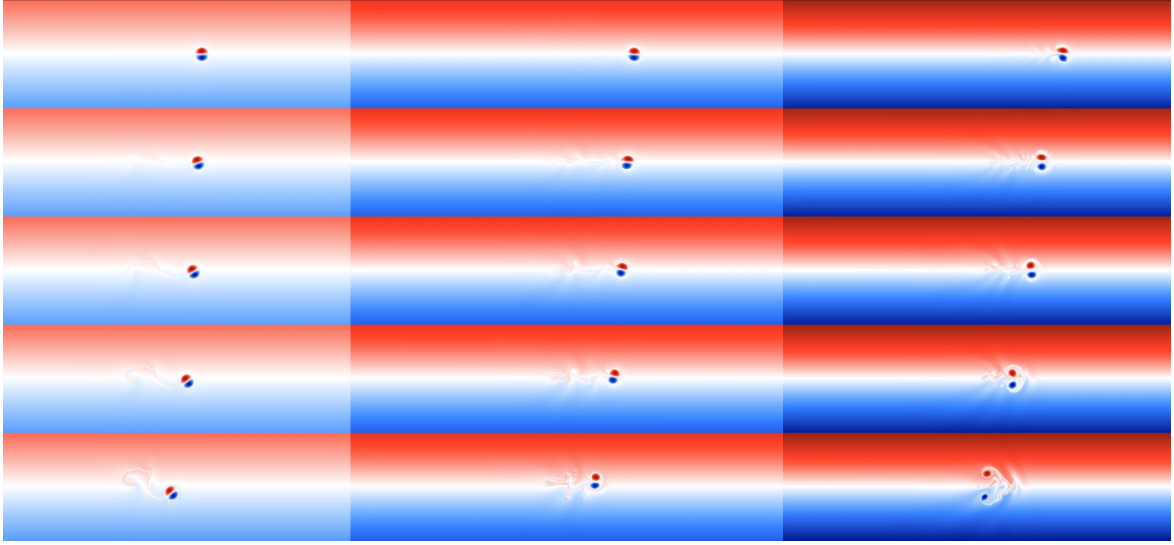


**Figure 7.2:** Snapshots of the dipole propagation for various values of  $\beta$  and  $\xi$ , using the Dedalus Python package with  $N = 2048$  (results are consistent with CABARET simulations): rows correspond to values of  $\xi$ , increasing from top to bottom ( $\xi = 5^\circ, 30^\circ, 45^\circ, 60^\circ, 90^\circ$ , respectively); columns correspond to values of  $\beta$ , increasing from left to right ( $\beta = 0.1, 0.2, 0.35$ , respectively).

consideration,  $\xi = 0^\circ, 5^\circ$  are used to describe the effects of weak tilting while greater values of  $\xi$  are used to describe the effects of large initial tilt. An example of fields for a tilted dipole are presented in Fig. 7.1.

To draw comparisons with our numerical results for initially tilted dipoles, we can look to the Nycander-Isichenko theory. For very strong dipoles ( $c \gg \beta$ ), [Nycander and Isichenko \(1990\)](#) derived an equation for the trajectory of  $(x_c, y_c)$ , corresponding to the center coordinate for an initially tilted dipole. In terms of the tilting angle  $\xi$ , their expression, which they showed accurately described the motion of quasistationary oscillating dipoles in a weakly inhomogeneous medium, can be reduced to

$$\frac{d\xi}{dt} = -\frac{\beta c}{M_d} y_c, \quad (7.4)$$

where  $M_d = |\int r^3 G(r) dr|$  (see Appendix B for the derivation of the tilt evolution). Using  $dy_c/dt = c \sin(\xi)$  together with (7.4), we obtain the well-known equation for the physical pendulum. In particular, for the case of small inclination to the zonal axis (e.g.,  $\xi = 5^\circ$ ), it follows from  $\sin \xi \sim \xi$  that

$$\xi(t) \sim R \cos(\omega t - \phi), \quad (7.5)$$

where  $\omega^2 = \beta c^2 / M_d$  is the frequency of small oscillations,  $R = \sqrt{\xi_0^2 + \xi_1^2}$ , where  $\xi_0$  is the small initial tilt,  $\xi_1 = \xi(\pi/2\omega)$  and  $\phi = \arctan(\xi_1/\xi_0)$  denotes the phase. This shows that one should expect oscillatory behaviour in the excursions of the dipole center from the equilibrium latitude for the tilted eastward-propagating LRD. In addition, the maximum excursion,  $y_t$ , is found in [Nycander and Isichenko \(1990\)](#) to behave according to

$$y_t = 2\sqrt{\frac{M_d}{\beta}} \sin(\xi/2). \quad (7.6)$$

Throughout our analysis, we can draw comparisons between our numerical results and the predictions of the Nycander-Isichenko theory. Furthermore, when performing our numerical analysis, we solve the problem using both the CABARET scheme (to remain consistent with other works in this thesis) and the Dedalus Python package, which uses spectral methods in space and a fourth-order Runge-Kutta scheme in time ([Burns et al., 2020](#)). Since the latter of these methodologies does not include implicit numerical diffusion, we estimated the numerical viscosity associated with our CABARET simulations and used this to set diffusion and hyperdiffusion parameters in the pseudo-spectral model (see Fig. 4.9). Since comparison between solutions in Fig. 7.3 appear consistent for a range of tilt values, we proceed by presenting solutions obtained using CABARET.

## 7.1 Small tilt

To analyse the tilted dipole evolution, we perform similar analysis as in Chapter 3 and 4, where we considered the time-series for a variety of quantities. These included: the zonal phase speed,  $c$ ; the meridional center displacement,  $y_c$ ; the zonal and meridional center differences,  $\Delta x$  and  $\Delta y$ , respectively; the enstrophy components,  $Z_{A,S}$  and the deformation of components,  $L_{A,S}$ . We shall continue to refer to these quantities in our tilted dipole investigations.

### 7.1.1 Case 1: $\beta = 0.35$

If we begin by considering a weakly intense dipole with  $\beta = 0.35$ , our simulations for the dipole propagation show disintegration in the interval  $[0, 200]$ , for all values of  $\xi$  we explore. Such results disagree with [Hesthaven et al. \(1993\)](#), where they only observed disintegration when  $\xi = 60^\circ, 90^\circ$  and instead observed relaxation along the zonal axis for  $\xi = 5^\circ, 30^\circ$ . Analysing curves obtained using our numerics in Fig. 7.4

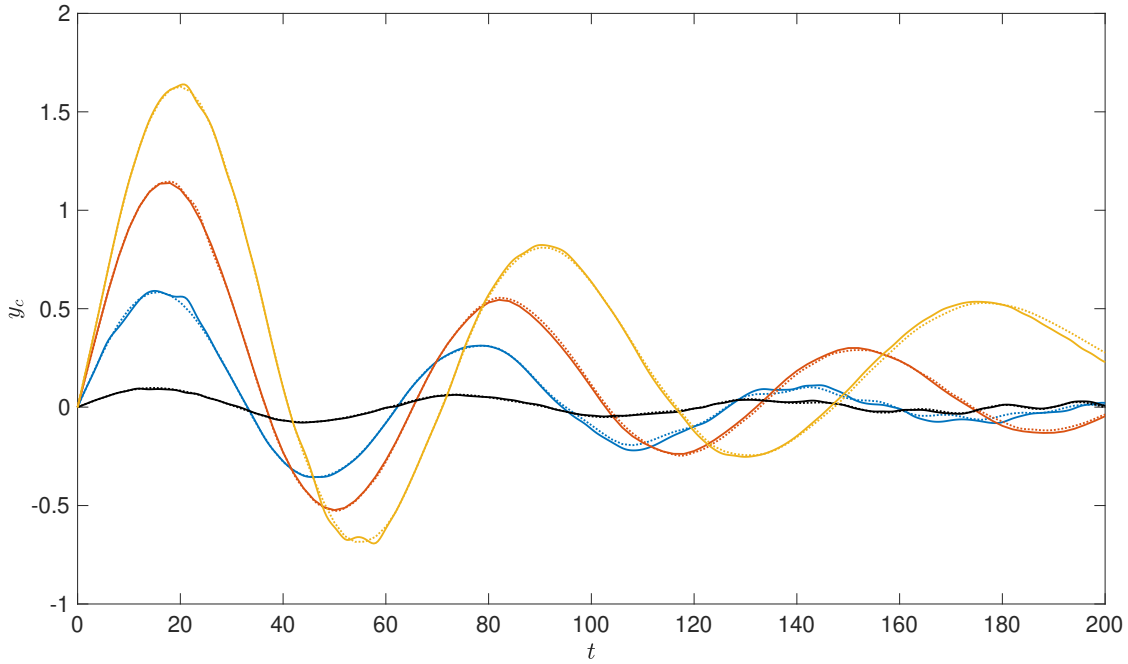


**Figure 7.3:** Comparison between CABARET (thick lines) and Dedalus (dotted lines) solutions (i.e.,  $y_c$ ) for tilted dipoles with  $\beta = 0.2$ : black curves correspond to  $\xi = 5^\circ$ ; blue curves correspond to  $\xi = 30^\circ$ , red curves correspond to  $\xi = 60^\circ$ ; yellow curves correspond to  $\xi = 90^\circ$ . The consistency in these curves is a strong case for numerical convergence.

for  $\xi = 5^\circ, 30^\circ$ , there are clear oscillations in the initial stages of  $Z_A$ . The maxima appear to correspond with the extrema of  $y_c$ , while the minima seem to correspond with the extrema of  $\Delta x$  (see Fig. 7.4c). From (7.6), the maximum excursion of the dipole in the meridional direction is approximated to be  $y_t \sim 0.083$  and  $y_t \sim 0.49$ , for  $5^\circ$  and  $30^\circ$  tilt, respectively. In the case of our numerical solutions, we find that  $y_t \sim 0.073$  and  $y_t \sim 0.45$ , for increasing tilt, which are within the estimations of the Nycander-Isichenko theory, but are smaller than those predicted and appear to become less exact as we increase the value of  $\xi$ .

As oscillations in  $\Delta x$  and  $y_c$  due to tilting (hereafter, called tilted oscillations) dampen over time, the size of the peaks in  $Z_A$  look to get smaller. Then, at  $t \sim 75$ , we begin to see divergence in the time-series for  $Z_A$  between the tilted dipoles of weak intensity. In particular, the case of  $\xi = 5^\circ$  sees approximately linear growth in the value of  $Z_A$  for  $75 \leq t \leq 115$ , whereas, when  $\xi = 30^\circ$  the solution sees decay in enstrophy during this interval. In addition, the spike in  $Z_A$  at  $t \sim 100$  for  $\xi = 30^\circ$  (dotted line) is associated with the change in direction of the dipole propagation (see Fig. 7.2). In the case when  $\xi = 5^\circ$  (thick line), this change in direction can be



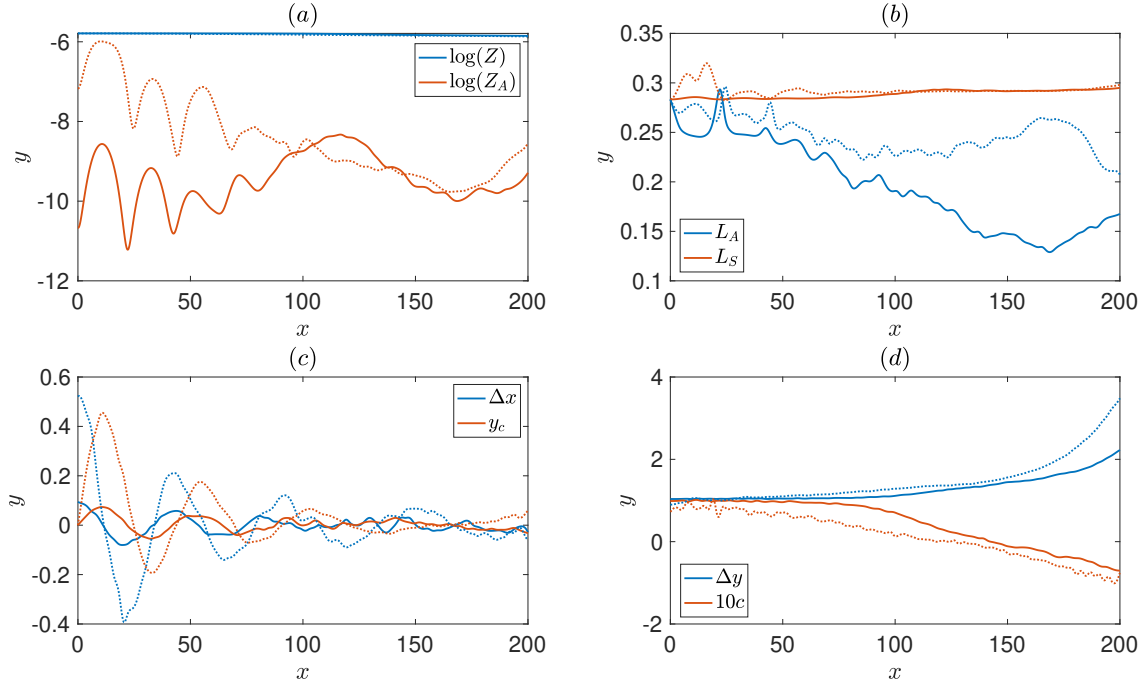


**Figure 7.4:** Panels illustrating physical fields associated with  $\beta = 0.35$  and  $\xi = 5^\circ$  (thick lines) and  $\xi = 30^\circ$  (dotted lines): (a) shows the logarithms of  $Z$  (blue) and  $Z_A$  (red); (b) shows the length scales of  $L_A$  (blue) and  $L_S$  (red); (c) shows the zonal center difference,  $\Delta x$  (blue) and the meridional center trajectory,  $y_c$  (red); (d) shows the meridional center difference,  $\Delta y$  (blue) and the rescaled zonal propagation velocity (red).

seen in the enstrophy changing from increasing to decreasing at  $t \sim 115$ .

While the case of small initial tilt with  $\xi = 5^\circ$  appears to transition from a tilting oscillatory phase into a dipole that oscillates about the zonal axis; seeing destruction related to the instability of zonally drifting dipoles (see Chapter 3), the characteristic differences in enstrophy curves (see Fig. 7.4a) in relation to  $\xi = 30^\circ$  suggest that there might be a change in destruction mechanism with increasing tilt. More specifically, it could be the case that dipoles with significant initial tilt are unable to adjust along the zonal axis and see destruction as a consequence of tilting. Whereas, if the tilt is small enough, then the vortex pair is capable of adjusting along the zonal axis, from which it propagates zonally and unravels as a consequence of Davies mode instability. This is consistent with the value of  $t_s$  being smaller in the presence of initial tilt than in the case of no tilt (effectively, small initial tilt acts to disturb the dipole and encourage linear instability growth). Clearly, analysing whether or not Davies modes develop on titled dipoles is important and we will explore this in the stronger dipole considerations.

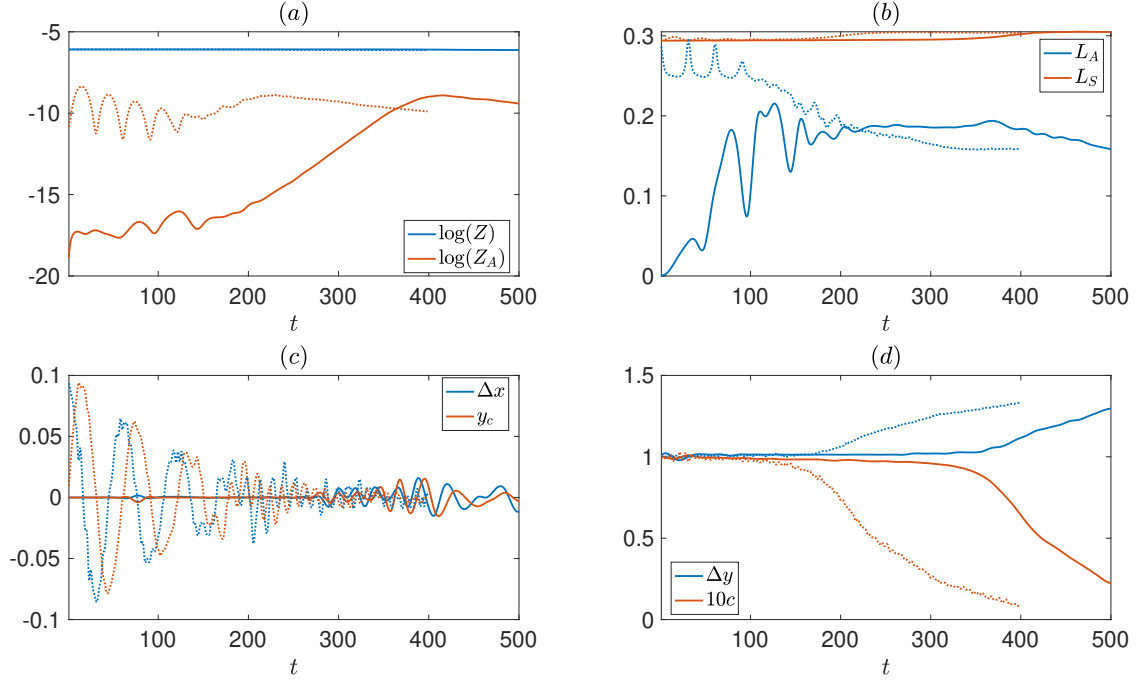


**Figure 7.5:** Time-series for invariants and derived quantities describing the  $\beta = 0.2$  dipole dynamics (thick line) and the analogous dynamics with  $\xi = 5^\circ$  (dotted line): (a) shows the logarithms of  $Z$  (blue) and  $Z_A$  (red); (b) shows the length scales of  $L_A$  (blue) and  $L_S$  (red); (c) shows the zonal center difference,  $\Delta x$  (blue) and the meridional center trajectory,  $y_c$  (red); (d) shows the meridional center difference,  $\Delta y$  (blue) and the re-scaled zonal propagation velocity (red). The curves corresponding to no tilt continue up until  $t \sim 500$  to illustrate the partner separation of the dipole.

### 7.1.2 Case 2: $\beta = 0.2$

To investigate similarities with the classical LRD propagation, we consider both no tilt and  $5^\circ$  tilt at initialisation, for a dipole with  $\beta = 0.2$  (see Fig. 7.5). On analysing both cases, we find that the total enstrophy,  $Z$ , for both very small tilt and no tilt appears approximately conserved in contrast to striking differences in  $Z_A$ . Firstly, the initial value for  $\xi = 5^\circ$  is nonzero zero (see Fig. 7.5a) and subsequent oscillations in  $\log(Z_A)$  are a consequence of alternating movement of the dipole center from north to south (as seen from  $y_c$  in Fig. 7.5c); in accord with [Hesthaven et al. \(1993\)](#). Until  $t \sim 100$ , the local minima of  $Z_A$  correspond to the local maxima of  $L_A$  (see Fig. 7.5b). Similar to the case of  $\beta = 0.35$  in the presence of tilt, these seem to be related to the extrema of tilt (see Fig. 7.5c) as well as with crossing of the dipole center with the  $t$ -axis (i.e.,  $y_c = 0$ ). Note that during this period, the zonal drift and the distance between partners remain nearly at their initial values for both slightly tilted and zero tilt cases (see Fig. 7.5a).

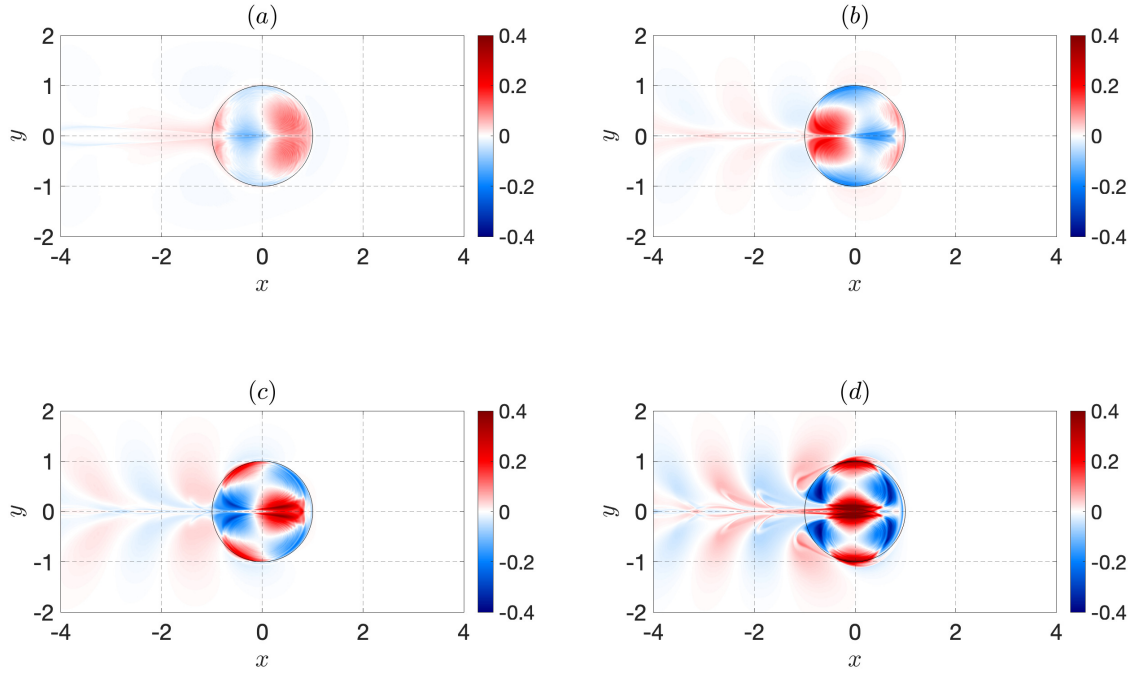


**Figure 7.6:** Snapshots of  $q_A$  for a dipole with  $(\beta, \xi) = (0.2, 5^\circ)$ : (a) occurs at  $t \sim 60$ , (b) occurs at  $t \sim 120$ , (c) occurs at  $t \sim 150$ , (d) occurs at  $t \sim 180$ . The circular boundary is a unit circular to highlight deformations in the separatrix.

Furthermore, we see deviations from decaying quasi-periodic oscillations related to the initial tilt:  $\log(Z_A)$  starts to grow nearly linearly until  $t \sim 200$ , although with a smaller rate than without tilt (see Fig. 7.5a); the scale  $L_A$  decreases to match the corresponding value at the stage of linear growth for an untilted LRD (see Fig. 7.5b); the zonal drift is decelerating while the partner separation increases (see Fig. 7.5d). Collectively, this appears to indicate a transition of the tilted LRD into a stage of intermediate linear growth of a critical mode, similar to the untilted dipole, which continues this phase up until  $t \sim 350$  when its zonal drift begins to decelerate in accord with increasing separation of partners (see Fig. 7.5d). In contrast, this phase for the tilted case is relatively short: for a slightly tilted LRD, after  $t \sim 200$  we observe decreasing values of  $Z_A$  (see Fig. 7.5a), accompanied by substantial zonal deceleration and increasing partner separation, significantly earlier than for untilted dipoles (see Fig. 7.5d).

To illustrate further the development of the A-component for the tilted LRD, we present snapshots of  $q_A$  in Fig. 7.6. Panel (a) shows a dipole pattern that looks slightly deviated away from the initial pattern in Fig. 7.1a. Because this pattern is

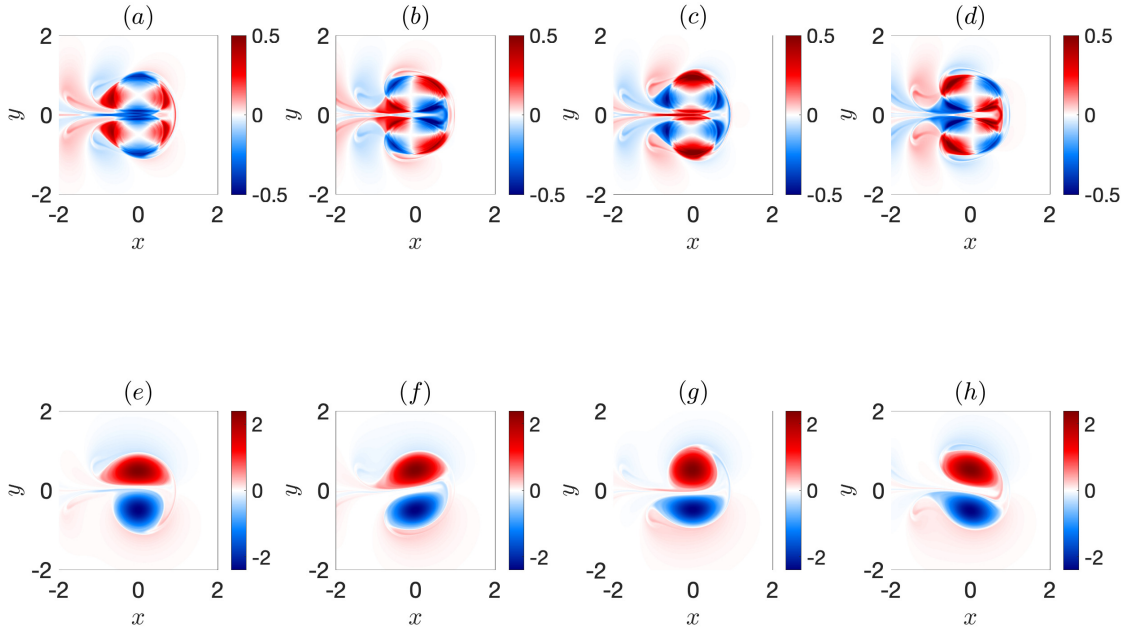


**Figure 7.7:** Upper panels show the PVA Davies mode development during  $150 \leq t \leq 200$ , with  $\beta = 0.2$  and  $\xi = 5^\circ$ , for different phases over a period of oscillation. Bottom panels show the corresponding deformations of the dipole PVA: (a) elongates the cyclone and compresses the anticyclone, as seen in (e); (b) leads to less elongation in the cyclone more elongation in the anticyclone, looking as a tilted and deformed dipole in (f); (c) behaves as (a), but with the opposite effect on partners in (g); (d) behaves as (b), but with the opposite effect on partners in (h).

derived from the tilted oscillations of the dipole motion across the zonal axis, we refer to the A-component as a developing T-mode during this phase. As the tilted oscillations begin to decay, we see the phase of the T-mode slowly transition in Fig. 7.6(b) to a more familiar Davies mode or A-mode pattern (Davies et al., 2023). It is clear from Figs 7.6c, d that the corresponding Davies mode has a period of oscillation. We estimate this numerically to be  $T \sim 16$ , which is consistent with the period of oscillation for Davies modes observed in Chapter 4. Moreover, the growth rate of  $q_m = \max(q_A)$  for  $150 \leq t \leq 200$  is  $\sigma \sim 0.015$ , which is consistent with a gentler slope of  $\log(Z_A)$  in Fig. 7.5a relative to the untilted case, where  $\sigma \sim 0.02$ . This can be interpreted as the slightly tilted dipole exhibiting the same instability as in the untilted case, but with weaker growth rate (see Fig. 7.7 to visualise how the Davies mode deforms the dipole structure).

In the case of a  $\beta = 0.35$  dipole, there are differences in enstrophy curves that

suggested that a Davies mode does not form in this case and instead the dipole sees disintegration through the tilting mechanism. When comparing curves for a  $\beta = 0.2$  dipole with  $\xi = 30^\circ, 45^\circ$  (see Fig. 7.8), the enstrophy behaviour differs from the very small and untilted enstrophy curves (see Fig. 7.5a), with there not appearing to be a linear growth stage, and instead an approximately linear decay phase occurs at around  $t \sim 200$  for  $\xi = 30^\circ$ . Moreover, during this decreasing portion, the values of  $L_A$  see increase for both  $\xi = 30^\circ, 45^\circ$  (see Fig. 7.8b), which differs from the case of  $\xi = 5^\circ$ , where the value of  $L_A$  decreased (see Fig. 7.5b).

In the case of no initial tilt, the Davies mode deforms up until the value of  $L_A$  stays roughly uniform between  $200 \leq t \leq 400$ . During this phase, the Davies mode continues to grow in amplitude as it oscillates, resulting in the destruction of the LRD propagation. In a similar way, when  $\xi = 5^\circ$ , the Davies mode forms in the interval  $100 \leq t \leq 150$ , where the value of  $L_A$  approaches similar values to those in the untilted case. The following decrease in  $L_A$  is consistent with the decrease in the untilted case after the linear growth stage, suggesting that the Davies mode contributes to the destruction of the  $\xi = 5^\circ$  dipole.

On the other hand, despite there being clear deceleration and partner separation in the dipole for  $\xi = 30^\circ, 45^\circ$  (see Fig. 7.8d), the increasing length scale of the A-component is due to adjustment of the dipole propagation. More specifically, we see a clear transition in the A-component, from a T-mode pattern (see Fig. 7.9a) into a Davies mode pattern (see Figs. 7.9b, c, d). Even though a Davies mode presents itself, the dipole also seems to adjust to an elliptical shape. This deformation of the dipole is likely a consequence of tilted oscillations, and this contributes to the deformation of the Davies mode. Regardless, given the object decelerates significantly over the time domain, the elliptical vortex could see destruction through Davies mode instability if given long enough. Alternatively, it is unclear whether a Davies mode would destroy an elliptical dipole, as decreases in enstrophy curves and critical mode amplitude (see Fig. 7.9) support the idea of dipole persistence (with eventual disintegration due to numerical viscosity).

Another interesting feature of the dynamics in this case is the change in wake structure. During the T-mode development, the trailing waves are a result of tilted oscillations, where the dipole sees considerable leakage through not being a steady state solution. Despite this, as the tilted oscillations decay, the dipole sees the development of a Davies mode, where the characteristic wake interacts with the trailing waves due to tilting. Through this interaction between waves, and potentially due to deformations in the dipole state, the wake structure thins itself out over

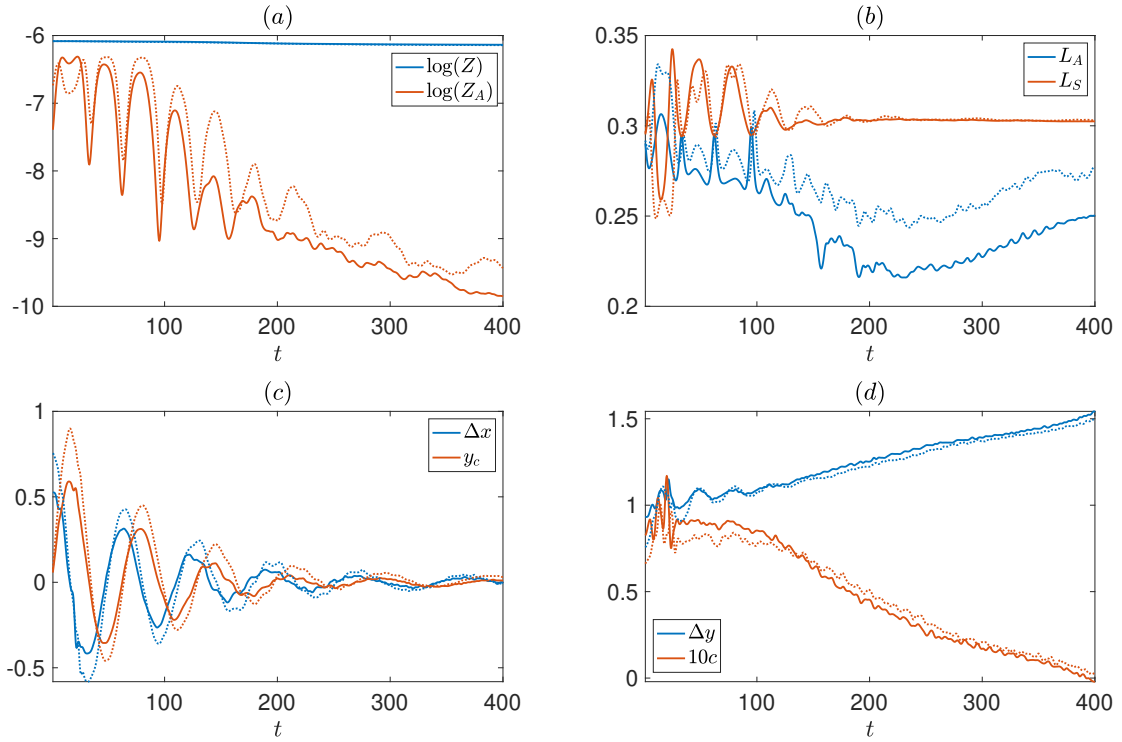


**Figure 7.8:** Time-series for invariants and derived quantities describing the  $\beta = 0.2$  dipole dynamics with  $\xi = 30^\circ$  (thick line) and  $\xi = 45^\circ$  (dotted line): (a) shows the logarithms of  $Z$  (blue) and  $Z_A$  (red); (b) shows the length scales of  $L_A$  (blue) and  $L_S$  (red); (c) shows the zonal center difference,  $\Delta x$  (blue) and the meridional center trajectory,  $y_c$  (red); (d) shows the meridional center difference,  $\Delta y$  (blue) and the re-scaled zonal propagation velocity (red).

time. Clearly, a detailed analysis of the wake is desirable, but given the scope of this chapter we do not present this material here.

## 7.2 Large tilt

In addition to the finding of steady state adjustment in [Hesthaven et al. \(1993\)](#), it was also demonstrated that weak dipoles in the presence of large tilt saw early-stage destruction. This mechanism is separate from the phenomena we related to untilted dipoles and is a consequence of waves forming in the large beta environment; allowing for significant deformations in the dipole state (see Fig. 7.9 for a visualisation of these collected waves in the background). Given some discrepancies we have found with the results of [Hesthaven et al. \(1993\)](#), it is important to investigate for the case of large tilt to see if their results for larger values of  $\xi$  still hold.

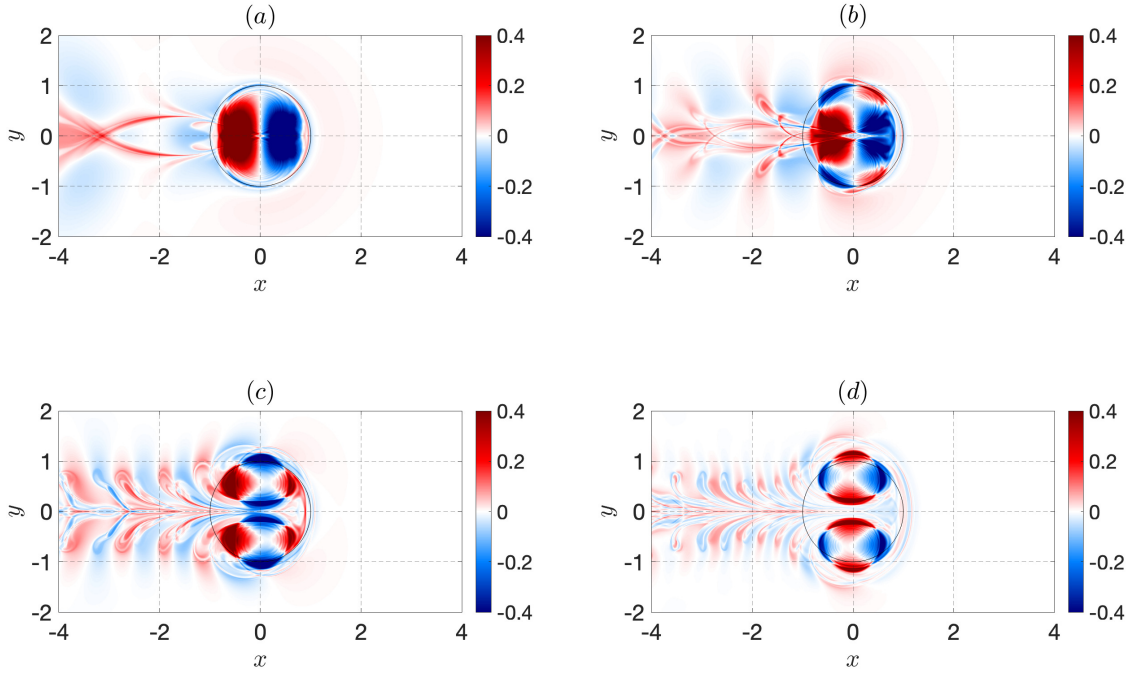


**Figure 7.9:** Transitions in the A-component corresponding to  $\beta = 0.2$  and  $\xi = 30^\circ$ : (a)  $t \sim 60$ ,  $q_m \sim 0.73$ ; (b)  $t \sim 130$ ,  $q_m \sim 0.62$ ; (c)  $t \sim 190$ ,  $q_m \sim 0.74$ ; (d)  $t \sim 270$ ,  $q_m \sim 0.51$ . The circular boundary is a unit circular to highlight deformations in the separatrix.

Beginning with  $\xi = 60^\circ$ , beyond the decaying tilted oscillations, it is clear from our numerical results that the values of  $L_A$  behave very differently to the previous tilt considerations in Figs. 7.5, 7.8. In particular, rather than seeing either an increasing or decreasing tendency, the deformation scale of the A-component experiences significant jumps in value during the interval  $200 \leq t \leq 400$  (see Fig. 7.10b). During this phase, the vortex exhibits much weaker deceleration than in the previous tilt cases (see Fig. 7.10d). In addition, the enstrophy does not appear to settle down and continues to oscillate significantly in value (see Fig. 7.10a), unlike in the previous tilt cases, where the enstrophy either reached a linearly increasing stage ( $\xi = 5^\circ$ ) or a linearly decreasing stage ( $\xi = 30^\circ$ ). This distinction in curves could be representative of steady state adjustment, as described in Hesthaven et al. (1993).

When considering the deformations in the A-component, we noticed that the T-mode structure persisted over the entire interval  $[0, 400]$ . Elaborating on this, the vortex pair experienced little partner separation and separatrix deformation before the partners oscillated together along the zonal axis (with deceleration beyond tilted oscillations potentially due to the presence of numerical viscosity). Throughout this



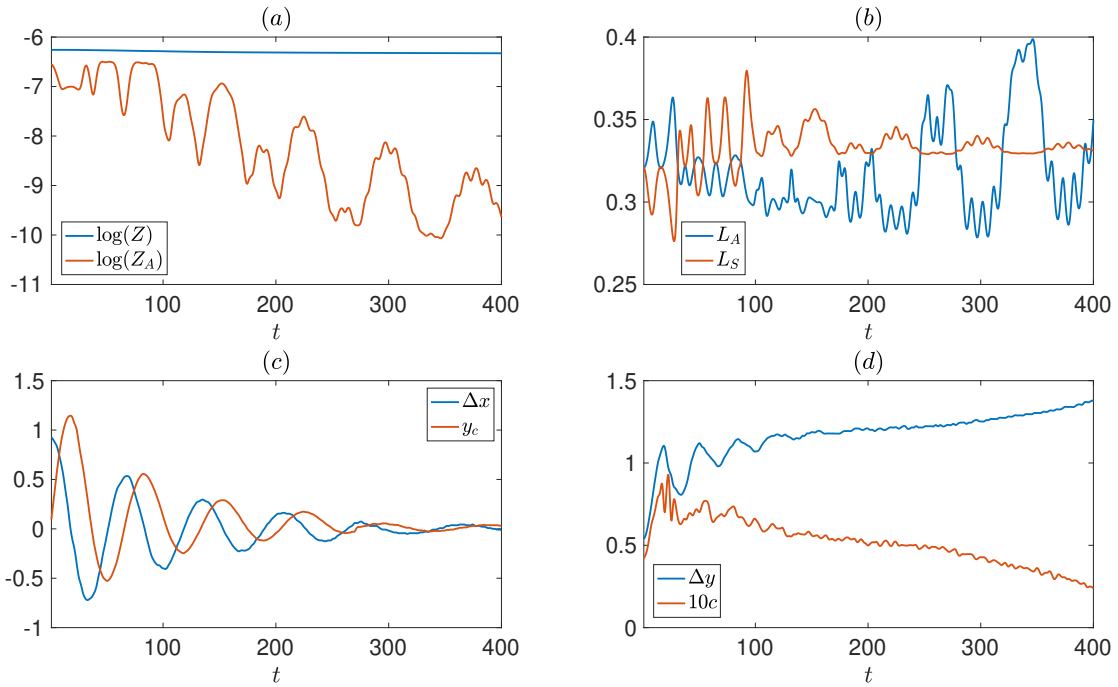


**Figure 7.10:** Time-series for invariants and derived quantities describing the  $\beta = 0.2$  dipole dynamics with  $\xi = 60^\circ$ : (a) shows the logarithms of  $Z$  (blue) and  $Z_A$  (red); (b) shows the length scales of  $L_A$  (blue) and  $L_S$  (red); (c) shows the zonal center difference,  $\Delta X$  (blue) and the meridional center trajectory,  $y_c$  (red); (d) shows the meridional center difference,  $\Delta y$  (blue) and the re-scaled zonal propagation velocity (red).

stage, the T-mode amplitude decreased considerably, but there was no presence of a growing Davies mode. This could be consequence of elliptical deformation of the separatrix. So far, we have only identified the existence of Davies modes for dipoles with a circular separatrix, but we have yet to investigate elliptical dipoles. In the case of elliptical dipoles, these could well be stable due to a lack of Davies mode formation. Regardless, a complex wake structure still appeared in the dipole propagation for large tilt. Despite this representation of PV leakage being characteristic of instability, the adjusted solutions seemed to follow an approximate steady trajectory with minor oscillations in the separate eddy cores. It is not clear how this is achieved and demands further study for future work.

Turning our attention to when  $\xi = 90^\circ$  (i.e., the dipole is initially positioned to propagate towards the North), our results shared consistency with [Hesthaven et al. \(1993\)](#), where the dipole experienced early-stage destruction through prolonged exposure to the trailing waves that collected in the center of the domain. Other similarities that we obtained were for the cases of  $\beta = 0.05$ , where regardless of tilt, these solutions seemed to adjust to a new steady state solution along the zonal axis. In the case of  $\beta = 0.1$ , we found that trends in enstrophy curves were



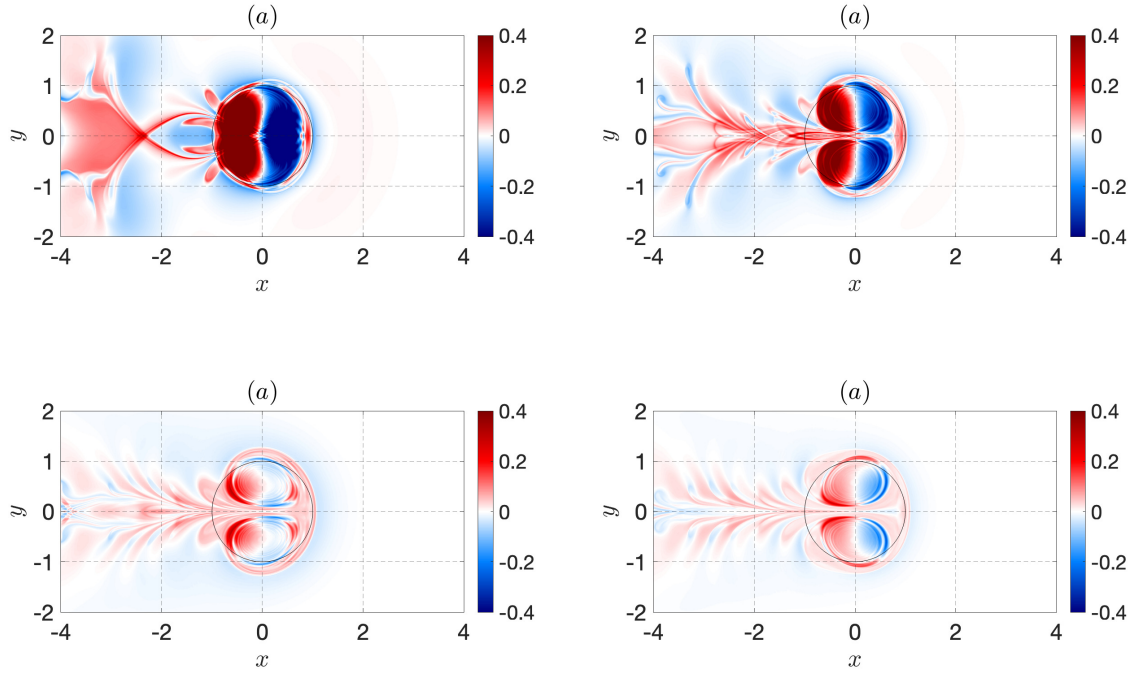


**Figure 7.11:** Transitions in the A-component corresponding to  $\beta = 0.2$  and  $\xi = 60^\circ$ : (a)  $t \sim 60$ ; (b)  $t \sim 130$ ; (c)  $t \sim 190$ ; (d)  $t \sim 270$ .

characteristically different between small and large tilt, however, simulations of the dipole propagation suggested these objects were capable of steady state adjustment. Since we observed strong dipole persistence in our numerical simulations for untilted dipoles in Chapter 3, it could be the case that small initial tilt solutions obey the untilted dynamics in the long time evolution (i.e., weakly unstable but long-lived dipole propagation along the zonal axis), while large initial tilt solutions adjust to a new elliptical steady state solution that is capable of uniform translation.

## 7.3 Summary

To summarise the findings of this chapter, we discussed the evolution of a variety of initially tilted LRDs. This analysis was previously performed in [Hesthaven et al. \(1993\)](#), however, we found both similarities and discrepancies with the results in this study. In the case of a weak  $\beta = 0.35$  dipole in the presence of small tilt (i.e.,  $\xi = 5^\circ, 30^\circ$ ), we observed decaying oscillations transition into propagation adjustment along the zonal axis. As the dipole evolution continued during this stage, the vortex pair began to oscillate and then proceeded to spontaneously break apart, as we

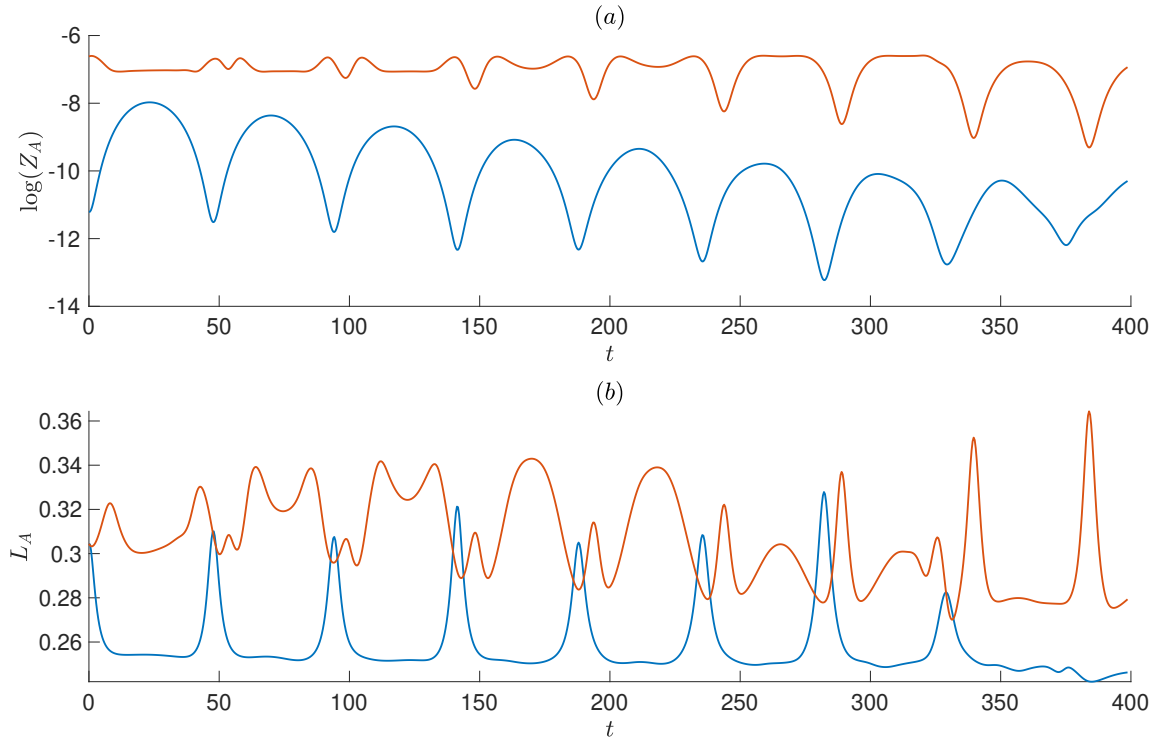


**Figure 7.12:** Strong dipole curves for  $\beta = 0.1$ : (a) shows the logarithms of  $Z_A$  with  $\xi = 5^\circ$  (blue) and  $\xi = 30^\circ$  (red); (b) shows the length scales of  $L_A$  for the same values of  $\xi$ .

observed for an initial LRD in Chapter 3. Such results disagree with those obtained in [Hesthaven et al. \(1993\)](#), where they instead observed an adjustment of the dipole to an approximately steadily eastward translating state along the zonal axis. This is likely a consequence of the numerics used in [Hesthaven et al. \(1993\)](#) not being able to capture the LRD instability due to the use of weak resolution relative to the resolution we use in this thesis. Despite this discrepancy, our results for  $\xi \geq 45^\circ$  are consistent with their results, where we both observed the disintegration of dipoles in this case.

In the case when  $\beta = 0.2$ , we did not observe disintegration for any value of  $\xi$  in the interval  $[0, 400]$ , however, we did uncover differences in behaviour for values of  $\xi$  either side of  $45^\circ$ . When the tilt was weak (i.e.,  $\xi < 45^\circ$ ), the dipole looked to adjust along the zonal axis after decaying oscillations due to the tilted initialisation. During the zonal propagation phase, we were able to associate a growing Davies mode pattern with the dipole motion, suggesting this will eventually break apart as in Chapter 3. On the other hand, when  $45^\circ < \xi < 90^\circ$ , we observed similar dynamics, though during the adjustment phase along the zonal axis, the

corresponding A-component did not resemble the Davies mode pattern. In particular, the dipole during this stage looked to have adjusted to a new steadily translating solution, as also observed in [Hesthaven et al. \(1993\)](#). Another similarity with this study was our results for  $\xi = 90^\circ$ , where we witnessed early stage disintegration due to the dipole being exposed to a large beta environment (i.e., disintegration due to dipole-wave interaction).

Overall, we found that our results disagreed with [Hesthaven et al. \(1993\)](#) when  $\xi < 45^\circ$ , but agreed otherwise. The disagreement in results is due to our solutions capturing the instability of the symmetric LRD solution, whereas, previous numerical simulations did not observe this particular dipole instability.

So far, the solutions we have considered have had known analytical representations. Despite these models being fascinating to analyse, there are many steady state solutions that cannot be expressed analytically, and so we will spend some time in the following chapter describing how we can extract solutions of this kind.

# Chapter 8

## Steady state solver

We derive a method to solve the nonlinear steady state equation (2.13) numerically. We do this with the intention of analysing the corresponding linear stability characteristics using our linear stability solver derived in Chapter 5. Up until this point, we have known the analytical form of the steady state dipole, however, there likely exist many steady state solutions that cannot be obtained analytically and could well act as better models for describing physical vortex motion. Since our linear stability methodology can be applied in a two-layer framework, we derive a nonlinear solver for a two-layer QG model and show how the method can be better optimised to extract LRD-type solutions in a 1.5-layer QG model. In theory, the optimisation process we carry out can be applied to any steady state solutions, provided integral constraints are known.

### 8.1 Newton's method

#### 8.1.1 Formulating the model

So far in this thesis, we have explored the dynamics of dipoles in a 1.5-layer model. These steady state solutions have an analytical representation described by (2.24) and (2.26). As briefly discussed in Chapter 2, there exists other steady state solutions related to the LRD, namely analogous solutions over meridional bottom slopes and dipole-rider steady states. Moreover, solutions with a non-circular separatix and those in a two-layer system have been studied in the literature (see Chapter 1), but it is not as straightforward to derive them analytically. In this case, numerical procedures are often employed to extract steady state solutions.

With this in mind, we take time in this chapter to derive methodology that can be

used to solve for arbitrary steady state solutions. For this purpose, we consider the two-layer QG equations on the beta-plane, in the presence of variable topography  $\eta_b(x, y)$  and layer-wise homogeneous zonal currents  $U_j$ :

$$\begin{aligned} & \left[ \frac{\partial}{\partial t} + \left( U_j - \frac{\partial \psi_j}{\partial y} \right) \frac{\partial}{\partial x} + \frac{\partial \psi_j}{\partial x} \frac{\partial}{\partial y} \right] q_j + \left[ \beta + S_j(U_j - U_{3-j}) + \alpha \delta_{2j} \frac{\partial \eta_b}{\partial y} \right] \frac{\partial \psi_j}{\partial x} \\ & + \alpha \delta_{2j} \frac{\partial \eta_b}{\partial x} \left( U_j - \frac{\partial \psi_j}{\partial y} \right) = \nu \nabla^4 \psi_j - \delta_{2j} \gamma \nabla^2 \psi_j, \quad j = 1, 2. \end{aligned} \quad (8.1)$$

Here,  $\alpha$  is a constant derived from nondimensionalisation and depends on how we scale the topography contribution (i.e., we can either use the same length scale introduced for horizontal variables, or we can introduce a vertical length scale for topography, as is standard in asymptotic analysis). If we impose a steady state vortex in the surface layer of the two-layer system, then we can transform our coordinate system so that our reference frame is translating with the vortex propagation. Therefore, if we denote the center coordinate of the upper layer steady state vortex by  $(x_c(t), y_c(t))$ , then we can rewrite (8.1) as

$$\begin{aligned} & \left[ \frac{\partial}{\partial t} + \left( U_j - \frac{dx_c}{dt} - \frac{\partial \psi_j}{\partial y} \right) \frac{\partial}{\partial x} + \left( \frac{\partial \psi_j}{\partial x} - \frac{dy_c}{dt} \right) \frac{\partial}{\partial y} \right] q_j + \left[ \beta + S_j(U_j - U_{3-j}) \right. \\ & \left. + \alpha \delta_{2j} \frac{\partial \eta_b}{\partial y} \right] \frac{\partial \psi_j}{\partial x} + \alpha \delta_{2j} \frac{\partial \eta_b}{\partial x} \left( U_j - \frac{\partial \psi_j}{\partial y} \right) = \nu \nabla^4 \psi_j - \delta_{2j} \gamma \nabla^2 \psi_j. \end{aligned} \quad (8.2)$$

If we seek solutions of the form  $\psi_j = \Psi_j + \epsilon \psi'_j$ , where  $0 < \epsilon \ll 1$ , we find at leading-order the steady state governance

$$\begin{aligned} & \left( u_j \frac{\partial}{\partial x} + v_j \frac{\partial}{\partial y} \right) Q_j + \left[ \beta + S_j(U_j - U_{3-j}) + \alpha \delta_{2j} \frac{\partial \eta_b}{\partial y} \right] \frac{\partial \Psi_j}{\partial x} \\ & + \alpha \delta_{2j} \frac{\partial \eta_b}{\partial x} \left( U_j - \frac{\partial \Psi_j}{\partial y} \right) = \nu \nabla^4 \Psi_j - \delta_{2j} \gamma \nabla^2 \Psi_j, \end{aligned} \quad (8.3)$$

where if  $c_x = dx_c/dt$  and  $c_y = dy_c/dt$ , then

$$u_j = U_j - c_x - \frac{\partial \Psi_j}{\partial y}, \quad v_j = \frac{\partial \Psi_j}{\partial x} - c_y, \quad (8.4)$$

and

$$Q_j = \nabla^2 \Psi_j + S_j(\Psi_{3-j} - \Psi_j). \quad (8.5)$$

In this framework, if we consider solutions on a discrete uniform square grid, we can

define the residual function

$$F_j^{m,n} = \left( u_j \frac{\partial}{\partial x} + v_j \frac{\partial}{\partial y} \right) Q_j^{m,n} + \left[ \beta + S_j(U_j - U_{3-j}) + \alpha \delta_{2j} \frac{\partial \eta_b}{\partial y} \right] \frac{\partial \Psi_j^{m,n}}{\partial x} + \alpha \delta_{2j} \frac{\partial \eta_b}{\partial x} \left( U_j - \frac{\partial \Psi_j^{m,n}}{\partial y} \right) - \nu \nabla^4 \Psi_j^{m,n} + \delta_{2j} \gamma \nabla^2 \Psi_j^{m,n}, \quad (8.6)$$

where  $m$  and  $n$  are zonal and meridional indices identifying nodes along these directions, respectively. Associated with the residual function is the popular nonlinear solution scheme, namely the Newton-Raphson method:

$$\mathbf{J}(\Psi^\mu)(\Psi^{\mu+1} - \Psi^\mu) = -\mathbf{F}(\Psi^\mu), \quad (8.7)$$

where  $\mu$  is the iteration step of the numerical scheme,

$$\Psi = (\Psi_1^{1,1}, \Psi_1^{2,1}, \dots, \Psi_1^{N,1}, \Psi_1^{1,2}, \dots, \Psi_1^{N,N}, \Psi_2^{1,1}, \dots, \Psi_2^{N,N})^T \in \mathbb{R}^{2N^2}, \quad (8.8)$$

$$\mathbf{F} = (F_1^{1,1}, F_1^{2,1}, \dots, F_1^{N,1}, F_1^{1,2}, \dots, F_1^{N,N}, F_2^{1,1}, \dots, F_2^{N,N})^T \in \mathbb{R}^{2N^2}, \quad (8.9)$$

the matrix  $\mathbf{J} \in \mathbb{R}^{2N^2 \times 2N^2}$  is the well-known Jacobian with entries

$$J_{ij}^{m,n,p,q} = \frac{\partial F_i^{m,n}}{\partial \Psi_j^{p,q}}, \quad (8.10)$$

and we have assumed that our solutions are computed on a uniform square grid with  $N$  nodes in each direction. Given the number of indices we are dealing with, it is convenient to introduce

$$k = m + (N-1)n, \quad \ell = p + (N-1)q, \quad (8.11)$$

which allows us to rewrite (8.10) as

$$J_{i,j}^{k,\ell} = \frac{\partial F_i^k}{\partial \Psi_j^\ell}. \quad (8.12)$$

In a block-matrix representation, we can express the Jacobian in the form

$$\mathbf{J} = \begin{bmatrix} J_{1,1}^{k,\ell} & J_{1,2}^{k,\ell} \\ J_{2,1}^{k,\ell} & J_{2,2}^{k,\ell} \end{bmatrix}. \quad (8.13)$$

### 8.1.2 Finite-difference discretisation

When employing discretisation methods in numerical analysis, there is no unique procedure to follow. In Chapter 5, we performed a linear stability analysis using a method that implemented second-order finite differences. For consistency with this approach, we proceed along the same lines. Thus, under second-order finite difference estimates, we can express the Jacobian entries as follows:

$$J_{j,j}^{k,k} = -20\nu - 4\delta_{2j}\gamma, \quad (8.14)$$

$$J_{j,j}^{k,k+1} = -2\tilde{u}_j - \frac{S_j\tilde{u}_j}{2} + \frac{\beta_j}{2} + \frac{\alpha\delta_{2j}T_y}{2} + 8\nu + \delta_{2j}\gamma + (2 + S_j)\frac{\partial\Psi_j^k}{\partial y} + \frac{1}{2}\frac{\partial}{\partial y}\nabla^2\Psi_j^k - \frac{S_j}{2}\frac{\partial\Psi_{3-j}^k}{\partial y}, \quad (8.15)$$

$$J_{j,j}^{k,k-1} = 2\tilde{u}_j + \frac{S_j\tilde{u}_j}{2} - \frac{\beta_j}{2} - \frac{\alpha\delta_{2j}T_y}{2} + 8\nu + \delta_{2j}\gamma - (2 + S_j)\frac{\partial\Psi_j^k}{\partial y} - \frac{1}{2}\frac{\partial}{\partial y}\nabla^2\Psi_j^k + \frac{S_j}{2}\frac{\partial\Psi_{3-j}^k}{\partial y}, \quad (8.16)$$

$$J_{j,j}^{k,k+N} = -2\tilde{v}_j - \frac{S_j\tilde{v}_j}{2} + 8\nu + \delta_{2j}\gamma - \frac{1}{2}\frac{\partial}{\partial x}\nabla^2\Psi_j^k - (2 + S_j)\frac{\partial\Psi_j^k}{\partial x} - \frac{S_j}{2}\frac{\partial\Psi_{3-j}^k}{\partial x} - \frac{\alpha\delta_{2j}T_x}{2}, \quad (8.17)$$

$$J_{j,j}^{k,k-N} = 2\tilde{v}_j + \frac{S_j\tilde{v}_j}{2} + 8\nu + \delta_{2j}\gamma + \frac{1}{2}\frac{\partial}{\partial x}\nabla^2\Psi_j^k + (2 + S_j)\frac{\partial\Psi_j^k}{\partial x} + \frac{S_j}{2}\frac{\partial\Psi_{3-j}^k}{\partial x} + \frac{\alpha\delta_{2j}T_x}{2}, \quad (8.18)$$

$$J_{j,j}^{k,k+1+N} = \frac{1}{2}\left(\tilde{u}_j + \tilde{v}_j + \frac{\partial\Psi_j^k}{\partial x} - \frac{\partial\Psi_j^k}{\partial y}\right) - 2\nu, \quad (8.19)$$

$$J_{j,j}^{k,k+1-N} = \frac{1}{2}\left(\tilde{u}_j - \tilde{v}_j - \frac{\partial\Psi_j^k}{\partial x} - \frac{\partial\Psi_j^k}{\partial y}\right) - 2\nu, \quad (8.20)$$

$$J_{j,j}^{k,k-1+N} = \frac{1}{2}\left(-\tilde{u}_j + \tilde{v}_j + \frac{\partial\Psi_j^k}{\partial x} + \frac{\partial\Psi_j^k}{\partial y}\right) - 2\nu, \quad (8.21)$$

$$J_{j,j}^{k,k-1-N} = \frac{1}{2}\left(-\tilde{u}_j - \tilde{v}_j - \frac{\partial\Psi_j^k}{\partial x} + \frac{\partial\Psi_j^k}{\partial y}\right) - 2\nu, \quad (8.22)$$

$$J_{j,j}^{k,k+2} = \frac{1}{2}\left(\tilde{u}_j - \frac{\partial\Psi_j^k}{\partial y}\right) - \nu, \quad (8.23)$$

$$J_{j,j}^{k,k-2} = \frac{1}{2}\left(-\tilde{u}_j + \frac{\partial\Psi_j^k}{\partial y}\right) - \nu, \quad (8.24)$$

$$J_{j,j}^{k,k+2N} = \frac{1}{2}\left(\tilde{v}_j + \frac{\partial\Psi_j^k}{\partial x}\right) - \nu, \quad (8.25)$$

$$J_{j,j}^{k,k-2N} = \frac{1}{2} \left( -\tilde{v}_j - \frac{\partial \Psi_j^k}{\partial x} \right) - \nu, \quad (8.26)$$

$$J_{j,3-j}^{k,k+1} = \frac{S_j}{2} \left( \tilde{u}_j - \frac{\partial \Psi_j^k}{\partial y} \right), \quad (8.27)$$

$$J_{j,3-j}^{k,k-1} = -\frac{S_j}{2} \left( \tilde{u}_j - \frac{\partial \Psi_j^k}{\partial y} \right), \quad (8.28)$$

$$J_{j,3-j}^{k,k+N} = \frac{S_j}{2} \left( \tilde{v}_j + \frac{\partial \Psi_j^k}{\partial x} \right), \quad (8.29)$$

$$J_{j,3-j}^{k,k-N} = -\frac{S_j}{2} \left( \tilde{v}_j + \frac{\partial \Psi_j^k}{\partial x} \right), \quad (8.30)$$

where  $\tilde{u}_j = U_j - c_x$ ,  $\tilde{v}_j = -c_y$ ,  $T_x = \partial \eta_b / \partial x$ ,  $T_y = \partial \eta_b / \partial y$  and  $\beta_j = \beta + S_j(U_j - U_{3-j})$ .

## 8.2 LRD initialisation

As a way to sanity check the algorithm we have developed, we can impose a known initial steady state solution to the problem and carrying out the iterative procedure on the field in the presence of a small perturbation. If our initial guess is a weakly disturbed steady state of the system, then our nonlinear solver should hopefully converge to the pure steady state solution. Given this reasoning, we consider a 1.5-layer model with an initial LRD profile placed in the middle of the fluid domain. In this framework, the complexity of the Jacobian structure will be simplified relative to the two-layer equivalent (see Fig. 8.1) and we can express the elements by the derivatives

$$J^{k,\ell} = \frac{\partial F^k}{\partial \Psi^\ell}. \quad (8.31)$$

In addition, for further simplicity, we set  $S = 0$  and assume both eddy viscosity and bottom friction are negligible, so that the residual function becomes

$$F^k = A_k(\beta + 4c_x + D_k) - C_k(c_x + B_k), \quad (8.32)$$

where

$$A_k = \frac{\partial \Psi^k}{\partial x}, \quad B_k = \frac{\partial \Psi^k}{\partial y}, \quad C_k = \frac{\partial}{\partial x} \nabla^2 \Psi^k + 4A_k, \quad D_k = \frac{\partial}{\partial y} \nabla^2 \Psi^k + 4B_k, \quad (8.33)$$

and  $c_y = 0$  due to us considering the LRD steady state.



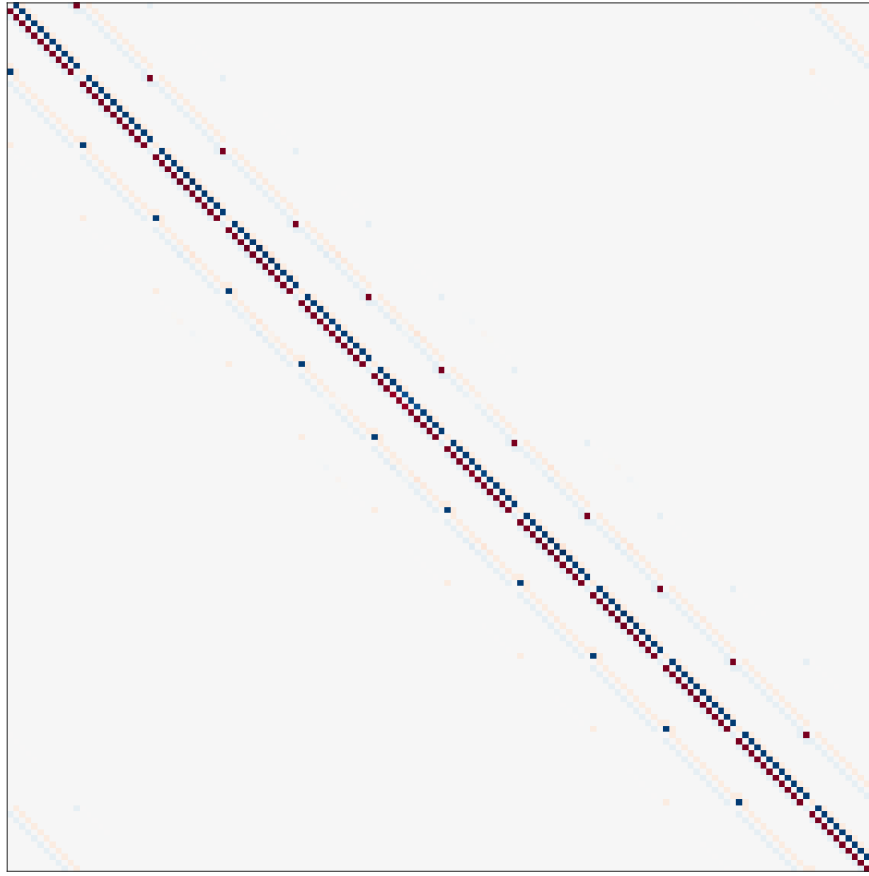


**Figure 8.1:** Diagonal structure for the Jacobian matrix in a 1.5-layer system (areas of grey refer to null entries, and the colour shading indicates the magnitude of values, with red being positive and blue being negative). Doubly-periodic boundary conditions are assumed.

### 8.2.1 Integral constraint

A feature of the LRD steady state solution is that it satisfies the integral constraint

$$\int \Psi(x, y) \, dx \, dy = 0, \quad (8.34)$$

where the integral is over the entire domain. Therefore, we can build this into the solver by imposing the following integral constraint:

$$\sum_{k=1}^M \Psi^k = 0 \implies \Psi^M = - \sum_{k=1}^{M-1} \Psi^k, \quad (8.35)$$

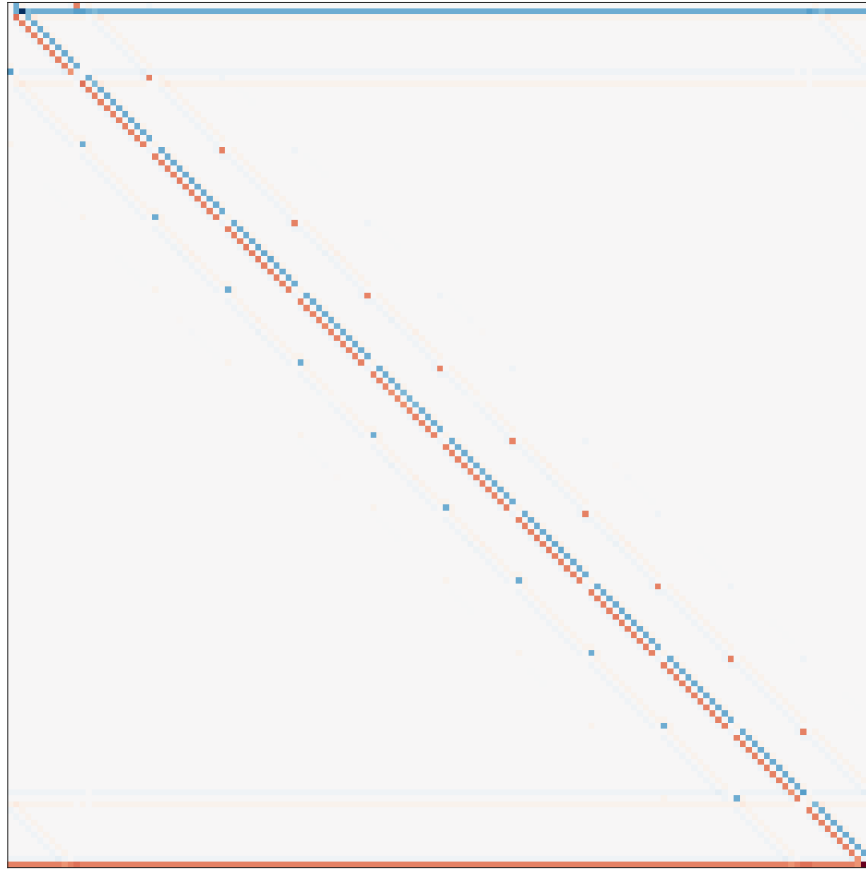


**Figure 8.2:** Jacobian structure for a 1.5-layer setup, in the presence of doubly-periodic boundary conditions and assuming the integral constraints (8.35). Areas of grey refer to null entries, and the colour shading indicates the magnitude of values, with red being positive and blue being negative.

with  $M = N^2$ . This becomes problematic for our Newton method in its present form since our system now becomes one with  $M$  equations with  $M - 1$  unknowns. In which case, the system is inconsistent and the Jacobian matrix is singular. Therefore, we must account for the integral constraint in our Newton method. To do this, we discard  $\Psi^M$  and  $F^M$  from  $\Psi$  and  $F$ , respectively, and reduce the size of our Jacobian to  $(M - 1)^2$ . Furthermore, we consider when each of the nodal values in  $F^k$  equals  $\Psi^M$ , so that we can replace each of these terms with the negative summation in (8.35) when appropriate, and differentiate the additional contributions. This results in a matrix that is predominantly sparse, but with 12 dense rows (see Fig. 8.2.1).

To see how these special cases are derived, we focus our attention on two particular

scenarios, namely  $\Psi^{k+N} = \Psi^M$  or  $\Psi^{k+N+1} = \Psi^M$ . On understanding these two situations, it is easy to extend the logic to the remaining 10 instances, and so beyond mathematically detailing these two special cases, we will only state the row entries for the other rare appearances.

**Case 1:**  $\Psi^{k+N} = \Psi^{\max}$

When this occurs, we can write

$$B_k = \frac{1}{2}(\Psi^M - \Psi^{k-N}) = -\frac{1}{2}\left(\sum_{m=1}^{M-1} \Psi^k + \Psi^{k-N}\right) = \frac{1}{2}\begin{cases} S_n - \Psi^n - \Psi^{k-N}, & n \neq k-N, \\ S_n - 2\Psi^{k-N}, & n = k-N, \end{cases}$$

where we define the excluded summation as

$$S_n = -\sum_{\substack{m=1 \\ m \neq n}}^{M-1} \Psi_n. \quad (8.36)$$

This is a powerful way to rewrite the negative summation, since we can choose  $\Psi^n$  to correspond to the term we are interested in differentiating. To see this, suppose we want to obtain  $J^{k,k+1}$ . Then we can write

$$B_k = \frac{S_{k+1} - \Psi^{k+1} - \Psi^{k-N}}{2},$$

so the term  $\Psi^{k+1}$  appears in both  $A_k$  and  $B_k$ . Therefore, it follows from differentiating the residual function that

$$J^{k,k+1} = \frac{1}{2}(\beta + 4c_x + C_k + D_k) = \tilde{J}^{k,k+1} + \frac{C_k}{2},$$

where  $\tilde{J}^{k,k+1}$  denotes the original Jacobian entry for this position in the matrix. Under similar arguments, it is easy to verify that

$$J^{k,\ell} = \tilde{J}^{k,\ell} + \frac{C_k}{2}, \text{ for } \ell = k-1, k-N, k \pm 2N,$$

and we note that  $F'_{m,m+N}$  does not exist for this special case. Moreover, we derived  $J^{k,k-N}$  by using the expression for  $B_k$  when  $n = k-N$ . These contributions are trivial since we only have to differentiate a linear function. However, if we consider  $J^{k,k+N+1}$ , we find that the residual function is quadratic in the variable we wish to differentiate with respect to, and so the unknown will appear in the Jacobian term.

However, with some algebraic manipulation, it is easy to eliminate this contribution and show that the pattern remains consistent. Mathematically, we can use the trick of adding zero, i.e.,

$$\begin{aligned}
 J^{k,k+1+N} &= \frac{\partial}{\partial \Psi^{k+N+1}} \left[ - \left( c_x + \frac{S_{k+1+N} - \Psi^{k-N}}{2} - \frac{\Psi^{k+1+N}}{2} \right) \left( C_k - \frac{\Psi^{k+1+N}}{2} + \frac{\Psi^{k+1+N}}{2} \right) \right. \\
 &\quad \left. + A_k D_k + (\beta + 4c_x) A_k \right] \\
 &= \frac{A_k}{2} + \frac{C_k}{2} - \frac{1}{2} \left( c_x + \frac{S_{k+1+N} - \Psi^{k-N}}{2} \right) + \frac{\Psi^{k+1+N}}{4} \\
 &= \frac{1}{2} (A_k - B_k - c_x + C_k) \\
 &= \tilde{J}^{k,k+1+N} + \frac{C_k}{2},
 \end{aligned}$$

which is reminiscent of what we have already seen. This pattern carries across for every single derivative, thus, when  $\Psi_{m+N} = \Psi_{\max}$ , we can write

$$J^{k,\ell} = \tilde{J}^{k,\ell} + \frac{C_k}{2} \quad \forall \ell. \quad (8.37)$$

**Case 2:**  $\Psi_{m+N+1} = \Psi_{\max}$

In this case, we see that

$$\begin{aligned}
 C_k &= \frac{\Psi^{k+2} - \Psi^{k-2} + \Psi^M - \Psi^{k+N-1} + \Psi^{k-N+1} - \Psi^{k-N-1}}{2} \\
 &= \begin{cases} -\Psi^{k-2} + S_n - \Psi^{k+N-1} + \Psi^{k-N+1} - \Psi^{k-N-1}, & n = k+2, \\ \Psi^{k+2} - 2\Psi^k + S_n - \Psi^{k+N-1} + \Psi^{k-N+1} - \Psi^{k-N-1}, & n = k-2, \\ \Psi^{k+2} - \Psi^{k-2} + S_n - 2\Psi^n + \Psi^{k-N+1} - \Psi_{k-N-1}, & n = k+N-1, \\ \Psi^{k+2} - \Psi^{k-2} + S_n - \Psi^{k+N-1} - \Psi^{k-N-1}, & n = k-N+1, \\ \Psi^{k+2} - \Psi^{k-2} + S_n - \Psi^{k+N-1} + \Psi^{k-N+1} - 2\Psi^n, & n = k-N-1, \\ \Psi^{k+2} - \Psi^{k-2} + S_n - \Psi^n - \Psi^{k+N-1} + \Psi^{k-N+1} - \Psi^{k-N-1}, & \text{otherwise,} \end{cases}
 \end{aligned}$$

$$D_k = \frac{\Psi^M - \Psi^{k-N+1} + \Psi^{k+N-1} - \Psi^{k-N-1} + \Psi^{k+2N} - \Psi^{k-2N}}{2}$$

$$= \begin{cases} S_n - 2\Psi^n + \Psi^{k+N-1} - \Psi^{k-N-1} + \Psi^{k+2N} - \Psi^{k-2N}, & n = k - N + 1, \\ S_n - \Psi^{k-N+1} - \Psi^{k-N-1} + \Psi^{k+2N} - \Psi^{k-2N}, & n = k + N - 1, \\ S_n - \Psi^{k-N+1} + \Psi^{k+N-1} - 2\Psi^n + \Psi^{k+2N} - \Psi^{k-2N}, & n = k - N - 1, \\ S_n - \Psi^{k-N+1} + \Psi^{k+N-1} - \Psi^{k-N-1} - \Psi^{k-2N}, & n = k + 2N, \\ S_n - \Psi^{k-N+1} + \Psi^{k+N-1} - \Psi^{k-N-1} + \Psi^{k+2N} - 2\Psi^n, & n = k - 2N, \\ S_n - \Psi^n - \Psi^{k-N+1} + \Psi^{k+N-1} - \Psi^{k-N-1} + \Psi^{k+2N} - \Psi^{k-2N}, & \text{otherwise,} \end{cases}$$

which is clearly more complicated in comparison to how we expressed  $B_k$  for the previous special case. Regardless, the mathematics is essentially the same, as we shall see. If we consider  $J^{k,k+1}$ , then we notice that our residual function is nonlinear in  $\Psi^{k+1}$ , yielding the calculation

$$\begin{aligned} J^{k,k+1} &= \frac{\partial}{\partial \Psi^{k+1}} \left[ - (c_x + B_k) \left( C_k + \frac{\partial \Psi^{k+1}}{2} - \frac{\partial \Psi^{k+1}}{2} \right) + A_k \left( D_k + \frac{\partial \Psi^{k+1}}{2} - \frac{\partial \Psi^{k+1}}{2} \right) \right. \\ &\quad \left. + (\beta + 4c_x) A_k \right] \\ &= \frac{\beta + 4c_x}{2} - \frac{(c_x + B_k)}{2} + \frac{\Psi^{k+1}}{2} + \frac{1}{2} \left( D_k - \frac{\Psi^{k+1}}{2} \right) - \frac{\Psi^{k-1}}{4} \\ &= \frac{1}{2} \left( A_k - B_k + D_k + \beta + 3c_x \right) \\ &= \tilde{J}^{k,k+1} + \frac{1}{2} (A_k - B_k + c_x). \end{aligned}$$

Similarly to what we found previously, this pattern appears throughout each of the calculations after some algebraic manipulation. However, there are two elements of this row where the pattern does not apply, those being  $J^{k,k+2}$  and  $J^{k,k+2N}$ . This is a consequence of the integral constraint eliminating these elements from the residual function and the derivatives evaluating to zero. Therefore, we can express the Jacobian elements for this row as

$$J^{k,\ell} = \begin{cases} \tilde{J}^{k,\ell} + \frac{1}{2} (A_k - B_k - c_x), & \ell \neq k+2, k+2N, \\ 0 & \ell = k+2, k+2N. \end{cases} \quad (8.38)$$

Now that we have addressed these two particular cases, we summarise the remaining entries as follows:

$$\Psi^{k+1} = \Psi^M : J^{k,\ell} = \tilde{J}^{k,\ell} - \frac{1}{2} (D_k + \beta + 2c_x) \quad \forall \ell, \quad (8.39)$$

$$\Psi^{k-1} = \Psi^M : J^{k,\ell} = \tilde{J}^{k,\ell} + \frac{1}{2}(D_k + \beta + 2c_x) \quad \forall \ell, \quad (8.40)$$

$$\Psi^{k+N} = \Psi^M : J^{k,\ell} = \tilde{J}^{k,\ell} + \frac{C_m}{2} \quad \forall \ell, \quad (8.41)$$

$$\Psi^{k-N} = \Psi^M : J^{k,\ell} = \tilde{J}^{k,\ell} - \frac{C_m}{2} \quad \forall \ell, \quad (8.42)$$

$$\Psi^{k+1+N} = \Psi^M : J^{k,\ell} = \begin{cases} \tilde{J}^{k,\ell} + \frac{1}{2}(A_k - B_k - c_x), & \ell \neq k+2, k+2N, \\ 0 & \text{otherwise,} \end{cases} \quad (8.43)$$

$$\Psi^{k+1-N} = \Psi^M : J^{k,\ell} = \begin{cases} \tilde{J}^{k,\ell} - \frac{1}{2}(A_k + B_k + c_x), & \ell \neq k+2, k-2N, \\ 0 & \text{otherwise,} \end{cases} \quad (8.44)$$

$$\Psi^{k-1+N} = \Psi^M : J^{k,\ell} = \begin{cases} \tilde{J}^{k,\ell} + \frac{1}{2}(A_k + B_k + c_x), & \ell \neq k-2, k+2N, \\ 0 & \text{otherwise,} \end{cases} \quad (8.45)$$

$$\Psi^{k-N-1} = \Psi^M : J^{k,\ell} = \begin{cases} \tilde{J}^{k,\ell} + \frac{1}{2}(-A_k + B_k + c_x), & \ell \neq k-2, k-2N, \\ 0 & \text{otherwise,} \end{cases} \quad (8.46)$$

$$\Psi^{k+2} = \Psi^M : J^{k,\ell} = \tilde{J}^{k,\ell} - \frac{1}{2}(B_k + c_x) \quad \forall \ell, \quad (8.47)$$

$$\Psi^{k-2} = \Psi^M : J^{k,\ell} = \tilde{J}^{k,\ell} + \frac{1}{2}(B_k + c_x) \quad \forall \ell, \quad (8.48)$$

$$\Psi^{k+2N} = \Psi^M : J^{k,\ell} = \tilde{J}^{k,\ell} + \frac{A_k}{2} \quad \forall \ell, \quad (8.49)$$

$$\Psi^{k-2N} = \Psi^M : J^{k,\ell} = \tilde{J}^{k,\ell} - \frac{A_k}{2} \quad \forall \ell. \quad (8.50)$$

In summary, the majority of the Jacobian is sparse and defined by the original elements we derived. A special feature of incorporating the integral constraint is that 12 dense rows are now scattered throughout the matrix and defined by the special cases we discussed in this chapter. In particular, the dense rows are defined for the following values of  $k$ :

$$k+1 = M \implies k = M-1 \text{ (final row),}$$

$$k-1 = M \implies k = M+1 = 2,$$

$$k+N = M \implies k = M-N,$$

$$k-N = M \implies k = M+N = N+1,$$

$$k+1+N = M \implies k = M-N-1,$$

$$k+1-N = M \implies k = M+N-1 = N,$$

$$k-1+N = M \implies k = M-N+1,$$

$$k - 1 - N = M \implies k = M + N + 1 = N + 2,$$

$$k + 2 = M \implies k = M - 2,$$

$$k - 2 = M \implies k = M + 2 = 3,$$

$$k + 2N = M \implies k = M - 2N,$$

$$k - 2N = M \implies k = M + 2N = 2N + 1,$$

as a consequence of the doubly-periodic boundary conditions. Hence, if we assume that unknown solutions we wish to seek satisfy certain integral constraints, akin to (8.35), then we can adjust the Jacobian structure in a similar way to how we have for the LRD initialisation.

In theory, this construction should return the LRD steady state profile, if it is used as an initial input when inverting (8.7). However, when executing our algorithm numerically, convergence is not achieved. Indeed, there could be an error in our derivation, though we believe our ill convergence is a consequence of high resolution being needed to extract fields accurately. Despite Newton's method being quadratically convergent, this is only true provided the Jacobian matrix is nonsingular. In the case of the LRD, horizontal derivatives of PVA at the separatrix are not all continuous, and so this results in a singular Jacobian. In this case, Newton's method is lucky to achieve linear convergence and could potentially never see convergence.

A means of handling discontinuities in derivatives at the separatrix could involve employing higher resolution when constructing the Jacobian and residual function. Unfortunately, the Jacobian sees growth according to  $\mathcal{O}(N^4)$ , and so the task of inverting such a large matrix becomes computationally taxing extremely quickly. From our linear stability results in Chapter 5, we observed that the minimum grid resolution required to extract the critical mode pattern was  $N = 512$ . This expensive computational task is outside the scope of this thesis, but it would be interesting to apply this method using a supercomputer.

## 8.3 Summary

In this chapter, we derived a finite-different Newton-Raphson method to solve for steady state solutions in various QG frameworks. The intention behind this was to apply our linear stability methodology used in Chapter 5 to a variety of steady state solutions that are not known analytically. To optimise the solver for extracting LRD

type solutions (not necessarily with circular separatrix), we incorporated an integral constraint into the nonlinear solver that is satisfied by the LRD. After some tedious mathematical manipulations, we showed that the Jacobian has a nonzero diagonal structure with 12 dense rows throughout the matrix.

Unfortunately, we were unable to extract steady states using this methodology, which appears to be a consequence of the limited resolution we can employ with the computational resources we have access to. It would be interesting to apply our method with high resolution to a series of known perturbed steady state solutions on a supercomputer to confirm whether or not the theory we have derived is correct.

With the two-layer QG equations being introduced in this chapter, we can consider a different class of geophysical stability problems that we were unable to in the 1.5-layer setting, those being the stability of fluid flows over topographic features. This subject will be what we discuss in detail in Chapter 9.



# Chapter 9

## Sinusoidal topographic flows

The majority of work presented in this chapter appears in the following publication to the Journal of Fluid Mechanics: '*Linear stability analysis for flows over sinusoidal bottom topography*', by J. Davies, H. Khatri and P. Berloff.

In this chapter, we investigate how a variable ocean bottom affects the most unstable linear modes in a baroclinic QG framework. For this purpose, we consider sinusoidal topographic variation in both zonal and meridional directions separately, and carry out the corresponding linear stability analyses. The effects of large-scale topography on baroclinic instability is explored and compared with small-scale sinusoidal topography studies

### 9.1 Two-layer QG approximation

For the purpose of our investigation, we choose the QG approximation as our analysis framework. This is motivated by other circulation models being computationally taxing to work with and Radko (2020a) suggesting similarity between the shallow-water and QG responses. Despite this, we expect significant differences to present themselves in more realistic model configurations, hence extending into the primitive equations is desirable for future research. Regardless, these differences will only be significant in the nonlinear regime, meaning the use of QG is sufficient for carrying out our linear stability analyses. Moreover, shallow-water and primitive equations are more appropriate in the case of small-scale topography, since the QG approximation can break down as a consequence of the topographic beta term seeing considerable increase relative to the planetary beta term.

Mathematically, we implement a two-layer rigid-lid model on an  $(\hat{x}, \hat{y})$ -Cartesian beta-plane with bottom topography allowed to vary (a schematic is shown in Fig.

9.1), which we denote by  $\hat{\eta}_b(\hat{x}, \hat{y})$ . To perform our analysis, we assume a zonally uniform background flow,  $\hat{U}$ , in the surface layer, with the abyssal layer remaining at rest. Our motivation behind considering a vertical velocity shear is to induce baroclinic instability in the system. The QG equations of interest can be written in the full nonlinear form

$$\frac{\partial \hat{\Pi}_j}{\partial \hat{t}} + \mathbb{J}(\hat{\psi}_j - \delta_{1j} \hat{U} \hat{y}, \hat{\Pi}_j) = \hat{\nu} \hat{\nabla}^4 \hat{\psi}_j - \delta_{2j} \hat{\gamma} \hat{\nabla}^2 \hat{\psi}_j, \quad (9.1)$$

the derivation of which can be found in Vallis (2017). The indices  $j = 1, 2$  refer to the reference layer (the top layer corresponds to  $j = 1$  and the bottom layer corresponds to  $j = 2$ ). The layer-wise streamfunction is denoted by  $\hat{\psi}_j$ ,  $\delta_{ij}$  denotes the Kronecker delta. The parameters  $\hat{\nu}$  and  $\hat{\gamma}$  represent eddy viscosity and bottom friction, respectively, and the layer-wise PV is given by

$$\hat{\Pi}_j = \underbrace{\hat{\nabla}^2 \hat{\psi}_j + \hat{S}_j(\hat{\psi}_{3-j} - \hat{\psi}_j)}_{\text{PVA, } \hat{q}_j} + \left[ \hat{\beta} + \hat{S}_j \hat{U} (\delta_{1j} - \delta_{1,3-j}) \right] \hat{y} + \frac{\delta_{2j} \hat{f}_0 \hat{\eta}_b}{\hat{H}_j}. \quad (9.2)$$

In our definition for the full PV field, we have the layer-wise stratification parameter,  $\hat{S}_j = \hat{f}_0^2 / \hat{g}' \hat{H}_j$ , with reduced gravity defined in terms of layer-wise density anomalies and gravitational acceleration, i.e.,  $\hat{g}' = \hat{g} \Delta \hat{\rho} / \hat{\rho}_1$ ,  $\Delta \hat{\rho} = \hat{\rho}_2 - \hat{\rho}_1$  and  $\hat{H}_j$  corresponds to the mean layer depths. Moreover,  $\hat{\beta}$  is the meridional gradient of the Coriolis parameter,  $\hat{f} = \hat{f}_0 + \hat{\beta} \hat{y}$ , where  $\hat{f}_0$  is the angular velocity due to the Earth's rotation at some reference latitude. Similar to Chapter 2, dimensional quantities are notated with hats. Hereinafter, we neglect terms due to eddy viscosity and bottom friction as they do not have any major effects on our linear stability results.

### 9.1.1 Nondimensionalisation

To highlight the key parameter values in our stability analysis, we nondimensionalise (9.1). When considering the dipole propagation, it was natural to choose length and velocity scales characterising the vortex translation. However, in this instance we introduce the horizontal length scale  $\hat{L}_H = \hat{L} / 2\pi$ , where the zonal and meridional length of the domain is  $\hat{L} = \hat{L}_x = \hat{L}_y$ , and the presence of  $2\pi$  acts to normalise angular frequencies and wavenumbers later on. More specifically, we choose  $\hat{L} = \sqrt{\hat{g} \hat{H} / \hat{f}_0}$ , where we have  $\hat{H} = \sum_{i=1}^2 \hat{H}_i$  defining the sum of the mean layer depths. In addition, we choose  $\hat{L}_V = \hat{H}$ ,  $\hat{T} = 1 / \hat{f}_0$  and  $\hat{V} = \hat{f}_0 \hat{L} / 2\pi$  to be our vertical length scale, time scale and velocity scale, respectively. In summary, we introduce

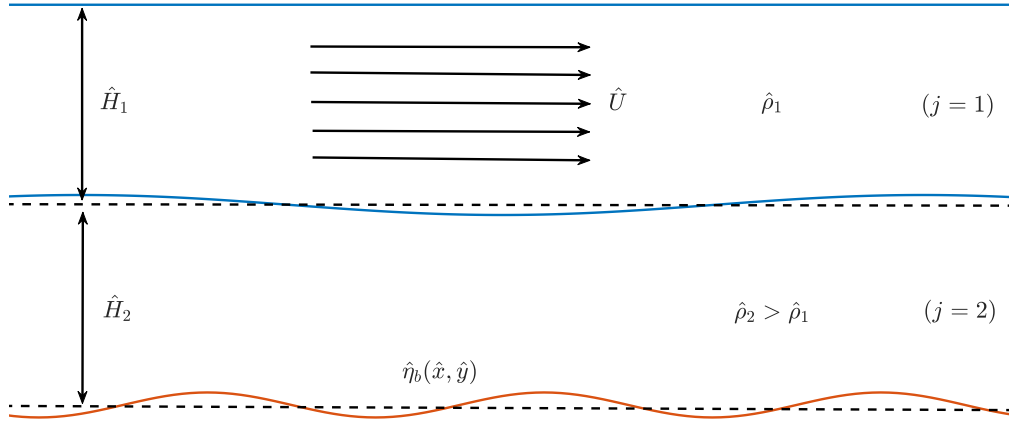


**Figure 9.1:** The model domain for the two-layer problem. An eastward background velocity is imposed in the surface layer, with the bottom layer assumed to be at rest. Bottom topography, mean layer depths and density anomalies are denoted by  $\hat{\eta}_b$ ,  $\hat{H}_j$  and  $\hat{\rho}_j$ , respectively ( $j = 1, 2$  is the layer index). The positive  $\hat{x}$ -axis is directed to the right and the positive  $\hat{y}$ -axis points into the figure.

the following nondimensional transformation:

$$(\hat{x}, \hat{y}) = \frac{\hat{L}}{2\pi}(x, y), \quad \hat{t} = \frac{t}{\hat{f}_0}, \quad \hat{U} = \frac{\hat{f}_0 \hat{L}}{2\pi} U, \quad \hat{\psi}_j = \frac{\hat{f}_0 \hat{L}^2}{4\pi^2} \psi_j, \quad \hat{\eta}_b = \hat{H} \eta_b, \quad (9.3)$$

where the dimensionless quantities we have introduced are notated without hats. Therefore, applying (9.3) to (9.1), we obtain a nondimensional system of the form

$$\frac{\partial \Pi_j}{\partial t} + \mathbb{J}(\psi_j - \delta_{1j} U y, \Pi_j) = 0, \quad (9.4)$$

where we define the nondimensional PV as

$$\Pi_j = \nabla^2 \psi_j + S_j (\psi_{3-j} - \psi_j) + \left[ \beta + S_j U (\delta_{1j} - \delta_{1,3-j}) \right] y + \frac{\delta_{2j} \hat{H} \eta_b}{\hat{H}_j}, \quad (9.5)$$

with  $\beta = \hat{L} \hat{\beta} / 2\pi \hat{f}_0$  and  $S_j = \hat{L}^2 \hat{S}_j / 4\pi^2$ .

### 9.1.2 Linearised model with sinusoidal topography

By applying the method of linearisation to (9.4), we obtain the linearised system of equations

$$\left( \frac{\partial}{\partial t} + \delta_{1j} U \frac{\partial}{\partial x} \right) q_j + \frac{\partial \psi_j}{\partial x} \left[ \beta + S_j U (\delta_{1j} - \delta_{1,3-j}) + \frac{\delta_{2j} \hat{H}}{\hat{H}_j} \frac{\partial \eta_b}{\partial y} \right] - \frac{\delta_{2j} \hat{H}}{\hat{H}_j} \frac{\partial \psi_j}{\partial y} \frac{\partial \eta_b}{\partial x} = 0, \quad (9.6)$$

with the nondimensional PVA given by

$$q_j = \nabla^2 \psi_j + S_j (\psi_{3-j} - \psi_j). \quad (9.7)$$

To formulate the stability problem in the presence of sinusoidal bottom topography, we assume for simplicity that the bottom irregularities in question are either zonal or meridional, but never both. With this in mind, we define both sinusoidal zonally oriented multiple ridges (ZR),

$$\hat{\eta}_b = \hat{\mathcal{A}} \sin(\hat{\alpha} \hat{y}), \quad (9.8a)$$

and sinusoidal meridionally oriented multiple ridges (MR),

$$\hat{\eta}_b = \hat{\mathcal{A}} \sin(\hat{\alpha} \hat{x}), \quad (9.8b)$$

where  $\hat{\mathcal{A}} = \hat{H} \mathcal{A}$  and  $\hat{\alpha} = 2\pi\alpha/\hat{L}$  are amplitude and wavenumber parameters, respectively, for sinusoidal ridges (see Fig. 9.2). It is useful to think about the nondimensional value of  $\alpha$  as the number of topographic ridges under consideration (increasing this value amounts to decreasing ridge width). Clearly, it follows that the nondimensional forms of the bottom topographies can be written as

$$\eta_b = \begin{cases} \mathcal{A} \sin(\alpha y) & \text{(ZR),} \\ \mathcal{A} \sin(\alpha x) & \text{(MR).} \end{cases}$$

In our assumption, we consider sinusoidal bottom irregularities with a single wavelength only. Despite this appearing simple in comparison to the real ocean bathymetry, the method described has the benefit of being applicable to any periodic topographic features.

On substituting (9.8a) and (9.8b) into (9.6), we can derive the following systems

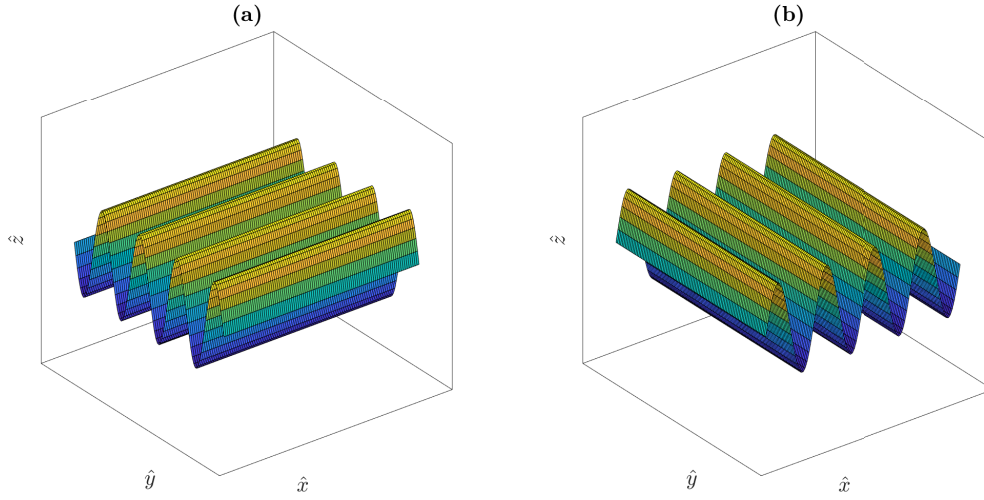


**Figure 9.2:** Sinusoidal topographies considered in our analysis. (a): zonally oriented multiple ridges (ZR), (b): meridionally oriented multiple ridges (MR).

in terms of perturbation streamfunctions and PV fields:

$$\left( \frac{\partial}{\partial t} + \delta_{1j} U \frac{\partial}{\partial x} \right) q_j + \frac{\partial \psi_j}{\partial x} \left[ \beta + S_j U (\delta_{1j} - \delta_{1,3-j}) + \frac{\delta_{2j} \hat{H} \mathcal{A} \alpha \cos(\alpha y)}{\hat{H}_j} \right] = 0, \quad (9.9a)$$

$$\left( \frac{\partial}{\partial t} + \delta_{1j} U \frac{\partial}{\partial x} \right) q_j + \frac{\partial \psi_j}{\partial x} \left[ \beta + S_j U (\delta_{1j} - \delta_{1,3-j}) \right] - \frac{\delta_{2j} \hat{H} \mathcal{A} \alpha \cos(\alpha x)}{\hat{H}_j} \frac{\partial \psi_j}{\partial y} = 0, \quad (9.9b)$$

for ZR and MR, respectively (see Fig. 9.2).

A caveat of our analysis is that it is concerned with uniform zonal flows only, despite it being known that topography generally has a significant impact on the horizontal orientation of the flow as well. For example, a purely zonal flow is less likely to occur over a zonally-varying topography as the flow tends to move meridionally over topographic features in order to conserve PV (e.g. see [Thompson, 2010](#); [Boland et al., 2012](#)). Despite this insight, we restrict our attention to zonal background flows for the sake of simplicity, and recommend the reader to refer to [Smith \(2007\)](#) if interested in nonzonal background flows.

### 9.1.3 Formulating the eigenvalue problem

The presence of variable topographic features introduces the product of topography with the perturbation streamfunction in the linearised system, and consequently

requires us to solve a generalised eigenvalue problem for the purpose of investigating linear instability. For example, the topography study [LaCasce et al. \(2019\)](#) applied Chebyshev grid discretisation in the meridional direction. Indeed, we could investigate the influence bottom irregularities have on baroclinic instability by discretising the linearised equations with respect to physical space in the direction of changes in ridge height. This means of approach derives a complex eigenvalue problem with coupled eigenmodes; e.g., [Berloff and Kamenkovich \(2013\)](#); [Khatri and Berloff \(2019\)](#) used finite-differences to study the stability of multiple jets and we employed a linear stability analysis using finite-differences in Chapter 5. However, this technique is computationally taxing, as it is relatively sensitive to the numerical grid resolution, meaning finer grids are normally required to achieve convergent results.

In our approach, we adopt the method of spectral discretization in terms of Fourier modes; applied in both spatial directions, and from this construct an eigenvalue matrix in terms of Fourier eigenmodes (see Appendix D for derivation details). Since the problem introduces a length scale for topography, the eigenmodes in the direction of varying topography become coupled. For example, in the case of a topography changing in the meridional direction only, our approach would yield a complex eigenproblem having coupled eigenmodes along the meridional wavenumber for every zonal wavenumber. The main advantage of this is that it can be used for any periodic topography, and the only limiting assumptions of the QG approximation are the restrictions on the variable bottom features we are allowed to consider. Furthermore, the method is computationally efficient since the derived linear stability problem can be solved with a limited number of wavenumbers, provided that baroclinic instability is adequately resolved with the spectral method implemented.

To proceed, we consider Fourier solutions of the form

$$\psi_j(x, y, t) = \sum_{k, \ell} \phi_j(k, \ell) e^{i(kx + \ell y - \omega t)}, \quad (9.10)$$

where  $\phi_j = \phi_j(k, \ell)$  is the nondimensional amplitude of the perturbation streamfunction,  $(k, \ell)$  is the nondimensional horizontal wavevector and  $\omega$  is the nondimensional eigenfrequency. Under this ansatz, the PV anomaly can be rewritten as

$$q_j = \sum_{k, \ell} \underbrace{\left[ S_j \phi_{3-j} - (k^2 + \ell^2 + S_j) \phi_j \right]}_{\tilde{q}_j} e^{i(kx + \ell y - \omega t)},$$

and so it follows that (9.9a) and (9.9b) become

$$\sum_{k,\ell} \left\{ (\omega - \delta_{1j}kU)\tilde{q}_j - k\phi_j \left[ \beta + S_jU(\delta_{1j} - \delta_{1,3-j}) + \frac{\delta_{2j}\hat{H}\mathcal{A}\alpha \cos(\alpha y)}{\hat{H}_j} \right] \right\} e^{i(kx+\ell y-\omega t)} = 0, \quad (9.11a)$$

$$\sum_{k,\ell} \left\{ (\omega - \delta_{1j}kU)\tilde{q}_j - k\phi_j \left[ \beta + S_jU(\delta_{1j} - \delta_{1,3-j}) \right] + \frac{\delta_{2j}\hat{H}\mathcal{A}\alpha \ell \cos(\alpha x)\phi_j}{\hat{H}_j} \right\} e^{i(kx+\ell y-\omega t)} = 0. \quad (9.11b)$$

We can further simplify (9.11a) and (9.11b) by introducing the cosine functions in exponential form. In the case of (9.11a), this yields

$$\begin{aligned} \sum_{k,\ell} \left\{ (\omega - \delta_{1j}kU)\tilde{q}_j - k\phi_j \left[ \beta + S_jU(\delta_{1j} - \delta_{1,3-j}) \right] e^{i(kx+\ell y-\omega t)} \right. \\ \left. - \frac{\delta_{2j}\hat{H}\mathcal{A}\alpha k\phi_j}{2\hat{H}_j} \left[ e^{i(kx+(\ell+\alpha)y-\omega t)} + e^{i(kx+(\ell-\alpha)y-\omega t)} \right] \right\} = 0. \end{aligned} \quad (9.12)$$

In order to eliminate the exponential dependence, we introduce the transformation  $\ell + \alpha \rightarrow \ell$  in the first exponential term on the second line, and  $\ell - \alpha \rightarrow \ell$  in the second exponential term on the second line, so that each term shares a common exponential contribution. Thus, following a similar procedure for both (9.11a) and (9.11b) (we make the transformation  $k \pm \alpha \rightarrow k$ ), it is possible to eliminate exponential terms to obtain the set of eigenproblems

$$\begin{aligned} k \left[ \beta + S_jU(\delta_{1j} - \delta_{1,3-j}) - \delta_{1j}U(k^2 + \ell^2 + S_j) \right] \phi_j + \delta_{1j}kUS_j\phi_{3-j} \\ + \frac{\delta_{2j}\hat{H}\mathcal{A}\alpha k}{2\hat{H}_j} \left[ \phi_j(k, \ell - \alpha) + \phi_j(k, \ell + \alpha) \right] = \omega \left[ S_j\phi_{3-j} - (k^2 + \ell^2 + S_j)\phi_j \right], \end{aligned} \quad (9.13a)$$

$$\begin{aligned} k \left[ \beta + S_jU(\delta_{1j} - \delta_{1,3-j}) - \delta_{1j}U(k^2 + \ell^2 + S_j) \right] \phi_j + \delta_{1j}kUS_j\phi_{3-j} \\ - \frac{\delta_{2j}\hat{H}\mathcal{A}\alpha \ell}{2\hat{H}_j} \left[ \phi_j(k - \alpha, \ell) + \phi_j(k + \alpha, \ell) \right] = \omega \left[ S_j\phi_{3-j} - (k^2 + \ell^2 + S_j)\phi_j \right], \end{aligned} \quad (9.13b)$$

for both ZR and MR, respectively (see Fig. 9.2). The motivation behind this approach is inspired by the work carried out in Lorenz (1972), where the same technique was used to study the stability of Rossby waves on a steady zonal background flow.

We can see that the presence of sinusoidal topography leads to a phase shift resulting in the coupling of individual eigenmodes. As a consequence of this, the

Symbol	Value	Dimensional	Nondimensional
$\hat{L}$	Domain size	2725 km	$2\pi$
$\hat{H}_j$	Layer depths	2 km	0.5
$\hat{U}$	Background flow	5 cm s <sup>-1</sup>	$1.586 \times 10^{-3}$
$\hat{f}_0$	Coriolis parameter	$7.27 \times 10^{-5}$ s <sup>-1</sup>	1
$\hat{\beta}$	Coriolis gradient	$2 \times 10^{-11}$ m <sup>-1</sup> s <sup>-1</sup>	0.1193
$\hat{S}_j$	Stratification	$8 \times 10^{-10}$ m <sup>-2</sup>	150.449
$\hat{\lambda}$	Rossby scale	25 km	$5.764 \times 10^{-2}$
$\hat{A}$	Ridge amplitude	200 – 800 m	0.05 – 0.2
$\hat{\alpha}$	Ridge wavenumber	$2.3 \times 10^{-6} - 9.2 \times 10^{-5}$ m <sup>-1</sup>	1 – 40
$\hat{L}_{\text{Top}}$	Ridge width	68.125 – 2725 km	$\pi/20 - 2\pi$

**Table 9.1:** Main parameter values chosen for the linear stability analysis presented in this chapter, assuming equal layer depths. Alternative parameter values used are mentioned in the main text.

linear stability problem becomes numerically expensive to solve. Even considering ZR and MR separately, we are required to solve matrices of size  $2N \times 2N$ , where  $N$  is the number of wavenumbers used in our analysis in each horizontal direction. Furthermore, when the topographic variability is a two-dimensional function in space, the resulting matrices are of size  $4N^2 \times 4N^2$ , which is an extremely expensive problem to solve. The study [Shevchenko et al. \(2016\)](#) offers methodology that can be used to work with extremely large linear stability problems, however, this requires a supercomputer and exceeds the expectations of this thesis. Hence, we handle zonal and meridional topographies separately. Regardless, it is possible to extend our approach to sinusoidal topographies that see variation in both directions, or other complicated periodic topographies of interest. Moreover, we expect our spectral method to outperform methods incorporating finite differences, since spectral approaches typically require fewer wavenumbers to achieve convergent results.

## 9.2 Results

### 9.2.1 Parameter justifications

To carry out our analysis, we must decide on how to truncate our Fourier series solutions. Since these series sum to infinity, truncation discards information about the higher order modes. Therefore, we look to consider as many wavenumbers as needed for numerical convergence of the spectral coefficients, as well as staying



within the range of the most unstable modes due to baroclinic instability.

A detailed breakdown of parameters used in our experiments is presented in table 9.1. For the sake of simplicity, we reduce the number of parameters in our problem by assuming that layer depths are equal, i.e.,  $\hat{H}_1 = \hat{H}_2 = \hat{H}_*$ , such that the total fluid depth is given by  $\hat{H} = 2\hat{H}_*$ , or equivalently, the stratification parameters in each fluid layer can be simplified as  $S_1 = S_2 = S_*$ . Following this, the coefficients of the topographic contribution in (9.13a) and (9.13b) become  $\mathcal{A}\alpha k$  and  $-\mathcal{A}\alpha\ell$ , respectively. We choose the stratification parameter such that the baroclinic Rossby radius,  $\hat{\lambda} = (2\hat{S}_*)^{-1/2} = 25$  km, which is reflective of the mid-latitude ocean (Chelton et al., 1998). From table 9.1, it is clear that the length and width of the horizontal domain can be expressed as  $\hat{L}_x = \hat{L}_y = 109\hat{\lambda}$ . The values of  $\hat{f}_0$  and  $\hat{\beta}$  used correspond to a latitude of  $30^\circ$  in the northern hemisphere, consistent with values used in Chapter 3.

Since we are making use of the QG approximation, it is easy to show that the nondimensional velocity in the surface layer must satisfy  $U \ll 1$  in order to achieve a small value for the Rossby number. In the two-layer framework, it is well-known that the PV gradient must have opposite sign between fluid layers for instability to occur (Pedlosky, 1964); from which the critical velocity in a flat-bottom ocean can be approximated to be  $U_c \sim 7.930 \times 10^{-4}$  (see Appendix C for further details). Thus, we choose a background velocity of value  $U = 1.586 \times 10^{-3}$  since this corresponds to  $5 \text{ cm s}^{-1}$  in dimensional form and this choice is guaranteed to force baroclinic instability in the system.

Additionally, both small topographic amplitudes relative to the deep layer thickness and gentle topographic gradients are required for the QG predictions to hold. Despite this, our analysis deals with large topography considerations. In particular, the most extreme case investigated assumes  $\alpha = 40$  and  $\mathcal{A} = 0.2$ , resulting in  $\mathcal{A}\alpha = 8$ , which is roughly 60 times greater than  $\beta = 0.1193$ . This can be interpreted as the topography contribution in (9.9b) dominating the  $\beta$  contribution. This definitely challenges the QG limit. Nonetheless, we consider these larger scales to analyse unstable modes for a broad range of wavenumbers. This is motivated by some studies demonstrating that the QG approximation can still do a reasonable job describing geophysical systems outside of the strict QG limitations (Williams et al., 2010).

Throughout this analysis, we compare our results for topographic length scales similar to or much greater than the baroclinic Rossby deformation scale, with the results of Benilov (2001) and Radko (2020a), which deal with length scales smaller

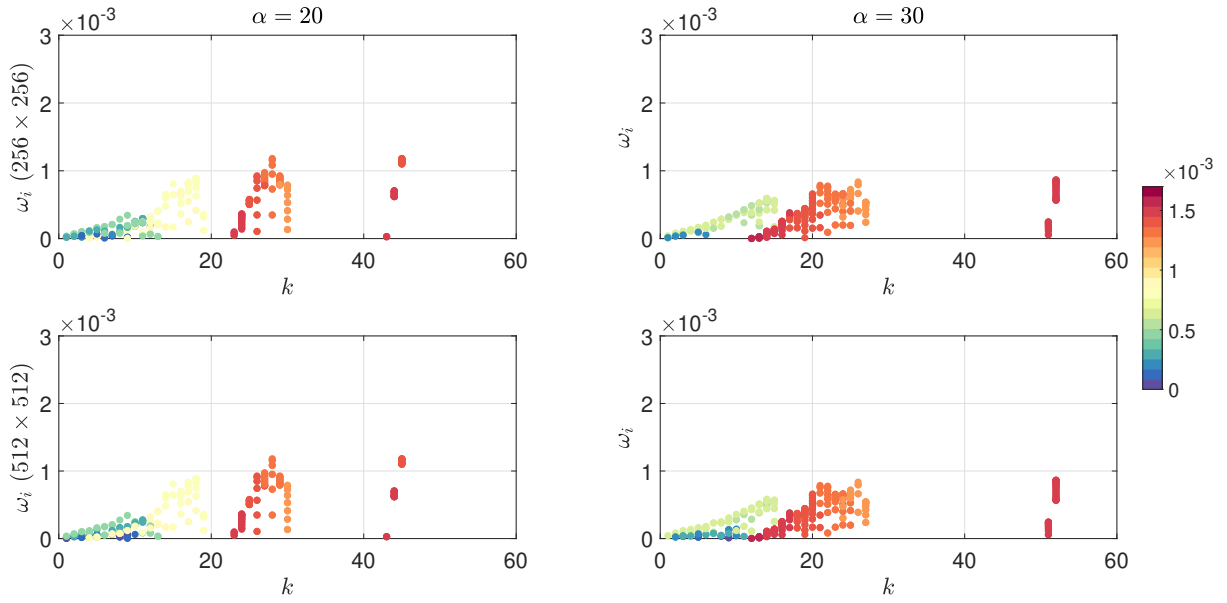


**Figure 9.3:** ZR results for  $\mathcal{A} = 0.1$  and  $\alpha = 20$  (left panels) and  $\alpha = 30$  (right panels): the top row shows results obtained using  $N = 256$ , while the bottom row shows results obtained using  $N = 512$ . Consistency in the distribution of unstable modes between grids acts as strong evidence for convergence of our linear stability results.

than the baroclinic Rossby deformation scale. The intention of this is to identify any similarities and differences between small and large scale topography effects. It is worth noting that for large-scale ridges, we could exploit the scale ratio and form some asymptotic expansion in this parameter (this would be the reciprocal of the small parameter in (Benilov, 2000a), i.e., the nondimensional equivalent of  $1/\hat{L}_{\text{Top}}$  would be assumed to be small). Applying this method would be a good way to verify our results, however, we do not present this here and leave this for future work.

Similar to our resolution analysis performed in Chapter 3, we made comparisons between solutions obtained using  $N = 128$ , 256 and 512 wavenumbers. We found some differences between the solutions with  $N = 128$  and  $N = 256$ , but the differences between the results with  $N = 256$  and  $N = 512$  were insignificant (see Fig. 9.3). In addition, the smallest resolvable wave length for  $N = 256$  is  $2\hat{L}/N \approx 20$  km, which is sufficient to resolve for baroclinic instability in our analysis. Therefore, we present solutions using  $N = 256$  in the remainder of this chapter.

### 9.2.2 Linear Stability Analysis

If we decompose  $\omega = \omega_r + i\omega_i$ , then we obtain stable solutions if  $\omega_i \leq 0$ , and unstable solutions if  $\omega_i > 0$  (note that we use different notation for linear growth in

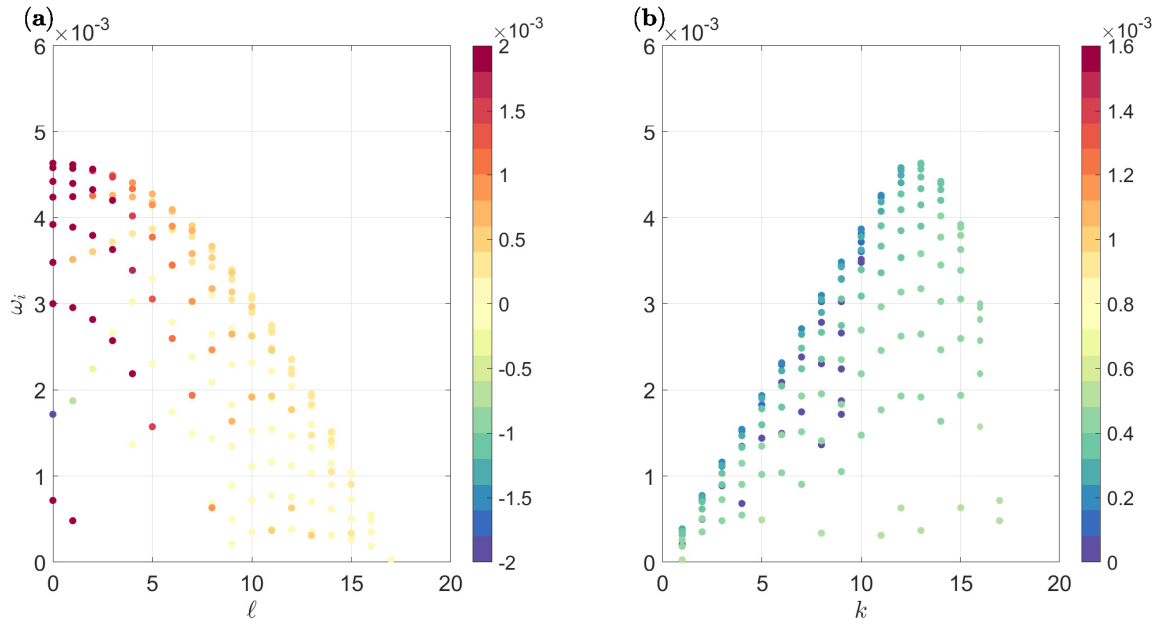


**Figure 9.4:** Nondimensional growth rates  $\omega_i > 0$  over flat topography (corresponding parameter values can be found in table 9.1). (a):  $(\omega_i, \ell)$ -plot, with meridional phase speeds  $c_y = \omega_r/\ell$  shown in the colorbar (the speed decreases with increasing  $\ell$ ). (b):  $(\omega_i, k)$ -plot, with zonal phase speeds  $c_x = \omega_r/k$  shown in the colorbar (the speed increases with increasing  $k$ ). Modes are symmetric about  $k, \ell = 0$ ; and so growth rates for only positive wavenumbers are presented.

this chapter to highlight the use of a different linear stability method to that used in Chapter 5). With this in mind, we solve the coupled eigenvalue problem (see 9.13a and 9.13b) for both ZR and MR. In the ZR (MR) case, the coupled eigenvalue problem was solved for each zonal (meridional) wavenumber separately to obtain the frequency solutions and corresponding eigenmodes. We discuss the results for a range of parameter values in the following subsections.

### A Flat Ocean Bottom

To begin our analysis, we consider the flat bottom case, for which the analytical solution is well known (Chen and Kamenkovich, 2013), and draw comparisons with results obtained in the presence of topography. For the flat bottom model, we solved (9.13a) with  $\mathcal{A} = 0$ , for every set of zonal and meridional wavenumbers  $(k, \ell)$  separately. The distribution of unstable modes (as seen in Fig. 9.4) is such that the fastest growing mode appears at  $\ell = 0$  and  $k = 13$ , with dimensionless maximum growth rate  $\omega_i = 4.632 \times 10^{-3}$  (or  $3.368 \times 10^{-7} \text{ s}^{-1}$  in dimensional form). In summary, the fastest growing mode over a flat bottom is meridionally oriented. The magnitudes of the wavenumbers corresponding to maximum growth depend on the

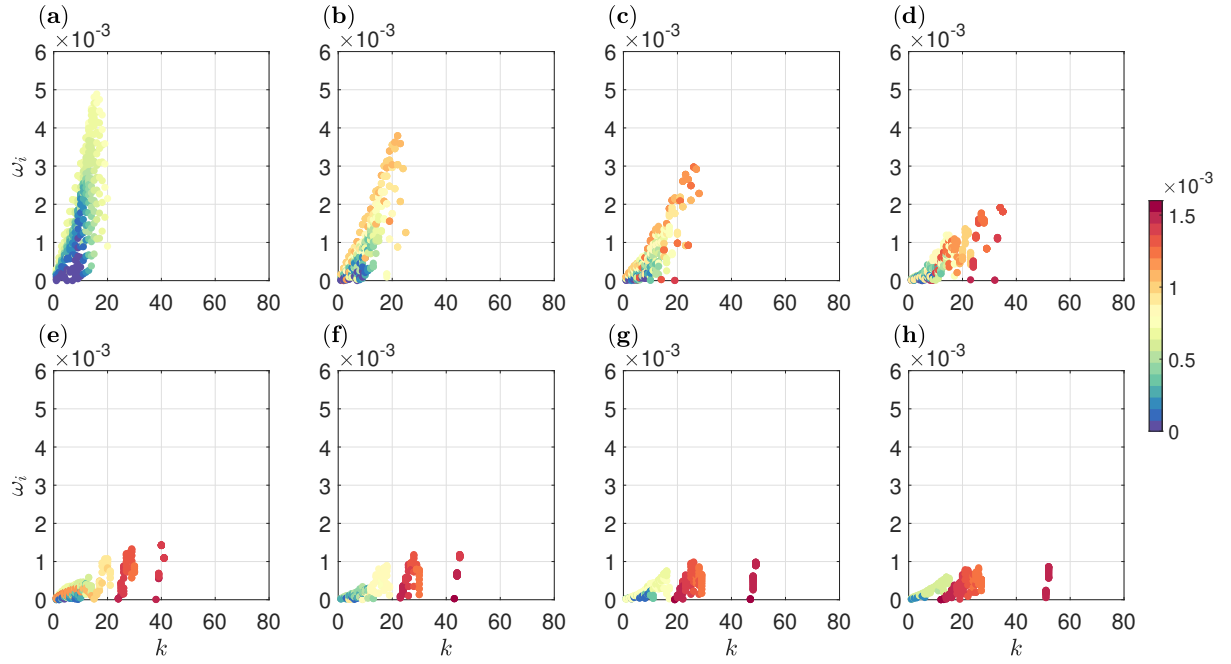


**Figure 9.5:**  $(\omega_i, k)$ -plot in the presence of ZR, with  $\mathcal{A} = 0.1$  (corresponding parameters are given in table 9.1). Subplots **a-h** assume  $\alpha = 1, 3, 5, 10, 15, 20, 25, 30$ , respectively (maximum growth decreases and modes shift towards larger wavenumbers with increasing  $\alpha$ ). Zonal phase speeds are shown in the colorbar (the speed increase with increasing  $k$  and  $\alpha$  and approach the velocity  $U$  in the upper layer, but never exceed it).

particular parameters of interest, namely the baroclinic Rossby deformation radius, the values of background velocity and the Coriolis gradient (for details, see [Berloff et al., 2009](#)). In our experiments, we assess the impacts of variable topography on both the baroclinic growth rates and the structure of the fastest growing modes.

### Zonally Oriented Multiple Ridges (ZR)

Firstly, we consider the frequency solutions in the presence of ZR (see Fig. 9.2a), which we obtained by solving (9.13a), in the  $(\omega_i, k)$ —parameter plane. This particular space is chosen since meridional wavenumbers are coupled in the presence of ZR, and so we solve the eigenproblem for all values of  $\ell$ , while keeping  $k$  fixed. Consequently, the frequency solutions can only be analysed for each zonal wavenumber. For more details of this procedure, we refer the reader to Appendix D.

In Fig. 9.5, the unstable growth rates are plotted against zonal wavenumber for  $\mathcal{A} = 0.1$  (the nondimensional topographic amplitude). The figure presents several plots, each assuming a different number of ridges (details of which are given in the figure caption). Comparing the plots in Fig. 9.5 with the corresponding flat-bottom

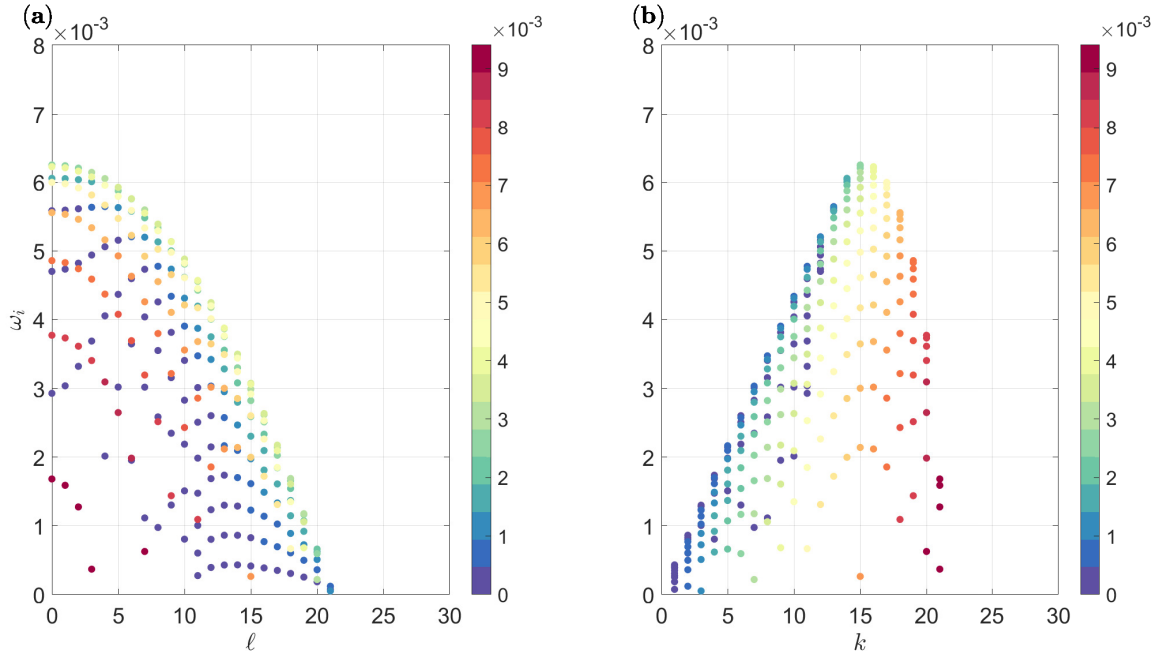


**Figure 9.6:** Unstable mode distributions for a constant topography slope in  $y$  of value equal to 0.1 (meant to correspond to the ZR case with value of  $\mathcal{A} = 0.1$  used in the study). This shows that maximum growth rate increases compared to the flat bottom case, suggesting that for small  $\alpha$ , the maximum growth rate increases at first. The colorbar corresponds to (a): meridional phase speeds, (b): zonal phase speeds.

solutions in Fig. 9.4, we see that the maximum growth rate decreases with increasing  $\alpha$  (the number of ridges), thus contributing to baroclinic stabilisation. This is consistent with Benilov (2001); LaCasce et al. (2019) also observed reduction in baroclinic growth rates in the presence of meridionally varying topography. However, we see that the maximum growth rate in Fig. 9.5a is greater than in the flat bottom case. This is possible as constant meridional topographic slopes can sometimes induce more instability (Chen and Kamenkovich, 2013). For a single ridge,  $\alpha = 1$ , the topographic wavelength is much larger than  $\hat{\lambda}$ ; hence, the slope changes slowly in the meridional direction. To confirm this, we performed our linear stability analysis for a constant topographic slope of value 0.1 in  $y$  (intended to corresponding to the case of ZR with  $\mathcal{A} = 0.1$ , as in Fig. 9.5). The results showed that the maximum growth rate increased relative to the flat-bottom case, confirming that, for small  $\alpha$ , the maximum growth rate increased (see Fig. 9.6). Moreover, with increasing  $\alpha$ , the distribution of unstable modes shifts towards larger zonal wavenumbers (the short-wave end of the spectrum), and the zonal wavelength of the most unstable mode decreases with increasing  $\alpha$ .

In Fig. 9.4b, it is clear that the zonal phase speed of unstable modes increases

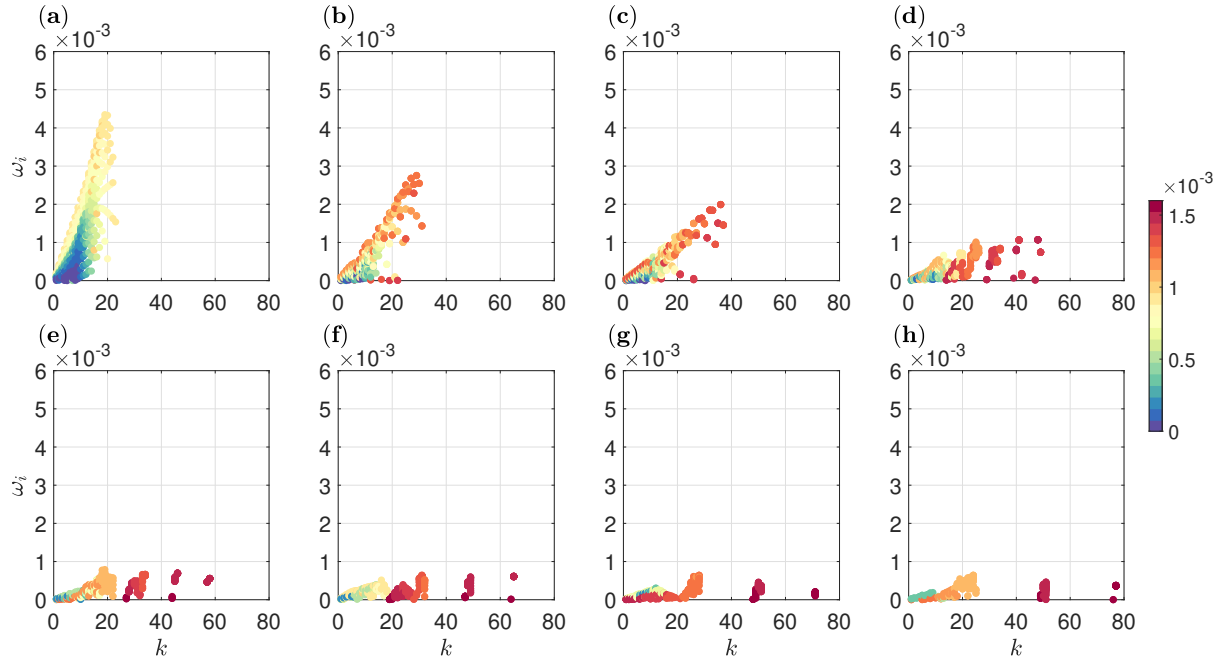


**Figure 9.7:** Equivalent to Fig. 9.5, but for  $\mathcal{A} = 0.2$  (maximum growth decreases, modes shift towards larger wavenumbers and zonal phase speeds increase with increasing values of  $\mathcal{A}$ ).

with increasing  $k$ . Comparing with Fig. 9.5a, we see that the addition of topography with a single ridge leads to an increase in the zonal phase speed. On analysing the other plots in Fig. 9.5, it appears that increasing the number of topographic ridges (i.e., reducing the ridge width) continues to induce faster zonal phase speeds associated with the unstable modes in the system. It is worth noting that the values of  $c_x$  approach the velocity imposed in the upper fluid layer, but never exceed this value. This can be seen from the dispersion relation for the flat-bottom case on the  $f$ -plane (Chen and Kamenkovich, 2013), and it can be shown that this is also the case on the  $f$ -plane in the presence of a meridional slope. The results of Chen and Kamenkovich (2013) show that the  $\beta$ -plane findings are similar to those obtained on the  $f$ -plane.

In Fig. 9.7, we present solutions for  $\mathcal{A} = 0.2$ , and on comparing with Fig. 9.5, we notice that an increase in the amplitude of ridges additionally decreases growth rates. This is evident from (9.13a) as baroclinic instability is affected by topographic gradients (the  $\mathcal{A}\alpha$  coefficient) when making the QG approximation. Thus, it follows that increasing either  $\mathcal{A}$  or  $\alpha$  leads to a reduction in growth rates. This result is neatly summarised in Fig. 9.8, where we show how the maximum growth rate responds to changes in the width and amplitude of ridges. From Fig. 9.8, it is clear

$\mathcal{A}$	$\alpha$	$\mathcal{A}\alpha$	$\max \omega_i$	$k$	$c_x$
0.1	10	1.0	$1.913 \times 10^{-3}$	34	$1.346 \times 10^{-3}$
0.2	5	1.0	$1.993 \times 10^{-3}$	36	$1.350 \times 10^{-3}$
0.1	20	2.0	$1.181 \times 10^{-3}$	45	$1.429 \times 10^{-3}$
0.2	10	2.0	$1.071 \times 10^{-3}$	48	$1.458 \times 10^{-3}$
0.1	30	3.0	$8.647 \times 10^{-4}$	52	$1.475 \times 10^{-3}$
0.2	15	3.0	$7.899 \times 10^{-4}$	19	$1.093 \times 10^{-3}$

**Table 9.2:** Comparison of the maximum growth rate and corresponding magnitudes of the zonal wavenumbers and zonal phase speeds for the same values of  $\mathcal{A}\alpha$ . Initially, small increases in  $\alpha$  contribute most to baroclinic stabilisation process. However, for larger increases in  $\alpha$ , increases in  $\mathcal{A}$  are more efficient at stabilising the system.

that increasing the number of ridges and topographic amplitude both act to decrease the maximum growth rate. However, the maximum growth rate will not necessarily be the same for the same magnitude of  $\mathcal{A}\alpha$  coefficient (see table 9.2). Clearly, the topographic wavelength is an important factor in governing the growth rates and the corresponding zonal wavenumber magnitude.

In regard to the zonal phase speeds, comparing corresponding panels in Fig. 9.5 with those in Fig. 9.7 reveals faster unstable modes in response to an increase in ridge amplitude. For a more precise assessment of similarities and differences between different topographic amplitude cases, we include maximum growth rates, zonal wavenumbers for which this occurs and the associated zonal phase speeds in table 9.2, for scenarios where  $\mathcal{A}\alpha$  has equal value. If changes in  $\mathcal{A}$  and  $\alpha$  contributed the same amount in suppressing baroclinic instability, then the magnitude of the maximum unstable growth would remain equal whenever the values of  $\mathcal{A}\alpha$  are the same. However, it is clear from table 9.2 this is not the case. Rather, for a small number of ridges (rows 1 and 2 of table 9.2), increasing  $\alpha$  appears to play a more dominant role in the baroclinic stabilisation process, rather than increasing the value of  $\mathcal{A}$  does. However, for larger values of  $\alpha$  (rows 3 through 6 of table 9.2), the roles reverse and the size of the maximum growth experiences a greater reduction in response to increasing  $\mathcal{A}$ . Other than row 6 of table 9.2, we see that increasing the value of  $\mathcal{A}$  causes the most unstable mode to experience a greater zonal shift. Similarly, the zonal phase speed exhibits larger growth with respect to  $\mathcal{A}$  (with the exception of row 6 of table 9.2, where this is attributed to the most unstable mode occurring at a much smaller value of  $k$ ).

An interesting finding comes from investigating how the zonal wavenumber corresponding to the maximum growth rate behaves in response to variations in

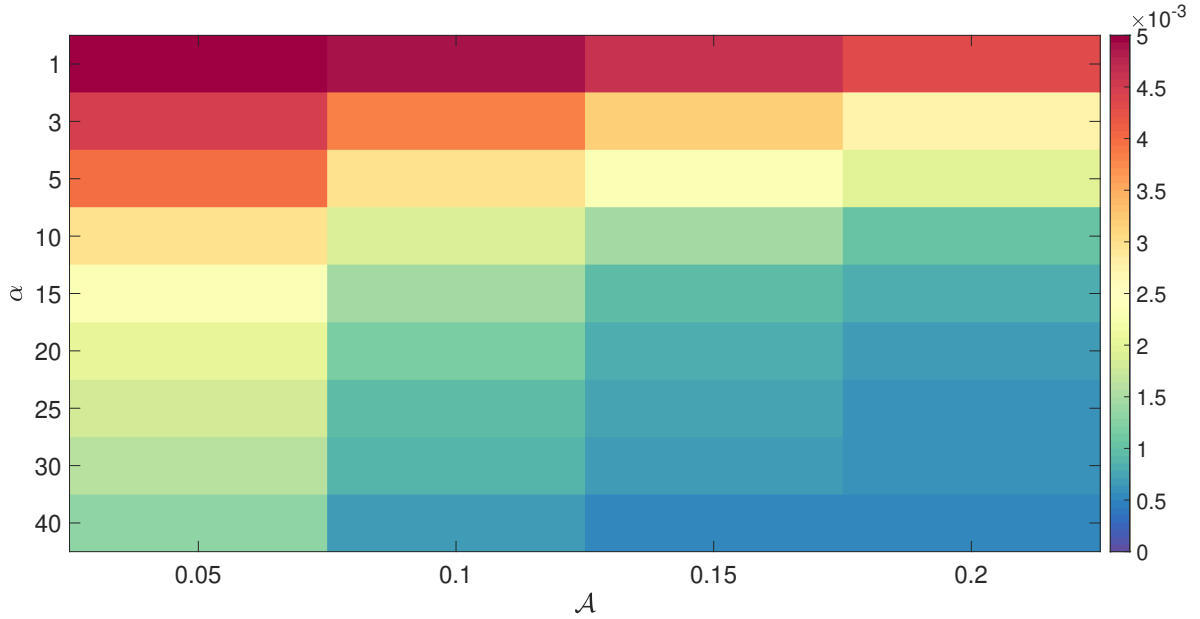


**Figure 9.8:**  $(\alpha, \mathcal{A})$ -plot for the maximum growth rate in the presence of ZR. Nondimensional growth rates are shown in the colorbar. For  $\mathcal{A} = 0$  (flat bottom), the maximum growth rate is  $4.6 \times 10^{-3}$  (from Fig. 9.4).

the value of  $\alpha$ . This behaviour is presented in the form of  $(\alpha, k)$ -contour plots for the maximum growth rate for each zonal wavenumber (see Fig. 9.9). As discussed above, the maximum growth rate occurs at a larger  $k$  with increasing  $\alpha$ . Moreover, for large enough  $\alpha$ , two separate branches arise, resulting in two growth rate maxima. The critical value for  $\alpha$  is approximately  $\alpha_c \approx 10$  in our analysis, but the value fluctuates with the magnitude of  $\mathcal{A}$ . In the right branch, the value of  $k$  corresponding to the growth rate maximum continuously increases with  $\alpha$ . This trend agrees with the more conventional understanding that the fastest growing eigenmodes tend to be of shorter wavelengths over nonzero bottom relief (Benilov, 2001; Chen and Kamenkovich, 2013), and this shift appears more pronounced for shorter topographic wavelengths. On the other hand, in the left branch, the value of  $k$  corresponding to the maximum growth rate decreases with  $\alpha$ .

We believe that the appearance of these two branches and the corresponding critical value for  $\alpha$  are related to the magnitude of the baroclinic Rossby radius. In the QG regime, it is expected that topography with wavelengths much smaller than  $\hat{\lambda}$  would be of less importance, since the typical scale of oceanic eddies is equal to or greater than the baroclinic Rossby radius. Indeed, submesoscale topography may complicate the dynamics (Radko, 2020a); however, we do not consider such effects in our experiments. From Fig. 9.9, the two branches appear for the topographic



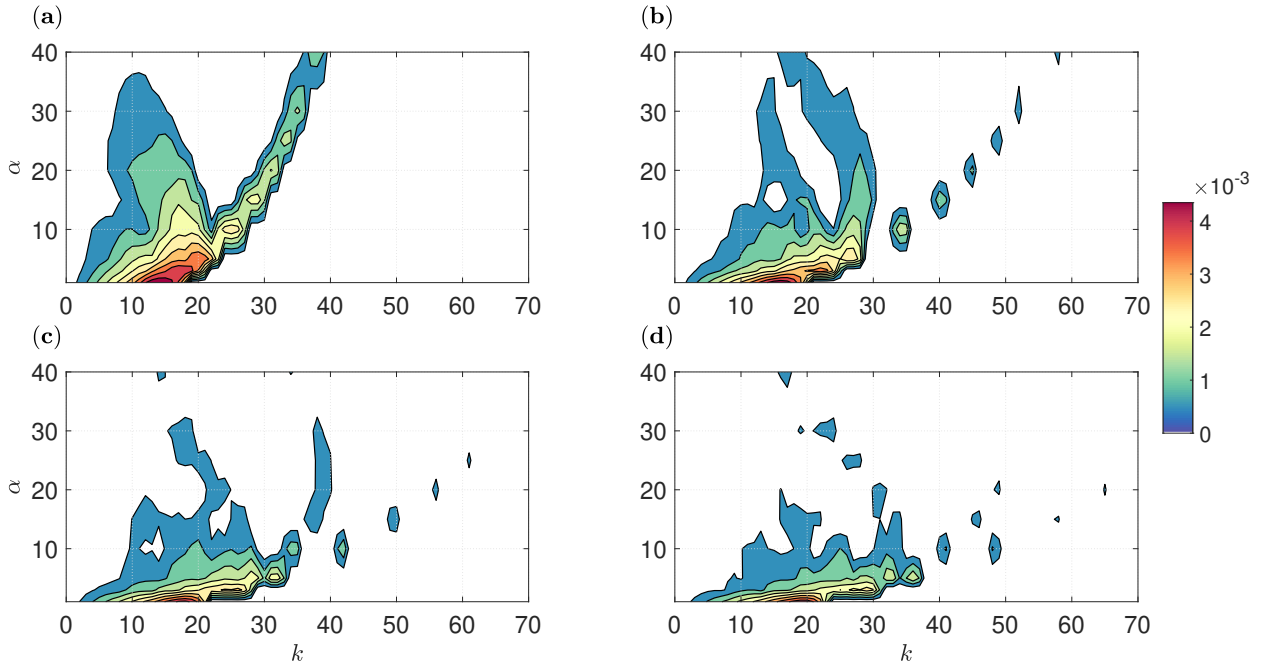


**Figure 9.9:** Maximum growth rate contours in nondimensional  $(\alpha, k)$ -parameter space. Subplots **a-d** assume  $\mathcal{A} = 0.05, 0.1, 0.15, 0.2$ , respectively. Growth rates are shown in the colorbar, with white regions referring to zero growth). Two branches form near  $\alpha \approx 10$  for different zonal wavenumbers depending on the value of  $\mathcal{A}$  (these branches evaporate as  $\mathcal{A}$  gets larger).

wavelength close to 270 km ( $\alpha_c \approx 10$ ) and this is roughly 1.7 times greater than  $2\pi\hat{\lambda}$ . Based on this, we expect that with further increases in  $\alpha$ , the left branch will eventually saturate at  $k$ , corresponding to the fastest growing mode in the flat bottom case (see Fig. 9.4), while the right branch may eventually disappear (as partially seen in Fig. 9.9c,d). Effectively, the coupling between the eigenmodes would become weak and the system would be reduced to a flat bottom ocean. On the other hand, another possibility for the appearance of the right instability branch could be the presence of linear instabilities on topographic scales (Benilov et al., 2004). Barotropic instability in the presence of a meridionally-varying jet profile was investigated in Benilov et al. (2004), regardless, it is unclear whether or not secondary instabilities could also appear in our baroclinic instability analysis.

Additionally, the spatial structure of the fastest growing eigenmode in the presence of ZR is also analysed. We present in Fig. 9.12 the spatial structure for the maximum eigenmode corresponding to  $\mathcal{A} = 0.1$  (panel a) and  $\mathcal{A} = 0.2$  (panel b) with  $\alpha = 1$ , and also include the same but with  $\alpha = 3$  in Fig. 9.13. Since we solve the coupled eigenproblem, the linear combination of all meridionally coupled eigenmodes at  $k$  corresponding to the largest growth rate are plotted in each case. Unlike the

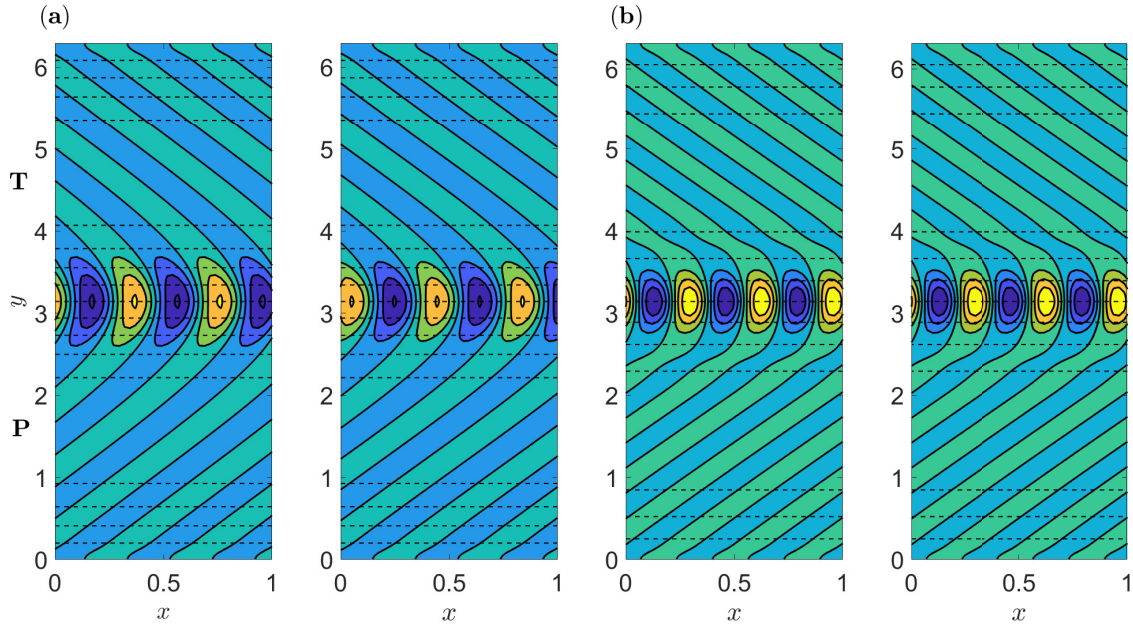


**Figure 9.10:** Contour plots for the perturbation streamfunctions attached to the maximum growth rate in the presence of ZR, with  $\alpha = 1$ . (a): top and bottom layers with  $\mathcal{A} = 0.1$ , (b): top and bottom layers with  $\mathcal{A} = 0.2$ . Dashed black lines denote topographic slopes and symbols **P** and **T** represent peak and trough regions of topography, respectively. The colorbar range is [min, max] from blue to yellow. The zonal extent of eddies reduces in size with increasing  $\mathcal{A}$ .

meridionally uniform eigenmodes (the Philips mode) over a flat bottom, the eigenmodes in the presence of ZR possess meridional variation. These are localised in regions of negative meridional gradients of topography, where baroclinic instability is expected to be the strongest. Another important aspect is that these eigenmodes have a curved structure and resemble oceanic banana-shaped eddies, which are formed in the vicinity of strong zonal flows (Berloff et al., 2011; Waterman and Hoskins, 2013). The shape of these oceanic eddies is a result of strong shear due to meridionally-varying background zonal flows, along with the regions of strongest zonal flows also having the largest meridional PV gradients in the surface layer. Similarly, in the presence of ZR, the fastest growing eigenmodes are localised in the regions of strongest meridional PV gradients in the lower layer. It is fascinating how the presence of variable topography can lead to these banana-shaped eigenmodes, even though the zonal flow is uniform. We believe that this banana-shape is a consequence of meridional variations in the zonal phase speeds of Rossby waves as the mean PV gradient varies meridionally. In the regions of the strongest meridional PV gradients, the linear dispersion relation predicts the zonal phase speeds to be the largest. Hence, the eddy shape can be distorted through the same eddy experiencing different

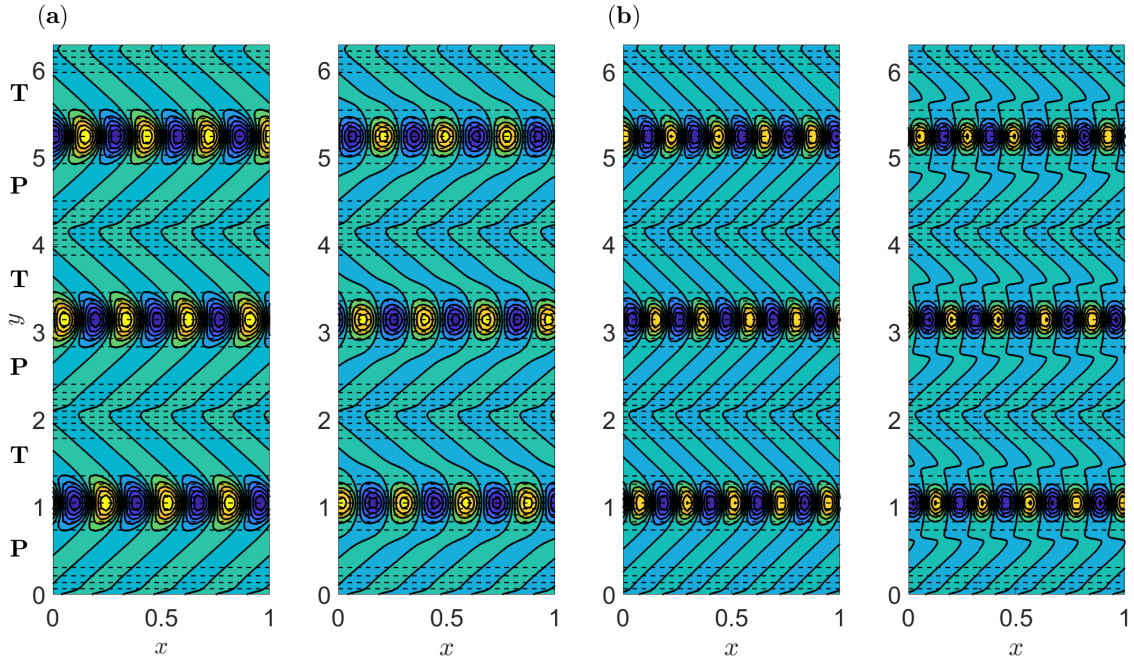


**Figure 9.11:** Same as Fig. 9.10, but with  $\alpha = 3$ . Dashed black lines denote topographic slopes and symbols **P** and **T** represent peak and trough regions of topography, respectively. The eigenmodes are eddy-chains sitting on the northern slopes of topography.

zonal phase speeds at different latitudes. We can apply the same argument for banana-shaped eddies present on meridionally-varying zonal background flows.

To evaluate the merit of our linear stability results, we also compared the spatial structure of growing eddies obtained from our linear stability analysis with streamfunction fields born from doubly-periodic numerical simulations. For this purpose, we used 1024 grid points in both horizontal directions when employing the CABARET simulations. As seen in Fig. 9.12, the spatial structure of growing eddies is consistent with our linear stability analysis predictions, as the differences are small, and are attributed to nonlinearities. Furthermore, positive and negative eddies in numerical simulations tend to be shifted slightly to the south and north, respectively (clearly seen in the last panel in Fig. 9.12). There is a possibility that cyclonic and anticyclonic eddies move meridionally in response to meridionally varying Coriolis frequency and topographic height. This offset structure of the eddies could be important for secondary instabilities and jet formation; however, we do not study such effects here.

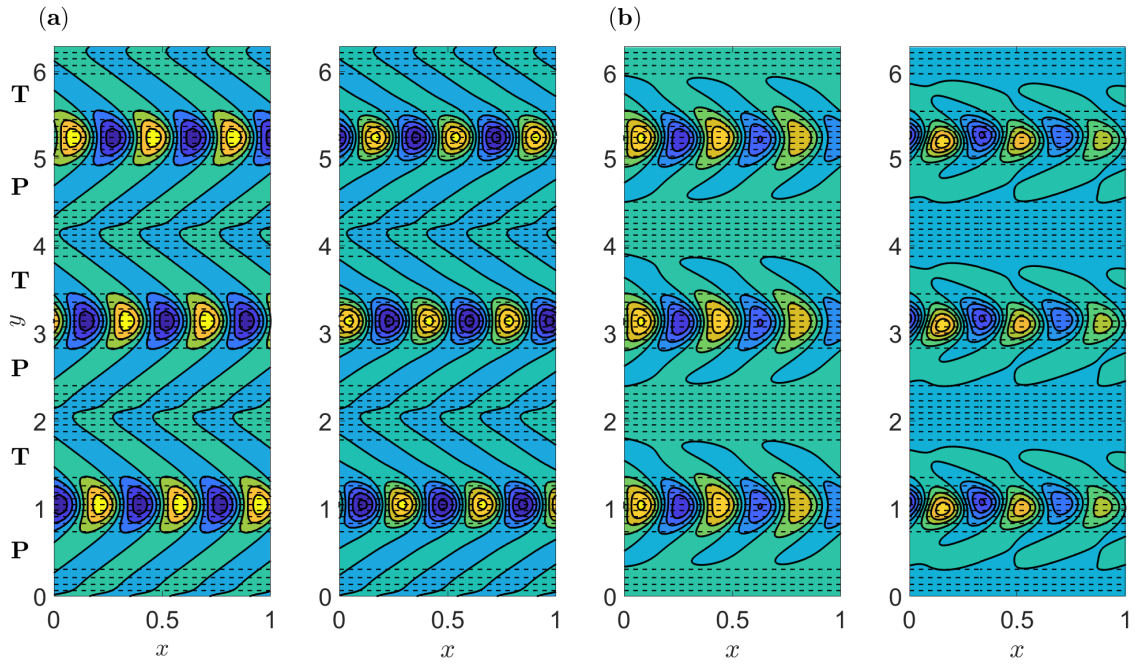


**Figure 9.12:** Comparison with numerical simulations in the presence of ZR for  $\mathcal{A} = 0.05$  and  $\alpha = 3$  (a): Structure of eigenmodes (left and right panels for the top and bottom layers, respectively) corresponding to the maximum growth rate, (b): Snapshot of streamfunction field obtained on a  $1024^2$  simulation at roughly 1000 days with parameter values as in table 9.1 (left and right panels for the top and bottom layers, respectively). Dashed black lines denote topographic slopes and symbols **P** and **T** represent peak and trough regions of topography, respectively. The colorbar range is  $[\min, \max]$  from blue to yellow. There are remarkable similarities between the linear solution and numerical simulations, where the differences in spatial structure are attributed to nonlinearities.

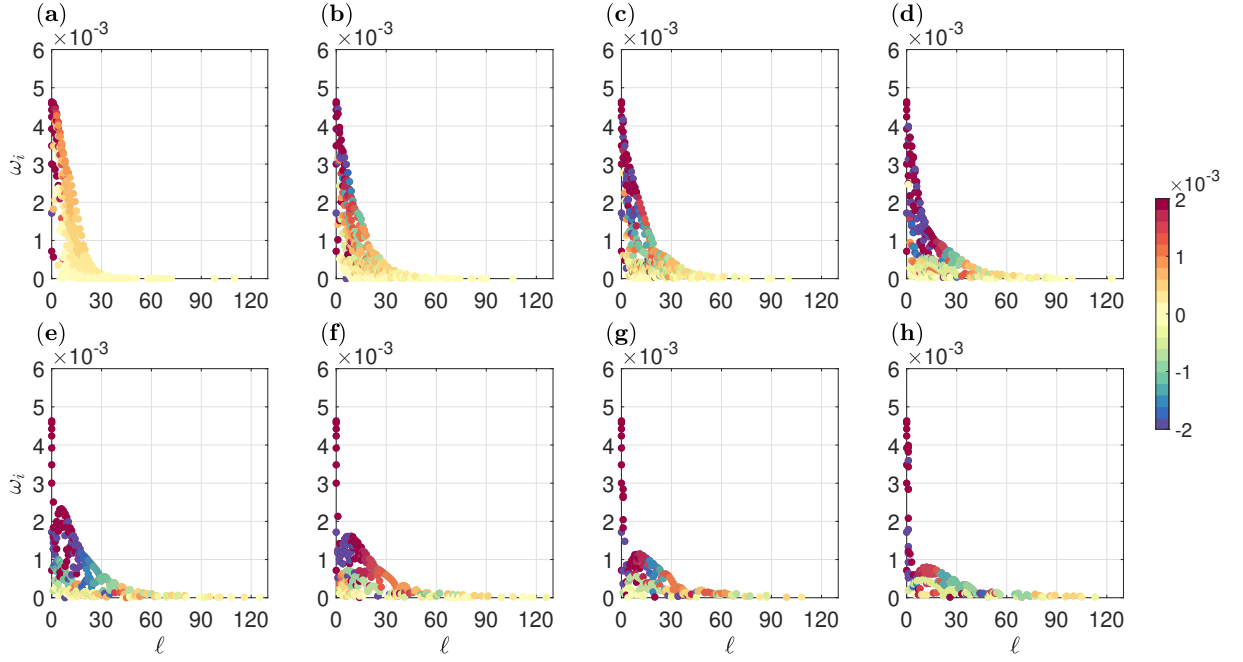


**Figure 9.13:**  $(\omega_i, \ell)$ -plot in the presence of MR, with  $\mathcal{A} = 0.1$  (see table 9.1 for parameter values). Subplots **a-h** assume  $\alpha = 1, 3, 5, 10, 15, 20, 25, 30$ , respectively (maximum growth remains constant and the distribution of unstable modes shifts towards larger wavenumbers with increasing  $\alpha$ ). Meridional phase speeds are shown in the colorbar (magnitude of speeds increase with increasing  $\ell$  and  $\alpha$ ). When  $\alpha = 15$ , a second maximum occurs and weakens with increases in  $\alpha$ .

### Meridionally Oriented Multiple Ridges

Similar to how we dealt with ZR, we considered the case of MR by solving the problem (9.13b) for all values of  $k$ , while fixing the value of  $\ell$  (see Fig. 9.2b). As such, we plot solutions in the  $(\omega_i, \ell)$ -parameter space, as seen in Fig. 9.13. By comparing these solutions with those in Fig. 9.4, we deduce that the magnitude of the maximum growth remains unchanged with MR and always occurs at  $\ell = 0$ . Despite this, the distribution of unstable modes shifts towards larger meridional wavenumbers with increasing  $\alpha$ , similar to what occurs in the presence of ZR. For large enough  $\alpha$ , a second peak close to  $\ell = 10$  appears in the growth rate distribution. The magnitude of this peak decreases with  $\alpha$ , indicating the suppression of instability for these wavenumbers. Moreover, the meridional phase speeds,  $c_y = \omega_r/\ell$ , associated with the unstable modes can be seen to increase in magnitude with  $\alpha$  and  $\mathcal{A}$  (as seen by comparing Fig. 9.13 with Fig. 9.14).

In Fig. 9.15, we look at how the maximum growth rate at different meridional wavenumbers is affected by the magnitudes of  $\alpha$  and  $\mathcal{A}$ . As mentioned above, the



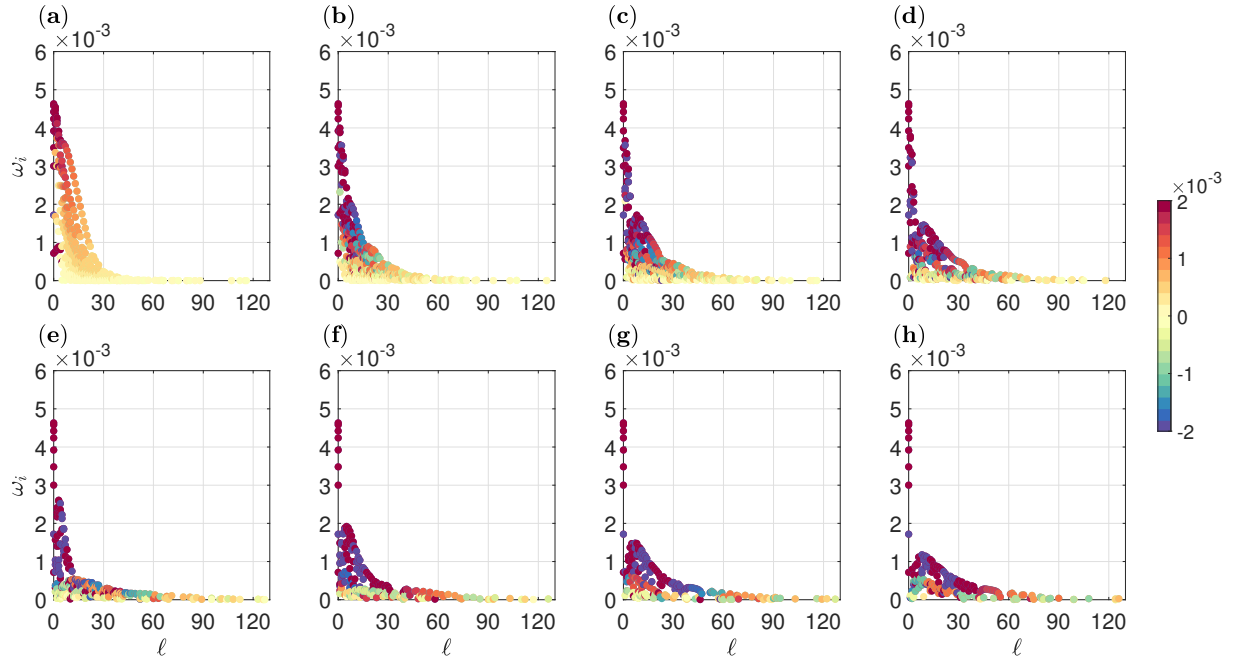


**Figure 9.14:** Same as Fig. 9.13, but with  $\mathcal{A} = 0.2$  (magnitude of phase speeds increase with increasing  $\mathcal{A}$ ). A second maximum appears for different values of  $\alpha$ .

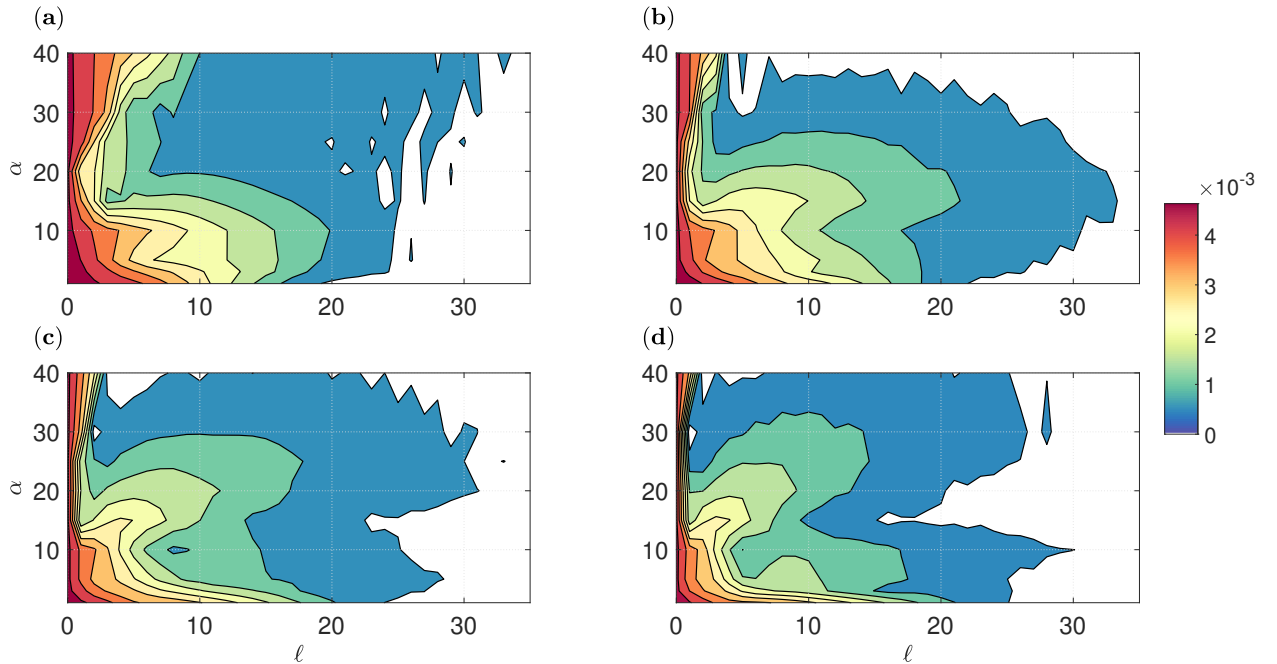


**Figure 9.15:** Nondimensional  $(\alpha, \ell)$ -contour plot for the maximum growth rate in the presence of MR. Plots **a-d** assume  $\mathcal{A} = 0.05, 0.1, 0.15, 0.2$ , respectively. Growth rates are shown in the colorbar (with white regions referring to zero growth rate) and these appear to decrease for larger  $\ell$  with increasing  $\mathcal{A}$ .

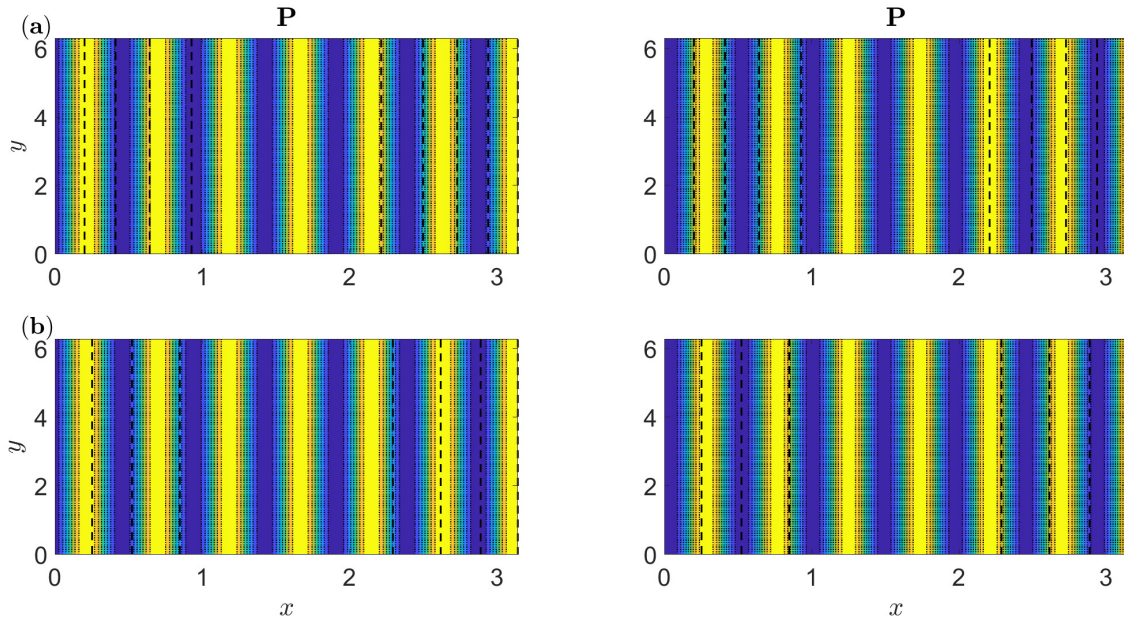


**Figure 9.16:** Eigenmodes corresponding to maximum growth with MR, with  $\alpha = 1$  (ridges are represented by dashed black lines and **(P)** denotes the topographic peak). Plots **a**, **b** refer to  $\mathcal{A} = 0.1, 0.2$ , respectively. The left (right) snapshot denotes the upper (lower) layer. We restrict attention to half an oscillation of topography only as the pattern repeats. Since the maximum growth rate does not change in the presence of MR, the streamfunctions are independent of  $\alpha$  and  $\mathcal{A}$ . Black dashed lines represent topographic slopes.

maximum growth rate always occurs at  $\ell = 0$ , and this is made more apparent in Fig. 9.15. Even for large  $\ell$ , the magnitude of growth rates look to be similar for different topographic amplitudes and it is not clear how sinusoidal bottom irregularity affects the overall stability. In summary, simply comparing the maximum growth rate is not sufficient in understanding the overall effect of topography on the stability of the system.

The spatial structure of the fastest growing eddies in the presence of MR is very similar to the fastest growing mode over a flat bottom. In particular, there appears to be just one prominent wavenumber in the zonal direction, which is controlled by the value of the baroclinic Rossby radius. Furthermore, unlike in the case of ZR, there is no localisation of the eigenmode with respect to MR. Similar to our analysis for ZR, we compare linear stability solutions with those obtained through solving the two-layer QG system in the presence of MR numerically. The purpose of this is to identify differences due to nonlinear contributions as well as verify our linear stability results. We present snapshots for  $\mathcal{A} = 0.05$  and  $\alpha = 1, 3, 15$  in Fig. 9.17, and these panels show clear consistency between our linear stability analysis for small

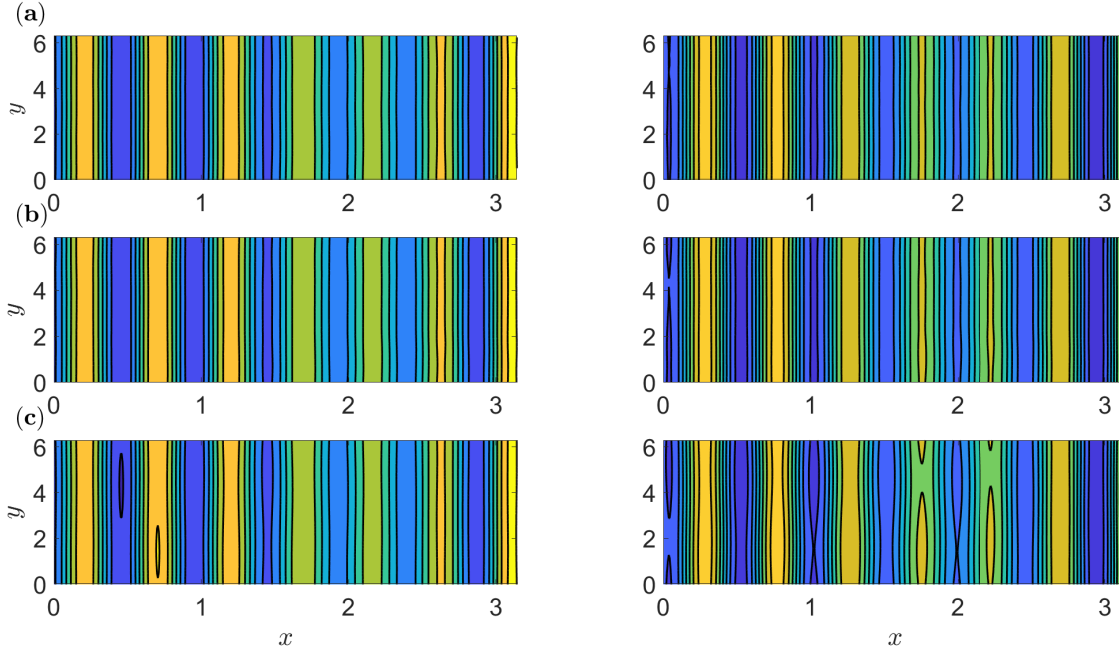


**Figure 9.17:** Numerical simulations with MR for  $\mathcal{A} = 0.05$ , run on a  $1024^2$  grid using parameter values as in table 9.1. (a): Snapshot of streamfunction field for  $\alpha = 1$ , (b): Snapshot of streamfunction field for  $\alpha = 3$ , (c): Snapshot of streamfunction field for  $\alpha = 15$ . The left (right) snapshot denotes the upper (lower) layer and the colorbar range is  $[\min, \max]$  from blue to yellow. Topographic slopes are not illustrated so differences in spatial structure can be easily identified.

values of  $\alpha$  and numerical results, suggesting that a zonally varying topography has no notable effects on the spatial structure of the fastest growing eigenmodes (this is limited to zonal background flows only). On the other hand, for  $\alpha = 15$ , some spatial variation in the meridional direction is seen in the meridionally oriented modes. This could be related to the second growth rate peak in Fig. 9.13. Hence, the shift in the distribution may affect the spatial structure of the fastest growing eddies over MR; nevertheless, the effect appears to be small. Alternatively, we could attribute this to the presence of secondary instabilities (Benilov et al., 2004) which are not captured by our baroclinic stability analysis.

### Number of Unstable Modes

In some cases, it may not be sufficient to just examine the maximum growth rate to evaluate the topographic effects on baroclinic instability, e.g., in Fig. 9.13, the maximum growth rate remains the same. Therefore, we also consider the growth rates of higher eigenmodes. To get a better picture of the extent topography weakens baroclinic instability, we specifically examine the changes in the total number of



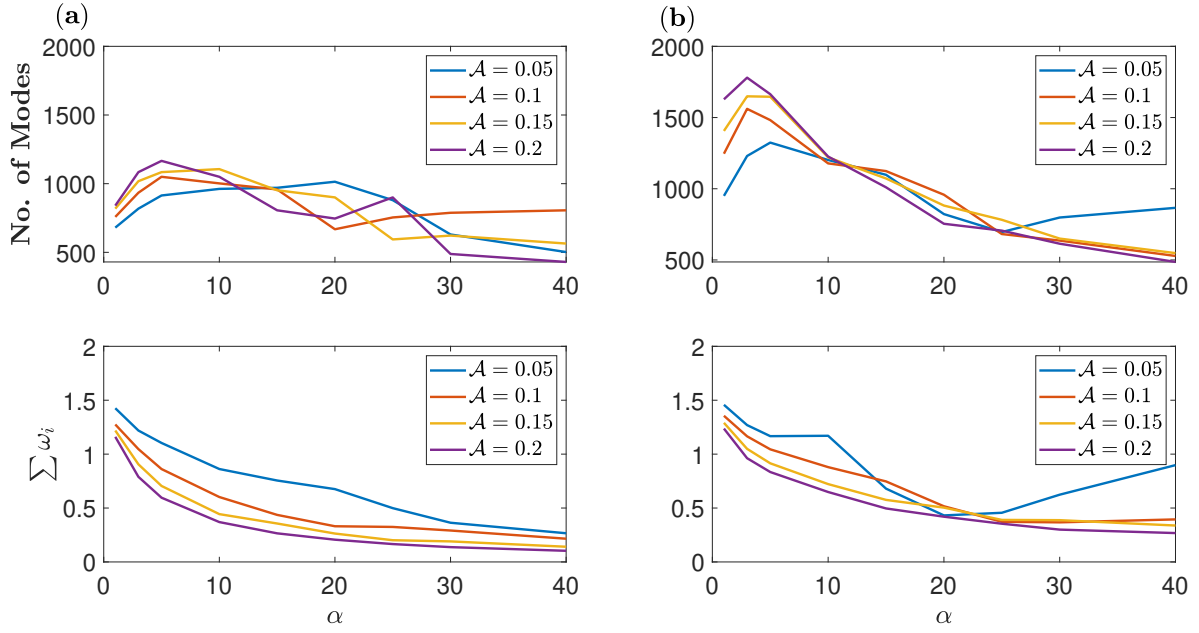


**Figure 9.18:** The number of unstable modes (top plots) and the sum of positive growth rates (bottom plots) as functions of  $\alpha$ . (a): in the presence of ZR, (b): in the presence of MR.

unstable modes, as well as in the sum of their growth rates (see Fig. 9.18). In the presence of ZR, the number of unstable modes shows a decreasing trend with  $\alpha$ . The same appears true for the sum of growth rates, which decrease with increasing  $\mathcal{A}$  as well as  $\alpha$ . Thus, overall the presence of ZR suppresses the baroclinic instability in the system. We reached the same conclusion when we looked at the maximum growth rate, which also decreases (Fig. 9.8).

On the other hand, in the presence of MR, the number of unstable modes first increases up to some small value of  $\alpha$ , but the number tends to decrease beyond this value of  $\alpha$ . As for the sum of positive growth rates, the general decreasing trend with  $\alpha$  indicates the suppression of baroclinic instability. This behaviour of increased stability is difficult to infer by just looking at the growth rate of the most unstable modes as the maximum growth rate shows negligible difference (Fig. 9.13). This approach is rather qualitative and is only used to make broader inferences on the effects of the number of ridges and topographic amplitude on the stability of the system.

### 9.2.3 Linear Stability for a Thin-Upper-Layer

Despite the choice of equal layer depths being convenient to work with, it is important to investigate how the results from the linear stability analysis change when the

fluid layers have distinct mean depths. For this purpose, we repeat our analysis for a configuration which assumes the upper layer has thickness much less than the lower layer (hereinafter, we will refer to this case as a thin-upper-layer). We could equally obtain solutions assuming a thick-upper-layer, however, this particular regime is not physically relevant when considering problems in ocean science. It is worth noting that choosing distinct layer depths results in different stratification parameters, hence, the critical velocity shear will also change and an inter-comparison of growth rates is not possible. With this in mind, we choose the background velocity magnitude,  $\hat{U}$ , to be double the respective critical velocity. We followed the same approach in our analysis in the equal-depth configuration, where  $\hat{U}/\hat{U}_c = 5 \text{ cm s}^{-1}/2.5 \text{ cm s}^{-1} = 2$ .

Here, we assume  $\hat{H}_1 = 400 \text{ m}$  and  $\hat{H}_2 = 3.6 \text{ km}$  for the thin-upper-layer case. The dimensional value of velocity adopted to force baroclinic instability in the system was  $\hat{U} = 25 \text{ cm s}^{-1}$ . Also, the magnitudes of stratification parameters in the top and bottom layers differ as a consequence of unequal layer depths. The value of the baroclinic Rossby radius was kept the same, i.e., 25 km, and the remaining parameter space is consistent with table 9.1. Since the case of ZR proved the most interesting in our results, we focus on this particular case when considering the problem of unequal layer depths.

In the thin-upper-layer case, as seen in Fig. 9.19 for  $\mathcal{A} = 0.1$ , we notice similarities with equal layer depths, such as eigenmodes shifting towards larger values of  $k$  with increasing values of  $\alpha$ , along with a depression of maximum growth for  $\alpha \geq 3$  (though there is an initial spike for  $\alpha < 3$ ) and increasing zonal phase speeds. Despite these similarities, some interesting behaviour becomes more evident when  $\alpha \geq 10$  (see Fig. 9.19  $d - h$ ). The distribution of unstable eigenmodes separate into two clusters, the first of which occurs when  $k = (0, 10)$  and the second when  $k = (10, 20)$ . Such cluster separation arises since the instabilities are connected to either  $\hat{\lambda}$  (the baroclinic Rossby radius) or  $\hat{L}_{\text{top}}$  (the topographic length scale), and when these scales become distinctly different, we begin to see two isolated branches.

In the first of these clusters, the maximum growth rate experiences greater depression in comparison to the second cluster maxima with increasing values of  $\alpha$ . Moreover, as  $k$  increases, the zonal phase speeds in the initial cluster increase, while those in the second cluster appear to decrease (albeit, the zonal phase speeds in the second cluster are much greater than those present in the first cluster). On the other hand, increasing the value of  $\alpha$  looks to reduce the zonal phase speeds in the first cluster, while encouraging the zonal phase speeds in the second cluster to

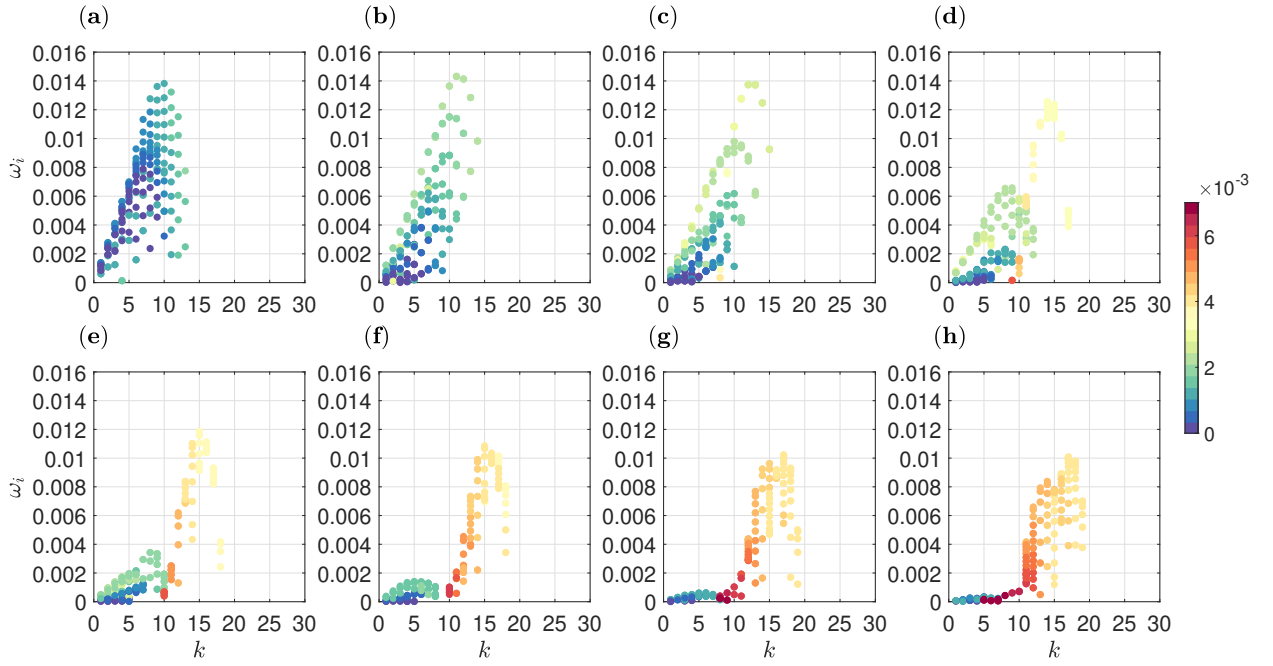


**Figure 9.19:** Thin-upper-layer configuration for ZR with  $\mathcal{A} = 0.1$ . Subplots **a-h** assume  $\alpha = 1, 3, 5, 10, 15, 20, 25, 30$ , respectively. The maximum growth rate increases for small values of  $\alpha = 1, 3$  and then decreases in the proceeding panels ( $\alpha \geq 5$ ). The distribution splits into two clusters, each having a distinct maximum. The maximum of the first cluster is greatly suppressed with increases in  $\alpha$  relative to the weakly suppressed second cluster maxima. The zonal phase speeds are shown in the colorbar.

see weak increases.

Investigating this behaviour for a larger topographic amplitude of  $\mathcal{A} = 0.2$  (see Fig. 9.20), the initial spike in growth rate is slightly greater than in Fig. 9.19, but is depressed when  $\alpha = 3$  rather than enhanced, as in the  $\mathcal{A} = 0.1$  case (Fig. 9.19). Again, the two unstable mode clusters are formed for  $\alpha \geq 10$  and the modes in these clusters exhibit similar behaviour to that seen for a smaller value of  $\mathcal{A}$  (Fig. 9.19). One notable difference is that in the larger topographic amplitude case, the two clusters become more disconnected compared to those in Fig. 9.19 when the value of  $\alpha$  increases. In addition, the eigenmode growth rates present in the first cluster are enhanced by a greater amplitude of topography, while the growth rates of eigenmodes present in the second cluster are instead depressed by this amplitude increase. One possibility for these differences is that the clusters formed for  $\mathcal{A} = 0.2$  are present at relatively larger zonal wavenumbers than in Fig. 9.19. Despite these differences, the behaviour of zonal phase speeds of eigenmodes in both clusters remains consistent with the characteristics seen in Fig. 9.19, with the exception being an enhancement in the value of the zonal phase speed of all eigenmodes.

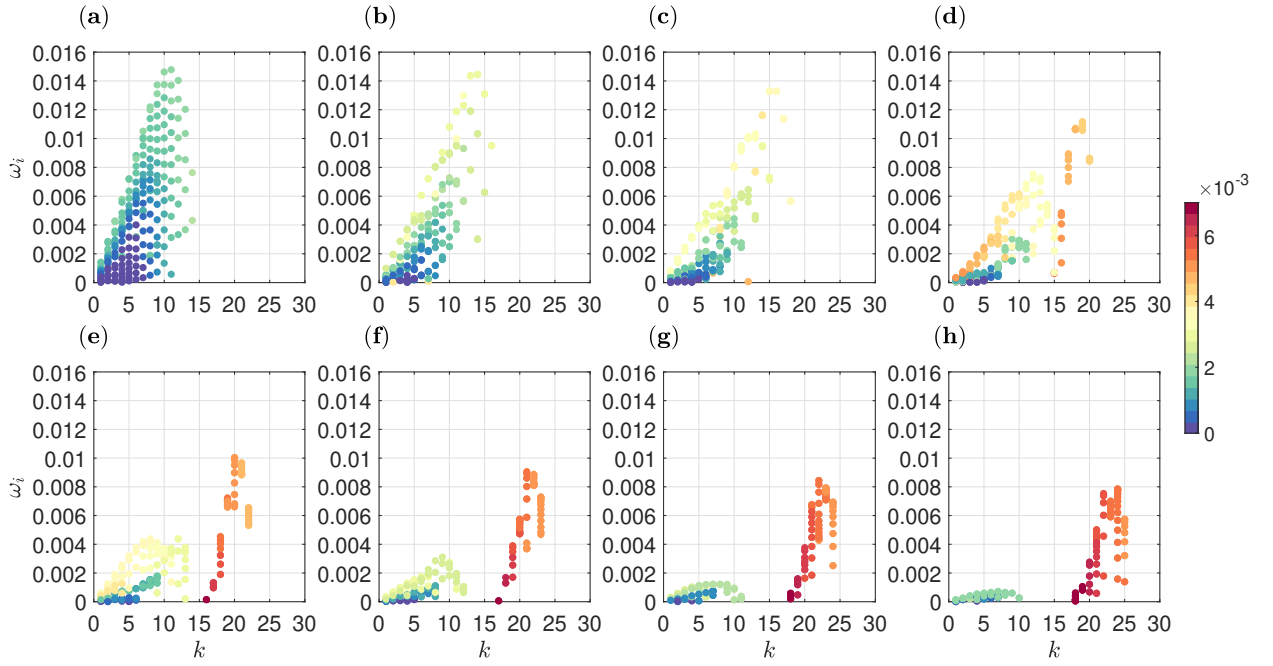


**Figure 9.20:** Thin-upper-layer configuration for ZR with  $\mathcal{A} = 0.2$ . Subplots **a-h** assume  $\alpha = 1, 3, 5, 10, 15, 20, 25, 30$ , respectively. The maximum growth rate increases for  $\alpha = 1$  and then decreases in the proceeding panels ( $\alpha \geq 3$ ). The distribution splits into two clusters, each with distinct maximum. Both cluster maxima weaken with increases in  $\alpha$ ; the decrease in the first cluster being greater than in the second. Comparing with Fig. 9.19, the first cluster maximum is enhanced with increased  $\mathcal{A}$ , while the second cluster maximum is depressed. The zonal phase speeds are shown in the colorbar.

### 9.3 Summary

In this chapter, we discussed a different problem to those considered in this thesis up until this point, that being the linear stability of homogeneous zonal currents over sinusoidal bottom relief (Davies et al., 2021). Our analysis was carried out in a two-layer QG model on the beta-plane and we considered zonally-oriented multiple ridges (ZR) and meridionally-oriented multiple ridges (MR) separately. As a consequence of assuming sinusoidal bottom topography, we were able to employ a spectral method to solve a system of eigenproblems that were coupled between fluid layers.

We found that in the case of ZR, the growth rate of the most unstable modes decreased as we increased the number of topographic ridges and the amplitude of topography. This is consistent with the findings of Benilov (2001) for small-scale sinusoidal topography, however, we also observed a branch division in the unstable mode spectra when the number of ridges exceeded a critical value. Along these branches the most unstable growth rates still decreased, however, the growth rate

along one branch was much smaller than on the other. In addition, the zonal phase speeds increased with increases in the zonal wavenumber.

The corresponding critical eigenmodes were extracted and found to resemble eddy chains, where the number of chains was proportional to the number of ridges of topography. To validate our linear stability results, we carried out high resolution numerical simulations and found consistency between the linear stability theory and our numerics. Similarly, in the case of MR, we found that these topographic features do not influence the most unstable growth rates directly, which is also consistent with the findings of Benilov (2001) for small-scale bottom features.

# Chapter 10

## Conclusion

### 10.1 Dipole results

Throughout this thesis, we have considered various stability problems that stem from the study of geophysical fluid dynamics. The majority of the research presented focuses on the dynamics of dipolar vortices. In particular, we considered the time evolution of zonally eastward drifting LRD steady state solutions in a 1.5-layer framework on the  $\beta$ -plane. In Chapter 3, these inviscid solutions were found to display zonal elongations and oscillatory behaviour; developing into the spontaneous symmetry breaking of the eddy pair. Prior to the numerical analysis in this thesis and the work [Davies et al. \(2023\)](#), eastward propagating dipoles were thought to be stable by many, based on previous numerical studies in the literature ([McWilliams et al., 1981](#); [Swaters and Flierl, 1989](#); [Carnevale et al., 1988](#)).

The dipole problem becomes even more interesting when we consider solutions of different intensities, i.e., changes in the value of  $c/\beta$ , where  $\beta$  is a free parameter and  $c$  is assumed to be fixed in our experiments. As the dipoles we considered intensified, we observed a delay in the partner separation and a lengthier deceleration of the dipole drift, up until the westward change in direction. Moreover, in the case of strong dipoles, these appeared to follow steady trajectories in our limited time integration numerical simulations.

Similar to weak dipoles, dipole-rider vortices with a very small rider contribution also exhibited the same dipole destruction phenomena. However, similar to the longevity of strong dipoles, we also found that dipole-rider vortices were capable of breaking into a pair of eddies. Through this separation process, waves are expelled from the solution and the eddies of opposite sign oscillated with one another in the meridional direction. After significant meridional translation, the eddy pair

continued to oscillate and followed an approximate zonal path; along which the vortex couple seemingly adjusted to an elliptical shape that performed uniform propagation (where any small deceleration was likely due to numerical viscosity). These findings are significantly different to those obtained for moderate/strong dipoles in Swenson (1987), where the dipole-riders considered were shown to be unstable.

In Chapter 4, we were able to associate the symmetry breaking of the eastward propagating vortex pair with a growing anomaly on the dipole that has even symmetry with respect to the zonal axis. This disturbance on the dipole was accurately represented by a normal mode representation, using snapshots obtained numerically. Therefore, this allowed us to conclude that the dipole destruction captured in our numerical results was related to the linear instability of the LRD. With this in mind, we deduced that the growing anomaly corresponded to a critical instability mode, which we called a Davies mode. Such growing patterns also appeared on strong dipoles, but these formed outside of the periodic domain and so it is difficult to ascertain whether the appearance of the Davies mode was natural or not.

To complement the evidence for linear instability of the LRD solutions, we carried out a linear stability analysis for dipoles with various intensities in Chapter 5. Our findings highlighted the existence of critical Davies modes, where the linear growth rates were found to decrease with increasing dipole intensity. Moreover, our analysis also found the period of oscillation to gently increase with dipole intensity, which was not clear from our numerical results. An interesting outcome of this work was for the strong dipole solutions, where the critical mode obtained was very different and the corresponding period of oscillation was significantly longer than the values found for weaker dipoles. However, this analysis also extracted lower order modes in the eigenspectra that resembled the Davies mode pattern. Based on these structures not being orthogonal, we speculated that they could interact with each other through nonlinear interactions. Alternatively, it could be the case that our finite difference linear stability method was not capable of extracting the strong dipole critical modes effectively, as a consequence of relatively weak resolution being employed (when compared to the resolution used for our numerical simulations in Chapter 3).

The study of nonlinear-self interaction was explored in Chapter 6, where we developed an understanding of the PV flux exchange in the dipole. Here, we showed that the PV content predominantly moves meridionally near the rear of the dipole. Furthermore, integral value considerations informed us that such PV movement contributed to 'dipole cooling', i.e. , the oscillatory behaviour of the Davies mode reduced the PV contrast in the dipole. In addition to this, we discussed the corresponding

energetics and showed that it was because of the asymmetry in the Davies mode that made it efficient at extracting energy from the background flow.

Motivated by our instability findings for the class of initialised LRD solutions, we investigated the dynamics of these dipoles in the presence of various degrees of tilt with respect to the zonal axis. In contrast to the results of [Hesthaven et al. \(1993\)](#), we demonstrated that solutions in the presence of weak initial tilt were capable of adjustment along the zonal axis, however, the destruction of the dipole followed soon after through the development of a Davies mode during this stage of the evolution. Moreover, when the dipole intensity was weak, we found that regardless of initial tilt, the outcome was destruction over time.

As we increased the initial tilting, the conditions were less favourable for the formation of a Davies mode. In particular, the early stage anomaly on the dipole produced through tilted oscillations (the so-called T-mode) was dominated by the Davies mode for angles less than  $45^\circ$ . In this case, after adjustment along the zonal axis, the dipole is likely to see destruction given long enough time elapses, due to the same mechanism as seen for an untilted LRD. On the other hand, for angles greater than  $45^\circ$ , the T-mode pattern persisted as the dipole adjusted along the zonal axis. From our numerical results for these scenarios, the dipole structures experienced little deformation as they continued to propagate with roughly uniform speed in the eastward direction. These results appeared consistent with the findings of [Hesthaven et al. \(1993\)](#), and it is likely that these tilted dipoles are capable of adjusting to new elliptical steady state solutions that do not experience instability due to a growing Davies mode. Given the limitations of our analysis and the extent of the parameter space, this problem should be the focus of future research.

We briefly derived a Newton method that can theoretically be used to solve for arbitrary steady state solutions in a two-layer framework. On initialising this method with an LRD steady state, we incorporated integral constraints into our equations to as a means of optimisation. In principle, if the integral constraints are known, they can be applied in a similar way to how we handled them in [Chapter 8](#). Unfortunately, this method did not achieve convergence, however, we believe this was likely a consequence of computational cost. The method makes use of finite differences, which suggests that the solutions of the nonlinear solver will be sensitive to grid resolution. In other words, the method requires high resolution to achieve convergence.



## 10.2 Topography results

The primary focus of the topography investigation was to present a linear stability analysis for oceanic flows in the presence of sinusoidal bottom irregularities. In accord with the aforementioned studies considering small-scale sinusoidal topography (Benilov, 2001; LaCasce et al., 2019; Radko, 2020a), eigenmodes are found to have maximum growth rates suppressed by ZR (Fig. 9.5) and unchanged by MR (Fig. 9.13). We observed a shift in the distribution of eigenmodes towards larger wavenumbers and an enhancement in phase speed magnitude with increasing values of  $\alpha$  and  $\mathcal{A}$  (these being the number of ridges and the topography amplitude, respectively). Moreover, the study by Radko (2020a) identified that MR slightly intensifies mesoscale eddies in the upper-layer relative to the flat-bottom case, motivating our finding of a second peak in the distribution of unstable modes, which occurs when  $\alpha \geq 15$  (see Fig. 9.13). The second peak is most pronounced for horizontal topography scales commensurate to  $2\pi\hat{\lambda}$  ( $\hat{\lambda}$  being the baroclinic Rossby radius as defined in table 9.1), with the peak being suppressed as  $\alpha$  increases. Similarly to that observed in Benilov (2001), flows localised in a thin-upper-layer experience a weaker stabilisation from the presence of ZR (Fig. 9.19). However, a notable finding of ours is the appearance of unstable modes in two separate clusters (Fig. 9.5 and Fig. 9.19) for topographic wavelengths roughly equal to  $2\pi\hat{\lambda}$  (Fig. 9.9). This suggests that periodic topography can excite baroclinic instability that is centred around two different length scales instead of just the baroclinic Rossby radius.

The spatial structure of the linear eigenmodes corresponding to the maximum growth are eddy-chains over ZR (Fig. 9.11) which sit along the northern topographic slopes (the number of chains increase in response to the number of ridges). These bear a remarkable resemblance to snapshots of streamfunction fields obtained through numerical simulations (those being CABARET solutions for (9.1)), with differences attributed to nonlinear terms we neglected in our analysis (Fig. 9.12). Over MR, the linear eigenmodes corresponding to maximum growth are meridionally oriented and very similar to the fastest growing mode over a flat bottom; remaining unchanged by parameter shifts in  $\mathcal{A}$  and  $\alpha$  (Fig. 9.16).

In addition, we also considered distinct layer depths in our analysis. When a thin-upper-layer configuration is assumed, the behaviour of eigenmodes in the presence of ZR experienced some changes of note (Fig. 9.19 and Fig. 9.20). In the weaker topography case considered (Fig. 9.19), the maximum growth rate was enhanced until  $\alpha \geq 5$ , where it the appearance of two clusters with distinct maxima

are evident again. The first maxima experiences a greater depression than the second with increases in  $\alpha$ . Zonal phase speeds increase in the first cluster with increases in  $k$  and are weakened with increases in  $\alpha$ . In the second cluster, zonal phase speeds decrease with increases in  $k$  and are enhanced by increases in  $\alpha$  (zonal phase speeds in the second cluster are greater than in the first cluster). When increasing the topography amplitude  $\mathcal{A}$ , the results are similar (see Fig. 9.20); however, there are subtle differences in terms of the locations of the two clusters and rates of change of growth rates with  $\alpha$ . These two clusters of unstable modes are not clearly seen in the linear stability analysis of the equal-depth configuration; nevertheless, two distinct growth maxima appear (Fig. 9.9).

### 10.3 Future research

Even with our findings of instability for initial steady state dipoles, it is still unclear whether or not there exists a critical threshold beyond which strong dipoles can continue to steadily translate in the eastward direction. This can likely be resolved by carrying out a higher resolution linear stability analysis, or performing significantly longer numerical simulations on a finer grid in a larger domain. The caveat with both approaches is the computational expense attached. However, the merit in a bifurcation study for the dipole problem is high, given the results of the distillation experiments we carried out in Chapter 4 for strong dipoles.

We briefly discussed some interesting results for dipole-rider vortices, however, it is clear that an extensive exploration of these solutions is a fruitful research avenue. Given we observed dipole destruction for  $\kappa = 0.01$ , but we also obtained what appeared to be adjustment to an elliptical dipole state when  $\kappa = 0.1$ , a broader survey of results is natural to work towards. Moreover, the numerical analysis of dipole-rider steady states should be used to motivate the use of parameters that can distinguish the dipole-rider dynamics into distinct categories (e.g., we observed very different behaviours for  $\kappa = 0.1, 0.01$ ). We did not explore the linear stability of dipole-rider initial states directly, however, this method is clear and a natural means of progression for research purposes.

Despite paying mention to the study of dipoles in the presence of background flow and topographic features in Chapter 2, these problems clearly deserve to be the focus of many studies given the instability findings in this thesis. We did not address these problems beyond introducing them, since the material presented was already considerable. However, it appears important to investigate how the dipole

instability develops in the presence of topographic features, since these have been shown to affect the overall flow stability (Chen and Kamenkovich, 2013). This would be particularly interesting in the case of stabilising weak dipoles and destabilising strong dipoles. We can also consider dipole-rider solutions of topographic features, which would also form an interesting set of initial value problems. Furthermore, the case of background flow deserves consideration mostly with westward propagating dipoles, where the existence criteria allows for cases where the dipole speed is both smaller and larger than the Rossby wave zonal phase speed. Exploring the linear stability of topographic LRDs and LRDs in the presence of background flow would also be a natural extension of this thesis.

Indeed, our discussion of tilted dipoles was informative and produced new results to those established previously in Hesthaven et al. (1993), as well as seeing some consistency for different cases. However, similar to our numerical results without tilt, our findings are limited by the time and space restrictions imposed by computational costs. We can overcome the space constraint by incorporating methodology such as cutting, which was used in Hesthaven et al. (1993). Alternatively, other methodology to better understand the dynamics of tilted dipoles is worth constructing for future investigations.

The results of our linear stability analysis for the dipole problem was powerful in extracting the Davies mode found in numerical simulations. Despite this, the resolution constraint is unfortunate and it would be desirable to perform such analysis using a supercomputer. In a similar vein to this, carrying out our Newton method iterations on a supercomputer would prove valuable to know if our method derived in Chapter 8 can be used to extract dipole steady states. If this is the case, then we can perform our linear stability analysis for the many steady states extracted with non-circular boundaries.

To expand on our topographic flow analysis, we can consider different bottom irregularities. Many studies have already investigated the problem of a topographic slope (Hart, 1975a,b; Boland et al., 2012; Chen and Kamenkovich, 2013; Khatri and Berloff, 2018; LaCasce et al., 2019), but more realistic bathymetry could consist of spatially localised ridges and isolated mountains. A number of manuscripts have investigated the effects of bottom features in isopycnal-layered as well as in primitive equation ocean models. Such works have found evidence of changes in the strength of baroclinic instability on either side of topography (e.g., see Abernathy and Cessi, 2014; Youngs et al., 2017; Patmore et al., 2019). In addition, our analysis only dealt with the presence of zonal background flows, however, since topography can affect

the orientation and direction of ocean flows, both zonal and meridional background flows could be the focus of future study.

Beyond this, our attention was with one-dimensional topography, since we argued that two-dimensional topography carries a large computational cost. Regardless, it is valuable to expand on works assuming two-dimensional bottom relief since the flow dynamics could potentially be more complicated than what we have identified in the simpler case we considered. It is also worth noting that despite our linear stability solutions being valuable and resembling high resolution numerical simulations, extending this work to a complete nonlinear or quasi-nonlinear analysis is desirable as topographic interactions are strongly affected by the energy cascade (Rhines, 1977). Despite frameworks such as shallow-water and primitive equations being better equipped to tackle the small-scale topography problem, it would be fascinating to explore how our QG results for large-scale topography change in different model regimes for values of  $\alpha$  and  $\mathcal{A}$ , especially when these push the QG limit and deal with topography of shorter wavelengths.



# Bibliography

- Abernathey, R. and Cessi, P. (2014). Topographic enhancement of eddy efficiency in baroclinic equilibration. *Journal of physical oceanography*, 44(8):2107–2126. pages 5, 154
- Barthel, A., McC. Hogg, A., Waterman, S., and Keating, S. (2017). Jet–topography interactions affect energy pathways to the deep southern ocean. *Journal of Physical Oceanography*, 47(7):1799–1816. pages 5
- Benilov, E. (2000a). The stability of zonal jets in a rough-bottomed ocean on the barotropic beta plane. *Journal of physical oceanography*, 30(4):733–740. pages 6, 129
- Benilov, E. (2000b). Waves on the beta-plane over sparse topography. *Journal of Fluid Mechanics*, 423:263–273. pages 6
- Benilov, E. (2001). Baroclinic instability of two-layer flows over one-dimensional bottom topography. *Journal of physical oceanography*, 31(8):2019–2025. pages 6, 7, 128, 132, 135, 147, 148, 152
- Benilov, E., Nycander, J., and Dritschel, D. (2004). Destabilization of barotropic flows small-scale topography. *Journal of Fluid Mechanics*, 517:359–374. pages 6, 136, 143
- Berloff, P. and Kamenkovich, I. (2013). On spectral analysis of mesoscale eddies. part i: Linear analysis. *Journal of Physical Oceanography*, 43(12):2505–2527. pages 125
- Berloff, P., Kamenkovich, I., and Pedlosky, J. (2009). A mechanism of formation of multiple zonal jets in the oceans. *Journal of Fluid Mechanics*, 628:395–425. pages 131

- Berloff, P., Karabasov, S., Farrar, J. T., and Kamenkovich, I. (2011). On latency of multiple zonal jets in the oceans. *Journal of Fluid Mechanics*, 686:534–567. pages 137
- Berloff, P. and Meacham, S. (1998). On the stability of the wind-driven circulation. *Journal of marine research*, 56(5):937–993. pages 55
- Boland, E., Thompson, A. F., Shuckburgh, E., and Haynes, P. (2012). The formation of nonzonal jets over sloped topography. *Journal of Physical Oceanography*, 42(10):1635–1651. pages 5, 124, 154
- Boyd, J. P. and Ma, H. (1990). Numerical study of elliptical modons using a spectral method. *Journal of Fluid Mechanics*, 221:597–611. pages 5
- Brion, V., Sipp, D., and Jacquin, L. (2014). Linear dynamics of the lamb-chaplygin dipole in the two-dimensional limit. *Physics of Fluids*, 26(6):064103. pages 4, 51, 54, 55, 71
- Burns, K. J., Vasil, G. M., Oishi, J. S., Lecoanet, D., and Brown, B. P. (2020). Dedalus: A flexible framework for numerical simulations with spectral methods. *Physical Review Research*, 2(2):023068. pages 94
- Carnevale, G. F., Vallis, G. K., Purini, R., and Briscolini, M. (1988). Propagation of barotropic modons over topography. *Geophysical & Astrophysical Fluid Dynamics*, 41(1-2):45–101. pages 4, 5, 22, 34, 149
- Chapman, C. C., Hogg, A. M., Kiss, A. E., and Rintoul, S. R. (2015). The dynamics of southern ocean storm tracks. *Journal of Physical Oceanography*, 45(3):884–903. pages 5
- Chelton, D. B., DeSzoeke, R. A., Schlax, M. G., El Naggar, K., and Siwertz, N. (1998). Geographical variability of the first baroclinic rossby radius of deformation. *Journal of Physical Oceanography*, 28(3):433–460. pages 128
- Chelton, D. B., Schlax, M. G., and Samelson, R. M. (2011). Global observations of nonlinear mesoscale eddies. *Progress in oceanography*, 91(2):167–216. pages 1
- Chen, C. and Kamenkovich, I. (2013). Effects of topography on baroclinic instability. *Journal of physical oceanography*, 43(4):790–804. pages 6, 21, 130, 132, 133, 135, 154

- Chen, C., Kamenkovich, I., and Berloff, P. (2015). On the dynamics of flows induced by topographic ridges. *Journal of Physical Oceanography*, 45(3):927–940. pages 5
- Chen, G., Han, G., and Yang, X. (2019). On the intrinsic shape of oceanic eddies derived from satellite altimetry. *Remote Sensing of Environment*, 228:75–89. pages 5
- Davies, J., Khatri, H., and Berloff, P. (2021). Linear stability analysis for flows over sinusoidal bottom topography. *Journal of Fluid Mechanics*, 911:A33. pages 147
- Davies, J., Sutyrin, G., and Berloff, P. (2023). On the spontaneous symmetry breaking of eastward propagating dipoles. *Physics of Fluids*, 35(4). pages ix, 54, 64, 73, 99, 149
- Dong, C., McWilliams, J. C., Liu, Y., and Chen, D. (2014). Global heat and salt transports by eddy movement. *Nature communications*, 5(1):3294. pages 1
- Dryden, H. L., Murnaghan, F. D., and Bateman, H. (1932). *Hydrodynamics*. pages 4
- Gill, A., Green, J., and Simmons, A. (1974). Energy partition in the large-scale ocean circulation and the production of mid-ocean eddies. In *Deep sea research and oceanographic abstracts*, volume 21, pages 499–528. Elsevier. pages 1
- Gille, S. T., Metzger, E. J., and Tokmakian, R. (2004). Seafloor topography and ocean circulation. *Oceanography*, 17(1). pages 5
- Hart, J. (1975a). Baroclinic instability over a slope. part i: Linear theory. *Journal of Physical Oceanography*, 5(4):625–633. pages 6, 154
- Hart, J. (1975b). Baroclinic instability over a slope. part ii: Finite-amplitude theory. *Journal of Physical Oceanography*, 5(4):634–641. pages 6, 154
- Hesthaven, J. S., Lynov, J.-P., and Nycander, J. (1993). Dynamics of nonstationary dipole vortices. *Physics of Fluids A: Fluid Dynamics*, 5(3):622–629. pages 4, 37, 91, 94, 97, 101, 102, 103, 104, 105, 106, 151, 154
- Hogg, N. and Stommel, H. M. (1985). The heton, an elementary interaction between discrete baroclinic geostrophic vortices, and its implications concerning eddy heat-flow. *Proceedings of the Royal Society of London. A. Mathematical and Physical Sciences*, 397(1812):1–20. pages 3
- Karabasov, S., Berloff, P. S., and Goloviznin, V. (2009). Cabaret in the ocean gyres. *Ocean Modelling*, 30(2-3):155–168. pages 27



- Khatri, H. and Berloff, P. (2018). A mechanism for jet drift over topography. *Journal of Fluid Mechanics*, 845:392–416. pages 5, 154
- Khatri, H. and Berloff, P. (2019). Tilted drifting jets over a zonally sloped topography: effects of vanishing eddy viscosity. *Journal of Fluid Mechanics*, 876:939–961. pages 5, 125
- Khvoles, R., Berson, D., and Kizner, Z. (2005). The structure and evolution of elliptical barotropic modons. *Journal of Fluid Mechanics*, 530:1–30. pages 5
- Killworth, P. D. (1980). Barotropic and baroclinic instability in rotating stratified fluids. *Dynamics of Atmospheres and Oceans*, 4(3):143–184. pages 6
- Kizner, Z., Berson, D., and Khvoles, R. (2002). Baroclinic modon equilibria on the beta-plane: stability and transitions. *Journal of Fluid Mechanics*, 468:239–270. pages 5
- Kizner, Z., Berson, D., and Khvoles, R. (2003a). Non-circular baroclinic beta-plane modons: constructing stationary solutions. *Journal of Fluid Mechanics*, 489:199–228. pages 5
- Kizner, Z., Berson, D., Reznik, G., and Sutyrin, G. (2003b). The theory of the beta-plane baroclinic topographic modons. *Geophysical & Astrophysical Fluid Dynamics*, 97(3):175–211. pages 5, 22
- Klocker, A. (2018). Opening the window to the southern ocean: The role of jet dynamics. *Science advances*, 4(10):eaao4719. pages 5
- Kravtsov, S. and Reznik, G. (2021). Monopoles in a uniform zonal flow on a quasi-geostrophic-plane: effects of the galilean non-invariance of the rotating shallow-water equations. *Journal of Fluid Mechanics*, 909:A23. pages 21
- Kravtsov, S. and Reznik, G. M. (2023). Quasi-geostrophic monopoles in a sheared zonal flow: Influence of the beta-effect and variable shear. *Physics of Fluids*. pages 21
- LaCasce, J., Escartin, J., Chassignet, E. P., and Xu, X. (2019). Jet instability over smooth, corrugated, and realistic bathymetry. *Journal of Physical Oceanography*, 49(2):585–605. pages 6, 7, 125, 132, 152, 154
- Larichev, V. and Reznik, G. M. (1976). On two-dimensional solitary rossby waves. In *Doklady Akademii Nauk*, volume 231, pages 1077–1079. Russian Academy of Sciences. pages 4

- Lazar, A., Zhang, Q., and Thompson, A. F. (2018). Submesoscale turbulence over a topographic slope. *Fluids*, 3(2):32. pages 5
- Lorenz, E. N. (1972). Barotropic instability of rossby wave motion. *Journal of the Atmospheric Sciences*, 29(2):258–265. pages 126
- Luzzatto-Fegiz, P. and Williamson, C. (2012). Determining the stability of steady two-dimensional flows through imperfect velocity-impulse diagrams. *Journal of fluid mechanics*, 706:323–350. pages 4
- Marshall, D. (1995). Influence of topography on the large-scale ocean circulation. *Journal of physical oceanography*, 25(7):1622–1635. pages 5
- McWilliams, J. C. (2008). The nature and consequences of oceanic eddies. *Ocean modeling in an eddying regime*, 177:5–15. pages 1
- McWilliams, J. C., Flierl, G. R., Larichev, V. D., and Reznik, G. M. (1981). Numerical studies of barotropic modons. *Dynamics of Atmospheres and Oceans*, 5(4):219–238. pages 4, 34, 149
- Meleshko, V. and Van Heijst, G. (1994). On chaplygin’s investigations of two-dimensional vortex structures in an inviscid fluid. *Journal of Fluid Mechanics*, 272:157–182. pages 4
- Muzylev, S. and Reznik, G. (1992). On proofs of stability of drift vortices in magnetized plasmas and rotating fluids. *Physics of Fluids B: Plasma Physics*, 4(9):2841–2844. pages 4
- Niino, H. and Misawa, N. (1984). An experimental and theoretical study of barotropic instability. *Journal of the atmospheric sciences*, 41(12):1992–2011. pages 6
- Nycander, J. (1992). Refutation of stability proofs for dipole vortices. *Physics of Fluids A: Fluid Dynamics*, 4(3):467–476. pages 4
- Nycander, J. and Isichenko, M. (1990). Motion of dipole vortices in a weakly inhomogeneous medium and related convective transport. *Physics of Fluids B: Plasma Physics*, 2(9):2042–2047. pages 93, 94, 168
- Orlanski, I. and Cox, M. D. (1972). Baroclinic instability in ocean currents. *Geophysical & Astrophysical Fluid Dynamics*, 4(1):297–332. pages 6

- Patmore, R. D., Holland, P. R., Munday, D. R., Naveira Garabato, A. C., Stevens, D. P., and Meredith, M. P. (2019). Topographic control of southern ocean gyres and the antarctic circumpolar current: A barotropic perspective. *Journal of Physical Oceanography*, 49(12):3221–3244. pages 154
- Pedlosky, J. (1964). The stability of currents in the atmosphere and the ocean: Part i. *Journal of the Atmospheric Sciences*, 21(2):201–219. pages 128
- Pedlosky, J. et al. (1987). *Geophysical fluid dynamics*, volume 710. Springer. pages 9
- Provenzale, A. (1999). Transport by coherent barotropic vortices. *Annual review of fluid mechanics*, 31(1):55–93. pages 1
- Radko, T. (2020a). Control of baroclinic instability by submesoscale topography. *Journal of Fluid Mechanics*, 882. pages 6, 7, 120, 128, 135, 152
- Radko, T. (2020b). Rectilinear propagation of quasi-monopolar vorticity patches. *Journal of Fluid Mechanics*, 904. pages 3, 42, 43, 59
- Radko, T. (2021). Playing pool on the beta-plane: how weak initial perturbations predetermine the long-term evolution of coherent vortices. *Journal of Fluid Mechanics*, 915. pages 3
- Radko, T. and Stern, M. E. (1999). On the propagation of oceanic mesoscale vortices. *Journal of Fluid Mechanics*, 380:39–57. pages 2
- Reznik, G. (2010). Dynamics of localized vortices on the beta plane. *Izvestiya, Atmospheric and Oceanic Physics*, 46(6):784–797. pages 4, 41
- Reznik, G. and Kravtsov, S. (2021). Monopoles in a zonal flow with constant shear on a quasi-geostrophic f-plane: Effects of galilean non-invariance. *Physics of Fluids*, 33(11):116606. pages 21
- Reznik, G. M. and Sutyrin, G. G. (2001). Baroclinic topographic modons. *Journal of Fluid Mechanics*, 437:121–142. pages 5, 22
- Rhines, P. B. (1977). The dynamics of unsteady currents. *The sea*, 6:189–318. pages 155
- Shevchenko, I. and Berloff, P. (2015). Multi-layer quasi-geostrophic ocean dynamics in eddy-resolving regimes. *Ocean Modelling*, 94:1–14. pages 27, 57

- Shevchenko, I. and Berloff, P. (2017). On the roles of baroclinic modes in eddy-resolving midlatitude ocean dynamics. *Ocean Modelling*, 111:55–65. pages 27
- Shevchenko, I., Berloff, P., Guerrero-López, D., and Roman, J. (2016). On low-frequency variability of the midlatitude ocean gyres. *Journal of Fluid Mechanics*, 795:423–442. pages 127
- Smith, K. S. (2007). Eddy amplitudes in baroclinic turbulence driven by nonzonal mean flow: Shear dispersion of potential vorticity. *Journal of physical oceanography*, 37(4):1037–1050. pages 124
- Stern, A., Nadeau, L.-P., and Holland, D. (2015). Instability and mixing of zonal jets along an idealized continental shelf break. *Journal of Physical Oceanography*, 45(9):2315–2338. pages 5
- Stern, M. (1975). Minimal properties of planetary eddies. pages 4
- Sutyrin, G. (2007). Ageostrophic instabilities in a baroclinic flow over sloping topography. In *Congrès français de mécanique*. AFM, Maison de la Mécanique, 39/41 rue Louis Blanc-92400 Courbevoie. pages 6
- Sutyrin, G., Hesthaven, J. S., Lynov, J.-P., and Rasmussen, J. J. (1994). Dynamical properties of vortical structures on the beta-plane. *Journal of Fluid Mechanics*, 268:103–131. pages vi, 4, 27, 28, 34, 36
- Sutyrin, G. and Radko, T. (2021). Why the most long-lived oceanic vortices are found in the subtropical westward flows. *Ocean Modelling*, 161:101782. pages 3
- Sutyrin, G., Radko, T., and Nycander, J. (2021). Steady radiating baroclinic vortices in vertically sheared flows. *Physics of Fluids*, 33(3):031705. pages 3
- Sutyrin, G. G. and Flierl, G. R. (1994). Intense vortex motion on the beta plane: Development of the beta gyres. *Journal of Atmospheric Sciences*, 51(5):773–790. pages 2
- Swaters, G. E. (2004). Spectral properties in modon stability theory. *Studies in Applied Mathematics*, 112(3):235–258. pages 4
- Swaters, G. E. and Flierl, G. R. (1989). Ekman dissipation of a barotropic modon. In *Elsevier oceanography series*, volume 50, pages 149–165. Elsevier. pages 4, 34, 149

- Swenson, M. (1987). Instability of equivalent-barotropic riders. *Journal of physical oceanography*, 17(4):492–506. pages 17, 23, 41, 43, 150
- Tamsitt, V., Drake, H. F., Morrison, A. K., Talley, L. D., Dufour, C. O., Gray, A. R., Griffies, S. M., Mazloff, M. R., Sarmiento, J. L., Wang, J., et al. (2017). Spiraling pathways of global deep waters to the surface of the southern ocean. *Nature communications*, 8(1):1–10. pages 5
- Tang, C.-M. (1975). Baroclinic instability of stratified shear flows in the ocean and atmosphere. *Journal of Geophysical Research*, 80(9):1168–1175. pages 6
- Thompson, A. F. (2010). Jet formation and evolution in baroclinic turbulence with simple topography. *Journal of Physical Oceanography*, 40(2):257–278. pages 5, 124
- Thompson, A. F. and Naveira Garabato, A. C. (2014). Equilibration of the antarctic circumpolar current by standing meanders. *Journal of Physical Oceanography*, 44(7):1811–1828. pages 5
- Thompson, A. F. and Richards, K. J. (2011). Low frequency variability of southern ocean jets. *Journal of Geophysical Research: Oceans*, 116(C9). pages 5
- Thompson, A. F. and Sallée, J.-B. (2012). Jets and topography: Jet transitions and the impact on transport in the antarctic circumpolar current. *Journal of physical Oceanography*, 42(6):956–972. pages 5
- Vallis, G. K. (2017). *Atmospheric and oceanic fluid dynamics*. Cambridge University Press. pages 9, 121
- Vanneste, J. (2003). Nonlinear dynamics over rough topography: homogeneous and stratified quasi-geostrophic theory. *Journal of Fluid Mechanics*, 474:299–318. pages 6
- Verkley, W. (1993). A numerical method for finding form-preserving free solutions of the barotropic vorticity equation on a sphere. *Journal of Atmospheric Sciences*, 50(11):1488–1503. pages 5
- Waterman, S. and Hoskins, B. J. (2013). Eddy shape, orientation, propagation, and mean flow feedback in western boundary current jets. *Journal of physical oceanography*, 43(8):1666–1690. pages 137

- Williams, P. D., Read, P. L., and Haine, T. W. (2010). Testing the limits of quasi-geostrophic theory: application to observed laboratory flows outside the quasi-geostrophic regime. *Journal of fluid mechanics*, 649:187–203. pages 128
- Youngs, M. K., Thompson, A. F., Lazar, A., and Richards, K. J. (2017). Acc meanders, energy transfer, and mixed barotropic–baroclinic instability. *Journal of Physical Oceanography*, 47(6):1291–1305. pages 5, 154

# Appendix A

## Paraboloid interpolation

To extract the PVA extrema and the centre coordinate for the dipole propagation at each time step, we implement the method of paraboloid interpolation. We can think about this algorithmically as follows:

- At each time step, identify the PVA extrema on the grid, for example,

$$q_{\max} = \max_{1 \leq m, n \leq N} q_{m,n},$$

where  $m, n$  are the zonal and meridional index positions, respectively, and  $N$  is the total number of grid points in each direction.

- If  $q_{\max} = q_{k,\ell}$ , where  $(k, \ell)$  is the node corresponding to the grid maxima, then consider the neighbours  $q_{k+1,\ell}, q_{k-1,\ell}, q_{k,\ell+1}, q_{k,\ell-1}$  and assume that the local behaviour can be approximated by a paraboloid, i.e.,

$$q_{m,n} = Ax_m^2 + By_n^2 + Cx_my_n + Dx_m + Ey_n,$$

for unknown constant coefficients.

- This yields the system of equations

$$\begin{aligned} q_{k,\ell} &= Ax_k^2 + By_\ell^2 + Cx_ky_\ell + Dx_k + Ey_\ell, \\ q_{k+1,\ell} &= Ax_{k+1}^2 + By_\ell^2 + Cx_{k+1}y_\ell + Dx_{k+1} + Ey_\ell, \\ q_{k-1,\ell} &= Ax_{k-1}^2 + By_\ell^2 + Cx_{k-1}y_\ell + Dx_{k-1} + Ey_\ell, \\ q_{k,\ell+1} &= Ax_k^2 + By_{\ell+1}^2 + Cx_ky_{\ell+1} + Dx_k + Ey_{\ell+1}, \\ q_{k,\ell-1} &= Ax_k^2 + By_{\ell-1}^2 + Cx_ky_{\ell-1} + Dx_k + Ey_{\ell-1}. \end{aligned}$$

- On solving for the constant unknowns, we proceed to find the pair  $(x, y)$  where the maxima occurs on the paraboloid by considering the derivative equations

$$\begin{aligned}\frac{\partial q}{\partial x} = 2Ax + Cy + D = 0 &\implies y = \frac{-2Ax - D}{C}, \\ \frac{\partial q}{\partial y} = 2By + Cx + E = 0 &\implies x = \frac{CE - 2BD}{4AB - C^2}, \quad y = \frac{4BD(1 - A) + C(CD - 2E)}{C(4AB - C^2)}.\end{aligned}$$

- If we apply a similar process for the minima, then we can define the dipole centre, as in Chapter 3.



# Appendix B

## Evolution of tilt

In [Nycander and Isichenko \(1990\)](#), an asymptotic theory of strong tilted dipoles was derived and the following equation for the dipole propagation was obtained:

$$\frac{d\mathbf{U}}{dt} = \frac{\mathbf{U} \times \hat{\mathbf{z}} \beta c \pi y_c(t)}{P_d}, \quad (\text{B.1})$$

where  $c$  is the dipole propagation speed,  $\mathbf{U} = c(\cos \xi, \sin \xi, 0)$  is a vector consisting of the components for the zonal and meridional propagation speeds,  $y_c$  is the meridional center coordinate of the dipole over time,  $\hat{\mathbf{z}} = (0, 0, 1)$ , we have assumed that the radius of the initial separatrix is 1 and

$$P_d = \left| \int Q \mathbf{x} \, dx \, dy \right|, \quad \mathbf{x} = (x, y)^T. \quad (\text{B.2})$$

If we expand out the vector product on the left-hand side, then it follows that

$$\frac{d\mathbf{U}}{dt} = \frac{\beta c^2 \pi y_c}{P_d} (\mathbf{i} \sin \xi - \mathbf{j} \cos \xi), \quad (\text{B.3})$$

and if we apply the chain rule, we can rewrite this in the form

$$\frac{d\xi}{dt} = -\frac{\beta c \pi}{P_d} y_c. \quad (\text{B.4})$$

Following this, if we express  $P_d$  in terms of polar coordinates, then we find that

$$\begin{aligned} P_d &= \left| \int_0^{2\pi} \int_0^1 (-rG(r) \cos \vartheta \sin \xi + rG(r) \sin \vartheta \cos \xi) (\mathbf{i} r \cos \vartheta + \mathbf{j} r \sin \vartheta) r \, dr \, d\vartheta \right| \\ &= \left| \int_0^{2\pi} \int_0^1 G(r) \left[ \mathbf{i} \left( -r^2 \cos^2 \vartheta \sin \xi + r^2 \sin \vartheta \cos \vartheta \cos \xi \right) \right. \right. \end{aligned}$$

$$\begin{aligned}
& + \mathbf{j} \left( -r^2 \sin \vartheta \cos \vartheta \sin \xi + r^2 \sin^2 \vartheta \cos \xi \right) \Big] r \, \mathrm{d}r \, \mathrm{d}\vartheta \Big| \\
& = \left| \int_0^{2\pi} \mathbf{i} \left( \cos^2 \vartheta \sin \xi - \sin \vartheta \cos \vartheta \cos \xi \right) + \mathbf{j} \left( \sin^2 \vartheta \cos \xi - \sin \vartheta \sin \vartheta \cos \xi \right) \mathrm{d}\vartheta \right| M(r) \\
& = \left| \mathbf{i} \left( \sin \xi \int_0^{2\pi} \cos^2 \vartheta \, \mathrm{d}\vartheta - \cos \xi \int_0^{2\pi} \sin \vartheta \cos \vartheta \, \mathrm{d}\vartheta \right) \right. \\
& \quad \left. + \mathbf{j} \left( \sin \xi \int_0^{2\pi} \sin \vartheta \cos \vartheta \, \mathrm{d}\vartheta - \cos \xi \int_0^{2\pi} \sin^2 \vartheta \, \mathrm{d}\vartheta \right) \right| M(r) \\
& = \pi |\mathbf{i} \sin \xi - \mathbf{j} \cos \xi| M(r),
\end{aligned}$$

which means we can deduce that

$$P_n = \pi M(r), \tag{B.5}$$

where

$$M(r) = \left| \int_0^1 r^3 G(r) \, \mathrm{d}r \right|, \tag{B.6}$$

and  $G(r)$  is defined as in Chapter 7.

# Appendix C

## Critical Velocity Shear

To justify our choice of velocity shear in Chapter 9, which we impose in the top fluid layer to induce baroclinic instability, we derive the instability condition for the two-layer QG model with a flat-bottom. In the absence of variable bottom topography, the linearised system of equations become

$$\left(\frac{\partial}{\partial t} + U \frac{\partial}{\partial x}\right) \left[ \nabla^2 \psi_1 + S_1(\psi_2 - \psi_1) \right] + (\beta + S_1 U) \frac{\partial \psi_1}{\partial x} = 0, \quad (\text{C.1a})$$

$$\frac{\partial}{\partial t} \left[ \nabla^2 \psi_2 + S_2(\psi_1 - \psi_2) \right] + (\beta - S_2 U) \frac{\partial \psi_2}{\partial x} = 0. \quad (\text{C.1b})$$

To analyse the stability of this system, we seek normal mode solutions of the form

$$\psi_j = \phi_j e^{ik(x-ct)+i\ell y}. \quad (\text{C.2})$$

On direct substitution of this normal mode form, we can rewrite the system of equations in the matrix form

$$\begin{bmatrix} (c - U)K^2 + cS_1 + \beta & (U - c)S_1 \\ cS_2 & (U - c)S_2 - cK^2 - \beta \end{bmatrix} \begin{bmatrix} \phi_1 \\ \phi_2 \end{bmatrix} = \begin{bmatrix} 0 \\ 0 \end{bmatrix}, \quad (\text{C.3})$$

with  $K^2 = k^2 + \ell^2$ . We retrieve nontrivial solutions when the coefficient matrix has zero determinant, i.e.,

$$Ac^2 + Bc + C = 0, \quad (\text{C.4})$$

where we have

$$A = K^2(K^2 + S_1 + S_2), \quad (\text{C.5})$$

$$B = \beta(S_1 + S_2) + 2K^2(\beta - S_2U) - UK^4, \quad (\text{C.6})$$

$$C = (\beta - S_2U)(\beta - K^2U). \quad (\text{C.7})$$

In the absence of shear in the top fluid layer, we obtain neutral modes, since the eigenvalue solutions are real:

$$c_+ = -\beta/(K^2 + S_1 + S_2), \quad c_- = -\beta/K^2. \quad (\text{C.8})$$

For non-zero velocity shear, we can simplify our problem by setting  $S_1 = S_2 = S$ , which amounts to assuming equal layer depths. Doing this reduces the quadratic coefficients to

$$A = K^2(K^2 + 2S), \quad (\text{C.9})$$

$$B = 2\beta(K^2 + S) - AU, \quad (\text{C.10})$$

$$C = \beta^2 - \beta U(K^2 + S) + SK^2U^2. \quad (\text{C.11})$$

For instability, we require the quadratic equation to have complex solutions, that is we desire  $D = B^2 - 4AC < 0$ , where  $D$  is the discriminant. If we assume an  $f$ -plane approximation ( $\beta = 0$ ), then the instability condition reads as

$$D = K^2(K^2 - 2S) < 0 \implies K^2 < 2S,$$

which tells us that we have baroclinic instability when the nondimensional condition,  $K^2 < 301$ , holds. Extending this analysis to the  $\beta$ -plane, the discriminant satisfies

$$D = AK^2(K^2 - 2S)U^2 + 2A\beta(K^2 + S)U + 4\beta^2S^2 < 0.$$

Assuming the instability condition we found on the  $f$ -plane, it is clear that the coefficient of the quadratic contribution is negative, telling us the quadratic equation for velocity shear has a maximum. Thus, we obtain the instability conditions  $U < U_-$  and  $U > U_+$ . Solving for  $U_{\pm}$ , we have

$$U_{\pm} = \frac{\beta \left[ -(K^2 + S)(K^2 + 2S) \pm \sqrt{K^8 + 6K^6S + 9K^4S^2 + 12K^2S^3 + 20S^4} \right]}{K^2(K^4 - 4S^2)}.$$

Invoking the instability condition  $K^2 < 2S$ , after some simplification, we arrive at the unstable mode condition,  $|U_{\pm}| > \beta/S$ . This is equivalent to requiring the mean PV gradients in the two layers to have opposite sign. Hence, the critical shear in the

top fluid layer is  $U_c = 7.923 \times 10^{-4}$  (or  $2.5 \text{ cm s}^{-1}$  in dimensional form).

# Appendix D

## Topography matrix system

Here, we detail the matrix decomposition for the topographic stability problem discussed in Chapter 9. Since the eigenproblems are coupled and involve combinations of phase shifted eigenmodes, the system is more complicated than the standard eigenvalue problem. We can rewrite the eigenproblems (9.13a) and (9.13b) in the matrix form

$$\mathcal{M}\phi = \omega\mathcal{N}\phi, \quad (\text{D.1})$$

where we define the eigenvector

$$\phi = \begin{bmatrix} \phi_1(k, -N/2) \\ \phi_1(k, -N/2 + 1) \\ \vdots \\ \phi_1(k, N/2 - 1) \\ \phi_1(k, -N/2) \\ \vdots \\ \phi_2(k, N/2 - 1) \end{bmatrix} \quad \text{or} \quad \phi = \begin{bmatrix} \phi_1(-N/2, \ell) \\ \phi_1(-N/2 + 1, \ell) \\ \vdots \\ \phi_1(N/2 - 1, \ell) \\ \phi_1(-N/2, \ell) \\ \vdots \\ \phi_2(N/2 - 1, \ell) \end{bmatrix},$$

for ZR or MR, respectively. In Chapter 9, we solved the ZR and MR systems for combinations of  $\mathcal{A} = 0.05, 0.1, 0.15, 0.2$  and  $\alpha = 1, 3, 5, 10, 15, 20, 25, 30, 40$ . If, for simplicity, we limit our attention to ZR with a single ridge, i.e.,  $\alpha = 1$ , then the matrix  $\mathcal{M}$  can be expressed in the block form

$$\mathcal{M} = k \begin{bmatrix} \mathcal{M}_1 \\ \mathcal{M}_2 \end{bmatrix}, \quad (\text{D.2})$$

where  $\mathcal{M}_1$  is the  $N \times 2N$  matrix

$$\begin{bmatrix} \beta - (k^2 + \ell_1^2)U & 0 & \ddots & 0 & S_1U & 0 & \ddots & 0 \\ 0 & \beta - (k^2 + \ell_2^2)U & \ddots & 0 & 0 & S_1U & \ddots & 0 \\ \ddots & \ddots & \ddots & \ddots & \ddots & \ddots & \ddots & \ddots \\ 0 & 0 & \ddots & \beta - (k^2 + \ell_N^2)U & 0 & 0 & \ddots & S_1U \end{bmatrix}, \quad (\text{D.3})$$

with  $\ell_j = -N/2 + j - 1$  for  $j = 1, 2, \dots, N$ , and  $\mathcal{M}_2$  is the  $N \times 2N$  matrix

$$\begin{bmatrix} 0 & 0 & \ddots & 0 & \beta - S_2U & \hat{H}\mathcal{A}/2\hat{H}_2 & 0 & \ddots & 0 \\ 0 & 0 & \ddots & 0 & \hat{H}\mathcal{A}/2\hat{H}_2 & \beta - S_2U & \hat{H}\mathcal{A}/2\hat{H}_2 & \ddots & 0 \\ \ddots & \ddots & \ddots & \ddots & \ddots & \ddots & \ddots & \ddots & \ddots \end{bmatrix}, \quad (\text{D.4})$$

where the right half of  $\mathcal{M}_2$  is tridiagonal. In a similar manner, the matrix  $\mathcal{N}$  can be expressed in the block form

$$\mathcal{N} = \begin{bmatrix} \mathcal{N}_1 \\ \mathcal{N}_2 \end{bmatrix}, \quad (\text{D.5})$$

with  $\mathcal{N}_1$  being the  $N \times 2N$  matrix

$$\begin{bmatrix} -(k^2 + \ell_1^2 + S_1) & 0 & \ddots & 0 & S_1 & 0 & \ddots & 0 \\ 0 & -(k^2 + \ell_2^2 + S_1) & \ddots & 0 & 0 & S_1 & \ddots & 0 \\ \ddots & \ddots & \ddots & \ddots & \ddots & \ddots & \ddots & \ddots \\ 0 & 0 & \ddots & -(k^2 + \ell_N^2 + S_1) & 0 & 0 & \ddots & S_1 \end{bmatrix}, \quad (\text{D.6})$$

and  $\mathcal{N}_2$  is the  $N \times 2N$  matrix

$$\begin{bmatrix} S_2 & 0 & \ddots & 0 & -(k^2 + \ell_1^2 + S_2) & 0 & \ddots & 0 \\ 0 & S_2 & \ddots & 0 & 0 & -(k^2 + \ell_2^2 + S_2) & \ddots & 0 \\ \ddots & \ddots & \ddots & \ddots & \ddots & \ddots & \ddots & \ddots \\ 0 & 0 & \ddots & S_2 & 0 & 0 & \ddots & -(k^2 + \ell_N^2 + S_2) \end{bmatrix}. \quad (\text{D.7})$$

This system can be solved for  $k = -N/2, -N/2+1, \dots, N/2-1$  and  $\mathcal{A} = 0.05, 0.1, 0.15, 0.2$ .

Since the phase shift in the eigenmodes is due to the presence of  $\alpha$ , increasing the number of ridges is equivalent to permuting entries in the matrix  $\mathcal{M}$  and multiplying the value of  $\mathcal{A}$  by  $\alpha$  (the matrix  $\mathcal{N}$  is the same for all values of  $\alpha$ ). In the case of MR, the process is similar, but we fix  $\ell$  and introduce  $k_j = N/2 + j - 1$  for  $j = 1, 2, \dots, N$ .